Theoretical and Experimental Improvements for Fast Microdialysis

by

Khanh Thieu Ngo

B.S. Chemical Engineering, University of Illinois at Urbana-Champaign, 2013

Submitted to the Graduate Faculty of the

Dietrich School of Arts and Sciences in partial fulfillment

of the requirements for the degree of

Doctor of Philosophy

University of Pittsburgh

2020

UNIVERSITY OF PITTSBURGH

DIETRICH SCHOOL OF ARTS AND SCIENCES

This dissertation was presented

by

Khanh Thieu Ngo

It was defended on

July 2, 2020

and approved by

Alexander Star, Professor, Chemistry

Shigeru Amemiya, Professor, Chemistry

Xinyan Tracy Cui, Professor, Bioengineering

Thesis Advisor: Stephen Weber, Chemistry

Theoretical and Experimental Improvements for Fast Microdialysis

Khanh Thieu Ngo, PhD

University of Pittsburgh, 2020

Microdialysis is the most widely used technique for intracranial sampling. Its versatility prompts important applications, from bedside traumatic brain injury monitoring to psychological disorder treatment. However, historically microdialysis methods have a time resolution of 5-30 mins, and thus are not well suited to obtain physiological information, such as rates of extracellular processes or the relationship between neurochemical levels and behavior. Building from recent work in our laboratory, we developed instrumentation for making dopamine measurements in awake and freely moving rats over extended periods at one-minute time resolution using microdialysis sampling analyzed with online HPLC (Fast Microdialysis).

Fast Microdialysis was used to investigate the beneficial effects of the anti-inflammatory drug dexamethasone (DEX) to penetration injury caused by dialysis probe implantation. Retrodialysis of DEX was found to potentiate both basal levels and stimulated release of striatal DA. Applying Fast Microdialysis to behavioral studies necessitated creation of a rotating operant chamber. Using this device, both trained- and untrained- animal's behavior correlated with DA release, however with different characteristics. Robust and fast determination of DA allowed for creation of new microdialysis techniques in the non-steady state regime to investigate morphology and neurotransmitter regulation. Thus, a comprehensive mathematical model was created to analyze transient responses measured by Fast Microdialysis. A robust, adaptive random sampling simplex approach was used to fit the model to transient data. Striatal tissue tortuosity, porosity and the reuptake rate constant of DA were determined from a single transient response on awake and freely moving rats.

Table of Contents

List of Tables

List of Figures

List of Equations

Preface

The most important lesson I learned during my graduate research is that you learn from failure, not from success. The second most important is that one cannot become a good scientist without an unwavering devotion for good science. Always learn, always strive to be better. That is my secret.

I thank my advisor, Professor Stephen Weber, for his generous and thoughtful guidance thorough my years at the University of Pittsburgh. His insightful advice and his continual push for a better understanding of chemistry has instilled in me a solid foundation to become a better scientist. I thank my dissertation committee members for their assistance. I thank my friends and colleagues in the Weber research group, particularly Steve Groskreutz and Anthony Horner for their help when I was a junior graduate student. I thank members of the University of Pittsburgh Machine Shop and Electronic Shop, particularly Tom Gasmire, for their support with creating and repairing my analytical instrument.

I thank my father Nguyen Chanh Ngo, from whom my passion of chemistry and science I was gifted from a very young age. I thank my wife, Vy Thi Yen Nguyen, whose love and support have helped pushed me through the hardest moments of my graduate research career.

1.0 Introduction

1.1 Fundamentals of Brain Microdialysis

The study of neurochemistry is vital to our continual quest for a better understanding of the nervous system. Within this vast field, *in vivo* measurements of neurotransmitters has shed light to the neurochemical processes behind learning and memory (dopamine, glutamate[1,2]), neurodegenerative disorders (dopamine[3], glutamate[4,5], serotonin[6]), and immune response (histamine[7], acetylcholine[8]), to name a very select few. These *in vivo* measurements are typically made with sensors that measure solutes directly in the brain tissue[9,10], probes that obtain a sample from the brain[11,12], or imaging techniques that measure a neurotransmitter's activities via a radioactive ligand[13,14]. Particularly, microdialysis has become the most extensively used technique[15,16] in the last two decades. The research described in this dissertation focuses on improving *in vivo* microdialysis measurements of dopamine (DA) in the rat striatum or nucleus accumbens, both of which have been the subject of numerous investigations to behavior[17-21], diseases[22-26] and related pharmacology[27-29].

Microdialysis is a solute sampling and delivery technique. The principle element of the microdialysis technique[12,15,30-35] is the microdialysis probe, the object that when inserted into a medium (e.g., brain tissue or agar gel) and perfused, enables sampling of and/or delivery to a small region of medium around the probe. The microdialysis probe consists of an inlet, an outlet, a cannula which houses the inlet and outlet, and a porous, semi-permeable dialysis membrane at end of the cannula **(**Figure 4.2-1**).** The probe is perfused typically with a solution that is isosmotic to and mimics the electrolyte balance of the external medium (e.g., artificial cerebral spinal fluid

when sampling from brain). The porous membrane allows solutes of molecular weight defined by the membrane's characteristic molecular weight cut-off (MWCO) to diffuse from the external medium through the membrane into the probe lumen (i.e. microdialysis sampling) or vice versa (i.e. retrodialysis). The solution, now called dialysate, passes out of the probe to an outlet, where is it collected for analysis.

1.2 Microdialysis' Time Resolution and Quantitative Analysis Problems

Microdialysis is typically coupled with analytical techniques for separation (e.g. liquid chromatography[36-38], electrophoresis[39-41]) and detection of analytes (e.g. amperometry[36,37,42], mass spectrometry[43-45]). The experiment can be online, where the probe outlet is connected directly to the analytical instrument for immediate analysis, or offline, where dialysate is collected and stored frozen prior to analysis. Naturally, microdialysis' distinguishing feature is its superior versatility in both sampling and detection, which has helped microdialysis to become the most popular *in vivo* analysis technique. To date, there are nearly 35,000 articles within the microdialysis topic on SciFinder compared to about 2,500 for the second most popular technique, Fast-Scan Cyclic Voltammetry (FSCV).

However, microdialysis suffers from two problems. One is speed. It is a relatively slow technique, where the typical sampling interval is on the order of 5-30 min [12,46,47] which contrasts with FSCV where sub-second measurements are routine[48]. Better time resolution for microdialysis is therefore highly desirable. The other problem is inferring solute concentrations in the brain extracellular space from the concentrations measured in the dialysate. Classical FSCV lacks the capability to directly determine basal level concentrations of neurotransmitters, but recently

developed related techniques[49-53] are potentially capable of estimating basal concentrations in the minute or less time regime. Microdialysis employs an experimental protocol[12,54,55] to obtain quantitative estimates of the solute concentrations in the brain. The experimental protocol is based on a mathematical model[56-66] with a set of assumptions and accuracy limitations stemming from these assumptions. Therefore, there are opportunities to create quantitative methods based on microdialysis that can improve the accuracy of estimates of solute concentrations in the brain and do so with a faster timescale than currently possible. This will lead to insights into biological processes that govern such concentrations.

1.3 Evolution of Fast Microdialysis

1.3.1 Pioneering Period of High Time Resolution Analysis for Fast Microdialysis

Efforts were made early on (1980s) in the development of the microdialysis technique to improve not only the dialysate analysis time but also sample dispersion during fluidic transport[67]. Justice and colleagues leveraged the then recent advancements in smallbore packed chromatographic columns and high-performance liquid chromatography to create a method for online *in vivo* microdialysis determination of DA at 5-min time resolution[68]. The importance of a faster time resolution needed to infer biological information was recognized, and offline measurements with 1-min sampling followed shortly[69-71]. Justice and colleagues established the technical feasibility and possibility to observe rapid fluctuations in neurotransmitter concentrations using microdialysis. However, technological challenges in separation and detection of low level neurotransmitters hindered adoption of high time-resolution microdialysis well into the 2000s.

Andrews *et al*.[72] found that 82% of microdialysis publications in 2012 were at 20-min time resolution and none was faster than 5-min. The opportunity to infer biological information from rapid fluctuations was unfortunately overlooked in favor of pharmacological and toxicological applications[73] where time resolution is generally not a pressing need[72].

1.3.2 Renewed Interest to High Time Resolution

With the maturity of high-performance liquid chromatography instrumentation, particularly the availability of sub 2 μm porous stationary phase particles, efforts[74,75] were renewed late in the 2000s to develop an online, *in vivo* microdialysis technique that is capable of continuous, hours long determination of low level (nM) neurotransmitters (Fast Microdialysis). Andrews and colleagues optimized their separation on commercially available HPLC instrument and analytical scale columns to achieve a 2-3 min time resolution online detection of serotonin (5-HT)[47,72]. Within the Weber group, prior the research described in this dissertation, capillary liquid chromatography systems were designed and optimized to demonstrate technical feasibility of a 1-min time resolution online detection of 5-HT[74,76,77] and dopamine[78] (DA), separately. Significant progress was also made with offline analysis. Kennedy and colleagues developed a segmented flow microdialysis technique that when coupled with mass spectrometry was capable of 2 s determination of neurotransmitters and metabolites[79-81]. These works presented experimental evidence validating the hypothesis that Justice had made three decades prior: there is biological information in the fluctuation of neurotransmitter concentrations in the brain observed by Fast Microdialysis.

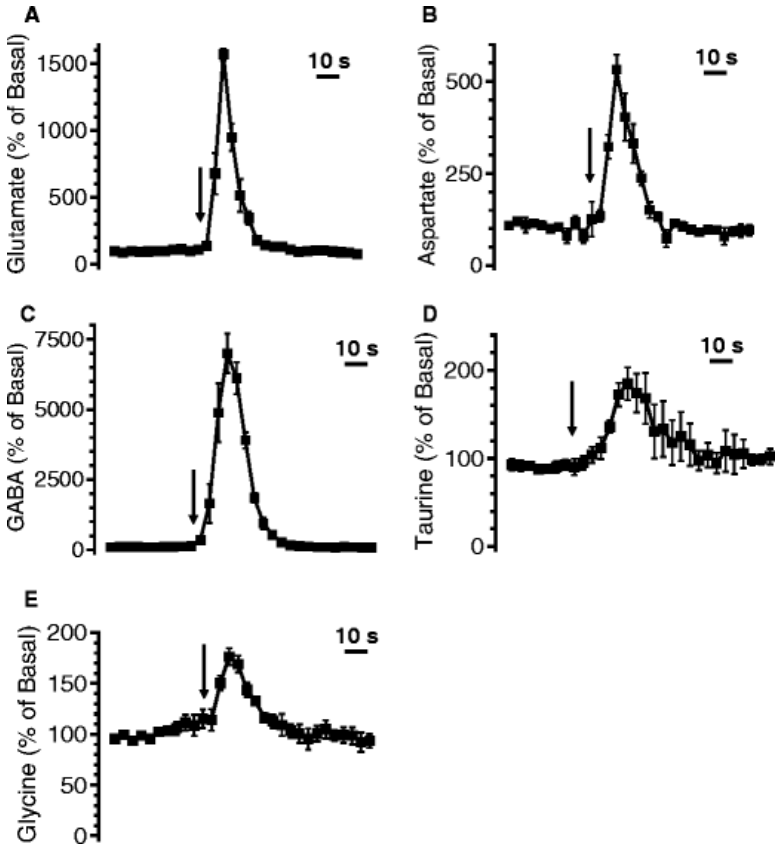

Figure 1.3-1. Seconds regime determination of (A) glutamate (B) aspartate (C) GABA (D) taurine (E) glycine using microdialysis sampling with segmented flow.

Reprinted with permission with permission from Wang, M.; Hershey, N. D.; Mabrouk, O. S.; Kennedy, R. T. Anal Bioanal Chem 2011**, 400, 2013-2023.**

1.4 Development of Microdialysis Theories

Microdialysis theories describe the mass transport of solute across the tissue to the probe, driven by diffusive flux resulting from solute concentration gradients between the tissue and the probe. Early work in microdialysis theory only considered this mass transport process[31,56,57], and did not considered other processes in the brain. The microdialysis probe is cylindrical, thus mass transport solutions in the cylindrical coordinates is most appropriate. Nevertheless, there are also

approximations[62,82,83] in the Cartesian coordinates to simplify the calculations. Bungay, Chen and Morrison have provided the most comprehensive discussion of mass transport in microdialysis in the cylindrical coordinates. Bungay *et al.* (1990)[84] used the concept of resistance/permeability to account for individual contribution of each transport layer (probe, probe membrane, and tissue) to the overall mass transport. He also considered biological processes that remove solute from the extracellular space and created a simple steady-state formulation for quantitative microdialysis that has been widely adopted. Bungay (2003)[65] later revised his steady-state model to include the trauma layer resulting from penetration injury during probe implantation[85-87]. Another solution for steady-state mass transport that incorporates a trauma layer was obtained by Chen (2006)[88]. Morrison *et al.* (1991)[60] developed the model with the fewest assumptions, as far as we are aware. It includes two source and uptake terms, for 'metabolism' and for exchange between brain tissue and capillary blood. The solution describes mass transport in the transient state. The mathematical expressions from Morrison's solution are very complex. Over the years, Bungay and colleagues simplified the mathematics of mass transport, and published (2011)[61] the most up-to-date model for transient microdialysis mass transport. He adapted an earlier solution by Chen (2002)[58,59] to create one-dimensional (1D) and two-dimensional (2D) mass transport models. The many models developed over the years, however, create confusion as to which model is most appropriate for experimental use. Furthermore, we note that none of these models involves the analytical system that follows microdialysis sampling. They only describe mass transport across the probe. The few models[77,89] that describe solute concentration in the dialysate as observed by the analytical system, on the other hand, do not involve microdialysis sampling. The research described in this dissertation, introduced below, sought to rectify both these issues.

1.5 Theoretical and Experimental Improvements for Fast Microdialysis

Prior the research described in this dissertation, the Weber group had developed one-minute *in vivo* measurements of neurotransmitters by microdialysis with online capillary HPLC, first for serotonin[74,76,77] and later for dopamine[78] (DA). This work was primarily a technical demonstration for online *in vivo* measurements with Fast Microdialysis to establish its feasibility. The instrumentation and data analysis were not capable of long-term studies, of correlating measurements of DA with learned behavior, or of using the improved time resolution to understand physiological processes in the brain. Furthermore, there were technical hurdles to significantly improving the time resolution of these measurements. The subsequent research, summarized below, addressed these issues, and established novel applications for brain microdialysis.

1.5.1 Investigating the Effects of a Drug Treatment

Michael and colleagues through a series of elegant works have found that microdialysis probe implantation causes trauma in the brain tissue surrounding the probe. This triggers an immune response adverse to good microdialysis measurements[62,63,65,88,90,91]. Their histology and FSCV studies found that this immune response can be mitigated with an anti-inflammatory drug[86,87,92,93] (e.g. Dexamethasone, DEX). The DEX treatment restored evoked DA response in injured tissue, however, tissue viability could not be conclusively determined[86,87]. Thus, we used Fast Microdialysis to investigate the effects of DEX treatment to basal concentrations and evoked DA responses in the rat striatum. A simultaneous Fast Microdialysis and local field potential measurement was used to elucidate tissue viability. We also made improvements in Fast Microdialysis instrumentation and data analysis to accommodate these experiments.

1.5.2 Rotating Operant Chamber for Fast Microdialysis

The improved Fast Microdialysis has a limit of quantitation of 1 nM, which is sufficient for DA determination in the nucleus accumbens[94], the brain region that is responsible for reward and reinforcement[95]. At the time resolution of one minute, the rapid fluctuation of DA concentrations could encode information related to the animal's behavior[69-71]. Existing behavioral instrumentation was not suitable for Fast Microdialysis. Thus, a rotating operant chamber was created to implement Fast Microdialysis to behavioral studies. The rotating operant chamber eliminates the need for use of a liquid swivel that adds band broadening and reduces time resolution of the analysis; while it also allows the animal to move freely and respond to stimuli without twisting of the capillaries supporting the dialysate flow. This was accomplished by modifying a BASi raturn with an on-board controller and adding operant behavior components that rotate with the raturn. Using the rotating operant chamber, rats were trained to perform learned tasks, while DA concentrations were determined with Fast Microdialysis. Correlation between the animal's behavior and rapid releases of DA were interpreted using Short Time Fourier Transform[96].

1.5.3 Theoretical and Experimental Framework for Analysis of Transient Response

From the two prior works[97,98], it was established definitively that there is biologically relevant information encoded in DA changes measured at one-minute time resolution. Together with the much-needed experimental work to increase the time resolution of the microdialysis measurements, theorical improvement is also necessary to describe the relationship between measured solute concentration at the detector and the neurochemical environment outside the probe. Theories exist[32,56-64,83,84,89,99-102] to describe the effects of tissue morphology and solute

uptake rate on the relationship between the concentration of a solute added to the perfusate going into the probe and the measured solute concentration coming out of the probe. However, there is no coherent and comprehensive mathematical description of how solute concentration, tissue morphology, and uptake rate govern the solute concentration profile at the detector measured by Fast Microdialysis in the non-steady state regime ("transient response") that is not in differential equations form. Thus, a new microdialysis technique (Comprehensive Quantitative Microdialysis, CQM) was developed to analyze transient responses measured with Fast Microdialysis and elucidate the relevant biological and systemic factors that affect the transient response.

2.0 Monitoring Dopamine Responses to Potassium Ion and Nomifensine by in vivo Microdialysis with Online Liquid Chromatography at One-Minute Resolution

The following chapter is reprinted (adapted) with permission from Ngo, K. T.; Varner, E. L.; Michael, A. C.; Weber, S. G. *ACS Chem Neurosci* **2017**, *8*, 329-338.

2.1 Chapter Summary

Recently, our laboratory has demonstrated the technical feasibility of monitoring dopamine at one-min temporal resolution with microdialysis and online liquid chromatography. Here, we monitor dopamine in the rat striatum during local delivery of high potassium/low sodium or nomifensine in awake-behaving rats. Microdialysis probes were implanted and perfused continuously with or without dexamethasone in the perfusion fluid for four days. Dexamethasone is an anti-inflammatory agent that exhibits several positive effects on the apparent health of the brain tissue surrounding microdialysis probes. Dopamine was monitored one or four days after implantation under basal conditions, during 10-min applications of 60 mM or 100 mM K^+, and during 15-min applications of 10 μM nomifensine. High K^+ or nomifensine were delivered locally by adding them to the microdialysis perfusion fluid using a computer-controlled, low-dead-volume six-port valve. Each day/K^+/dexamethasone combination elicited specific dopamine responses. Dexamethasone treatment increased dopamine levels in basal dialysates (*i.e.*, in the absence of K^+ or nomifensine). Applications of 60 mM K^+ evoked distinct responses on days one and four after

probe implantation, depending upon the presence or absence of dexamethasone, consistent with dexamethasone's ability to mitigate the traumatic effect of probe implantation. Applications of 100 mM K^+ evoked dramatic oscillations in dopamine levels that correlated with changes in the field potential at a metal electrode implanted adjacent to the microdialysis probe. This combination of results indicates the role of spreading depolarization in response to 100 mM K^+. With one-min temporal resolution we find that it is possible to characterize the pharmacokinetics of the response to the local delivery of nomifensine. Overall, the findings reported here confirm the benefits arising from the ability to monitor dopamine via microdialysis at high sensitivity and at high temporal resolution.

2.2 Introduction

Microdialysis has been widely employed for intracranial chemical monitoring.[30,33,45,103,104] Microdialysis probes are robust and can be used in both anesthetized and awake animals ranging from rodents to primates, including human patients. They collect a broad array of small molecules below the molecular weight cutoff of the dialysis membrane, several varieties of which are available in the required hollow-fiber format. The dialysis process produces samples that are free of tissue fragments, proteins, blood, and other forms of contamination. The dialysate samples can either be collected, stored, and analyzed later,[105-107] or analyzed in near-real time by online methods.[67,108] Online analysis decreases the chance of sample degradation during storage and eliminates delays in obtaining the results. Online analysis is often performed with liquid chromatography (LC)[35,71,109] or capillary electrophoresis[110,111] coupled to detectors employing laser-induced fluorescence,[112,113] mass spectrometry,[114,115] or electrochemistry.[116-119]

Recent progress in improving the time resolution of microdialysis sampling of neurotransmitters builds on earlier work.[109] Developments in LC separation speed have enabled online collection and analysis of serotonin (5-HT) at three-[72] and later two-min intervals[47] on commercial instruments. We have used capillary LC with electrochemical detection to determine both dialysate DA and 5-HT (separately) in near real time at one minute intervals.[76-78] Electrical stimulation to induce DA transients demonstrated that our approach yields an overall time resolution of at least one-minute.[78]

While there are many studies of DA release induced by retrodialysis of high K^+/low Na^+ at modest time resolution, we are not aware of any at one-minute time resolution. It would be of interest to learn what information is gained by measuring at this time resolution. Thus, in this study, we describe the remarkable variety of dialysate dopamine transients elicited by a ten-minute high K^+/low Na^+ stimulation[120] (60 mM or 100 mM K^+; we denote these as "high K^+" below). Having seen oscillations in 5-HT concentrations resulting from high K^+ stimulation, we anticipated that DA may respond similarly. Thus, we used a 10-min stimulation to accommodate the 2-3 min period of the oscillations.[77] Responses in awake rats were measured one- and four days after probe implantation. One group of animals had microdialysis probes perfused with artificial cerebrospinal fluid only (aCSF). A second group had microdialysis probes perfused continuously with aCSF containing dexamethasone[87,90,121,122] via retrodialysis. We refer to the latter set of probes as "local dexamethasone by retrodialysis" probes (LDR probes), and the former as "control" probes.

2.3 Methods

2.3.1 Chemical and Materials

Chemicals (disodium EDTA, sodium acetate, sodium 1-octanesulfonate (SOS), acetonitrile, glacial acetic acid, NaCl, KCl, $CaCl_2$, $MgCl_2$, and NaH_2PO_4) were purchased from either Fisher Scientific (Fair Lawn, NJ) or Sigma (St. Louis, MO) and used as received. Dexamethasone sodium phosphate was from APP Fresenius Kabi USA, LLC, Lake Zurich IL. Ultra-pure water used was filtered using a Millipore Mili-Q Synthesis A10 system (Belford, MA).

Artificial cerebrospinal fluid (aCSF: 142 mM NaCl, 1.2 mM $CaCl_2$, 2.7 mM KCl, 1.0 mM $MgCl_2$, and 2.0 mM NaH_2PO_4, pH 7.4) was used as the perfusion fluid for the microdialysis probes. The high K^+ aCSF solutions were kept isotonic by lowering the Na^+ concentration (60 mM K^+ aCSF: 84.7 mM NaCl, 1.2 mM $CaCl_2$, 60 mM KCl, 1.0 mM $MgCl_2$, and 2.0 mM NaH_2PO_4. 100 mM K^+ aCSF: 44.7 mM NaCl, 1.2 mM $CaCl_2$, 100 mM KCl, 1.0 mM $MgCl_2$, and 2.0 mM NaH_2PO_4). Dexamethasone sodium phosphate (APP Pharmaceuticals LLC, Schaumburg, IL) and nomifensine maleate (Sigma-Aldrich, St. Louis, MO) were diluted in aCSF. The microdialysis perfusion fluids were filtered with Nalgene sterile filter units (Fisher, Pittsburgh, PA; PES 0.2 μm pores).

2.3.2 Probe Construction

Concentric-style microdialysis probes (4 mm membrane length) were built in-house (200 μm I.D, 280 μm O.D, 13 kDa MWCO Spectra/Por hollow fiber, Spectrum Laboratories Inc. Rancho, Dominquez, CA) see[78] for details. The probe inlet consists of 100 cm of fused silica

capillary (75 μm I.D., 150 μm O.D. Polymicro Technologies, Phoenix, AZ). The outlet capillary is of the same type but 115 cm in length. Each capillary is connected to 10 cm of 75 μm I.D., 360 μm O.D. fused silica to facilitate the connection of inlet and outlet lines to nanobore injection valves (described below). We estimate based on system volumes and perfusion flow rate that transport of a stimulant slug to the probe membrane takes 9.84 minutes, and a sample slug takes 9.05 minutes from the probe to the injection valve. The difference is mainly due to the internal volume of the probe which counts towards the inlet flow path. Prior to use, the probes were soaked in 70% ethanol and then immersed in and flushed with filtered perfusion fluid (aCSF or aCSF with dexamethasone) for several hours before implantation into the rat.

2.3.3 Surgical Procedure and Implantation

All use of animals was approved by the University of Pittsburgh Institutional Animal Care and Use Committee. Prior to surgery, rats (male Sprague−Dawley, 250−350g, Charles River, Raleigh, NC) were acclimated overnight to a Raturn Microdialysis Bowl (MD-1404, BASI, West Lafayette, IN). The next day, rats were anesthetized with isoflurane (5% v/v induction, 2.5% v/v maintenance) and implanted with microdialysis probes using aseptic stereotaxic surgical techniques. Using flat skull coordinates, each probe was slowly lowered into the striatum (1.6 mm anterior, 2.5 mm lateral from bregma, and 7.0 mm below the dura) at 5 μm/s using a micropositioner (David Kopf Instruments Model 2660, Tujunga, CA). The histology of the probe track in the striatum using these same coordinates has been documented numerous times by our group.[86,122] The probe was secured with bone screws and acrylic cement and the incision was closed with sutures. Anesthesia was removed and the animals were returned to the Raturn system and given free access to food and water for the duration of the experiment. Continuous perfusion

was maintained for the entire duration of the experiment. During procedures involving dexamethasone, the probe was perfused with 10 μM dexamethasone for the first 24 hours and then with 2 μM dexamethasone for the remainder of the experiment.

2.3.4 Online Microdialysis-LC-EC

The microdialysis/liquid chromatography system was similar to the one previously described.[76] A schematic diagram is shown in Figure 2.7-28. Perfusate was introduced using a syringe pump (Harvard Apparatus, Holliston, MA), running at 0.610 μL/min. The perfusate syringe contained 1.0 mL of perfusate and was refilled every 24 hours, at least 3 hours prior to any *online* measurement. To facilitate the introduction of a stimulant-containing solution, we used a 6-port nanobore injection valve (electrically actuated, Valco Instruments, Houston, TX) to introduce solution from a 9.5 μL fused silica loop (280 μm I.D., 360 μm O.D, Polymicro Technologies, Phoenix, AZ). The valve was configured so that the loop could be loaded with stimulant-containing solution while perfusate flow is maintained. To introduce the stimulating solution, the valve position was switched from load to inject position by computer control at predetermined times for durations equal to the stimulus duration. So-called timed injections suffer less spreading of the concentration profile at the trailing edge than injections that permit the entire loop to be pushed into the inlet capillary. During valve position switching, flow is interrupted for 105 milliseconds. The stimulus reaches the probe 9.8 minutes after switching. Therefore, any DA response due to switching the position of the valve would be seen approximately ten minutes prior to the response to the stimulus. We do not see any such response to the valve position switching itself in the data.

The outlet of the microdialysis probe carrying dialysate was connected directly to the inlet of the injection valve of the LC system (8-port nanobore, electrically actuated, Valco Instruments,

Houston, TX) so that the dialysate is loaded into one of the two 600 nL, fused-silica sample loops (75 μm I.D., 360 μm O.D, Polymicro Technologies, Phoenix, AZ). While one sample loop is being loaded, the contents of other sample loop are injected into the column, separated, then detected at the end of the column using amperometric electrochemical detection. The dialysate flow from the brain to the detector is uninterrupted, except for during injection valve switching (230 milliseconds), thus achieving *in vivo,* online detection of dopamine.

For the chromatography, 4.5 cm long, 150 μm ID fused silica capillary columns were packed in-house at 20,000 psi with 1.7 μm BEH C18 reverse-phase particles (Waters, Milford, MA). Mobile phase was delivered using a Shimadzu LC-30DA pump with a maximum pressure of 18,900 psi (130 MPa) to achieve a flow rate of 7.5 μL/min during experiments. Column and injector were heated to 40 ^{o}C.

Separation of dopamine was achieved using ion-pairing reversed phased liquid chromatography with mobile phase containing 100 mM sodium acetate, 1.75 mM SOS, 0.150 mM EDTA, 3% v/v acetonitrile and 2% v/v acetic acid. The mobile phase was filtered and degassed with three passes of vacuum filtration using 0.22 μm nylon filter (Osminics, Minnetonka, MN). Analytes were detected at 400 mV (vs. Ag/AgCl 3M NaCl) using BASi radial-style flowcell, 3-mm glassy carbon electrode with 25 μm thick gaskets, and BASi Epsilon potentiostat (West Lafayette, IN).

2.3.5 Experimental Design

Microdialysis probes were implanted and dialysate dopamine was measured in awake, freely moving male Sprague-Dawley rats. Each probe was either perfused continuously for four

days with aCSF containing dexamethasone (via retrodialysis) or aCSF alone (control). On day 1 and day 4 after surgery (approximately 24 h and 96 h, respectively), once per hour, each rat was stimulated with 10-min retrodialysis of 60 mM K+ and 100 mM K+ (twice each), and 15-min retrodialysis of 10 μM nomifensine (at the end of the experiment, when possible). Stimulant/drug retrodialysis times were achieved by controlling the valve position (see Figure 2.7-28).

Dopamine transients as well as basal level dopamine in the dialysate were measured continuously at one-minute time resolution for the entire duration of the experiment, approximately six hours. Data were processed using an automated MATLAB script. For the purpose of principal component analysis, the 11 contiguous peaks that deviate the most from basal level during the K+ stimulation window were identified as the transient by the script. All MATLAB-identified peaks were confirmed by a human.

2.3.6 LC-EC and Field Potential Simultaneous Measurement

In a second set of experiments dopamine and the field potential were measured simultaneously during potassium stimulations. For the field potential measurements, a tungsten wire (50 μm diameter, 4 mm length) was glued next to the microdialysis probe so that the wire was parallel to the probe membrane, with approximately 0.5mm between the wire and the membrane (see Figure S29). A second tungsten wire was used as a reference and placed in the contralateral hemisphere of the brain. Both wires were attached to a larger nickel/chromium wire for electrical connection and protected with a plastic covering. Measurement were made using a Powerlab/4sp running LabChart Pro (AD Instruments). A 0.1 Hz low pass filter was used.

2.4 Results and Discussion

2.4.1 One-minute Resolution Online Measurement of Dopamine

Separation of dialysate using the online system under conditions described in the experimental section result in completely resolved DA peaks, with DA retention times of approximately 44 s (Figure 2.4-1). Chromatograms were obtained continuously, with injections occurring once every minute for the entire six- to eight-hour duration of the experiment. For all conditions, there are no other peaks in the chromatogram near the DA peak. The DA retention time when measured during an online experiment is within 3% of the retention time measured from aqueous DA standards, as well as DA-spiked dialysate. Dialysate DA concentrations are calculated from average slopes and intercepts from a pair of linear calibration curves obtained prior to and after each day-long experiment (Figure 2.7-1). The slopes and intercepts from the two calibration curves were typically within 5% of each other. Figure 2.4-2 shows a DA dialysate concentration obtained one day after implantation of an LDR probe. The five transients are (from left to right) the dialysate dopamine responses to 10-min stimulations with 60 mM K^+ (twice), 100 mM K^+ (twice), and a 15-min stimulation with 10 μM nomifensine. Both K^+ and nomifensine were, like the dexamethasone, delivered through the probe.

Previous studies with K^+ stimulated 5-HT[47] and DA,[123] using a range of K^+ concentrations and stimulation times (25 – 120 mM K^+ for 1-10 min) found that a 50-60 min recovery interval between stimulations is sufficient to avoid the influence of a prior stimulation on the effect of a following stimulation. The range of potassium concentrations and stimulation times encompasses our experimental conditions. Thus, during this work, we allowed a 50-min recovery time between each stimulus. Each of these data sets contains three measurable quantities: basal levels, transients

caused by 10 min K^+ stimulations, and the transient caused by the 15-min nomifensine stimulation. These will be assessed in that order below.

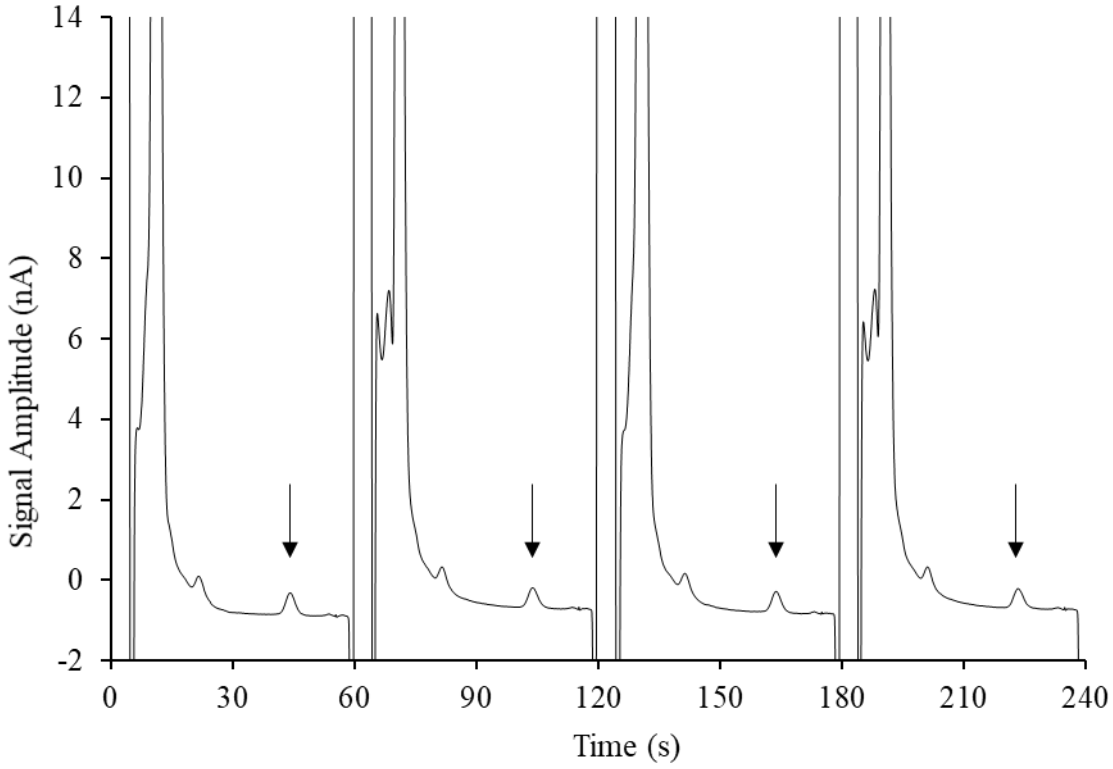

Figure 2.4-1. Four chromatograms of striatal dialysate by online LC-EC from a longer sequence of injections. Consecutive 500 nL samples of dialysate were collected under basal conditions and analyzed online at one-min intervals. The dopamine peaks appear 44 s after each sample is injected onto the capillary column.

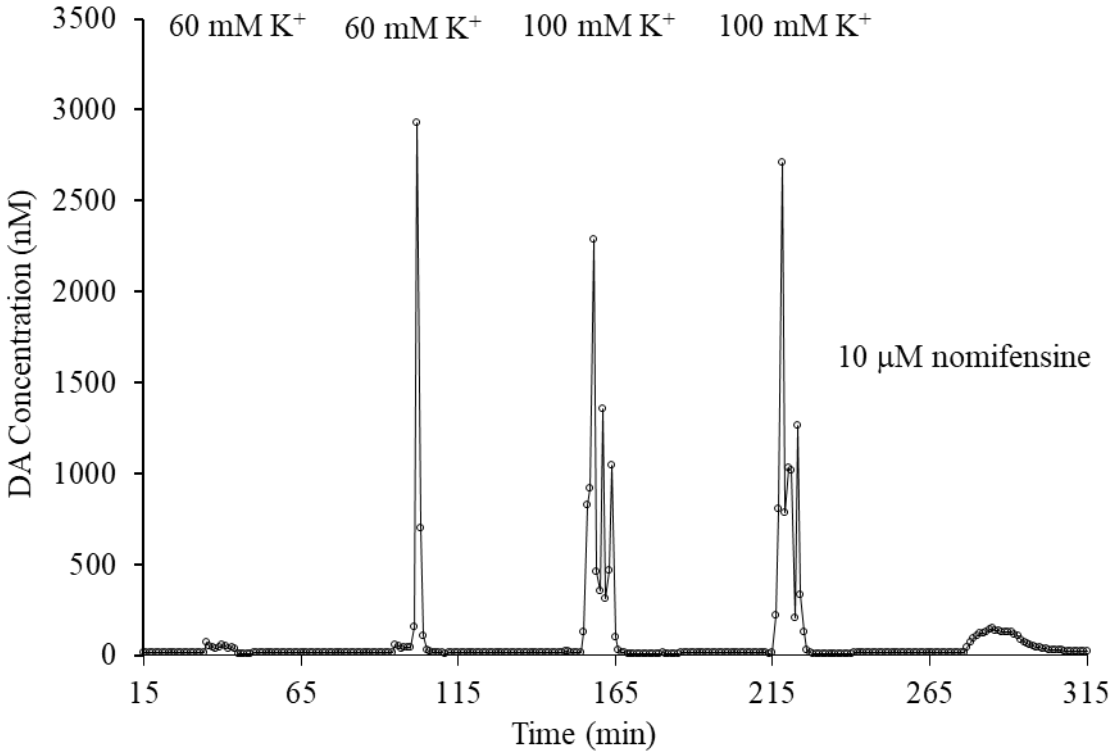

Figure 2.4-2. DA dialysate concentration measured during an experimental run (day 1, [K^+] = 60 or 100 mM, with an LDR probe).

The five transients seen are dopamine responses to 10-min retrodialysis of 60 mM K^+ (twice), 100 mM K^+ (twice) and 15-min retrodialysis of 10 μM nomifensine.

2.4.2 Basal

We define basal levels as DA levels in dialysate measured at least 10 minutes and at most 40 minutes from a transient. Figure 2.4-3 shows the frequency distributions of the one-minute measurements for each of the four conditions day = 1 and 4; with LDR or control probes. Consider first the data for control probes. These data have a skewed distribution indicating that there are more observations with basal levels below the mean than above the mean. The mean basal DA with control probes is comparable to published results from other groups as well as by our

group.[78,86,124] The distributions obtained with LDR probes show multiple maxima with a clearly separate distribution on day 4. This separate distribution is a single animal's basal data. The basal levels also appear to be on average higher with LDR probes, thus we did a two-way ("day" and "dexamethasone") analysis of variance on the mean basal DA with and without the aforementioned single animal's high basal DA data (Full ANOVA and regression output are in Table 2.7-1-Table 2.7-3). "Day" is not significant, but "dexamethasone" is significant ($p = 0.013$, $n = 22$) when the aforementioned high basal DA data are included. The pattern is similar from ANOVA without the aforementioned high basal DA data, but the significance is higher ($p = 0.0017$, $n = 21$). A linear regression using the variable "dexamethasone" with values of 0 for control and 1 for LDR probes leads to the simple relationship: basal dialysate [DA]/nM = 10.4 + dexamethasone*4.4 ($p = 0.0013$, $n = 21$) without the single animal's high basal DA data, and [DA]/nM = 10.4 + dexamethasone*6.7 ($p = 0.0097$, $n = 22$) with those data. We conclude that the basal dialysate DA level increases in the presence of dexamethasone retrodialysis.

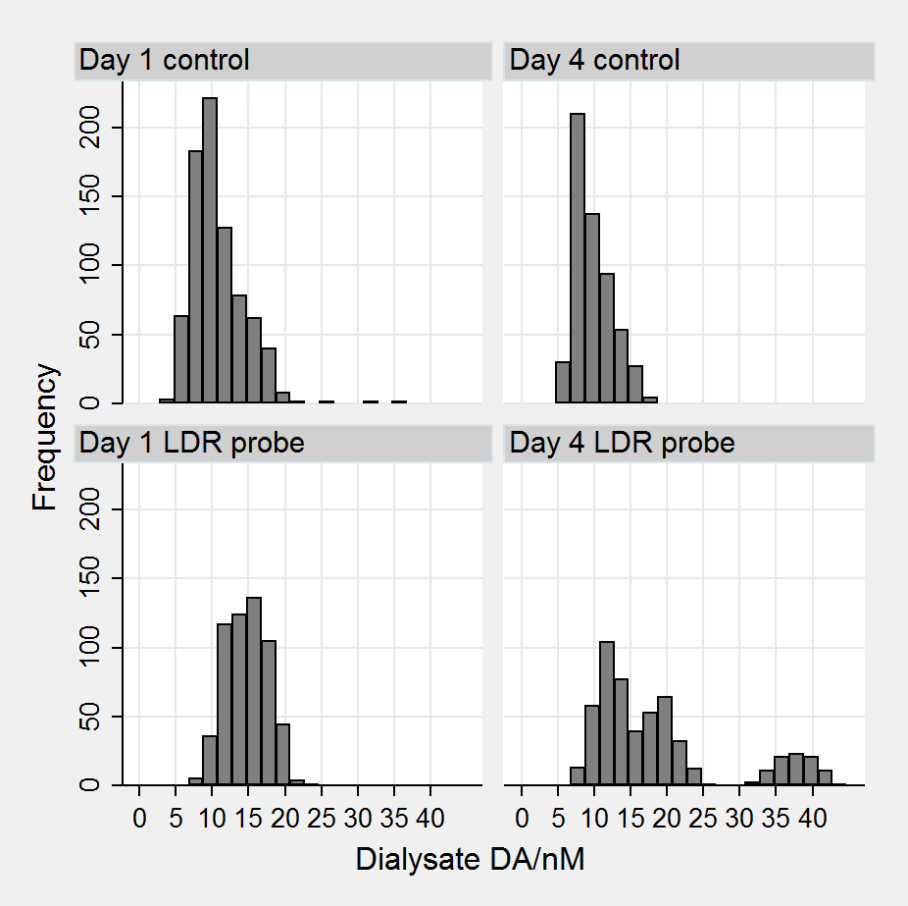

Figure 2.4-3. Frequency distributions of the basal concentrations measured each minute for the four conditions day = 1 and 4, probe = control and LDR.

Note there are seven animals represented in day 1 control. There are five animals contributing data for the other three cases. The "frequency axis" represents single, one-minute measurements.

2.4.3 Potassium Stimulations

As mentioned above, we anticipate oscillations in DA dialysate concentrations during a high K^+ stimulation. It is therefore important to consider what the time resolution of the entire microdialysis/liquid chromatography system is. Previously,[77] we determined the effect of the transport tubing and the microdialysis probe itself on the shape of a nominally instant change in 5-HT concentration *in vitro.* Importantly, we validated the use of a calculated Taylor dispersion

standard deviation for the spreading induced by the inlet and outlet capillaries. The individual contributions in the current set up are approximately 8.2, 8.7, and 8.8 s in the inlet, probe, and outlet, respectively. The variances add, so the overall time resolution is eroded with a standard deviation of 14.8 s based on spreading of the stimulus pulse on passing through the inlet/probe and the DA response passing through the outlet/probe. The practical result is that a perfectly sharp concentration step of a stimulant would be "smoothed" slightly on its way to the probe. The resulting DA transient would also be smoothed slightly within the probe and on the way to the liquid chromatograph's injection valve. As a result, we expect to see the results of a 10-min stimulation as an approximately 11-min response. We can categorize the DA responses to the 88 K^+ stimulations that we observed as follows. Dialysate DA transients in response to K^+ stimulations can be positive or negative, they can be small (less than 100 nM) with no spiking (n = 37), have one spike (n = 16) or have multiple spikes (n = 35). We can also compare the average of the DA transients over the entire 11 minutes from a single 100 mM K^+ stimulation to the basal level. In doing so, we see results in accord with analogous experiments using 20-min resolution offline microdialysis,[125,126] namely dialysate DA transients of up to 50 – 60 times basal level.

Figure 2.4-4 shows some of the dialysate DA transients we recorded from the experimental runs (all of them are in Figure 2.7-2 to Figure 2.7-21). While there is variability from stimulus to stimulus and from rat to rat, there are qualitative trends. The 100 mM K^+ stimulations on day 1, control or LDR probe, yielded multiple (three or more) large spikes (200 nM or more, e.g., Figure 2.4-4e). Using similar equipment, we recently reported high-amplitude oscillations of serotonin.[77] The same group on day 4 yields mostly transients with one or two spikes on top of a 50 – 100 nM base, e.g., Figure 2.4-4f but similar responses may be seen on day 1 (Figure 2.4-4a). The 60 mM K^+ transients measured with control probes on day 1 exhibit either transients similar to those in

Figure 2.4-4a or small spikes, with a larger spike (but small compared to those produced by 100 mM K^+) at the leading edge (Figure 2.4-4c). On day 1, responses obtained with LDR probes are highly variable encompassing nearly all of the transients described above. Transients induced by 60-mM K^+ on day 4 were typically small, although probes perfused with aCSF alone produced decreases in DA levels (Figure 2.4-4d) while LDR probes produced negligible to slightly positive responses with a negative transient after the cessation of the stimulations such as in Figure 2.4-4b. A reduction in dialysate DA in response to a 20 – 30 mM K^+ stimulation 24 h post-striatal implantation has previously been reported in one study.[127] It must be noted that, however, the measurements were done after 80 minutes of high K^+ perfusion. Such prolonged perfusion of high K^+ reduces DA extraction fraction[128] which will alter dialysate DA concentration.

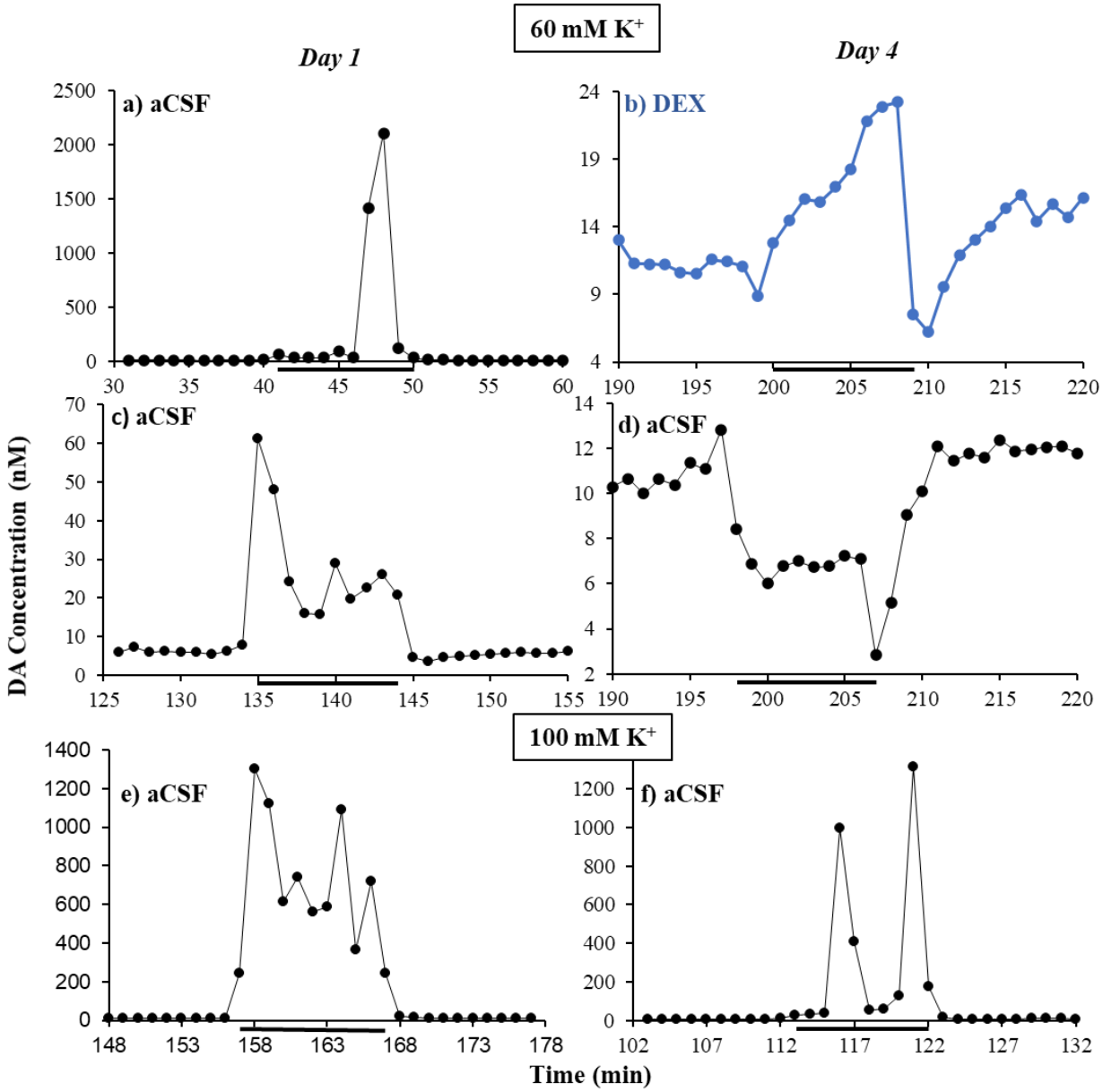

Figure 2.4-4. Qualitatively distinct dialysate DA responses observed during the experiments. Left: day 1. Right: day 4. Top: (a-d) 60 mM K^+. Bottom: (e-f) 100 mM K^+. The example in blue is from an LDR probe. The group is selected to be representative to transient characteristics, not conditions. K^+ stimulations are denoted by the black bar. Note the differing vertical scales. A complete set of images of all transients observed can be found in the Supplementary Information, Figure 2.7-2 to Figure 2.7-21.

2.4.3.1 Principal Component Analysis of Dopamine Transients

There are clear qualitative differences between responses to 60 mM K^+ and 100 mM K^+ stimulations on both day 1 and day 4. However, there is also significant variability in the responses to each type of stimulation. Thus, we turned to principal component analysis (PCA) to help to classify the observed responses. All of the scatter plots of scores are in the Supplementary Information. Figure 2.4-5 shows such a plot for the day 4, 60 mM K^+ responses from both control and LDR probes. The first two principal components represent more than 95% of the variance in the data. Importantly, the PCA scores reveal a clear separation of the responses obtained with control from those of LDR probes. The solid symbols in the score plots represent the mean of each cluster of points. Converting those mean scores to hypothetical laboratory observations leads to Figure 2.4-6. The result is striking – responses with LDR probes tend to show *positive* amplitudes while responses with control probes show *negative* amplitudes. To confirm the PCA result, we also show the mean responses for each of the five animals in the two categories (ten transients in each). The correspondence of the average and the result from the first two principal components gives confidence in the observation. The PCA analysis of the analogous day 1 data shows that there is a greater variety of responses. There is a cluster of very similar responses (see score plot in Figure 2.7-22) with the same characteristics as Figure 2.4-4c, a small dialysate DA increase from basal level. Others are represented by Figure 2.4-4a and f, mostly small increases from basal levels with one or two high amplitude spikes. This level of response has been observed extensively in many of the microdialysis studies noted earlier (in the introduction). The short, one-min spike, on the other hand, would not have been observable without one-min time resolution.

Figure 2.7-25 is the scatter plot of scores from all transients from 100 mM K^+ stimulations. Here, it is noteworthy that the score plot shows a clustering based on “day”, but

not based on “dexamethasone”. We conclude from this classification that the more extreme perturbation of 100 mM K^+ (compared to 60 mM) elicits a response mostly based on the time from implantation. The transients are for the most part oscillations of high magnitude.

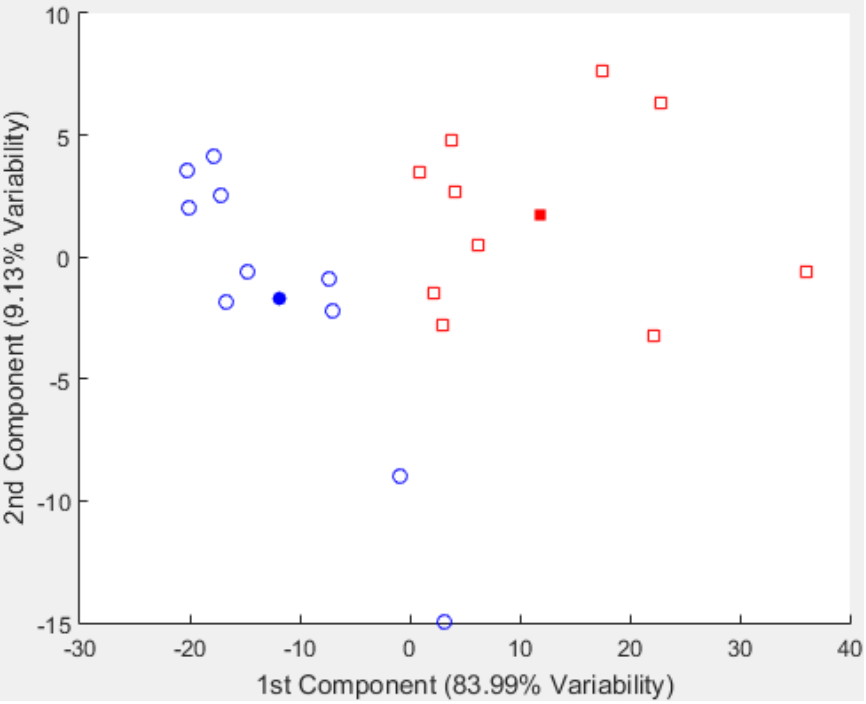

Figure 2.4-5. Scatterplot of scores of the first two principal components of all transients from day 4, 60 mM K^+ stimulations.

Blue circles represent data from animals with control probes, and red squares represent animals with LDR probes. The filled circle and square represent the centroid of respective types computed from the first two principal components.

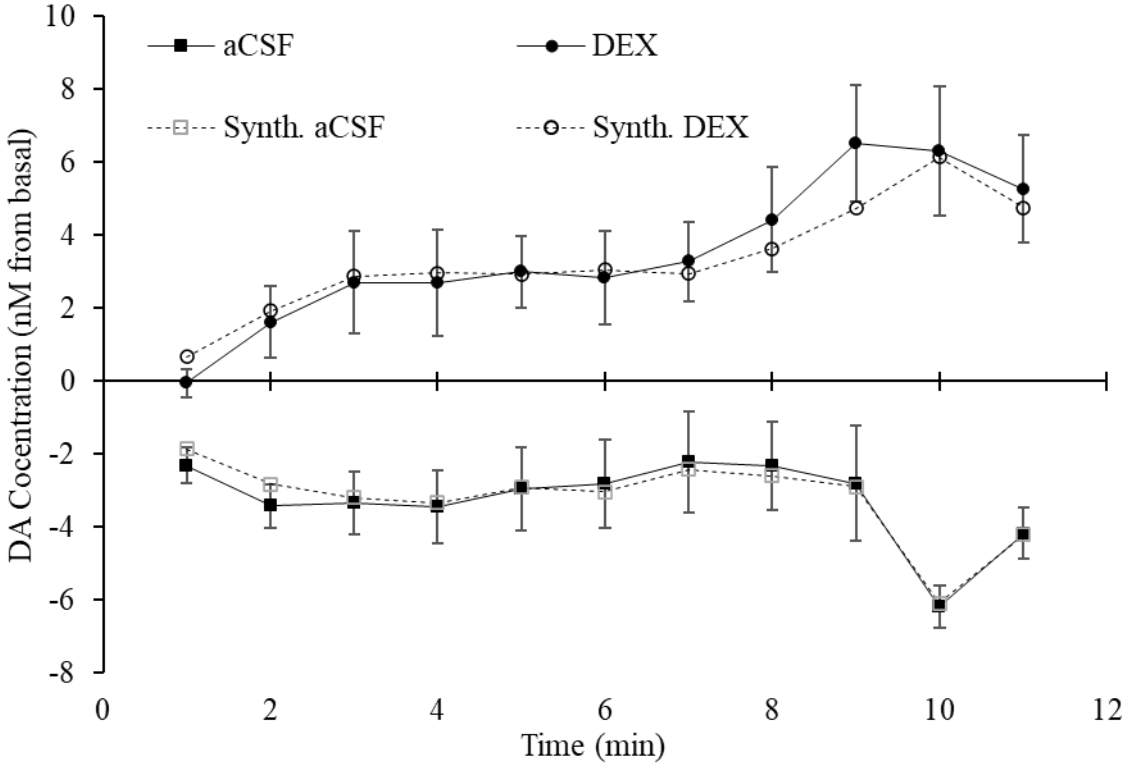

Figure 2.4-6. Comparison of transients from LDR (top) and control (bottom) probes on day 4 with a 60 mM K^+ stimulation.

Open symbols: Synthesized dopamine transients from the first two principal components. Solid symbols: experimental transients from averaging the responses at each minute.

2.4.3.2 Simultaneous Measurement of Dialysate DA and Field Potential

In two separate animals, we implanted a microdialysis probe with an attached tungsten wire for field potential measurements (Figure 2.7-27). Figure 2.4-7 compares the simultaneously measured dialysate dopamine and field potential transients recorded on day 1 with LDR probes and 100 mM K^+ (left) and 60 mM K^+ (right) stimulations. High amplitude oscillations of dialysate dopamine levels during 100 mM K^+ stimulations correlate to the oscillations in field potential with the same oscillation period of roughly 3-min, while the lack of dialysate dopamine oscillations during 60 mM K^+ stimulations correlates to similarly insignificant change in field potential.

Such slow oscillations in field potential are an indication of spreading depolarization.[129] which is a pathological event. Spreading depolarization and spreading depression comprise a set of complex processes that can originate from many irregular brain conditions and these manifest in several ways.[129,130] The role of microglia in spreading depression is, likewise, complicated. They were found to promote spreading depression in one polarization (M1 microglia), and increase the threshold for spreading depression in another polarization (M2a microglia).[131] Their presence is strictly required for ischemia-induced, but not for high K^+-induced, spreading depression.[132] Although the effect of glia on spreading depolarization and depression is complicated, and not completely understood, it is nonetheless noteworthy that we see effects of dexamethasone both on gliosis[122] and on the response *in vivo* to K^+ stimulations.

With day 4 60 mM K^+ experiments, we observed a small *increase* in dialysate DA level from LDR probes and a small *decrease* in dialysate DA level for control probes. While the small increase, again, is expected. The small decrease is unexpected and striking as it has been seen once but not reproduced.[123,127] We hypothesize that the decrease in dialysate DA level is a depression of neural electrical activity without accompanying spreading depolarization. The condition in these experiments, namely the proliferation of activated microglia and ischemia, is conducive[129,131,132] to spreading depression, which can lead to reduced cerebral blood flow[129] and silenced synaptic activity,[130] possibly reducing spontaneous DA release to below basal levels.

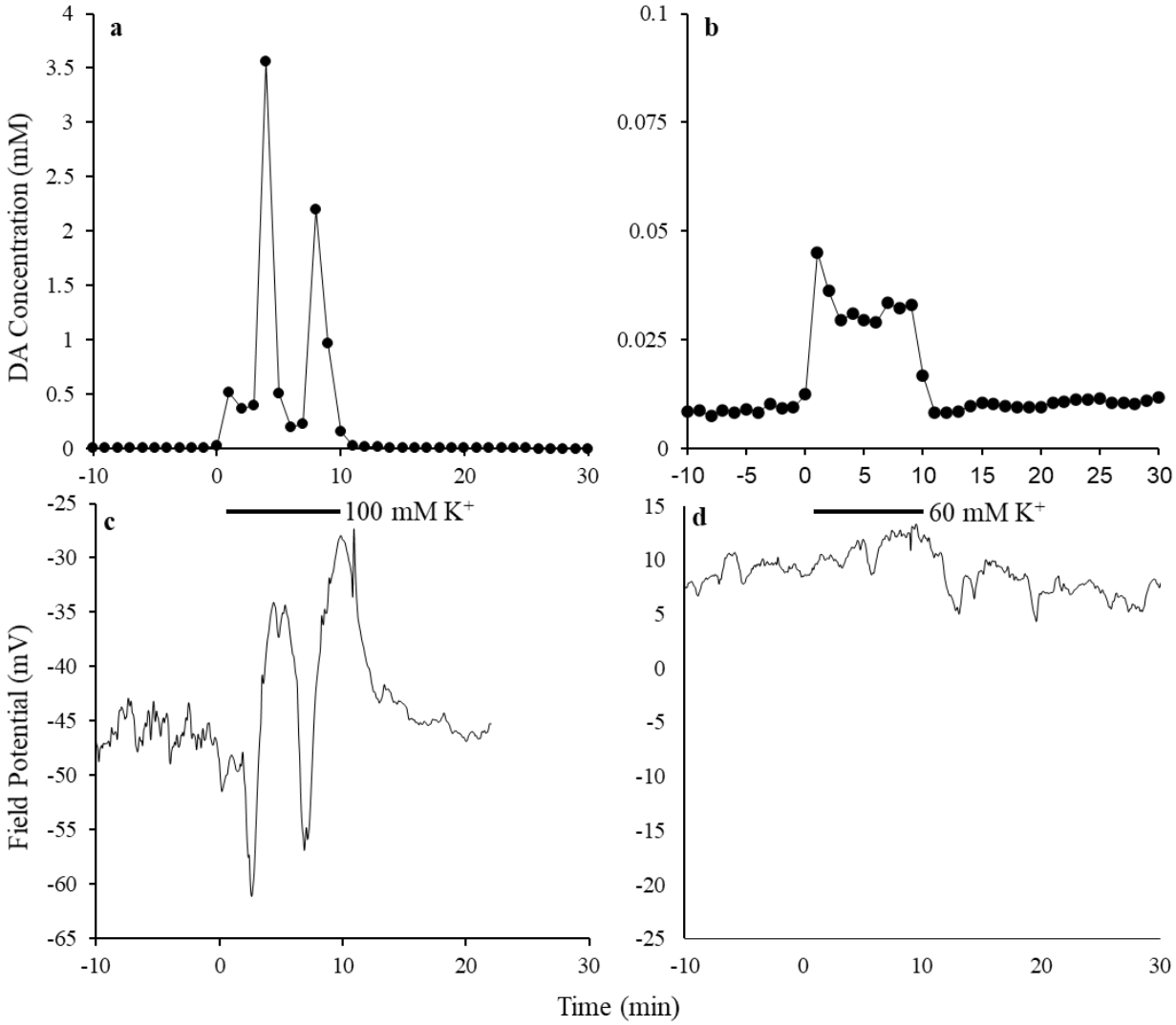

Figure 2.4-7. Simultaneous measurement of dialysate DA and field potential in an awake animal.

Left: 100 mM K^+ stimulation. Right: 60 mM K^+ stimulation. Measurements made on day 1 with LDR probes.

2.4.3.3 Comparison to Observations by Fast-Scan Cyclic Voltammetry

Fast-scan cyclic voltammetry (FSCV) in combination with carbon fiber microelectrodes is an alternative method for monitoring extracellular DA in the brain. A well-known application of FSCV is the monitoring of DA transients evoked by electrical stimulation of DA axons in the medial forebrain bundle (MFB). Previously, we monitored electrically evoked DA transients with carbon fiber microelectrodes placed in striatal tissues in close proximity to microdialysis probes

and with carbon fiber electrodes positioned in the outlet of the probe.[122] While a ten-minute, elevated K^+ stimulation would not be expected to elicit the same response as a 25 s MFB stimulation, there are noteworthy contrasts between the responses observed during this work with K^+ stimulation and that done previously with electrical MFB stimulation.

First, regardless of the time point after probe implantation (4 hr, 1 day, 5 days), electrically evoked DA responses were not observed by FSCV in the tissue adjacent to, or at the outlet of, probes perfused with aCSF without dexamethasone. These findings are difficult to interpret in isolation as they might either indicate an absence of DA terminals near the probe or the presence of DA terminals in some abnormal condition that suppresses electrically evoked DA release. Histology using two well-established markers for DA terminals, tyrosine hydroxylase and the dopamine transporter, identified DA terminals of a near-normal appearance in the tissues adjacent to the probes at time points beyond 4 hrs, suggesting the presence of DA terminals, albeit in some abnormal condition. The present results appear to support this conclusion, as 100 mM K^+ stimulation evokes DA responses from animals with control probes on days 1 and 4. This result implies the presence of terminals near the probe capable of releasing DA upon direct K^+-induced depolarization, even though electrically evoked DA release is suppressed in the absence of dexamethasone. This supports our prior conclusion that DA terminals survive the traumatic consequences of probe implantation, which we have called the traumatic penetration injury (TPI).

Second, during our work using FSCV to determine the effect of dexamethasone retrodialysis on dopamine measurements by microdialysis, we noticed dramatic differences between electrically evoked DA transients on Day 5 with control probes vs LDR probes.[122] As just mentioned, with control probes, electrically evoked responses were not observed on day 5 either next to or at the outlet of probes. However, responses were normal next to LDR probes and were

well-above detection limits at the probe outlet. In the current work, there is a similar dramatic difference in the responses from control vs. LDR probes with 60 mM K^+ stimulation on day 4, namely there are decreases from basal with control probes, (Figure 2.4-4d, Figure 2.4-6) and increases with LDR probes (Figure 2.4-4d, Figure 2.4-6). Again, these contrasting stimulation responses between control and LDR probes do not correlate with the histological appearance of DA terminals near the probes: The DA terminals appear normal on day 5 after probe implantation both with and without local dexamethasone via retrodialysis. However, these contrasting stimulation responses do correlate with the histological appearance of astrocytes and microglia on day 5, when glial activation is robust near control probes but nearly absent near LDR probes. Thus, our measurements of both electrically evoked and K^+-evoked DA transients support the conclusion that dexamethasone facilitates the re-establishment of normal DA activity in the tissues affected by the TPI during probe implantation.

In contrast to the case for 60 mM-induced transients and as deduced from the principal component analysis, dialysate DA responses to stimulation with 100 mM K^+ on days 1 and 4 did not depend on the presence of dexamethasone in the perfusion fluid. This is likely due to this high concentration of K^+ being able to "force" the depolarization of DA terminals, possibly due to the induction of spreading depolarization, regardless of the presence or absence of activated glia. Thus, the responses to stimulation with 100-mM K^+ are unique in that they appear to be the only ones we have recorded to date that are unaffected by activated glia.

2.4.3.4 Comments on the Nature of the Transients

Altering perfusate compositions can lead to changes in measured dialysate dopamine by at least three mechanisms. One mechanism is reverse transport via the dopamine transporter, DAT.[133] Low Na^+ perfusate, 50 mM, with choline replacement and normal K^+, induces dopamine efflux

into the extracellular space by this mechanism.[134] Using low Na^+ perfusate, but replacing Na^+ with K^+ rather than choline also evokes dopamine release[135] even in the presence of nomifensine to block the first mechanism, reverse transport.[134] Thus, high K^+ elicits DA release by a second mechanism, depolarization. Finally, changes in the perfusate composition, including high K^+ [128] can lead to changes in relative recovery/extraction fraction, e.g. by altering DA uptake rates.[136-138] It is also possible for physical changes in the tissue to alter the effective diffusion coefficient, altering dialysis recovery.[139] We have not attempted to unravel the contributions of each of these mechanisms to our observations. However, we have associated high amplitude oscillations during 100 mM K^+ stimulation to spreading depolarization via simultaneous field potential measurements. It is interesting to speculate that some of the features that we see at high temporal resolution may be related to differences in the foregoing effects of high K^+/low Na^+ stimulation. Another intriguing possibility for future investigations is whether any of the variability that we see under the same stimulation conditions is related to the striatum's physiological heterogeneity.[140]

2.4.4 Pharmacokinetics of Nomifensine

The DA responses to nomifensine stimulation can be modeled using a first-order model for rising and falling rates fitted with different time constants. Two-way ANOVA analysis of the time constants (Figure 2.7-26) show that neither the day of the experiment or dexamethasone treatment affects the nomifensine rising and falling characteristics. The maximum amplitude, however, is day-dependent, being lower on day 4 after implantation compared to day 1. Nomifensine is introduced by retrodialysis, so a significant contribution to the dynamics is the diffusion of nomifensine within the tissue. The results obtained indicate that the diffusion rates are not

significantly different among the various conditions. The rising rate constant is found to be about two times higher than the falling rate.

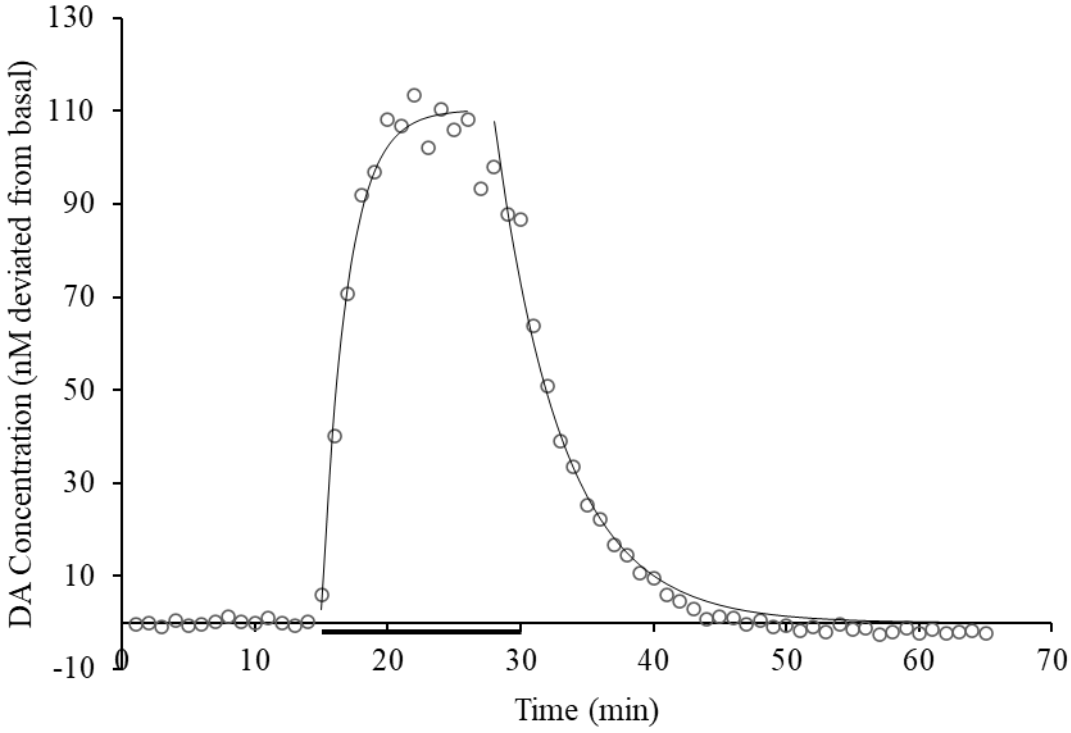

Figure 2.4-8. Fitting of nomifensine response to exponential decay model.

Time constants (min^{-1}) Rising = 0.52 Falling = 0.20 Avg. Amplitude = 121.

2.5 Conclusions

In the present study, we have shown that *in vivo* monitoring of dopamine at one-minute time resolution using online microdialysis-LC-EC reveals patterns of responses to chemical stimulation or local drug treament by retrodialysis with considerably more information than can be obtained with lower resolution measurements. We find that using LDR probes increases basal dialysate DA levels. A high concentration of 100 mM K^+ induces spreading depolarizations in the

striatum with control or LDR probes. This is consistent with the presence of functional DA terminals near the probe in both cases. Remarkably, the 60 mM K^+ transients are positive after four days with the LDR probe while they are negative (and of a similar magnitude) with control probes.

Given that spreading depolarization is a pathological condition, we are led to wonder whether the practice of stimulating release of neurotransmitters with K^+ concentrations on the order of 100 mM in order to assess the experimental set up is wise. There are certainly legitimate reasons to use this method, but the lowest concentration of potassium ion that elicits a response is most likely preferred.

We note that the dexamethasone treatment had no significant effect on an essentially pathological response to 100 mM K^+, while it had a significant and qualitatively obvious effect on exposure to a lower K^+ concentration. This is interesting in that it implies that the effect of dexamethasone is more easily discerned with less extreme perturbations of the tissue. This is consistent with evidence from FSCV and immunohistochemistry experiments. We infer that dexamethasone-induced reduction of gliosis, in combination with the higher time resolution microdialysis, improves the ability to observe dopamine system function when microdialysis probes have been chronically implanted.

2.6 Acknowledgement

Funding for this work was provided by National Institutes of Health under award number R01 MH104386 and a Graduate Research Fellowship from the National Science Foundation, DGE-1247842 (ELV). We also thank Dr. Ed Bouvier and Dr. Moon Chul Jung of Waters

Corporation for the generous gift of packing materials, and Dr. Chi Leng Leong and Professor Martyn Boutelle for the equipment necessary for the field potential measurements.

2.7 Supplementary Information

Additional information as noted in text. Figure 2.7-1-Figure 2.7-21 contain all dialysate DA concentration plots measured during experimental runs, with Figure 2.7-1 also includes pre- and post-calibration measurements. Figure 2.7-22-Figure 2.7-24 show scatter plots of scores of relevant PCA analyses. Figure 2.7-25 is a PCA comparison of 100 mM transients, including averaged and synthesized average from PCA analysis, of day 1 vs day 4. Figure 2.7-26 has the plot and ANOVA result for nomifensine fitting. Figure 2.7-27 shows the construction of microdialysis and field potential probes. Figure 2.7-28 contains a schematic diagram of the experimental setup. Table 2.7-1-Table 2.7-3 contain ANOVA analysis and regression of basal dialysate dopamine concentration.

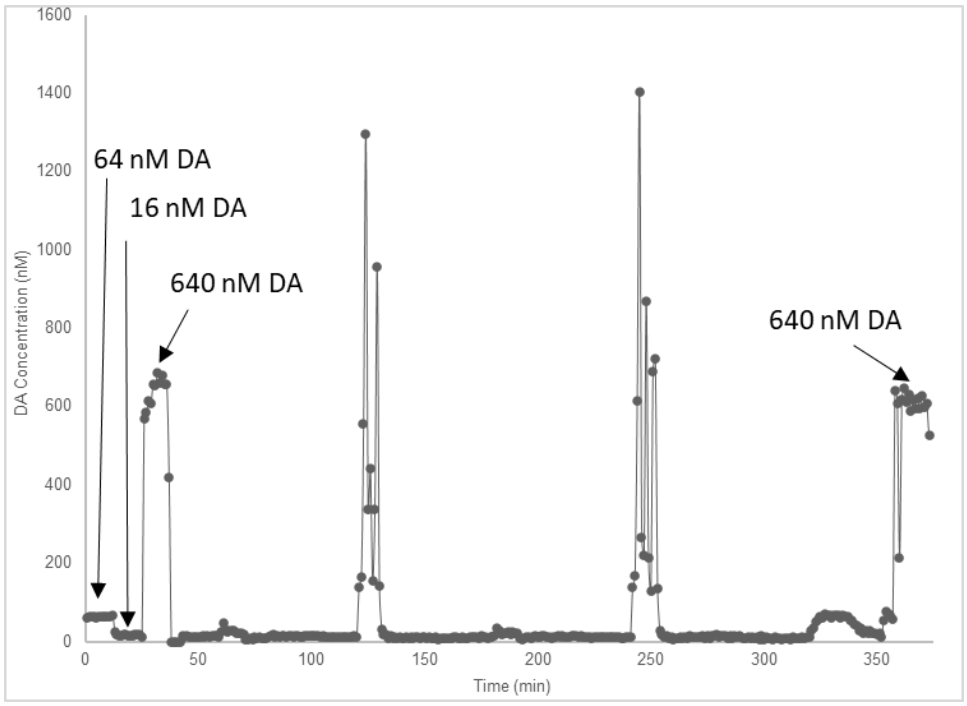

Figure 2.7-1. DA concentration measured during an experimental run including pre-calibration (64, 16 and 640 nM DA respectively) and post-calibration (640 nM DA).

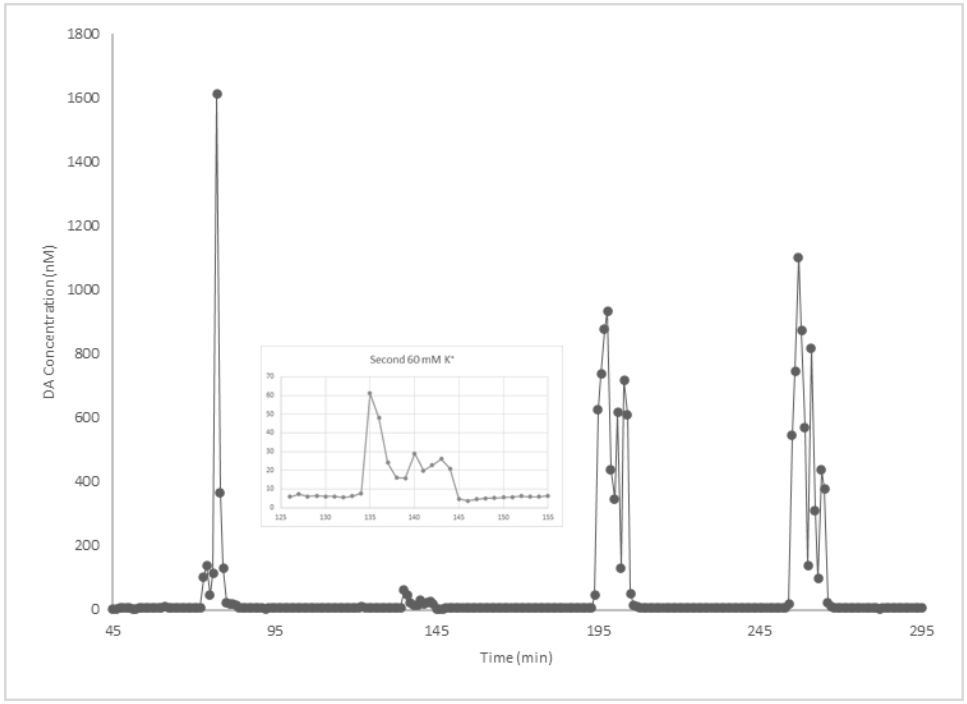

Figure 2.7-2. DA concentration measured during an experimental run. Rat 1, Control, day 1. Stimulation sequence: (10 min each) 60 - 60 - 100 -100 mM K^+.

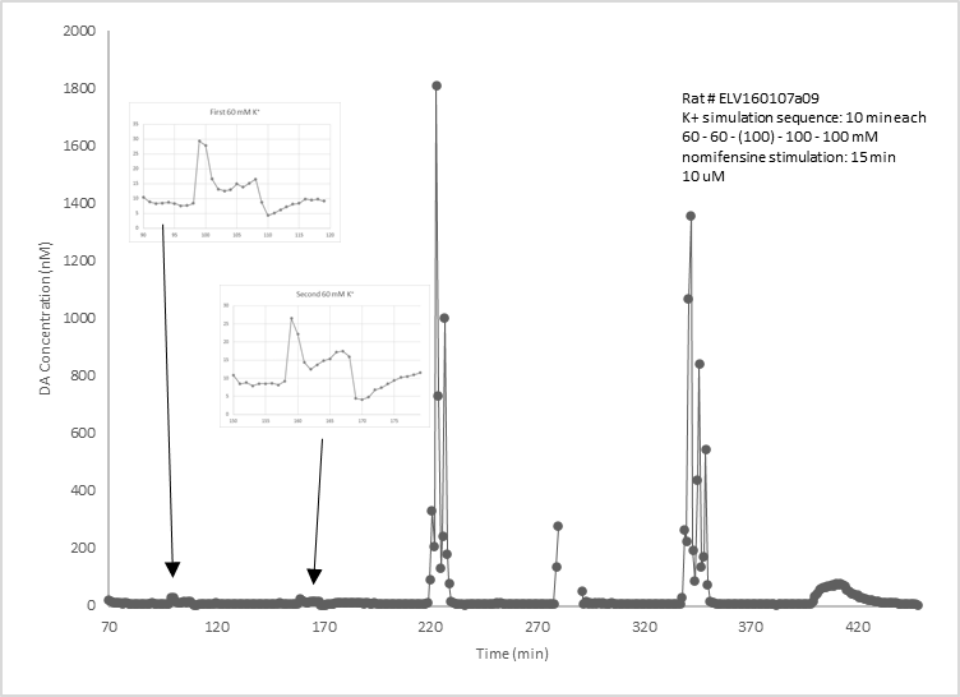

Figure 2.7-3. DA concentration measured during an experimental run. Rat 4, Control, day 1.

K^+ stimulation sequence: (10 min each) 60 – 100 - 60 - 100 mM nomifensine stimulation: 15 min 10 μM.

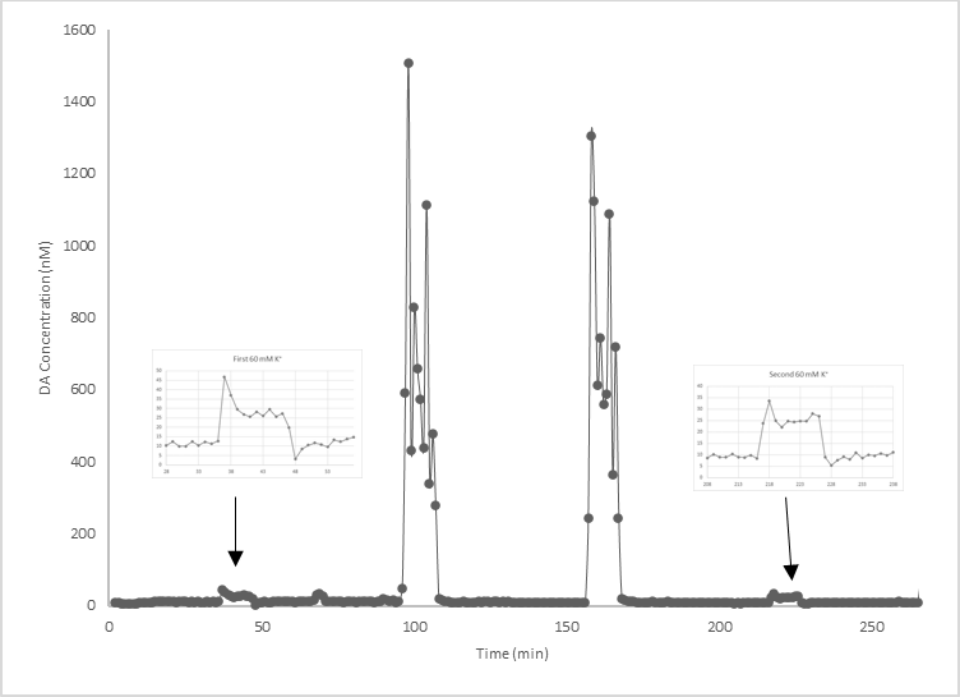

Figure 2.7-4. DA concentration measured during an experimental run. Rat 6, Control, day 1.

K^+ stimulation sequence: (10 min each) 60 – 100 - 100 - 60 mM.

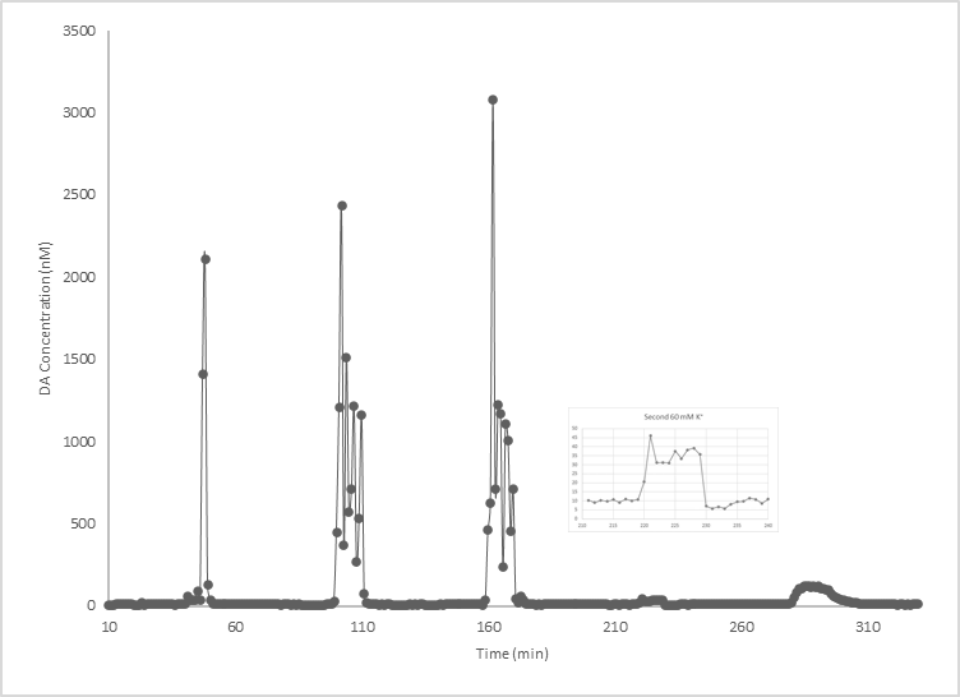

Figure 2.7-5. DA concentration measured during an experimental run. Rat 7, Control, day 1.

K^+ stimulation sequence: (10 min each) 60 - 100 - 100 - 60 mM nomifensine stimulation: 15 min 10 μM.

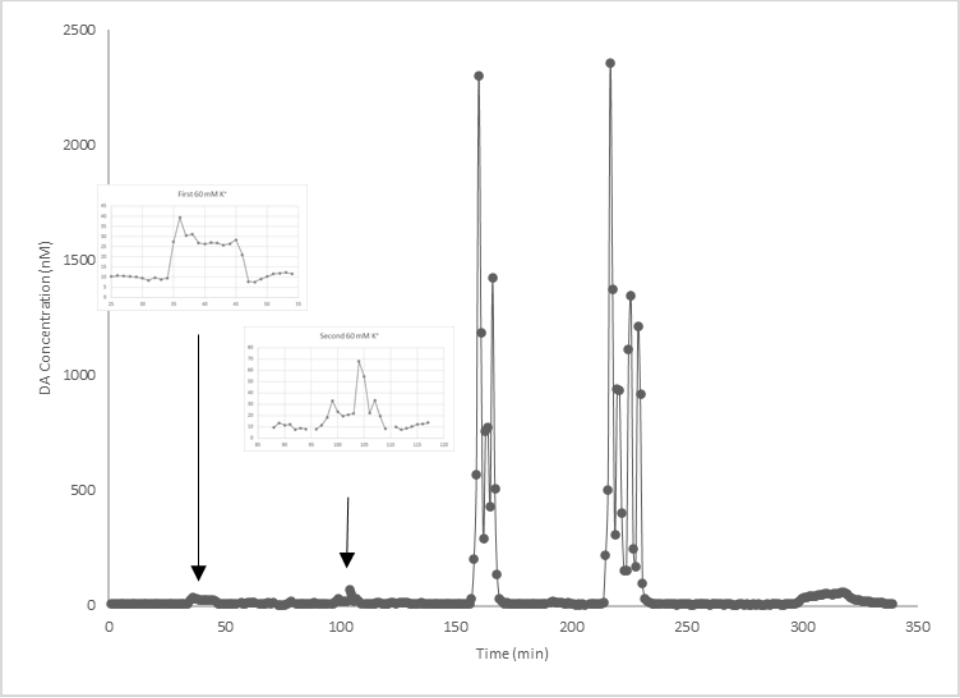

Figure 2.7-6. DA concentration measured during an experimental run. Rat 9, Control, day 1.

K^+ stimulation sequence: (10 min each) 60 - 100 - 100 - 60 mM nomifensine stimulation: 15 min 10 μM.

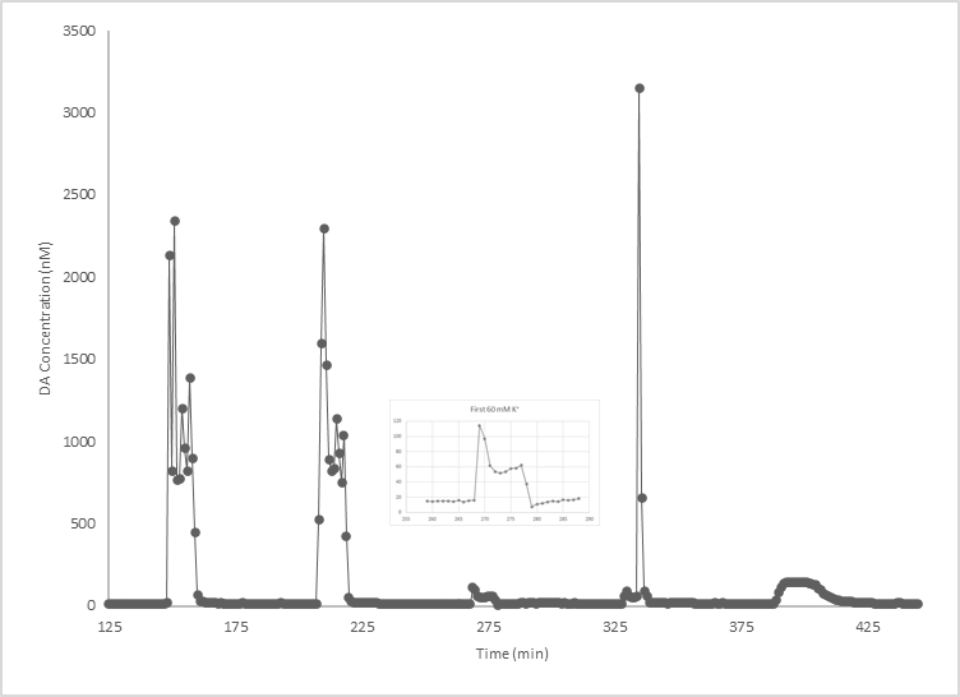

Figure 2.7-7. DA concentration measured during an experimental run. Rat 11, Control, day 1.

K^+ stimulation sequence: (10 min each) 100 - 100 - 60 - 60 mM nomifensine stimulation: 15 min 10 μM.

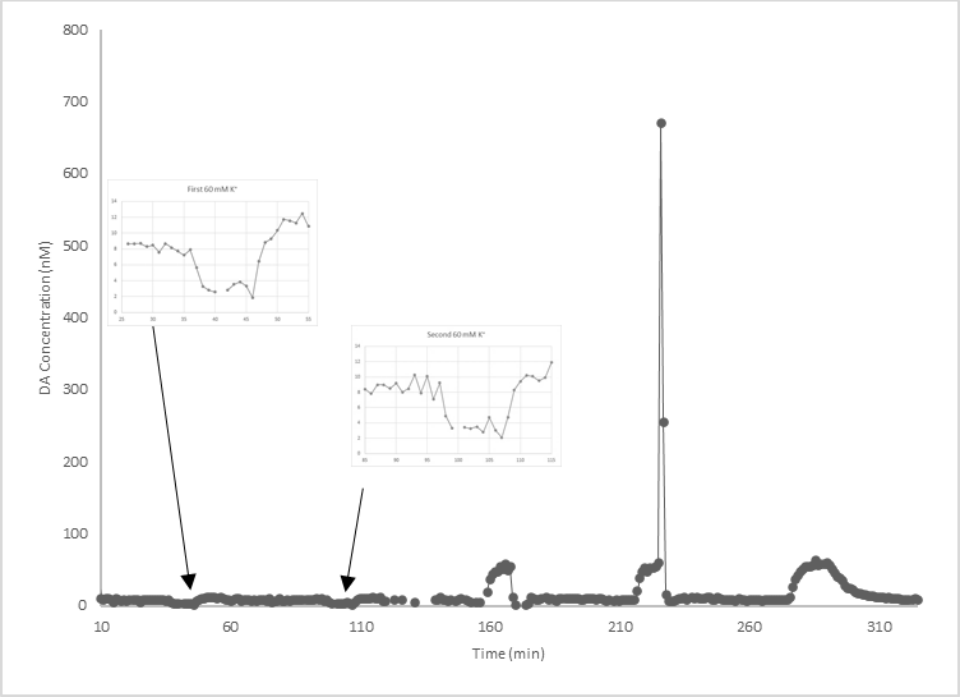

Figure 2.7-8. DA concentration measured during an experimental run. Rat 2, Control, day 4.

K^+ stimulation sequence: (10 min each) 60 - 60 - 100 - 100 mM nomifensine stimulation: 15 min 10 μM.

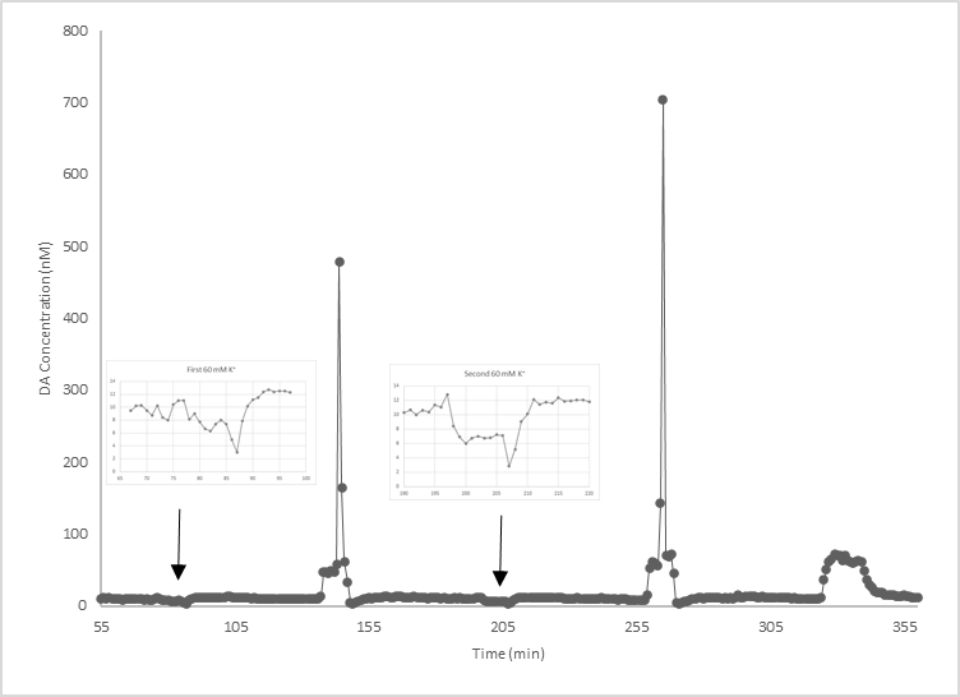

Figure 2.7-9. DA concentration measured during an experimental run. Rat 4, Control, day 4.

K^+ stimulation sequence: (10 min each) 60 – 100 - 60 - 100 mM nomifensine stimulation: 15 min 10 μM.

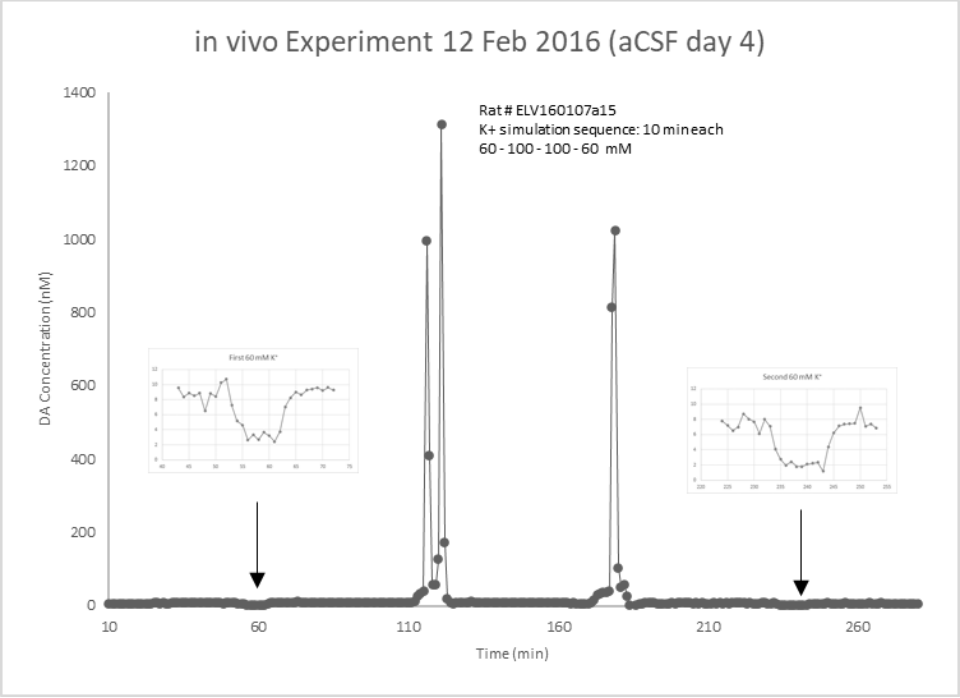

Figure 2.7-10. DA concentration measured during an experimental run. Rat 7, Control, day 4.

K^+ stimulation sequence: (10 min each) 60 - 100 - 100 - 60 mM.

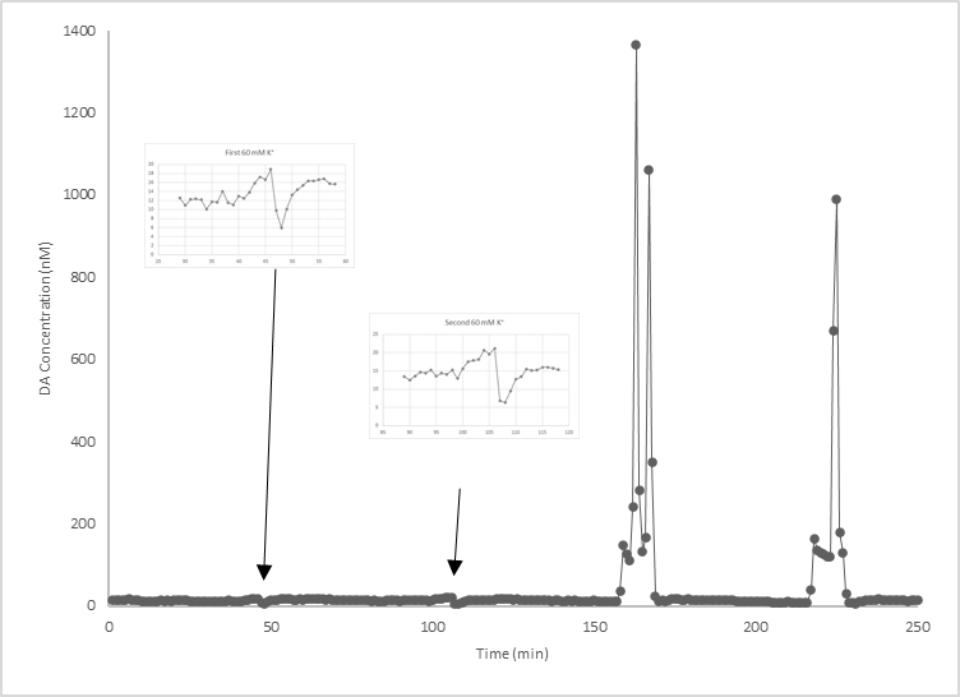

Figure 2.7-11. DA concentration measured during an experimental run. Rat 9, Control, day 4.

K^+ stimulation sequence: (10 min each) 60 - 100 - 100 - 60 mM.

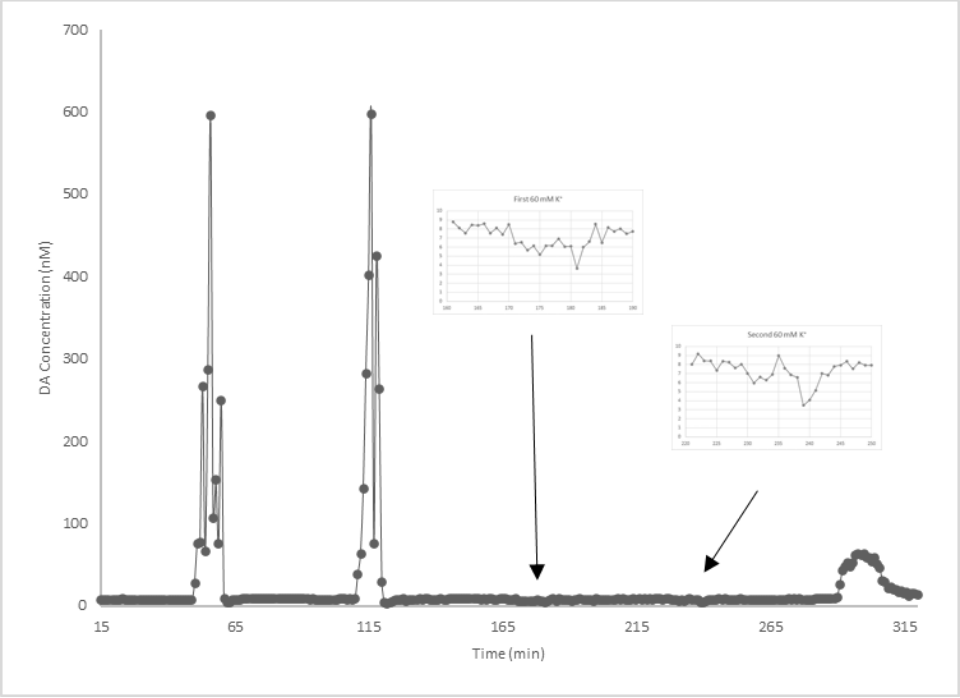

Figure 2.7-12. DA concentration measured during an experimental run. Rat 11, Control, day 4.

K^+ stimulation sequence: (10 min each) 100 - 100 - 60 - 60 mM nomifensine stimulation: 15 min 10 µM.

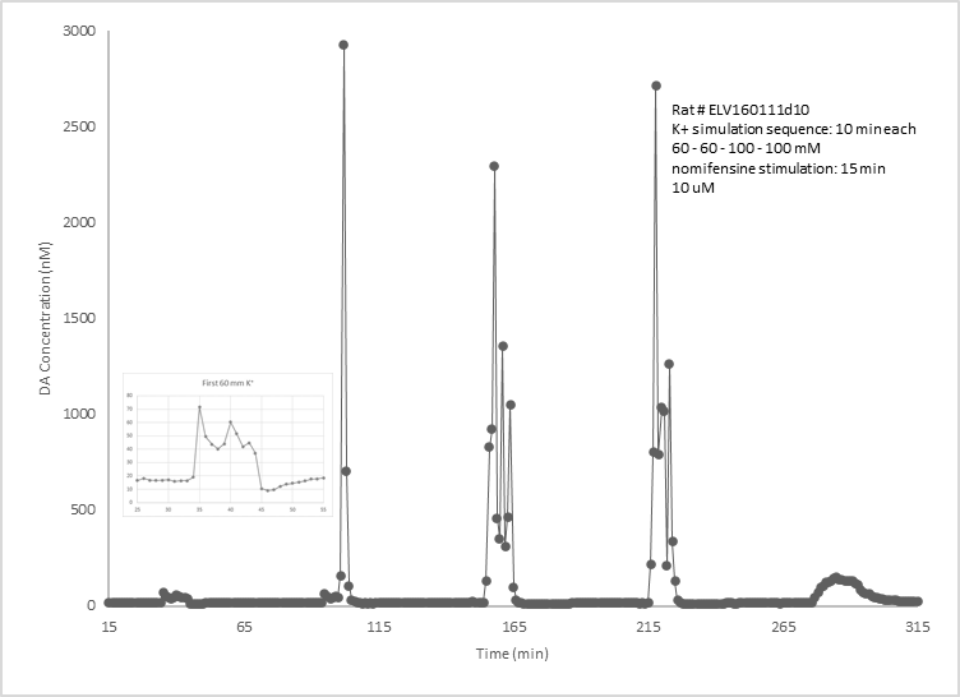

Figure 2.7-13. DA concentration measured during an experimental run. Rat 3, LDR probe, day 1. K^+ stimulation sequence: (10 min each) 60 - 60 - 100 - 100 mM nomifensine stimulation: 15 min 10 μM.

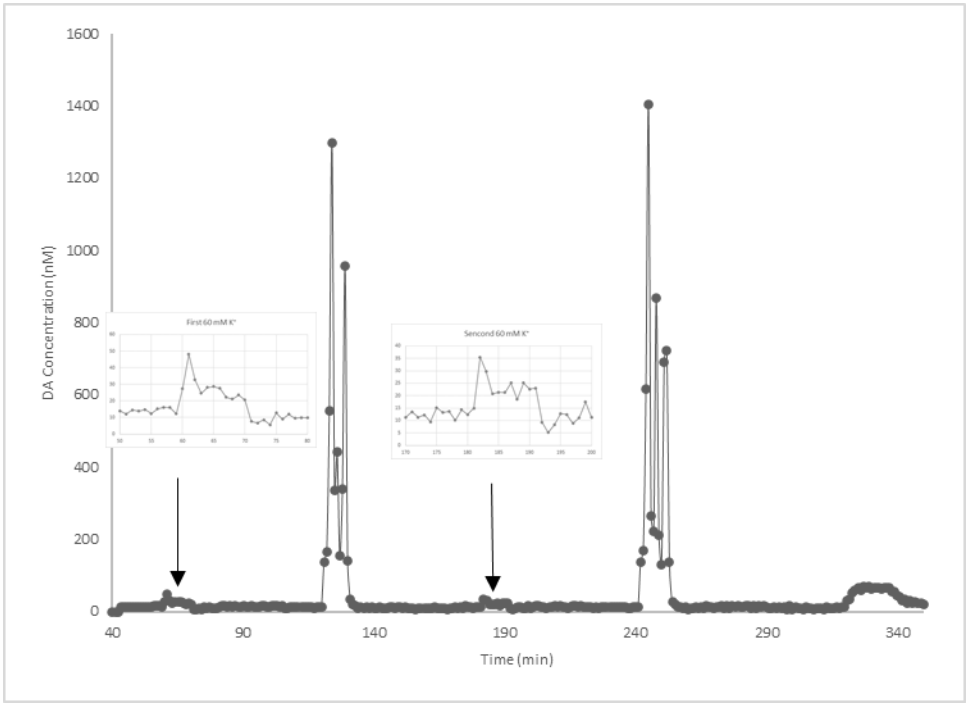

Figure 2.7-14. DA concentration measured during an experimental run. Rat 5, LDR probe, day 1. K^+ stimulation sequence: (10 min each) 60 – 100 - 60 - 100 mM nomifensine stimulation: 15 min 10 μM.

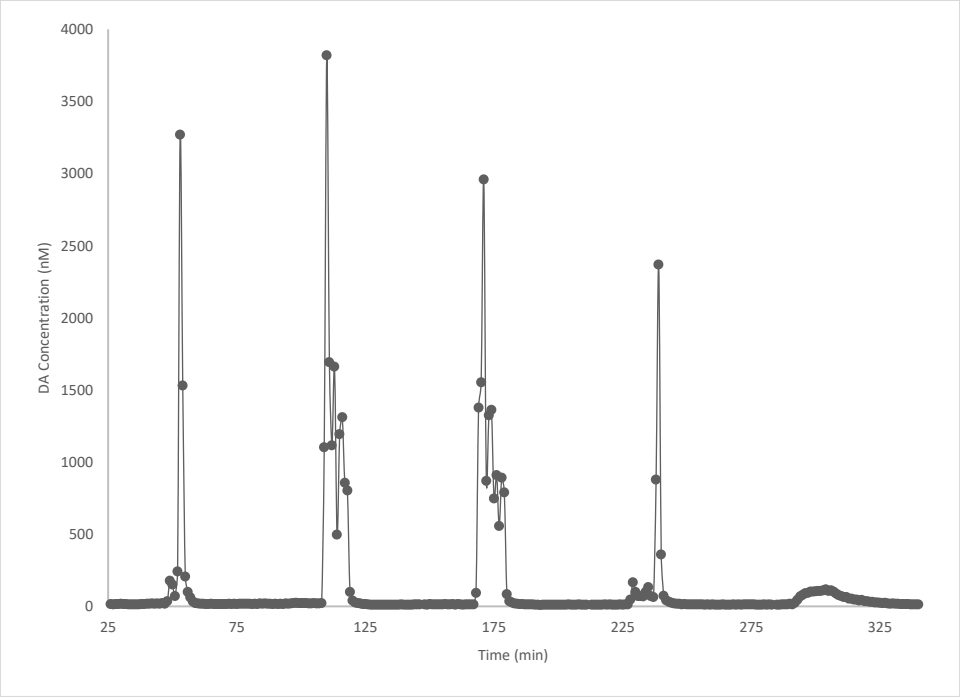

Figure 2.7-15. DA concentration measured during an experimental run. Rat 8, LDR probe, day 1. K^+ stimulation sequence: (10 min each) 60 - 100 - 100 - 60 mM nomifensine stimulation: 15 min 10 μM.

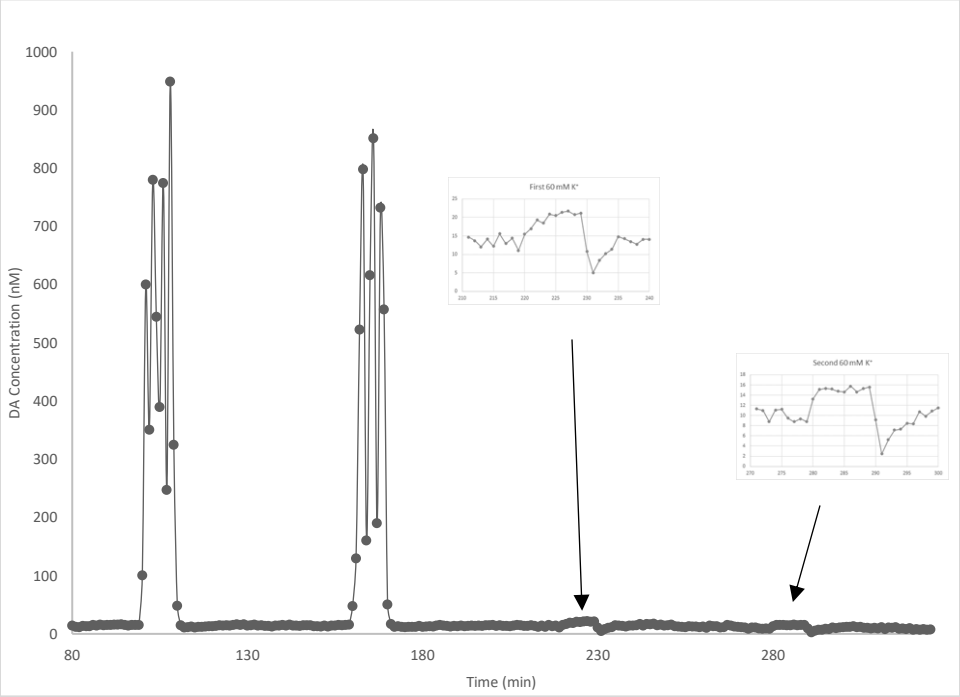

Figure 2.7-16. DA concentration measured during an experimental run. Rat 12, LDR probe, day 1. K^+ stimulation sequence: (10 min each) 100 - 100 - 60 - 60 mM.

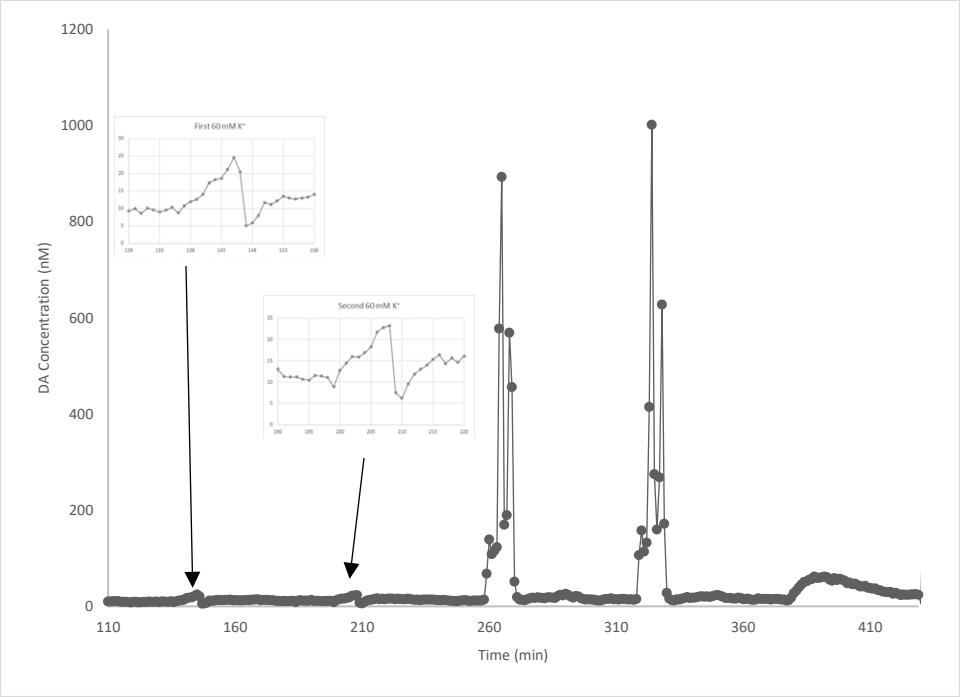

Figure 2.7-17. DA concentration measured during an experimental run. Rat 3, LDR probe, day 4.

K^+ stimulation sequence: (10 min each) 60 - 60 - 100 - 100 mM nomifensine stimulation: 15 min 10 μM.

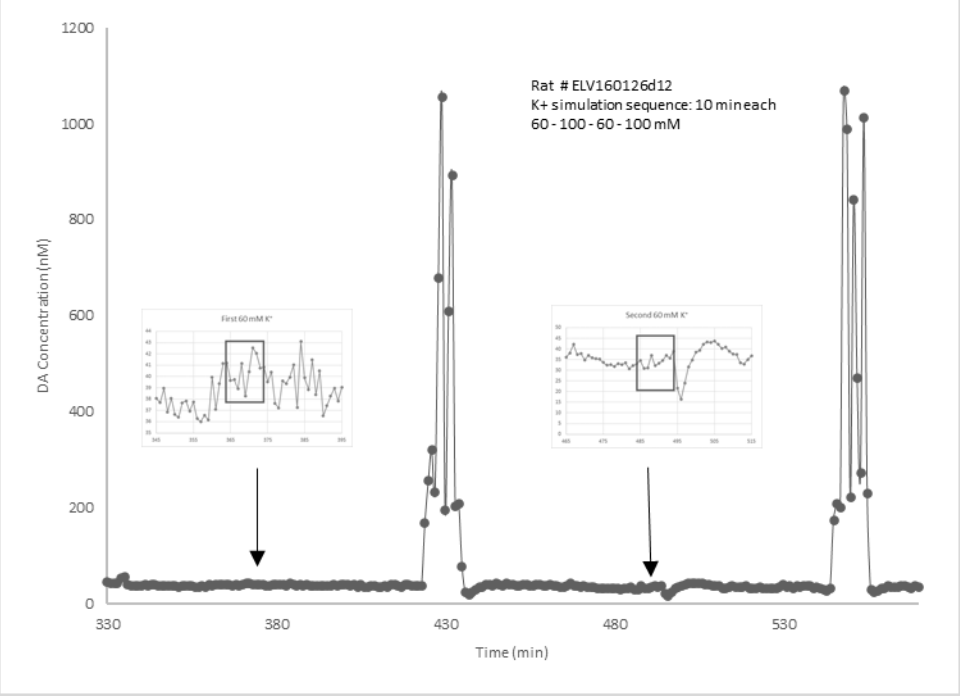

Figure 2.7-18. DA concentration measured during an experimental run. Rat 5, LDR probe, day 4.

K^+ stimulation sequence: (10 min each) 60 – 100 - 60 - 100 mM.

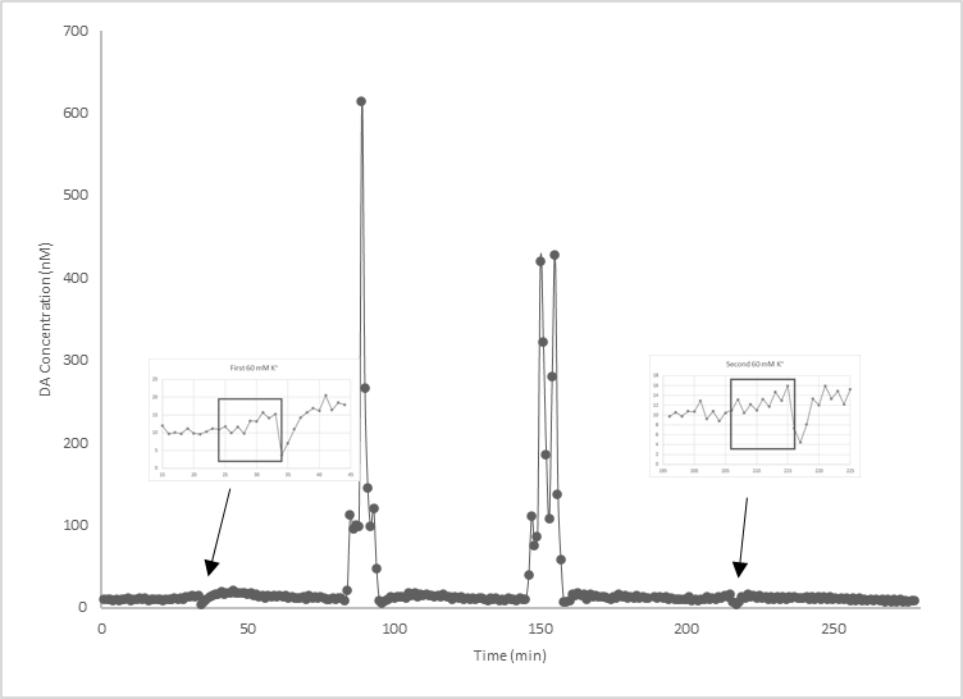

Figure 2.7-19. DA concentration measured during an experimental run. Rat 8, LDR probe, day 4. K^+ stimulation sequence: (10 min each) 60 - 100 - 100 - 60 mM.

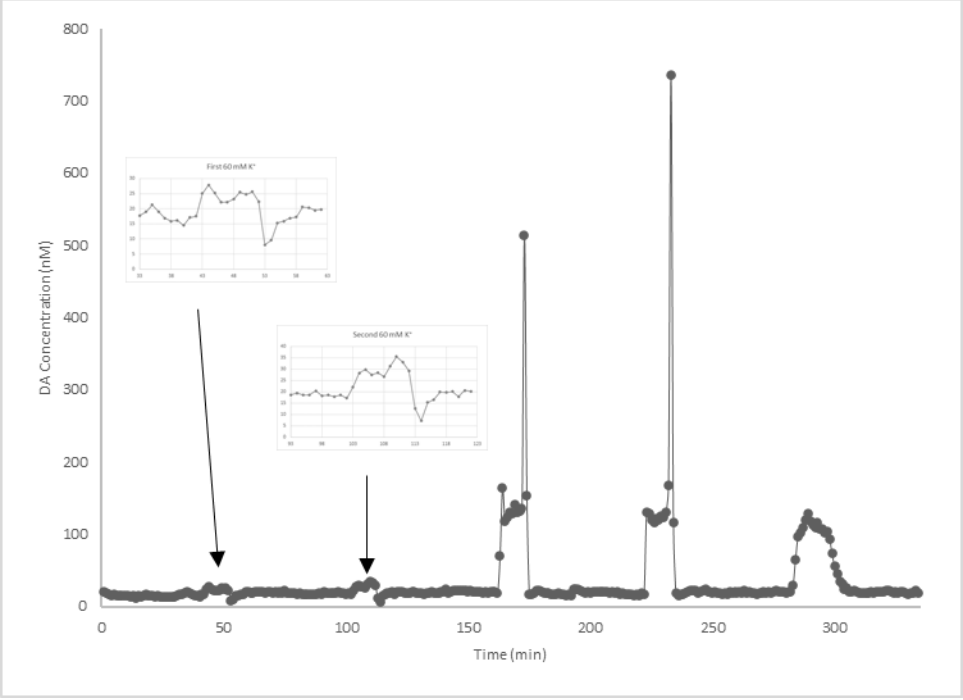

Figure 2.7-20. DA concentration measured during an experimental run. Rat 10, LDR probe, day 4. K^+ stimulation sequence: (10 min each) 60 - 60 - 100 - 100 mM nomifensine stimulation: 15 min 10 μM.

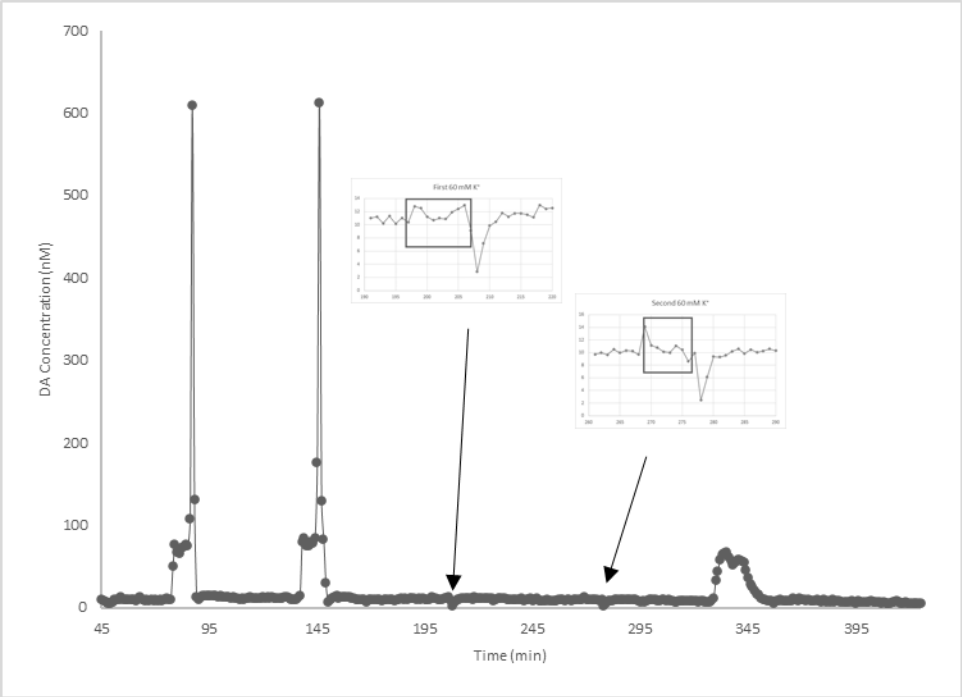

Figure 2.7-21. DA concentration measured during an experimental run. Rat 12, LDR probe, day 4. K^+ stimulation sequence: (10 min each) 100 - 100 - 60 - 60 mM nomifensine stimulation: 15 min 10 μM.

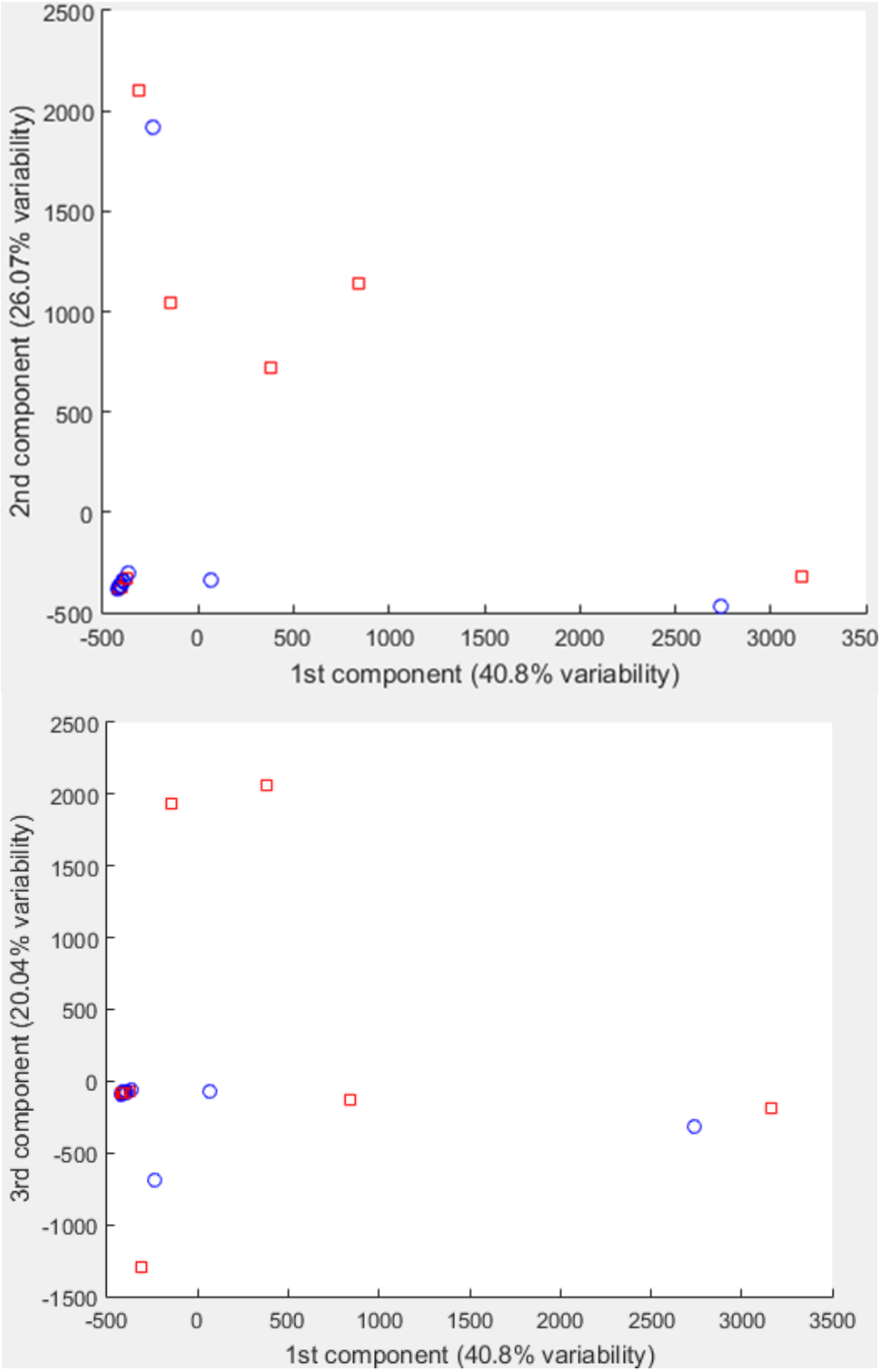

Figure 2.7-22. PCA scatter plot of scores of all transients from day 1 60 mM K^+.

Blue circles represent controls, and red squares represent LDR probe.

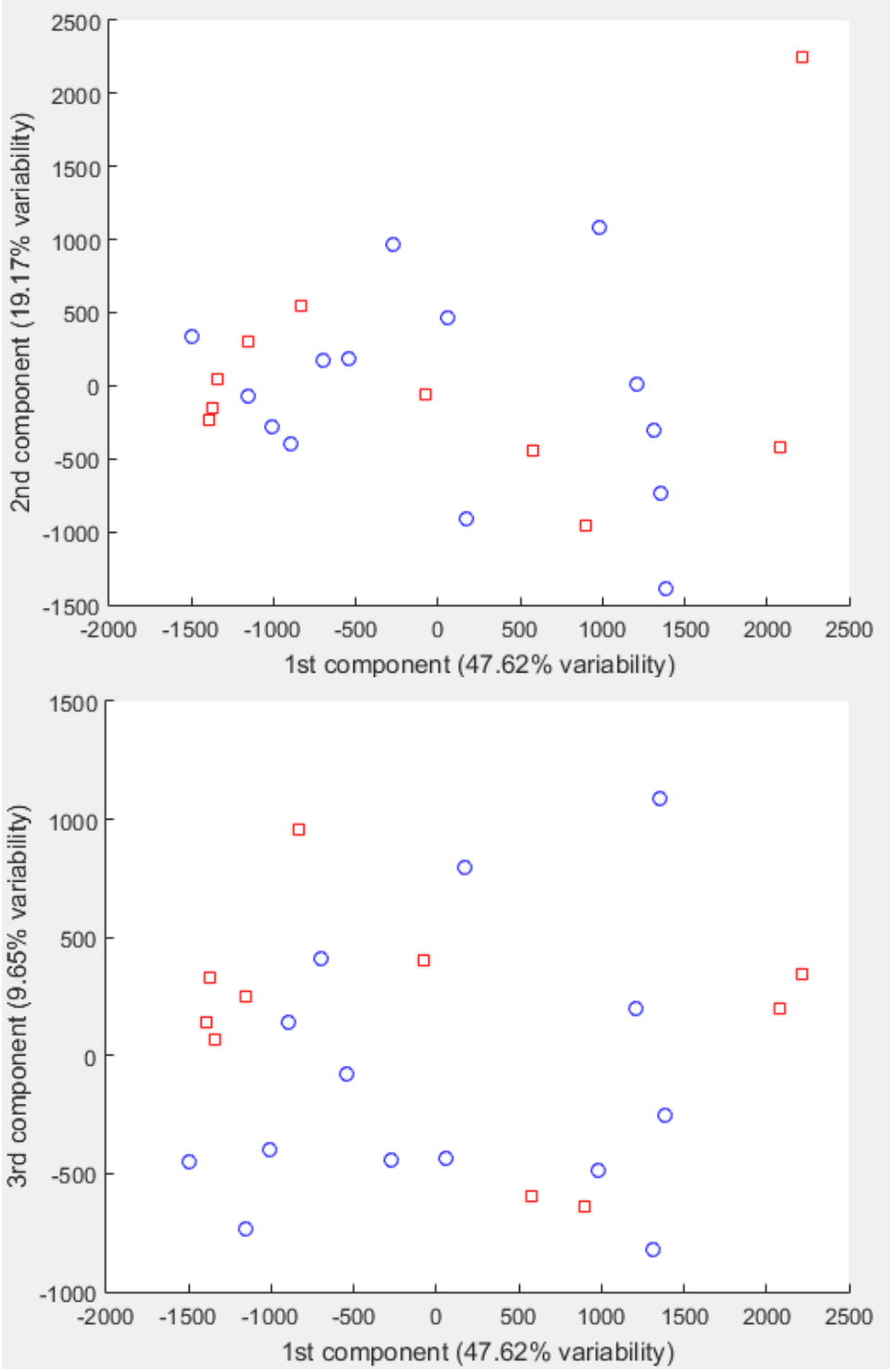

Figure 2.7-23. PCA scatter plot of scores of all transients from day 1 100 mM K^+.

Blue circles represent controls, and red squares represent LDR probe.

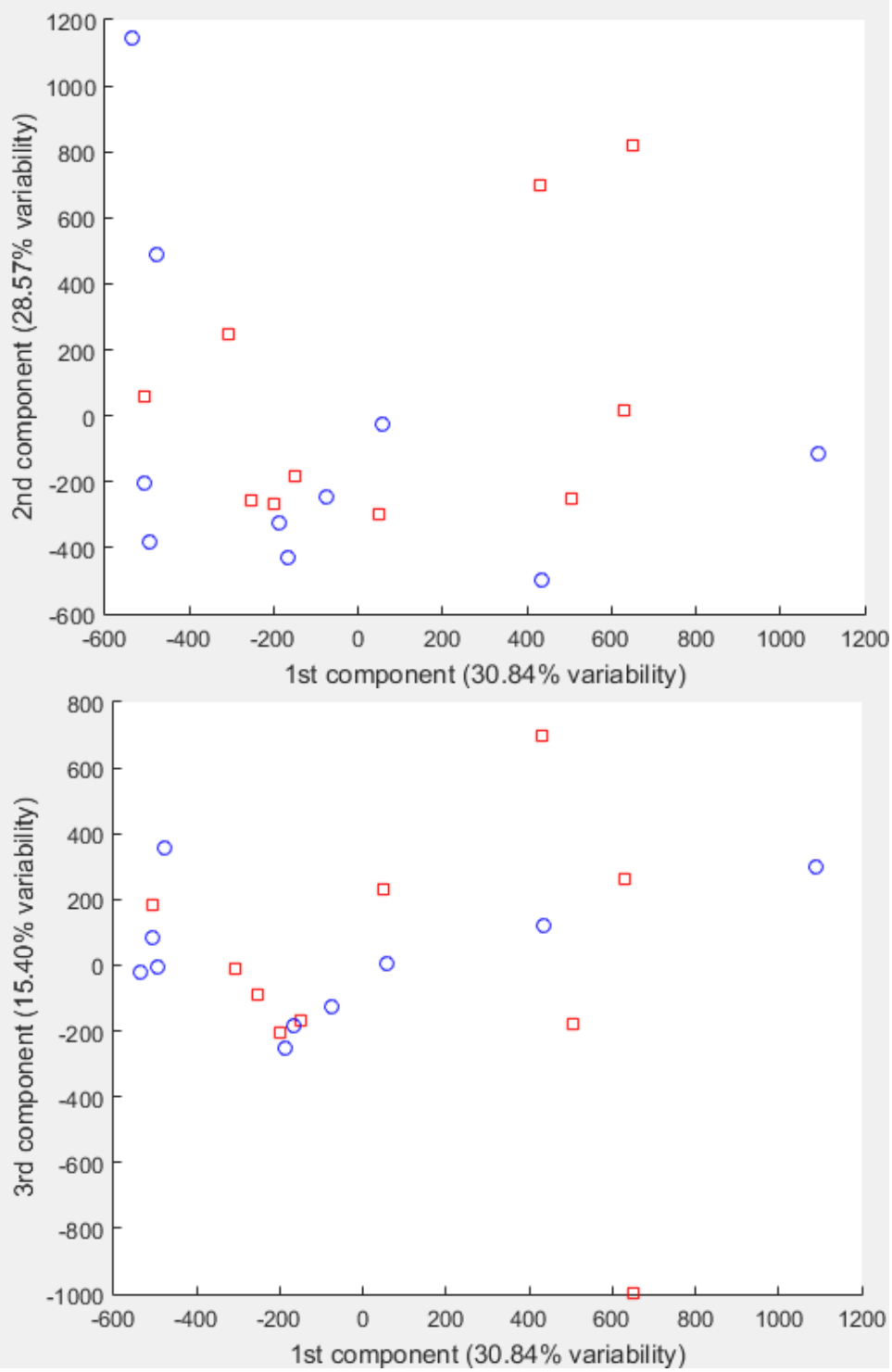

Figure 2.7-24. PCA scatter plot of scores of all transients from day 4 100 mM K^+.

Blue circles represent controls, and red squares represent LDR probe.

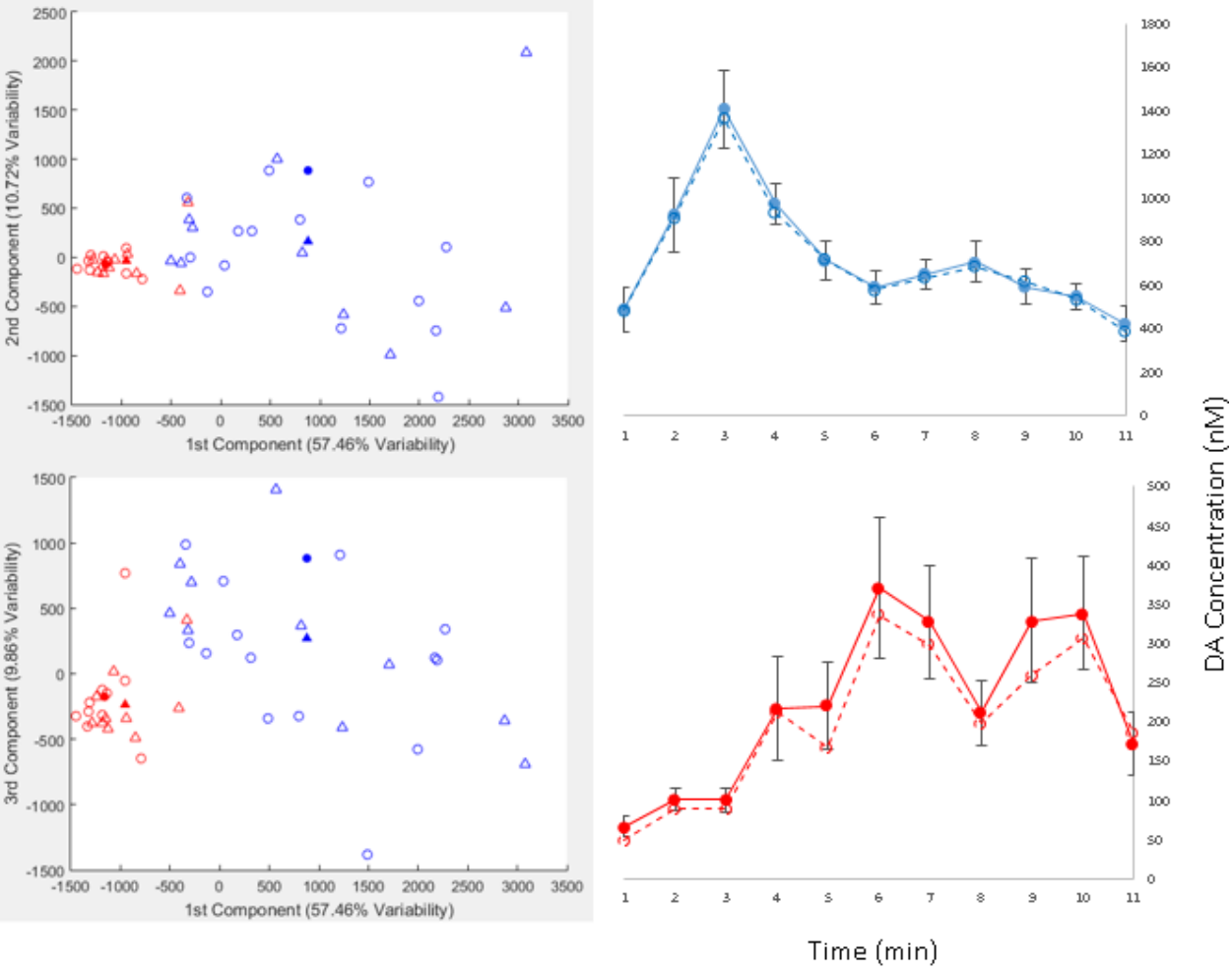

Figure 2.7-25. PCA comparison of transients 100 mM K^+, both days, both probes.

Left side: Red circle: day 4, 100 mM K^+, control probe. Red triangle: day 4, 100 mM K^+, LDR probe. Blue circle: day 1, 100 mM K^+, control probe. Blue triangle: day 1, 100 mM K^+, control probe. Right side: Blue: day 1 Red: day 4. Dashed line: Synthesized dopamine transients from the first two principal components. Solid line: averaged transients.

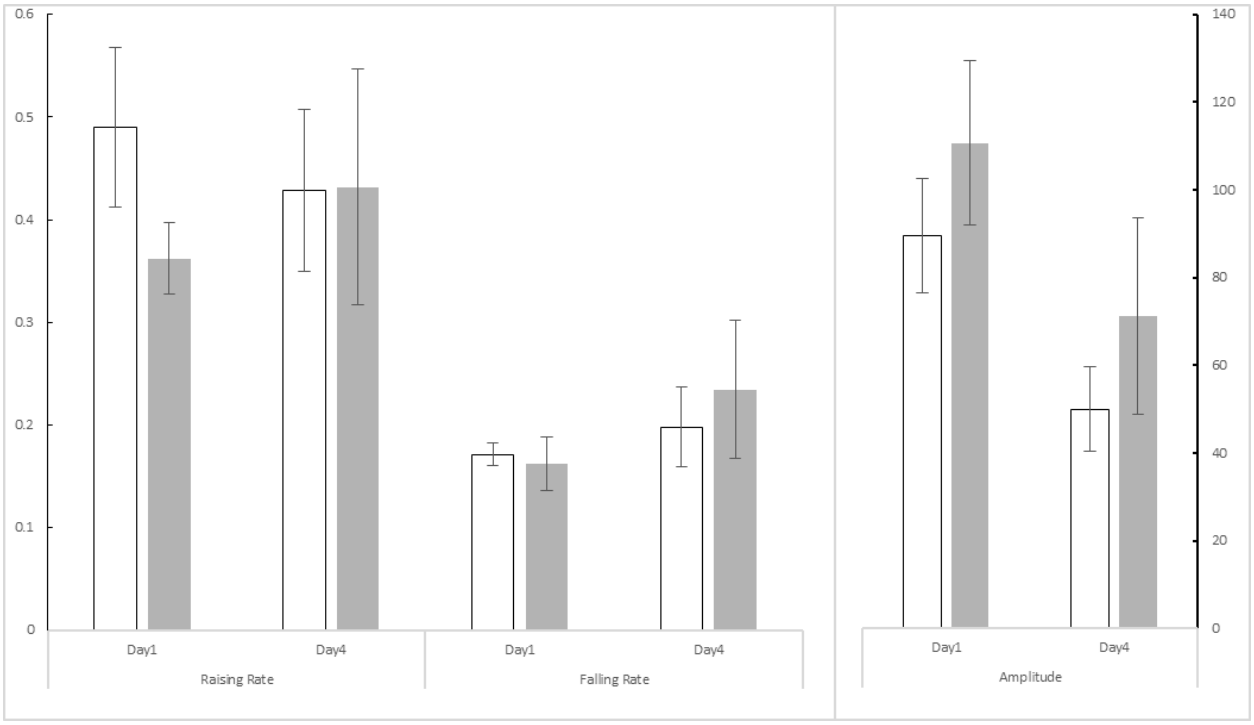

Figure 2.7-26. Average nomifensine maximum amplitude, raising and falling constant (AVG ± SEM). Unfilled: control probe, filled: LDR probe. In each of the three panels the day 1 data have n = 6 (control) and n = 4 (LDR probe) and the day 4 data have n = 3 for each bar. Amplitude, rising time constant, and falling time constant values were analyzed with individual 2-way ANOVA's with day (1 and 4) and probe (control and LDR) as the factors. For both the rising and falling time constants neither probe, day, nor the interactions were significant ($p > 0.05$). For the overall amplitude day was a significant factor ($F(1,12) = 5.376$; $p < 0.05$) while probe and the interaction were not significant.

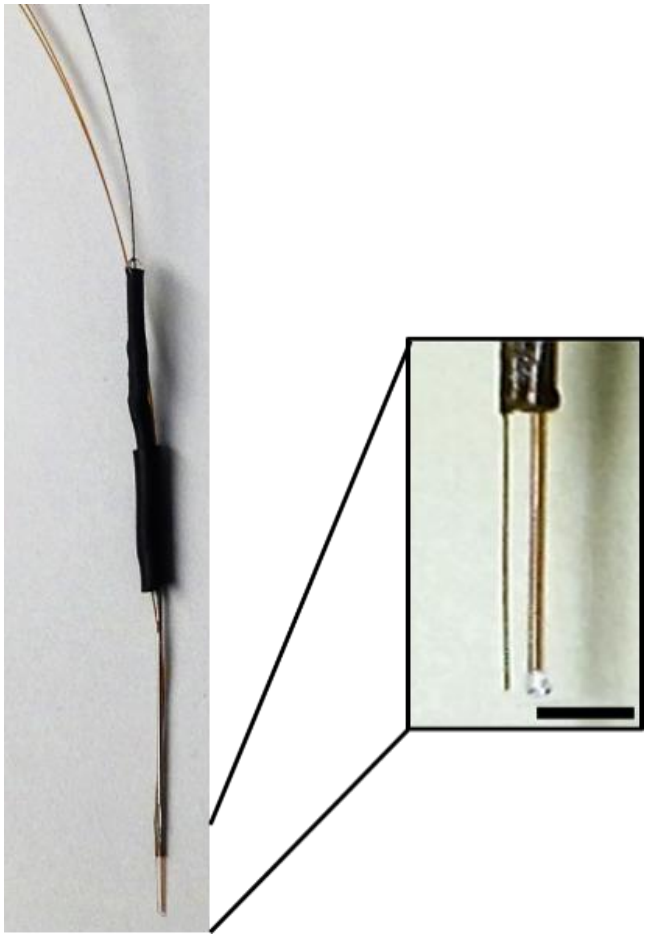

Figure 2.7-27. A tungsten wire was glued next to the microdialysis probe.

The scale bar in the inset is 1mm. A second tungsten wire was used as the reference and placed in the contralateral hemisphere.

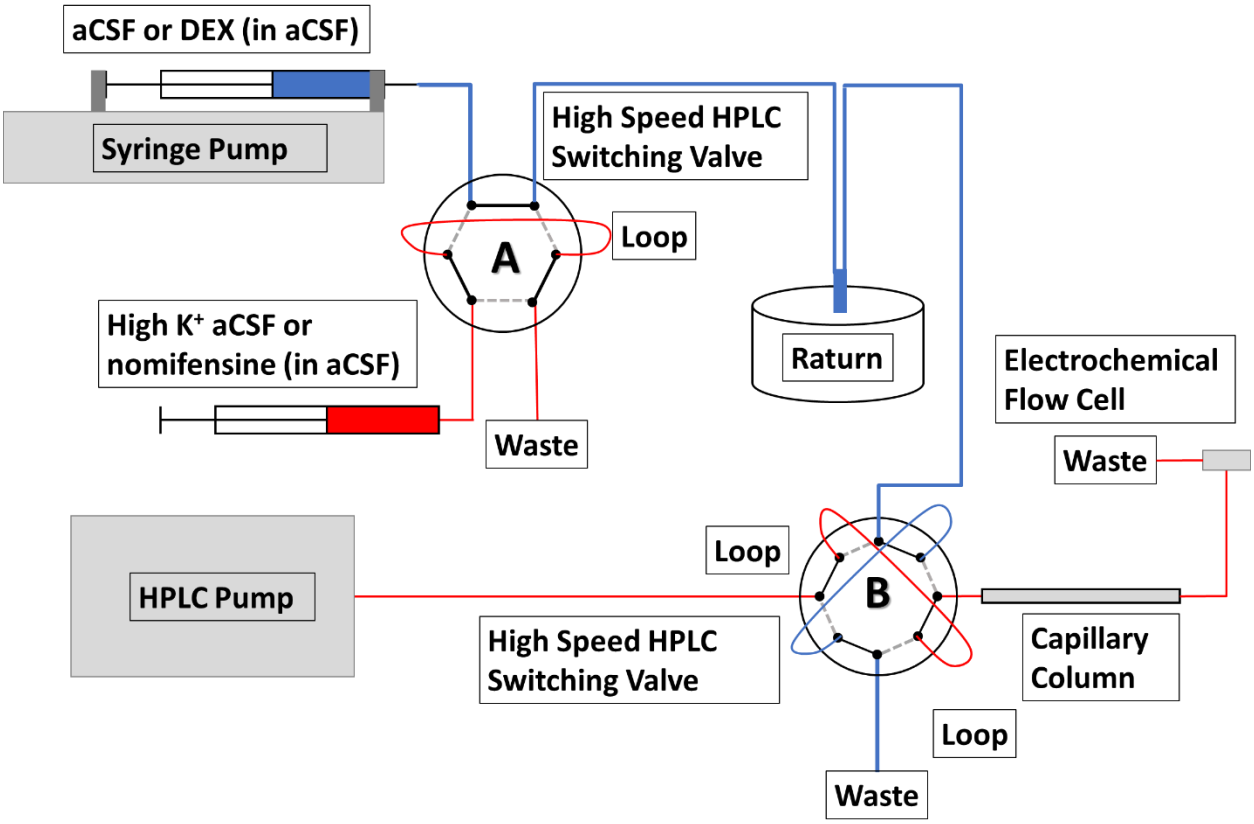

Figure 2.7-28. Schematic for the flow paths of the online microdialysis system. Perfusate/microdialysate flow path is shown in blue, bold. The flow path starts from the perfusate reservoir, a 1.0-mL syringe, through switching valve A, then through the 75 μm I.D. capillary into the microdialysis probe, through injection valve B, and finally to waste. The perfusate reservoir/syringe can last for 27 hours at 610 nL/min flow rate. The high speed HPLC valves A and B have switching times of 105 ms and 230 ms, respectively. The valves are computer-controlled. Valve B switches once per minute. Valve A's switch times are synchronized with valve B's so that when A is switched, A and B switch simultaneously.

Table 2.7-1. ANOVA analysis of basal dopamine concentration with day and drug considered as factors.

Outlier set excluded.

Source	Partial SS	df	MS	F	Prob > F	
Model	101.43638	2	50.718192	6.80	0.0063	Number of obs = 21
Day	.35640134	1	.35640134	0.05	0.8294	Root MSE = 2.73137
Drug (dex)	101.33559	1	101.33559	13.58	0.0017	R-squared = 0.4303
Residual	134.28685	18	7.4603806			Adj R-squared = 0.3670
Total	235.72324	20	11.786162			

Table 2.7-2. Regression of basal dopamine concentration with drug considered as factor.

Source	SS	df	MS	Number of obs = 22		
Model	245.6836	1	245.6836	F(1, 20) = 8.17		
Residual	601.6788	20	30.08394	Prob > F = 0.0097		
Total	847.3624	21	40.35059	R-squared = 0.2899		
				Adj R-squared = 0.2544		
				Root MSE = 5.4849		
mean	Coef.	Std. Err.	t	P>|t|	[95% Conf.	Interval]
Drug (dex)	6.711333	2.348486	2.86	0.010	1.812476	11.61019
_cons	10.40667	1.583349	6.57	0.000	7.103858	13.70948

Table 2.7-3. Regression of basal dopamine concentration with drug considered as factor. Outlier set excluded.

Source	SS	df	MS	Number of obs = 21		
Model	101.079984	1	101.079984	F(1, 19) = 14.26		
Residual	134.643252	19	7.08648694	Prob > F = 0.0013		
Total	235.723235	20	11.7861618	R-squared = 0.4288		
				Adj R-squared = 0.3987		
				Root MSE = 2.662		
mean	Coef.	Std. Err.	t	P>|t|	[95% Conf.	Interval]
drug	4.433333	1.173852	3.78	0.001	1.976433	6.890233
_cons	10.40667	.7684664	13.54	0.000	0.798248	12.01509

3.0 A Rotating Operant Chamber for Use with Microdialysis

The following chapter is reprinted (adapted) with permission from Degreef, B.; Ngo, K. T.; Jaquins-Gerstl, A.; Weber, S. G. *J Neurosci Methods* **2019**, *326*, 108387.

3.1 Chapter Summary

3.1.1 Background

Recently, the time resolution of microdialysis followed by a chemical separation for quantitative analysis has improved. The advent of faster microdialysis measurements promises to aid in behavioral research on awake animals. However, microdialysis with awake animals generally employs a fluidic commutator (swivel). The swivel's volume is inimical to the time resolution of the measurements.

3.1.2 New Method

Animals can be housed in rotating cages so that the swivel is not required, but rotating operant chambers are not available. Here we describe the design and construction of a rotating operant chamber with microdialysis capability. We modified a rotating cage by adding operant behavior testing components to the side of the bowl-shaped cage. A modular on-board controller facilitates operant component/computer communication. A battery provides power to the

controller and the operant components. The battery and controller rotate with the cage, and the controller communicates with the computer wirelessly.

3.1.3 Results

The rotating operant chamber can be used to train a rat to retrieve a sucrose pellet following a cue. Microdialysis and online liquid chromatography can be used to measure dopamine at one-minute intervals while the rat moves freely and interacts with operant behavior testing components.

3.1.4 Comparison with Existing Method(s)

We are not aware of one-minute dopamine measurements in awake animals in an operant chamber.

3.1.5 Conclusions

Rotating cage modifications are straightforward. One-minute observations of striatal dopamine can be accomplished while an animal is awake, moving, and interacting with its surroundings.

3.2 Introduction

Microdialysis, since its inception[30] in the 1980s, has become a standard sampling method for animal-based biological, pharmacological, and neurochemical research. An animal with a microdialysis probe placed in the brain can be awake and move freely while perfusate is continuously pumped and dialysate collected or analyzed on-line, enabling neurochemical determinations during behavior[141]. Microdialysis is also valued for its ability to sample a broad array of small molecules. The recent literature shows that many different types of behavior have been examined while sampling the brain's extracellular space with microdialysis: fear conditioning[142-144], wakefulness activity[145], and operant conditioning[146-148]. On the other hand, the microdialysis sampling times were relatively long - ranging from 5-30 minutes.

Recently we and others have developed the technology to improve the time-per-measurement in online measurements of microdialysate based on high-performance liquid chromatography (LC) on awake, behaving animals. We have demonstrated one-minute continuous measurements of striatal dopamine[97] for many hours and, separately, serotonin[77,78] by microdialysis/LC. The Andrews group made extensive two-minute striatal serotonin observations[47]. The Boutelle group has measured energy-related analytes by microdialysis with online continuous monitoring using sensors at 30 s per data point[149]. On anesthetized animals, the Bowser group has developed a variety of microdialysis-electrophoresis assays capable of simultaneous detection of as many as 16 amino acids at 12.5 – 60 s per measurement[150-152]. Fraction collection and offline analysis of segmented microdialysis flow demonstrated measurements taken every several seconds[81,153,154]. The time scale of microdialysis will never reach that of electrophysiology or fast-scan cyclic voltammetry, however improving the time-scale of microdialysis will make measurements related to behavior more meaningful.

It is important to understand that the overall time resolution of a microdialysis measurement depends on many factors, only one of which is the rate at which measurements are made. The other main contributor is the spreading of solute zones in the fluidic components of the microdialysis system: connecting tubing, the probe itself, and a swivel (if one is used). The spreading, or dispersion, of solutes in the fluid stream of dialysate degrades time resolution. These limitations define the ability of microdialysis to detect meaningful transients such as the time-dependent response to the leading edge of a retrodialyzed plug of solution containing, e.g., a neurotransmitter[61,155]. The use of long connecting tubing and/or tubing with a large inner diameter, probes with large void volumes, and swivels all act to degrade time resolution or the system's response time. Tubing dimensions can be optimized to provide the minimum dispersion given a particular dialysate flow rate and acceptable pressure[156], but the use of a swivel will still cause significant dispersion making one-minute time resolution for the overall microdialysis system impossible.

The foregoing observations present a challenge to those interested in the use of microdialysis in behavioral studies. The use of a swivel allows researchers to do experiments in operant chambers, but it also results in a time resolution that is insufficient to capture rapid changes. Using a rotating bowl cage permits the elimination of the swivel, but as far as we are aware, rotating operant chambers do not exist. Here, we describe a system for doing microdialysis in a rotating operant chamber (MD-ROOC) that facilitates rapid microdialysis sampling while making observations of animal behavior.

3.3 Methods

3.3.1 Microdialysis Probes

Chemicals for artificial cerebrospinal fluid (aCSF: 142 mM NaCl, 1.2 mM $CaCl_2$, 2.7 mM KCl, 1.0 mM $MgCl_2$, and 2.0 mM NaH_2PO_4, pH 7.4) were purchased from either Fisher Scientific (Fair Lawn, NJ) or Sigma (St. Louis, MO). Concentric microdialysis probes (200 μm I.D, 280 μm O.D, 4 mm length) were constructed with hollow fiber membranes (13 kDa MWCO, part # 132294, Specta/Por RC, Spectrum Laboratories Inc., Ranco Dominguez, CA). The inlet tubing was connected to a 1.0 mL gastight syringe (Hamilton 81320, Hamilton Company, Reno, NV) using PEEK reducer and adapter (part # P-659, F-120, P-720, IDEX Corporation, Lake Forest, IL). The syringe was driven by a microliter syringe pump (PHD 4400, Harvard Apparatus, Holliston, MA) at a rate of 0.60 μL/min. The inlet and outlet tubing were fused silica capillaries (75 μM I.D., 150 μM O.D., 100 cm long; Polymicro Technologies, Phoenix, AZ). The aCSF used in these experiments contained the sodium salt of dexamethasone phosphate (APP Pharmaceuticals, Schaumburg, IL) to minimize tissue damage and mitigate immune response following probe implantation[86,87]. This formulation of aCSF will be referred to as "DEX". For the first 24 h in use, the aCSF contained 10 μM of dexamethasone phosphate. Thereafter it contained 2 μM of dexamethasone phosphate. Perfusion of the probe was maintained continuously for the entire duration of the experiment.

3.3.2 Rotating Operant Chamber

The operant behavior testing (OBT) components were obtained from Med Associates, Inc. (Fairfax, VT): nose poke (ENV-114AM), cue light (ENV-221M), tone generator (ENV-223AM), pellet dispenser (ENV-203) and pellet receptacle (ENV-200R2M). Lithium-Ion batteries (12 V, 10 Ah Model: CR12V10Ah with BMS protection circuit) were purchased from Dakota Lithium Battery (Seattle, WA). An MD-ROOC uses one battery at a time. A bidirectional digital I/O interface (NI 9401), wireless data acquisition unit (cDAQ 9191) and interface software (LabVIEW 2016) originated from National Instruments (Austin, TX). The wireless-LAN router (E1200 N300 Wi-Fi Router) was from Linksys (Irvine, CA). The battery delivers the power for all OBT and National Instruments components. A locally constructed digital interface contains an in-house built printed circuit board that accepts digital inputs to control MedAssociates components as well as receiving signals from the nose poke. Figure 3.7-1-Figure 3.7-3.

Ordinarily, OBT components use 28 V for both power and control signals. However, they can be configured, or modified, to use 12 V signals instead. Table 3.3-1 lists the modifications necessary to allow the OBT components to be operated at 12 V.

Table 3.3-1. Modifications to Med-Associates devices to allow use of 12 VDC battery.

Name	Modification
Food hopper	U1 and U2 jumpered U9 voltage regulator replaced with a 12 VDC to 5 VDC regulator SPR01M-05
Nose poke	U3 jumpered
Cue light	Light bulb replaced with a 12 VDC LED, Dialight 586-2406-220F

3.3.3 Microdialysis Probe Implantation Procedure

All procedures involving animals were approved by the Institutional Animal Care and Use of Committee of the University of Pittsburgh. Male Sprague-Dawley rats (250-350 g, Hilltop, Scottsdale, PA) were anesthetized with isoflurane (5% v/v induction, 2.5% v/v maintenance, Henry Schein Animal Health, Elizabethtown, PA), and 2:1 N_2O:O_2 (Matheson Tri-Gas, Bernards, NJ). Rats were wrapped in a heating blanket (37°C) and placed in a stereotaxic frame. The incisor bar was adjusted so the dorsal-ventral measurements at lambda and bregma were no more than 0.01 mm apart (flat skull). A small craniotomy (3x5 mm) was made over the dorsal striatum. Microdialysis probes, continuously perfused, were lowered slowly into the dorsal striatum (1.6 mm anterior and 2.5 mm lateral from bregma) or the ventral striatum (1.6 mm anterior and 1.4 mm lateral from bregma) over the course of approximately 30 min to final position of 7 mm or 8mm (respectively) below dura (Figure 3.3-1A). Probes were secured with bone screws and acrylic cement. Anesthesia was removed and animals were placed in a BASi Raturn chamber (MD-1404, Bioanalytical Systems Inc., West Lafayette, IN) for housing.

As the goal of these animal studies was to demonstrate the MD-ROOC's capabilities, we used three animals with the probe in the dorsal striatum and one animal with the probe in the ventral striatum. Data from one of each are shown.

3.3.4 Online Microdialysis-LC-EC

The microdialysis/liquid chromatography system was similar to one we previously described[97]. Perfusate was introduced using a syringe pump (Harvard Apparatus PHD 4400). The syringe contained 1.0 mL of perfusate and was refilled every 24 hrs at least three hours prior to

any online measurement. The outlet of the microdialysis probe, carrying dialysate, was connected directly to the inlet of the injection valve of the LC system (8-port nanobore, electrically actuated, C72NX-4678D, Valco Instruments, Houston, TX) so that the dialysate is loaded into one of two 600 nL, fused-silica sample loops (75 μm I.D., 360 μm O.D, Polymicro Technologies, Phoenix, AZ). While one sample loop is being loaded, the contents of the other sample loop is injected onto the column, separated, and then detected at the end of the column using amperometric electrochemical detection.

As for chromatography, 4.5 cm long, 150 μm ID fused silica capillary columns were packed in-house with 1.7 μm BEH C18 reversed-phase particles (Waters, Milford, MA) at approximately 1400 bar. Mobile phase was delivered using a Shimadzu LC-30DA pump with a maximum pressure of 1300 bar to achieve a flow rate of 7.5 μL/min during experiments. The column was heated to 40°C with a thermostatted column heater. Separation of dopamine was achieved with a mobile phase containing 100 mM sodium acetate, 1.75 mM SOS, 0.150 mM EDTA, 3.0 % v/v acetonitrile, and 2.0 % v/v acetic acid. The mobile phase was filtered and degassed with three passes of vacuum filtration using a 0.22 μm nylon filter (Osminics, Minnetonka, MN). Analytes were detected at 400 mV (vs Ag/AgCl 3 M NaCl) using a radial-style flowcell, 3 mm glassy carbon electrode with a 25 μm thick gasket and amperometry potentiostat (flowcell: MF-1091, MW-5051; potentiostat: EC Epsilon, Bioanalytical Systems Inc., West Lafayette, IN). Dopamine peaks from chromatograms were integrated using MATLAB and compared against pre- and post-run calibration curves to calculate dopamine concentration[97]. The sensitivity of the assay for DA was 0.10 ± 0.02 nA·s/nM and the limit of quantitation was 1.0 nM.

3.3.5 Animal Training and Observations

3.3.5.1 Naïve Animal

One animal was observed in an unmodified Raturn without training, from now on called a naive rat. This animal was placed on food restriction for 1 week (roughly 12g of Purina home chow per rat per day). A microdialysis probe was implanted into the ventral striatum using the surgical procedures described above. He was allowed to recover for 24 hours in his home cage, an unmodified Raturn chamber. On the day of the observation, his Raturn chamber was moved to the online microdialysis-LC-EC setup. After a three hour period for perfusate flowrate stabilization[97], dialysate DA chromatograms were recorded at one-minute intervals continuously for three hours while the animal's movements were recorded on video. Basal DA was established during the first hour. At the one-hour mark, we placed into the bowl roughly 16g of food (Purina home chow). The rat had free access to this food until the end of the three-hour observation. A schematic representation of naive rat observations is shown in Figure 3.3-1B.

3.3.5.2 Trained Animals

Prior to microdialysis probe implantation, two rats were placed on a food restriction regimen (roughly 12g of Purina home chow per rat per day) to maintain them at approximately 85% of their free-feeding bodyweight throughout training and testing. Reduced food intake ensured motivation during conditioning. Behavioral training sessions over 14 contiguous days lasted one hour and took place between 10:00 am and 5:00 pm in the rotating operant chamber. The goal was for the animals to learn to use the nose poke in order to receive a reward. During behavioral sessions, a cue light, mounted on the wall of the rotating operant chamber next to the nose poke, was turned on when the nose poke became active. If the rat triggered the nose poke

while it was active, a tone was generated for two seconds, at which time the pellet dispenser delivered a sucrose pellet (chocolate sucrose pellets, 45 mg-TestDiet, St.Louis, MO) to the food receptacle as a reward. Then, the cue light was turned off and the nose poke was deactivated for 10 s (Figure 3.3-2). The cue light is a 120 mW, 12 V LED white light. The tone generator emitted sound at 2900 Hz and 65 dB.

After 14 days of training, microdialysis probes were implanted into the dorsal striatum and observations began 24 hours later. Initially, microdialysis-LC-EC was used to record basal dialysate DA concentration for two hours while the rat was in his home cage. Next, the rat was placed into the rotating operant chamber for one hour during which time the animal's behavior was recorded (video) while one-minute DA chromatograms were obtained. Rats were then placed back into their home cage for another hour while the DA measurements continued (Figure 3.3-1C). For both training and observation, no limit was placed on the number of rewards that could be earned. Rats were tethered during testing but were not during training.

3.3.6 Video Recording

Photo/video capturing of the animals and subsequent handling of the data are approved by the Institutional Animal Care and Use of Committee of the University of Pittsburgh.

We used a security video system (4 Channel Security System, SWDVK-445954, Swann Communications U.S.A. Inc., Santa Fe Springs, CA) to capture the behavioral experiments. There are two cameras which were set up orthogonally, top down from the top of the bowl and side view, to attempt to capture rat activity with minimal blind spots. The cameras are equipped with IR LEDs to enable video recording in a dark environment.

The cameras run on their own digital video recorder (DVR) system. The videos are time stamped and the DVR's internal clock is checked daily before each experiment to ensure that the video's time stamp and experimental data can be properly coordinated. Correlating microdialysis measurements with video data requires correcting for the time delay required for flow to take the sample to the loop injector. The time delay is 10.0 min for the naive observation and 12 min for the trained observation.

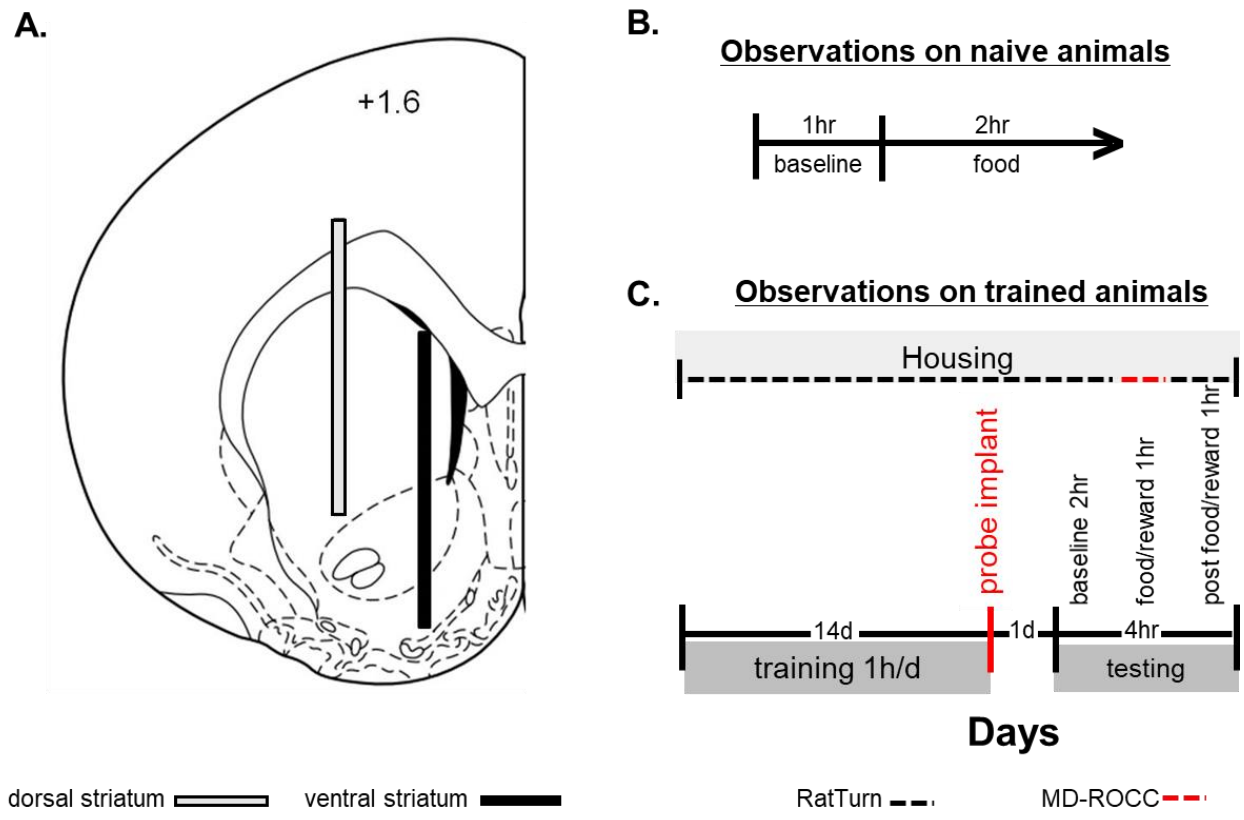

Figure 3.3-1. Schematic representation of (A) microdialysis probe placements for rats in the dorsal striatum (gray) the ventral striatum (black). Numbers represent distance (mm) of coronal section from bregma. (B) Schematic representation of naive observation and (C) training and housing schedule for observation on trained animals.

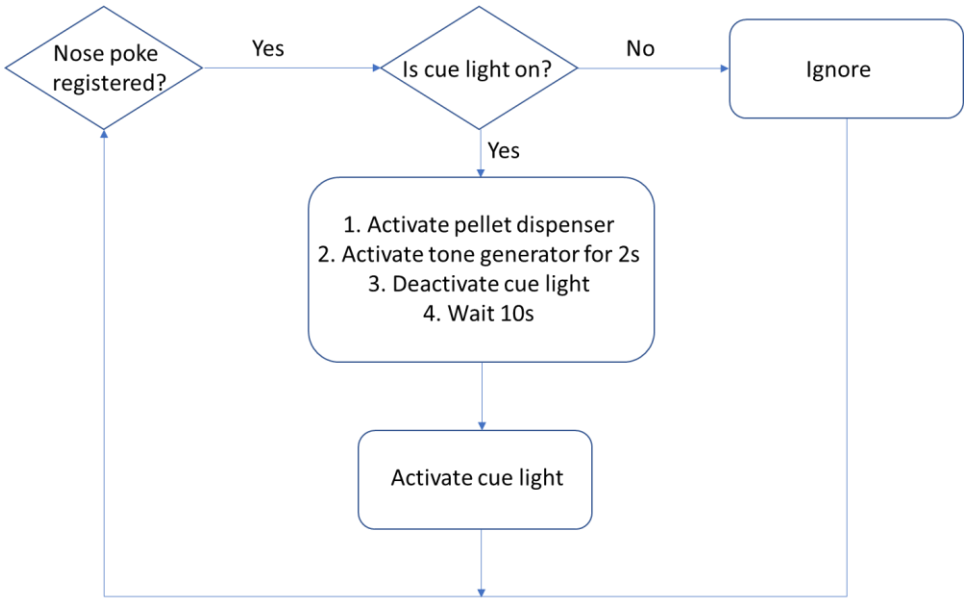

Figure 3.3-2. Instrument training control logic demonstrating instrument responses to animal's behavior. Here the animal is being trained to poke nose once every 12 s to retrieve a sucrose pellet.

3.4 Results and Discussion

3.4.1 Construction of the MD-ROOC

3.4.1.1 Cage Modifications

The system is based on the stand-alone Raturn System from BASi (MD-1404, Bioanalytical Systems Inc., West Lafayette, IN). See Figure 3.7-6 or a side-by-side comparison between our MD-ROOC and an unmodified Raturn. Figure 3.4-1 shows the modifications to the Raturn system. We did not modify the Raturn's harness/controller or motor. We first determined experimentally that an unmodified Raturn can function normally without any observable slippage or slowdown with up to 18 kg of weight on the platform that supports the bowl. Thus, we set an upper limit for the total weight of the required components at 18 kg. To preserve motor drive life

and minimize chances for unexpected weight impact to the MD-ROOC's performance we strove to add as little weight as possible to the Raturn.

All inessential metal housing and original mounting hardware was removed from each operant component to save on weight as well as to make it easier to mount them on the curved surface of the bowl. The OBT components (Figure 3.4-1B) were added to or inserted into the side wall of the rat bowl 15 cm above the cage floor. The components were positioned appropriately for trained feeding observations (Figure 3.4-2). All wires connected to the OBT components were routed along the outside of the bowl and then through small openings in the base support which holds the on-board controller modules (Figure 3.4-1C). Details regarding the on-board controller modules are in a separate section below.

To accommodate the on-board controller modules, the entire Raturn platform was raised 18 cm. We made a circular cradle (Figure 3.4-1A.4) from polyacrylate plastic and aluminum just large enough to hold the desired devices. The cradle was suspended from an upper ring which rests on the inner edge of the rotating mechanism underneath the bottom of the bowl. This allowed the electronic components to rotate together with the bowl while minimizing the moment of inertia. The collective weight of the OBT components is an estimated 1 kg, not including food pellets. A counterweight of 2 kg added to the bowl opposite to the food hopper maintains balance (Figure 3.4-1A.1). The total weight of the additions, including the cradle and on-board controller, is approximately 6 kg. We observed during all training sessions and experiments that the Raturn retains its ability to spin, stop, and change spin direction without slippage.

The presence of the food hopper/chute outside the bowl required moving the support for the motion sensor/harness laterally. The motion sensor/harness arm is attached to a new support

(Figure 3.4-1A.2, see Figure 3.7-4 for detailed blueprint) with the same mounting points and mounting screws as used with the original support.

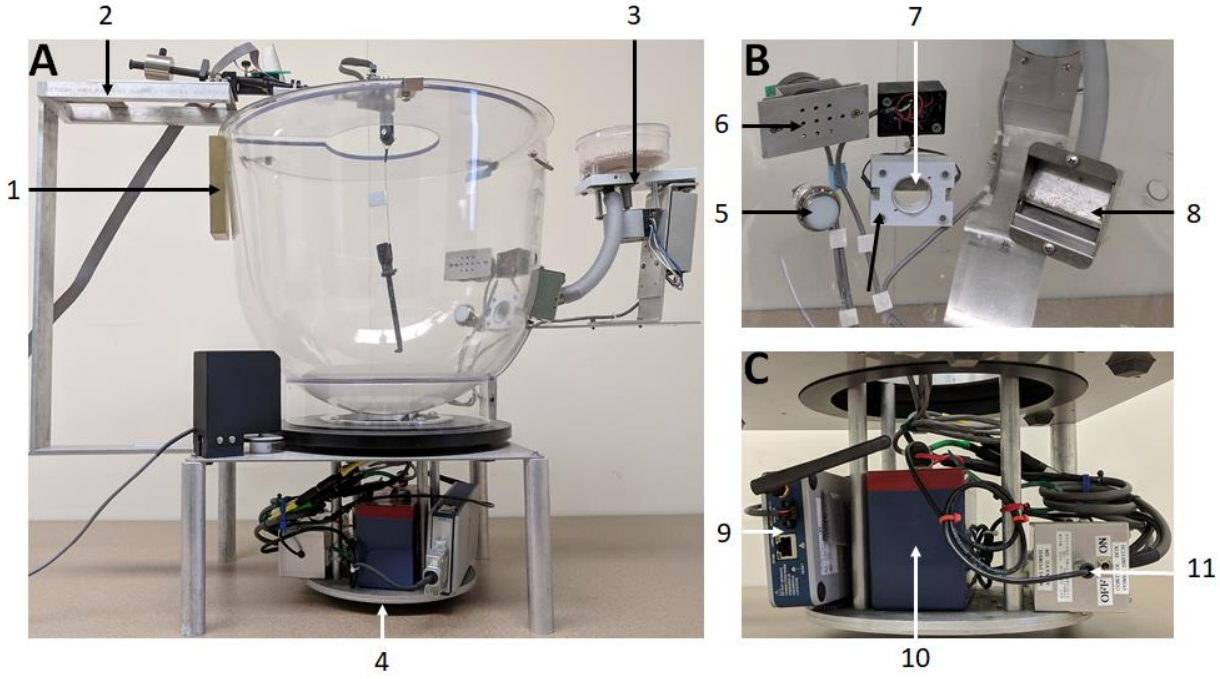

Figure 3.4-1. Photographs of the ROOC.

A. Exterior modifications: Counterweight (1), motion sensor/harness support structure (2), pellet dispenser (3), cradle (4). B. OBT components: Cue light (5), tone generator (6), nose poke (7), pellet receptacle (8). C. On-board controller: Wireless interface (9), battery (10), digital interface (11).

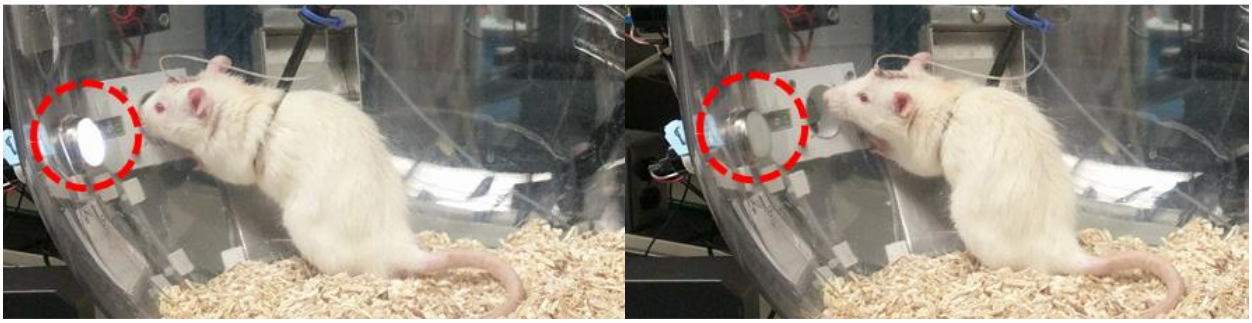

Figure 3.4-2. Pictures depicting an operant conditioning training sequence.

Once a nose poke is registered, the cue light red circles) is deactivated.

3.4.1.2 On-board Controller

The OBT components were powered and controlled by an on-board controller. The on-board controller was made to be small and light and use the minimum possible power so that it can be attached to and spin with the Raturn without interruption for many hours. It uses Wi-Fi to communicate with a router attached to a computer running a LabVIEW script that can be tailored easily to experimental needs. Specifically, the on-board controller has three modules (Figure 3.4-3): Module 1 (Figure 3.4-1C.10) is a 12 V, 10 Ah lithium ion rechargeable battery, module 2 (Figure 3.4-1C.11) is a digital interface, a printed circuit board that controls the operant components based on instructions from the computer and also sends signals from the operant component back to the computer and module 3 (Figure 3.4-1C.9) is a wireless interface that communicates with the computer. Module 2 was designed and built in-house (see Figure 3.7-1-Figure 3.7-3 for circuit diagrams) for instrument control functionality and to regulate the voltage and current from the battery to appropriate specifications with a secondary purpose of limiting current use as much as possible.

Module 2, the digital interface, plays the central role in controlling and powering the OBT components and sending/receiving TTL signals from the wireless interface (Figure 3.4-3). The wireless interface handles all communications with the computer. For example, the nose poke powered by the 12 V battery via the digital interface. When a nose poke is registered, it sends an inverted 12 V signal back to the digital interface, which then generates a 5V TTL signal which is sent to the wireless interface and ultimately is acquired by the computer. The digital interface also uses the 12 V battery to create power at 5 V for the wireless interface.

The modules are connected to operant conditioning components via ¼” TRS plugs with female terminals located in the cradle. The battery is also connected to the digital controller

(module 2) using ¼" TRS connections. This style of connection was chosen for ease of connection and disconnection, so that that the battery can be swapped out with a second, fully charged one in a matter of seconds. We aimed for a minimum MD-ROOC usage time of 24 hrs when we selected the 10 Ah battery. Higher capacity lithium-Ion or lead-acid batteries are available, however the cost in weight and space outweighs the benefit of increased use time. Experimentally, we found that the entire setup can be battery-powered continuously for approximately 37 hours when the cue light is on continuously, tone generator is activated for 2 seconds every minute, and the food hopper is activated once per minute, simulating a 60 s trained feeding schedule.

The wireless router is connected to the computer via an Ethernet cable. While it is possible to set up direct wireless communication between the computer and the wireless DAQ, or between computer and wireless router, we found that wired connection between computer and wireless router, then wireless router to wireless DAQ provided the most consistent connection. We observed no dropped connections during animal experiments with this arrangement. In contrast, the "all-wireless" arrangement was prone to dropping connections. It should be noted that the environment around the MD-ROOC has several analytical instruments and components for online analysis of the dialysate thus a high-powered wireless router is very important for a stable connection.

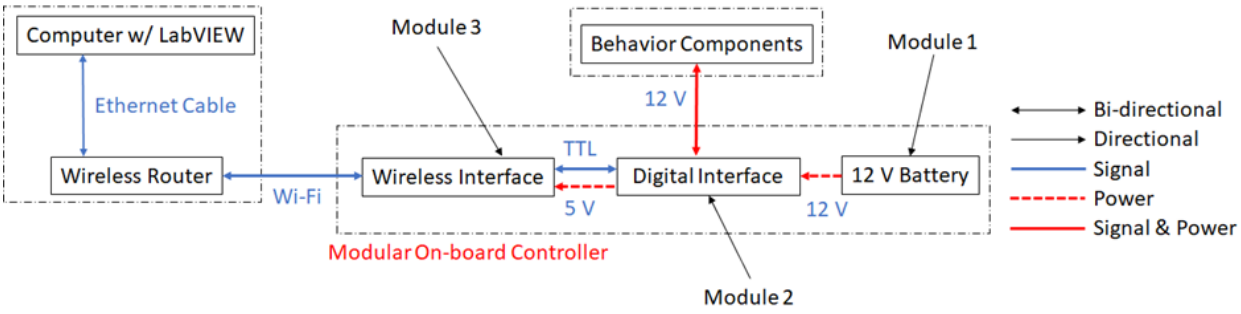

Figure 3.4-3. Schematic overviewing OBT Components controlling scheme.

The computer and wireless router is stationay and is powered by ordinary power sources. OBT components and the controller is mobile and is entirely battery powered.

3.4.2 Observations on Animals

3.4.2.1 Naive Animal

We carried out measurements and observations on a naive animal in order to assure ourselves that the recording and microdialysis systems were functioning as expected. It turns out that the observations are interesting, so we present them here. Dialysate DA concentrations were determined with online microdialysis-LC-EC at one minute per measurement from an awake, freely moving rat in a Raturn. During the session, the rat was also video recorded, and the recording was analyzed frame-by-frame to categorize the animal's locomotive status to six classes: sleep, awake but not moving, grooming, small twitch during sleep, limb movement during sleep, and eating. The time stamp on the video and transport time of the dialysate from the dialysis probe to the LC were used to correlate DA measurements with the animal's locomotive status. Shown below (Figure 3.4-4) are DA concentrations in dialysate from the ventral striatum during the three-hour naive feeding observation, where 0 minutes marks when we placed food into the bowl.

We measured a statistically significant difference between DA concentrations when the rat was actively feeding versus when it was sleeping after feeding (25.2 ± 1.0 nM, time from 1 to 14 min vs 12.0 ± 0.3 nM, time from 15 to 120 min). We also recorded spontaneous DA release when the rat was sleeping and making no observable movements at -55 min, as well as when the rat was sleeping and there was clear limb movement at -25 min.

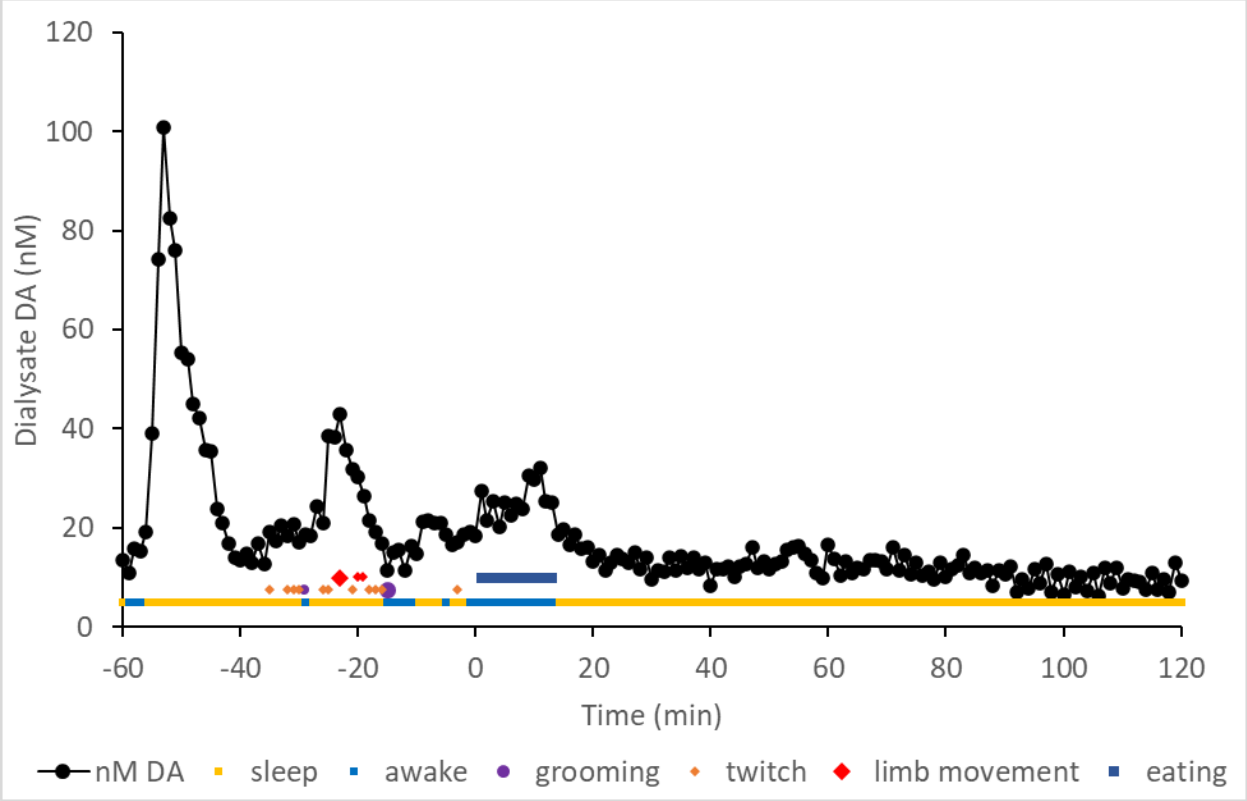

Figure 3.4-4. Dialysate DA concentrations (nM) in the ventral striatum during observations of a naive rat presented with food in a Raturn.

The size of behavior data points represents relative amplitude of locomotor activity. Overlapping data points are plotted on separate y-axis positions to improve visibility. Food was presented at time zero. Trained animals.

3.4.2.2 Trained Animal

We assessed the utility of the MD-ROOC with trained animals. During these observations, dorsal striatal DA was monitored with online microdialysis-LC-EC at one minute per measurement and the rat's movement was video recorded while the rat was in the home cage, moved to the MD-ROOC (see Supplementary Information Video MD-ROOC Bowl Change[98,157]), then moved back to the home cage, as described above. The rat was able to move freely and use the OBT components without tangling microdialysis probe tubing (see Supplementary Information Video MD-ROOC Operation[98,158] ENREF 158), Figure 3.4-4 shows DA concentration as a function of time before, during (marked with a black line) and after feeding sessions. In this particular observation, two hours of DA concentrations were acquired prior to feeding; this is indicated from time -120 minutes to 0. We observed a large DA release lasting 11 minutes at half height centered at -31 minutes. Video recording showed that the rat was sleeping and was still during this time. Note that two spontaneous releases also occurred in the naive rat when the rat was sleeping at -50 and -25 minutes. DA transients occurred throughout the feeding and resting phases of the experiment.

From the data collected from the nose poke and frame-by-frame analysis of the video recording, we were also able to analyze the food retrieval behavior of the rat (Figure 3.4-5-Figure 3.4-7). During the time in the MD-ROOC, feeding phase, the rat continuously used the nose poke to obtain sucrose pellets until it was sated and came to rest. Peak food acquisition was during the first 15 minutes. Also present during this time was a DA transient. After 15 minutes, food acquisition rate decreased with a small spike at 35 minutes and the rat remained inactive for the last 15 minutes of the hour.

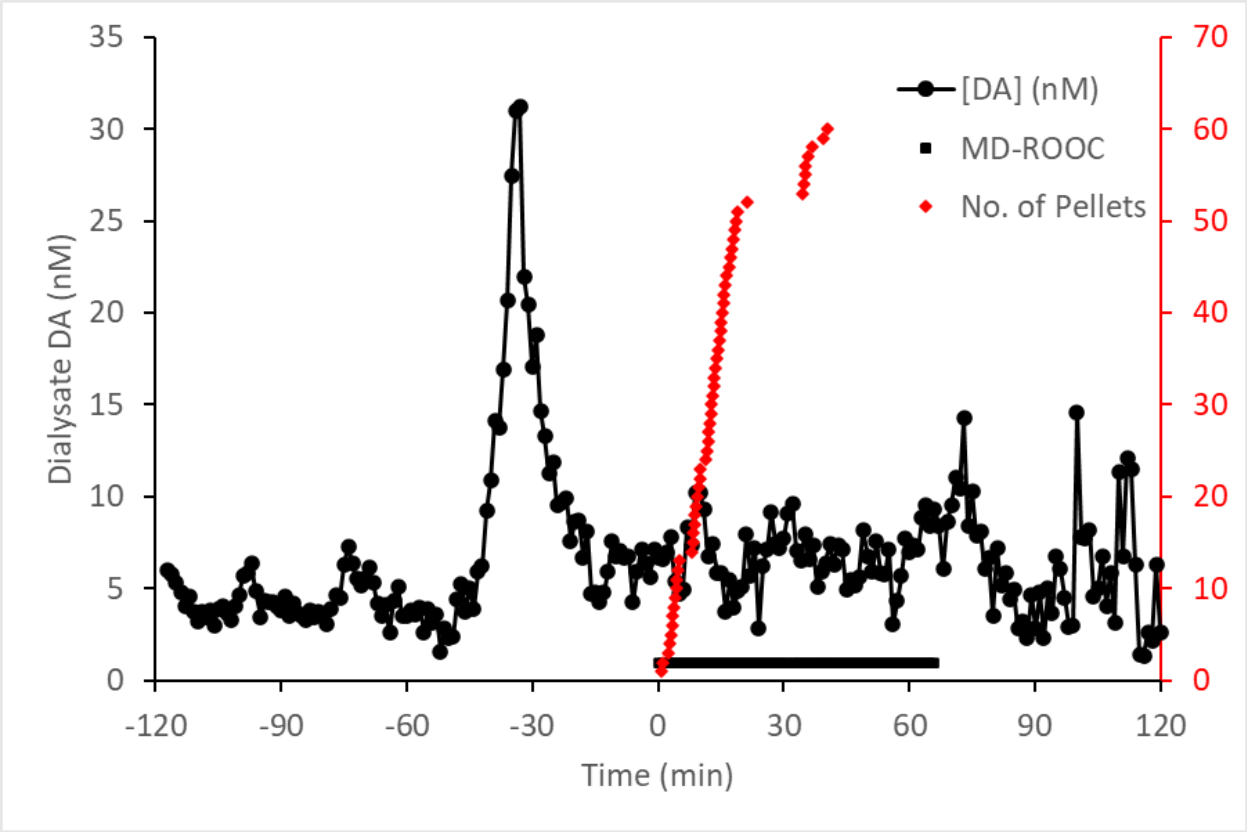

Figure 3.4-5. DA concentrations (nM) in the dorsal striatum and number of pellets eaten during a trained feeding session.

Rat was moved from Raturn to ROOC at time zero, and was moved back to Raturn at 60 min.

3.4.2.3 High Frequency DA Fluctuations Glimpsed from High Time Resolution DA Measurements

We used short-time Fourier transformation (STFT) [96] to perform a spectral analysis of the DA concentration data shown in Figure 3.4-4 and Figure 3.4-5. The resulting spectra are shown in Figure 3.7-4 and Figure 3.4-6, , respectively. The STFT spectral analysis allows us to compute the relative power in each frequency bin plus the time dependence of the power in each frequency bin. A discrete Fourier transform (DFT) of an 11-minute wide section was computed and assigned to the central time point in the window. Frequency components are organized into bins, or frequency

range, according to DFT formulation [159], which are then assigned to the lowest frequency in the bin. The 0.091 min^{-1} bin or 1/11 min^{-1}, for example, represents frequencies from 1/11 min^{-1} to 2/11 min^{-1}. And for our experiment, a signal in in this frequency bin measures a DA concentration change that occurs over a time interval of 5.5 to 11 minutes. We used Nuttall's minimum 4-term Blackman-Harris filter [160] ("Nuttall's window") to reduce artificial oscillations in the spectra while still keeping good frequency resolution (see Supplementary Information Appendix D for MATLAB code). The window was moved by one minute, and the process was repeated to build up a picture of the relative power [161] of each frequency component at each minute. In our case, this relative "power" is actually a ratio of dialysate concentrations raised to the second power. Thus, the "power" spectral density (PSD) is plotted on a decibel scale relative to 1 nM^2. Except near the beginning and end of the time series, individual time data points contribute to 11 spectra. The y-axis shows a range of 0.091 to 0.45 min^{-1}, as this is the limit of frequencies that the Fourier transformation can resolve with a data length of 11 data points at one-minute time resolution.

The spectrograms share some features with the DA concentration time series. Most notably, there are peaks (e.g. time at -32, 73 and 100 min) in the spectrogram (Figure 3.4-6) at the same position as transients in the DA concentration time series (Figure 3.4-5). This is because the rising and falling portions of the transients represent high frequency information. However, spectral analysis also reveals a correlation with feeding behavior that is not apparent in the correlation of DA concentrations with feeding behavior. Table 3.4-1 shows Pearson correlation coefficients, *r*, between the rat's feeding activity (quantitated as the 11-min moving average of the number of pellets eaten per minute) and PSD in each frequency bins as well as the 11-min moving average of dialysate DA concentration. It is apparent that the rat's feeding activity does not correlate to dialysate DA concentration, but it does correlate to dialysate DA variation specifically

at the 0.45 min^{-1} frequency bin (Figure 3.4-7), which coincidentally is the highest frequency bin that our system can measure. This implies that there is measurable neurochemical information in the frequency domain based on a 1-min microdialysis sampling rate.

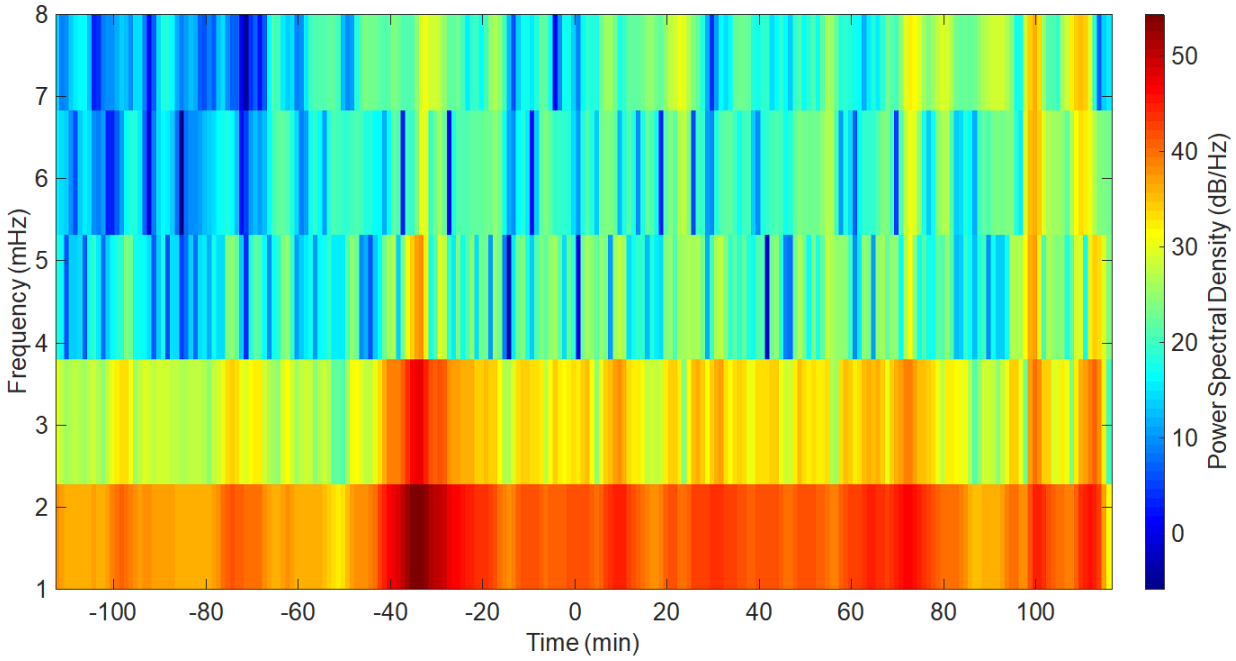

Figure 3.4-6. Spectrogram using short-time Fourier transform (Nuttall's window width of 11 minutes). Each narrow rectangular "point" is the PSD from the time corresponding to the point and the five point to its right and left (except at the time limits). The result shows the PSD at each frequency during the trained feeding experiment. The reference "power" is 1nM^2.

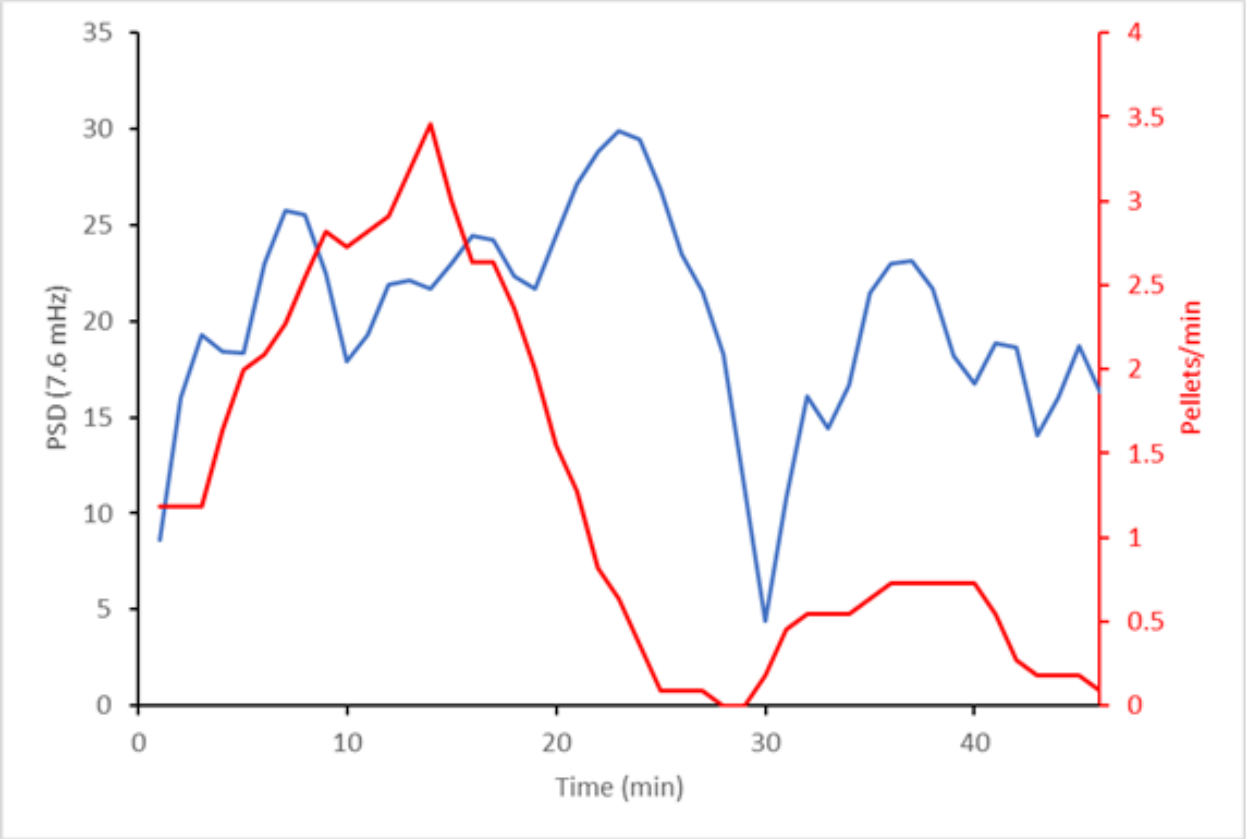

Figure 3.4-7. Correlation between feeding activity and high frequency DA variation.

In blue is PSD at 0.45 min^{-1} and in red is 11 point moving mean of number of pellets eaten. The two time series have a Pearson correlation coefficient, r, of 0.31, during time 1 to 46 minutes that the animal was actively feeding.

Table 3.4-1. Correlation of feeding activity with DA concentration and power spectral densities.

Signal	*r*
11-point average [DA]	0.061
PSD < 0.091 min^{-1}	0.095
PSD 0.091 min^{-1}	0.084
PSD 0.18 min^{-1}	0.043
PSD 0.27 min^{-1}	0.057
PSD 0.36 min^{-1}	0.040
PSD 0.45 min^{-1}	0.31

3.5 Conclusions

We have demonstrated that a rotating cage suitable for fast microdialysis measurements can be modified easily to make a simple operant chamber. Trained rats readily use the nose poke to obtain food in line with their training. The fast dialysis measurements reveal transient changes in dialysate DA that can be correlated with behavior. Like the online microdialysis-LC-EC system, the MD-ROOC is built from commercially available parts with a flexible design that can be expanded to operant chamber components not included in this work. While we tested no biological hypotheses here, we have shown that one-minute DA measurements can be made simultaneously with either a naive rat or a trained rat using its training to acquire food according to a learned task. We found that there is behavioral information encoded in the 1-min time resolution DA measurements that is not available from traditional 10 min microdialysis.

3.6 Acknowledgement

This work was supported by the National Institutes of Health through grant R01 MH104386. We acknowledge and thank the members of the Dietrich School of Arts & Sciences Electronics and Machine shops.

3.7 Supplementary Information

3.7.1 Electronic Circuit and LabVIEW VI Diagram

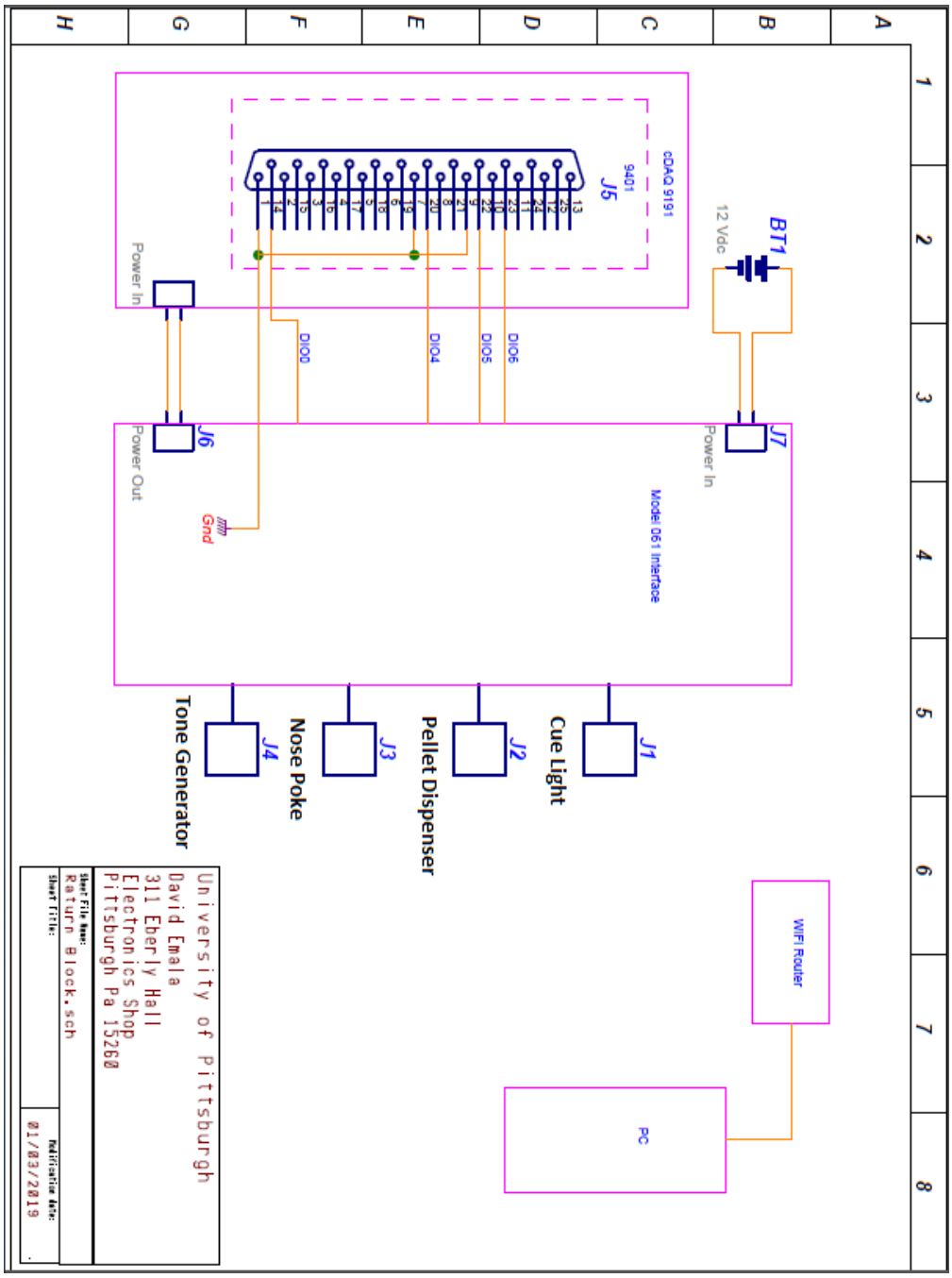

Figure 3.7-1. Electrical block diagram of the on-board controller: wiring between digital I/O and operant behavior component.

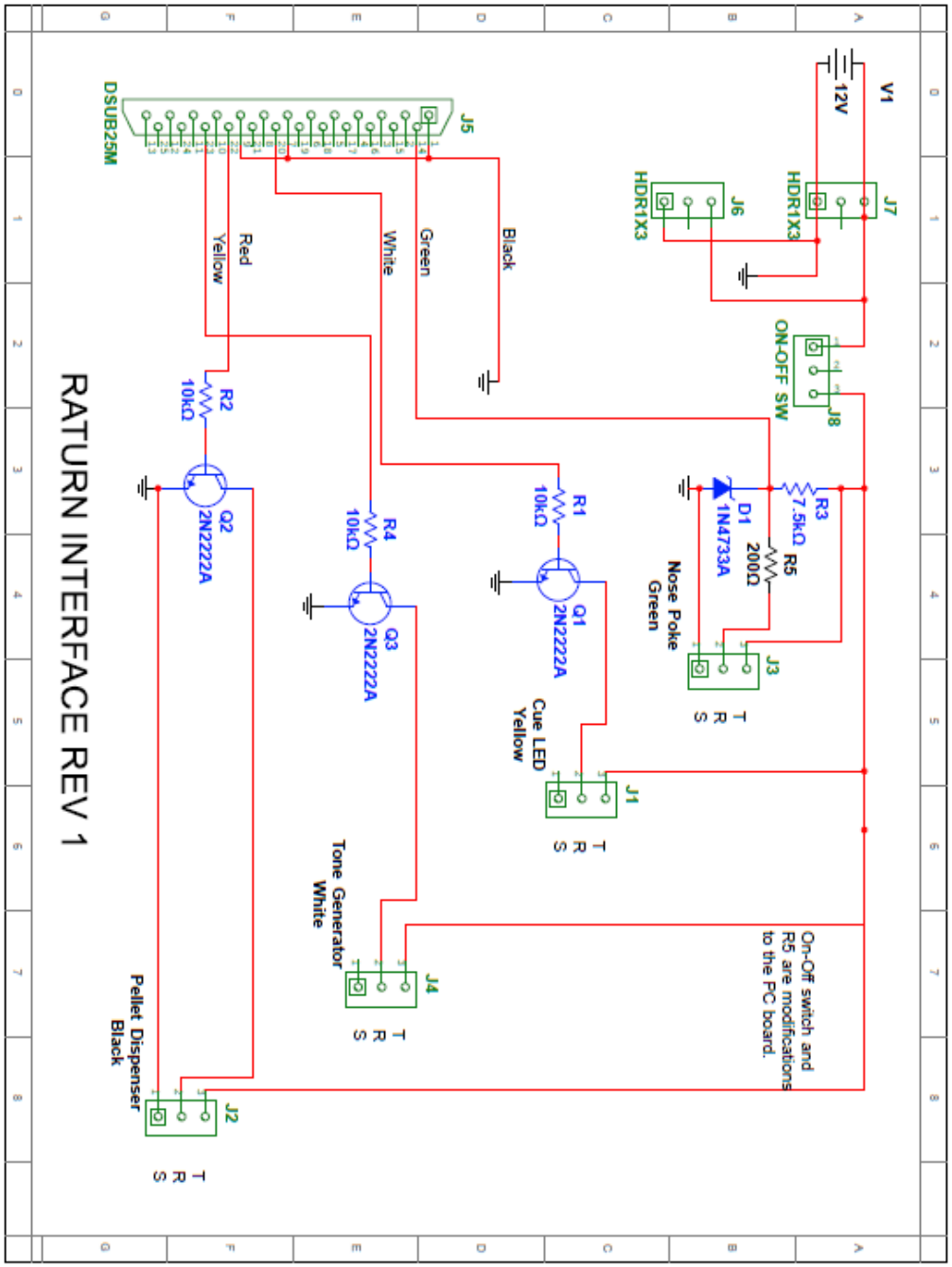

Figure 3.7-2. Electrical diagram of the power supply and digital controller.

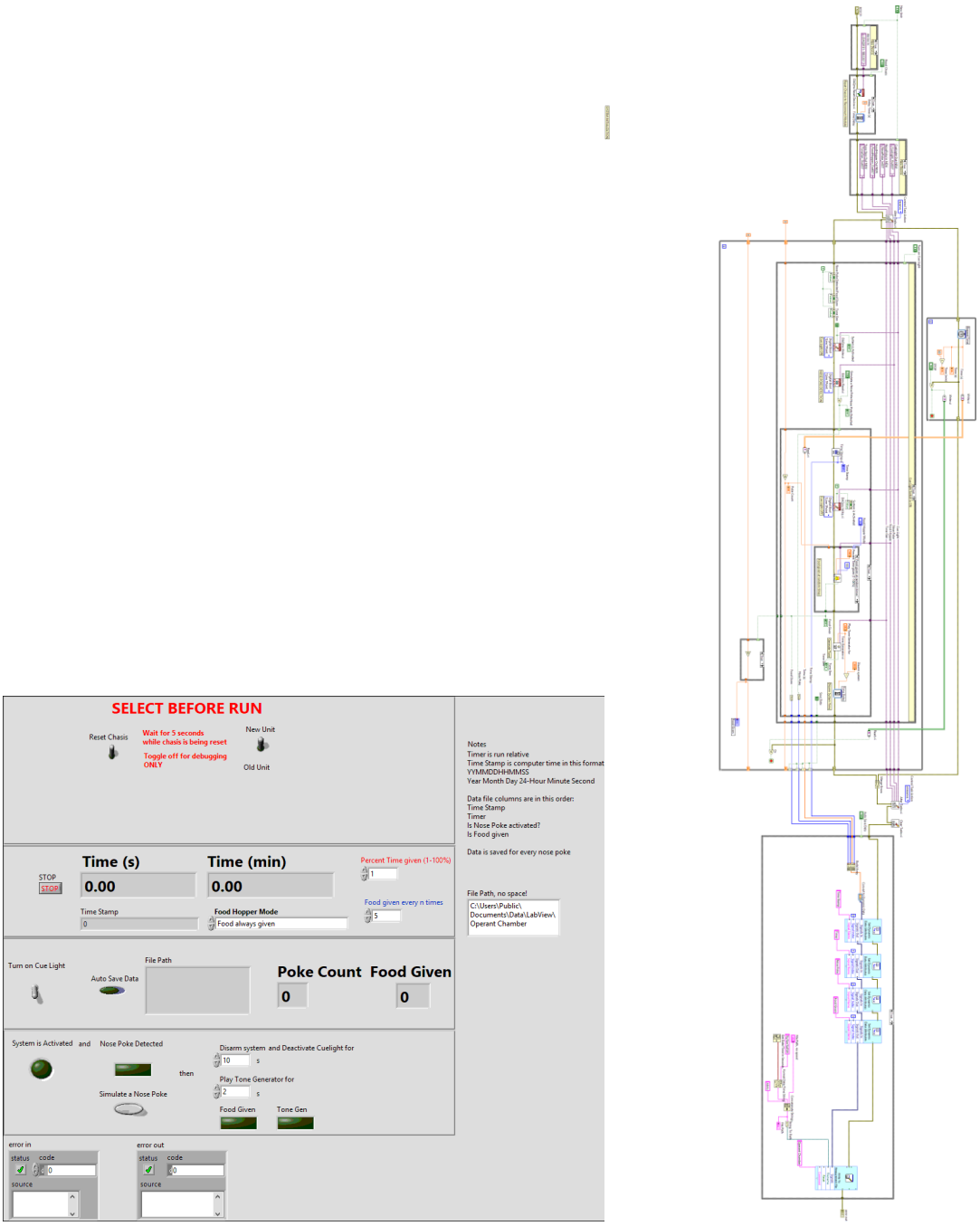

Figure 3.7-3. Front and back panel of the LabVIEW VI that controls the raturn.

3.7.2 Raturn Component Blueprint

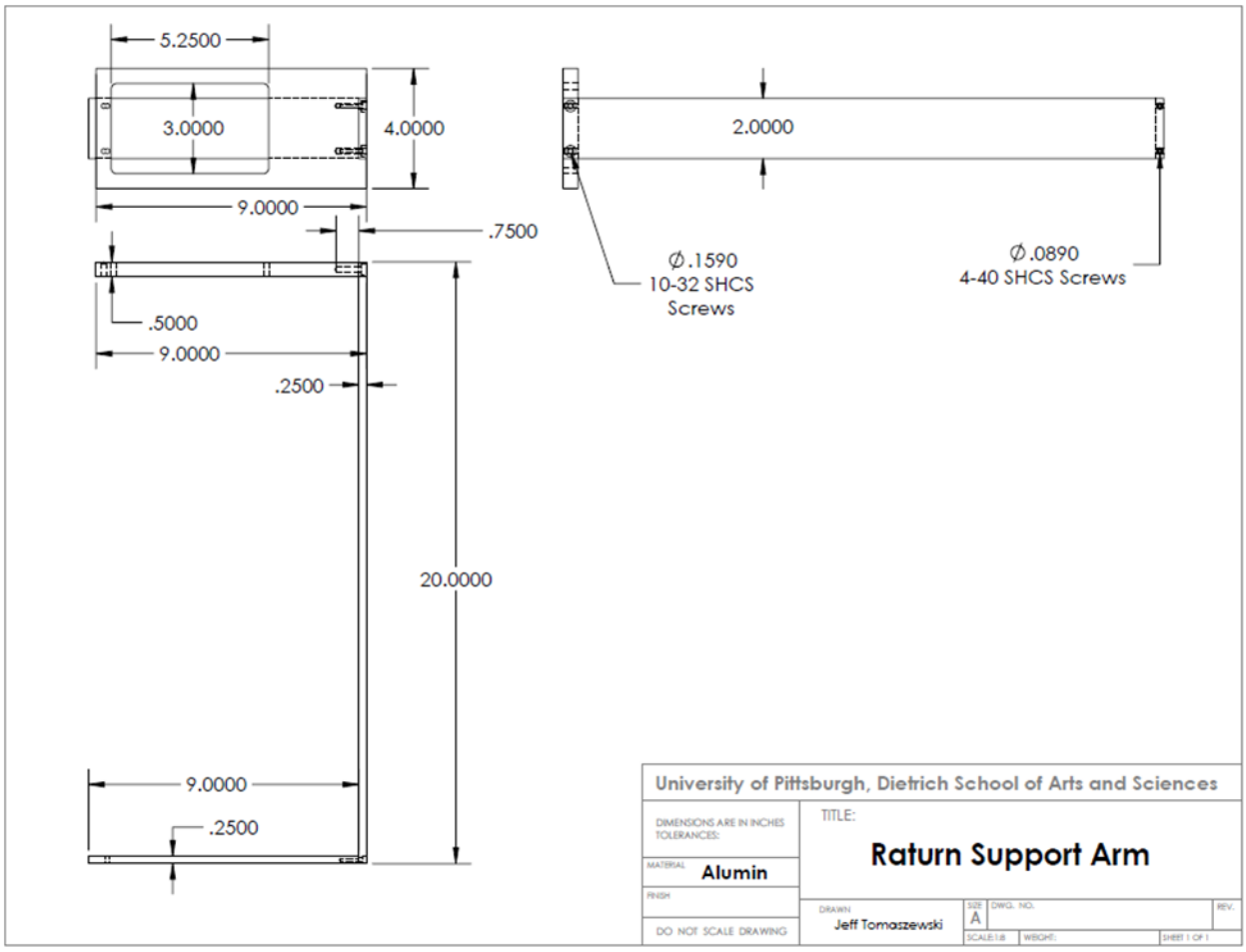

Figure 3.7-4. Raturn replacement support arm blueprint.

3.7.3 Additional Figures

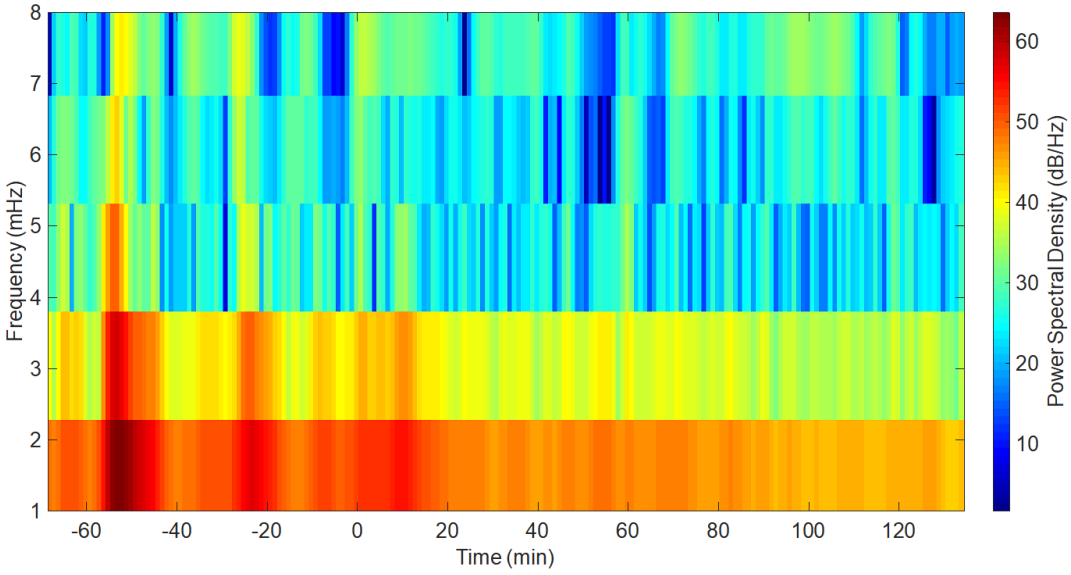

Figure 3.7-5. Spectrogram using short-time Fourier transform (Nuttall's window length of 11, with 10 overlapping data point) showing spectral power density of each frequency during the naive feeding experiment.

The power amplitude is in decibel, with reference power is 1 nM^2.

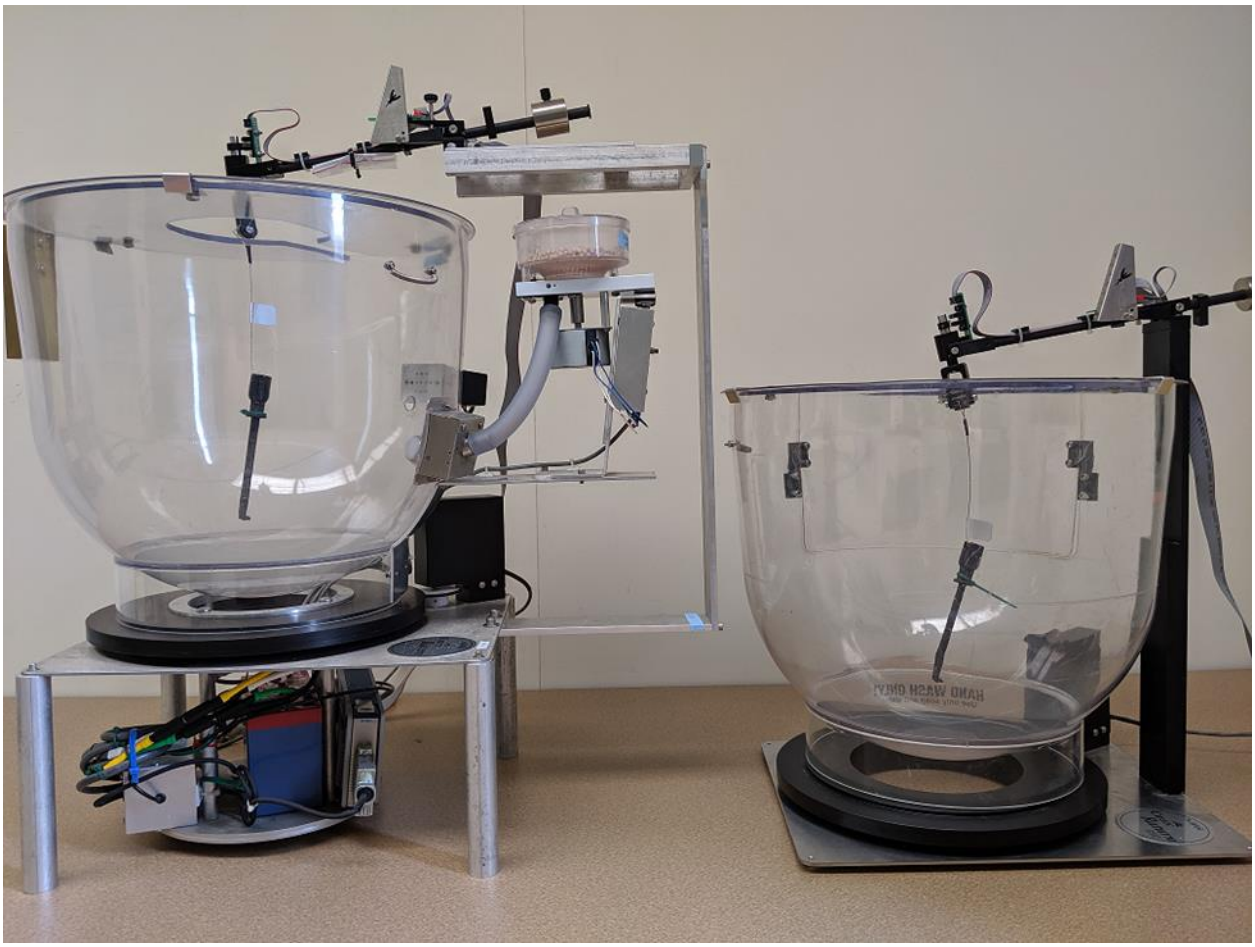

Figure 3.7-6. A side-by-side comparison between a modified Raturn (left) and an unmodified Raturn (right).

3.7.4 MATLAB Code

```
load('spectrogram_data.mat'); %load data, contains vector X for DA
concentration
                              %and t for time
window_width = 11; %set window width
num_overlap = 10; %number of data point overlapped
sample_rate = 1/60; %1 min sampling, which is 1/60 Hz
tX = min(t)+(window_width-1)/2:1:max(t)-(window_width-1)/2; %truncate time
axis
%calculate spetrogram using Nuttall-defined minimum 4-term Blackman-Harris
window
[s,f,t,p,fc,tc] = spectrogram(X, nuttallwin(window_width), num_overlap,
window_width, sample_rate, 'onesided', 'yaxis','psd');
%plot spectrogram
figure;imagesc(f*1000,tX,10*log10(abs(p')));
axis tight;
colormap(jet);
```

```
view(-90,90);
title(['Spectrogram [DA](t) Nuttalls Blackman-Harris Width'
num2str(window_width)],'FontSize',20)
c = colorbar;
c.FontSize = 20;
c.Label.String = 'Power Spectral Density (dB/Hz)';
xa = get(gca,'XAxis');
set(xa,'FontSize',20);
xlabel('Frequency (mHz)','FontSize',20)
xlim([1 8])
ya = get(gca,'YAxis');
set(ya,'FontSize',20);
yticks('auto')
ylabel('Time (min)','FontSize',20)
```

4.0 Comprehensive Quantitative Microdialysis: Mathematical Method and Reconciliation of Preceding Theories

4.1 Chapter Summary

The development of one-minute or less determination of bioactive solutes *in vivo* (Fast Microdialysis) has shown that there is biologically relevant information encoded in the fluctuations of measured solute concentration over time. As experiments progress toward faster time resolution, it is appropriate to construct a framework to methodically elucidate biological (e.g. uptake rate, tissue morphology) and system (e.g. transport time, dispersion) information from observable experimental quantities. Thus, we created the Comprehensive Quantitative Microdialysis (CQM) which includes an approximate mathematical model for microdialysis based on earlier work, an experimental method, and a curve fitting method to determine sought-for parameters that affect time-dependent solute concentration at the detector ($C_{det}(t)$). In this chapter, we present the mathematical portion of CQM which is adapted, in part, from earlier work by Chen *et al*. (2002) and Bungay *et al*. (2011). The mathematical model is based on tissue and microdialysis probe permeabilities. An analytical expression describes $C_{det}(t)$ as a function of time resulting from a step concentration change of the solute at the probe inlet C_{in}. Notably, the model also includes hydrodynamic dispersion of solute during transport in the inlet/outlet capillaries of the microdialysis probe and the transfer function of the detector in the overall model. We also created a MATLAB simulation tool to demonstrate the effects of these factors to $C_{det}(t)$ to aid experimental design. We showed that the MATLAB simulation tool accurately predicts an *in vitro* well-stirred experiment.

4.2 Introduction

Microdialysis is a sampling and delivery technique[12,30,31,56] in which solutes are sampled or delivered via mass transport through a semipermeable membrane separating the lumen of the microdialysis probe and the external medium (Figure 4.2-1). Quantitative microdialysis techniques determine the relationship between the concentration of a solute in the dialysate sample (C_{out}) and that of in the perfusate solution (C_{in}) and in the external medium[55]. Since the primary mechanism of mass flow of solutes to and across the membrane is diffusion which is driven by concentration gradients, the processes that affect diffusion and concentration gradients also determine C_{out}. These processes include, but are not limited to, convective flow inside (dialysate flowrate) or outside (*in vitro* stirring) the probe, chemical reactions (in the context of brain microdialysis, uptake[162] and release[163,164] of neuroactive species), and diffusion through the external medium (which, in brain microdialysis, is affected by tissue porosity and tortuosity[165-167]). C_{out} is therefore dependent upon diffusion in the extracellular space as affected by tissue morphology, and release and uptake in the extracellular space both at the basal conditions and as affected by exogenous agents. We note that quantitative microdialysis experiments[54] typically operate in the steady-state domain so that C_{out} is constant during an experiment at a constant C_{in}. In principle, a change in C_{in} will result in a time-dependent, or transient response in C_{out} ($C_{out}(t)$) that could be measured and would provide information about the parameters that affect mass transport listed just above. In fact, there are several theory papers, to which we return below, that describe $C_{out}(t)$ resulting from a such a perturbation[57-61,64,84]. Existing experimental efforts[61,168-170] to obtain mass transport information related to the aforementioned theories involved hours-long transients due to the poor time resolution of microdialysis as practiced until recently.

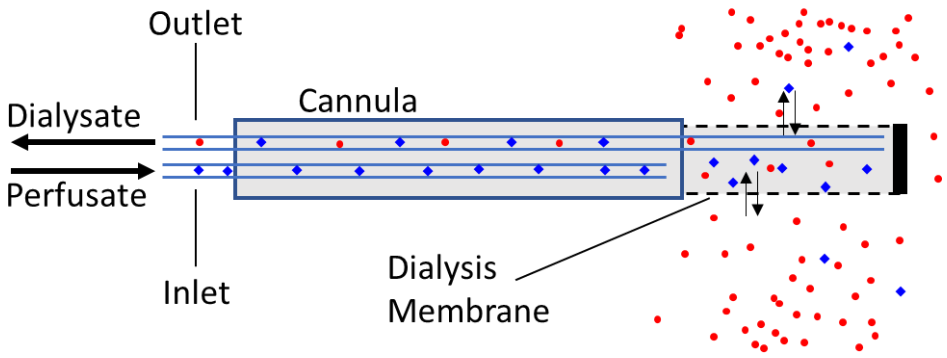

Figure 4.2-1. An illustration of the concentric microdialysis probe.

The red circle species demonstrates a sampling process, and the blue diamond species demonstrates a retrodialysis (delivery) process.

Measuring transient responses in $C_{out}(t)$ will require an understanding of how the microdialysis/analytical instrument affects the response time of the measurement. Any attempt to measure microdialysis transients requires better time resolution than the typical 5 – 30 minutes per measurement[47,171]. In addition, the probe inlet and outlet are connected to long capillaries, and swivels may be used in awake animal work. The capillaries add hydrodynamic dispersion and the probe itself and swivels similarly add longitudinal dispersion, both of which degrade time resolution. Furthermore, in systems where periodic, discrete measurements are made, e.g., sample collection or liquid chromatography, a concentration averaging occurs because a single sample comes from an extended time period[77]. In systems where the outlet directs dialysate flow past a continuously monitoring sensor, there is a conceptually similar (but mathematically distinct) averaging dictated by the response time of the sensor. Pragmatic experimental needs make measurement of transients difficult.

On the other hand, there has been significant progress recently on many of these issues. For solutes that can be determined over the long term with a sensor or selective detector, the outlet tubing can be connected directly to the sensor/detector for online analysis[92,172]. The outlet tubing can also be connected directly to an instrument, capillary liquid chromatography or capillary/chip

electrophoresis, to provide online measurements at three minutes or less per sample[47,72,77,78,97,152,154,173-175]. Offline analysis techniques are capable of measurements as fast as two seconds per sample[80,81]. This analysis time was achieved by using segmented flow to minimize hydrodynamic dispersion. On the inlet side, C_{in} can be changed rapidly by using an automated syringe/valve system[77,97]. The dispersion of solute zones in an open capillary under laminar flow, hydrodynamic dispersion[176], is well-understood, and theory has successfully predicts experiments[77,177]. Thus, despite the difficulties involved, it is becoming possible to envision using microdialysis to obtain information from transient responses in $C_{out}(t)$ from a perturbation in C_{in} at the minute timescale.

The observable experimental result from a microdialysis experiment in which C_{in} is changed is not $C_{out}(t)$, rather it is the time-dependent signal obtained from a quantitative analytical measurement from a detector, $C_{det}(t)$. Processes in the analytical system contribute to the overall time response of the system. Thus, a mathematical model that that seeks to describes how $C_{det}(t)$ is related to processes occurring in the brain must account for both the brain the analytical system. We have developed a technique (named Comprehensive Quantitative Microdialysis, CQM) for obtaining quantitative estimates related to microdialysis sampling (e.g. solute uptake and diffusion in tissue) and the analytical system (e.g. solute dispersion) based on the transient response in solute concentration experimentally measured at the detector $C_{det}(t)$ following a step change in solute concentration in the inlet C_{in}. CQM has three components: a mathematical model, an experimental method, and a curve-fitting method. Here, we describe the mathematical model.

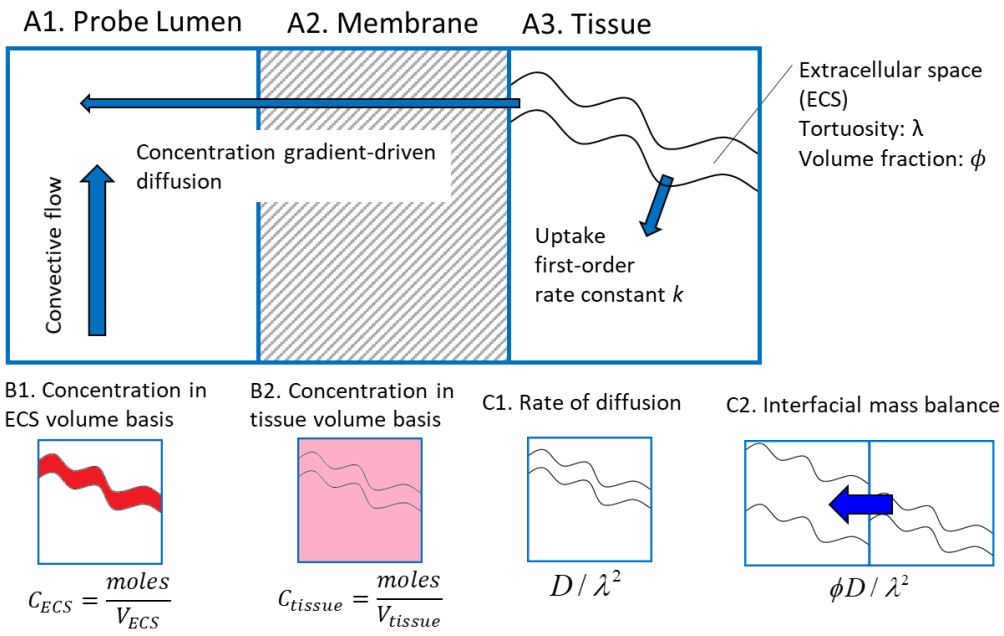

Figure 4.2-2. Graphical illustrations of the mass transport model and key mass transport quantities. Top: the three regions where mass transport occurs (A1) Probe lumen, (A2) Membrane, and (A3) Tissue. The blue arrows indicate the direction of mass transport in a sampling experiment. Bottom: Concentrations in (B1) ECS volume basis (red) and (B2) Tissue volume basis pink. Rates of diffusive mass transport is affected by tortuosity (C1). Diffusive flux is also affected by porosity (C2).

Microdialysis sampling relies on mass transport. It is important to acknowledge that the insertion of the microdialysis probe into brain tissue injures the tissue near the probe forming a so-called trauma layer[62,82,85,90,178,179] which can alter mass transport. We previously found differences in the steady-state dialysate DA measured in rats treated with a locally delivered anti-inflammatory drug compared to untreated rats[97]. Mathematical models[65,88] in cylindrical coordinates incorporating a trauma layer exists for the *steady-state* concentration of a sought-for species (e.g. dopamine, DA) in microdialysis. In this model there are four volumes through which DA diffuses, namely, the normal tissue, the trauma layer, the membrane, and the lumen of the microdialysis probe. As the thickness of the trauma layer is decreased, the steady-state model's prediction becomes equivalent to the prediction of steady-state models that do not incorporate a trauma layer.

However, as far as we are aware there is no *transient* theory or model that incorporates a trauma layer in cylindrical coordinates. Therefore, the core of the model used here is an established microdialysis mass transport model in which there are three physically separate media (Figure 4.2-1) through which solutes diffuse, namely the tissue, the membrane, and the lumen of the microdialysis probe. Expressions for time-dependent microdialysis based on this model exist[56-66], including closed-form analytical expressions (e.g. Amberg and Lindefors (1989) [57], Morrison *et al.* (1991) [60], Peters and Michael (1998) [62]) which are the most suitable for curve-fitting. The existing theoretical approaches vary in both their geometries and the biological processes that influence mass transport. Of course, the more accurate the model is the more complex the mathematics are. For example, Amberg and Lindefors (1989) [57] derived an equation in cylindrical coordinates, but considered only diffusion, not uptake kinetics; while Peters and Michael (1998) [62] derived an equation that includes both diffusion and uptake, but in one Cartesian spatial dimension. As far as we are aware, the model with the fewest assumptions is Morrison *et al.* (1991) [60]. It contains two source and uptake terms, one for 'metabolism' and one for exchange between brain tissue and capillary blood, but the resulting equations are very complex. Bungay and coworkers over the years have used the concept of the permeability[61,65,84] to simplify the mathematics while including uptake kinetics and the cylindrical coordinate system. Based on the normal microdialysis probe dimensions, and for known parameters related to solute diffusion and uptake, we have identified the Bungay (2011) one-dimensional (radial) model[61], which is adapted from a pair of papers[58,59] from Chen and colleagues (2002), as being optimal – a balance of accuracy and computational burden, especially as it allow us to create a comprehensive model consisting solely of short, closed-form analytical expressions. Note that we will frequently refer to

these three identified papers as Bungay (2011) [61], Chen (2002a) [59] and Chen (2002b) [58] without a citation.

In the work we describe here we describe similarities and differences in mathematical derivations and numerical evaluations in Bungay (2011) and Chen (2002a, b). We clarify the use of an "effective" or "apparent" diffusion coefficient when diffusion occurs in a porous matrix. We incorporate hydrodynamic dispersion in open capillaries (Taylor-Aris) and the probe, the transit time of solute from the probe to the detection system (which is needed to establish the time at which an observed change occurred in the brain), and the influence of the detection system's response time. We created a MATLAB tool to aid experimental design by simulating experimental results from known tissue, probe, and analytical system parameters. The overarching goal of this two-part study is to improve quantitative microdialysis and explore future directions for microdialysis studies. In a second paper[180], we describe an experimental and data analysis method to obtain quantitative estimates of parameters relating to microdialysis sampling and the detection system used. We also investigate the robustness of the CQM method, and microdialysis as a whole, over a range of possible experimental condition including anticipated improvement in time resolution.

4.3 Experimental

4.3.1 Materials

Analytical-grade chemicals for dopamine standards in artificial cerebrospinal fluid (dopamine, L-ascorbic acid, aCSF: 142 mM NaCl, 1.2 mM $CaCl_2$, 2.7 mM KCl, 1.0 mM $MgCl_2$,

and 2.0 mM NaH_2PO_4, pH 7.4) and liquid chromatography mobile phases (sodium acetate, sodium octyl sulfonate, EDTA, acetonitrile, and acetic acid) were acquired from either Fisher Scientific (Fair Lawn, NJ) or Sigma (St. Louis, MO). Ascorbic acid (50 μM) was added to dopamine standards to prevent oxidation of dopamine[67].

4.3.2 Microdialysis Probe

Concentric microdialysis probes (280 μm diameter, 4 mm length membrane) were constructed with hollow fiber membranes (13 kDa MWCO, Specta/Por RC, Spectrum Laboratories Inc., Ranco Dominguez, CA). The inlet and outlet were fused silica capillaries (75 μM I.D., 150 μM O.D., 110 cm long, Polymicro Technologies, Phoenix, AZ). The inlet capillary was connected to a 1 mL gastight syringe (Hamilton 81320, Hamilton Company, Reno, NV) with a 100-psi backpressure regulator and a bubble-induced dampener[181]. Perfusate flow was driven by a microliter syringe pump (PHD 4400, Harvard Apparatus, Holliston, MA) at a flowrate of 0.80 μL/min. The outlet capillary of the microdialysis probe was connected directly to the LC system.

4.3.3 *In Vitro* Online Microdialysis-HPLC

The liquid chromatography system was similar to our previous work[97,98], where the outlet capillary of the microdialysis probe was connected directly to the LC injector (8-port nanobore, electrically actuated, C72NX-4678D, Valco Instruments, Houston, TX) and dialysate was continuously sampled for analysis. The probe was suspended in a heated (37°C), well-stirred cuvette for the duration of the experiment. The LC injector had two sample loops of 0.80 μL each.

For every 45 s analysis cycle, one loop was is filled with dialysate from the probe and dialysate in the other loop was injected for separation.

Capillary columns (7.5 cm long, 150 μm ID fused silica) were packed with 1.7 μm BEH C18 reversed-phase particles (Waters, Milford, MA) at approximately 1400 bar. Mobile phase was delivered using a Shimadzu LC-30DA pump with a maximum pressure of 1300 bar to achieve a flow rate of 8.5 μL/min during experiments. The column was heated to 47.5°C with a thermostatted column heater. Separation of dopamine was achieved with a mobile phase containing 100 mM sodium acetate, 1.75 mM SOS, 0.150 mM EDTA, 3.0 % v/v acetonitrile, and 2.0 % v/v acetic acid. The mobile phase was filtered and degassed with three passes of vacuum filtration using a 0.22 μm nylon filter (Osminics, Minnetonka, MN).

4.3.4 Amperometric Detection

Dopamine was detected at 400 mV (vs Ag/AgCl 3 M NaCl) using a BASi radial-style flowcell, 3 mm glassy carbon electrode with a 25 μm thick gasket and BASi Epsilon potentiostat (West Lafayette, IN). Dopamine concentration was determined from chromatographic peak area, integrated using MATLAB then compared against pre- and post-run calibration curves. The detector sensitivity for DA was 0.106 ± 0.002 nA·s/nM (AVG±SEM) with a limit of quantitation of 1.0 nM (defined as RSD ≤ 10%).

4.3.5 Time Interleaved Sampling Microdialysis

Time interleaved sampling is a technique where multiple analog-to-digital converters are used to acquire discreet digital data from a single continuous analog signal, but each converter's

acquisition times are offset from one another in order to increase the time resolution of the signal[182]. An array of *N* converters with each having its acquisition times offset from the others by a time that is a multiple of a fraction 1/*N* of the sampling interval can improve the sampling frequency by *N* times. Time interleaved sampling microdialysis is an analogous technique which utilizes the same principle, where instead of *N* detectors simultaneously measuring a single transient response, a single detector is used to measure *N* repeats of the transient response, all of which are assumed to be identical.

4.3.6 MATLAB Simulation

We wrote MATLAB scripts (MATLAB R2019a Update 2, MathWorks, Natick, MS) that reproduce transient calculations in published work. All MATLAB routines cited here can be found with embedded annotation in Supplementary Information 4.6.1. Specifically, Ngo2020_BungayFig2.m calculates dimensionless external medium transient permeability, as defined in Bungay (2011), following a step input in a no-net-flux type experiment[183]. This script replicates Bungay (2011) Fig. 2 exactly[61]. Ngo2020_ChenFig4.m calculates membrane resistance, external medium resistance and total resistance given known probe and tissue properties. This script replicates Chen (2002a) Fig. 4 exactly[59].

The major script, Ngo2020_simulation.m calculates the experimentally observed solute concentration detected at electrochemical detector given known probe construction, tissue and analytical system properties (Table 4.4-2). The script simulates a discrete detection system using chromatographic separation with a 45 s sampling time. This script also permits calculation of other important experimental results, such as extraction fraction or transient relaxation time. Using this script, one can quickly explore the effects of different experimental parameters as well as tissue

conditions on solute concentration profiles measured at the probe outlet, LC injector or LC detector and use this knowledge expeditiously to design new experiments.

4.4 Results and Discussion

Table 4.4-1. Experimental conditions and parameters used for simulating in vitro microdialysis sampling of a well-stirred solution.

Symbol	Description	Value	Unit	Source
L	Membrane length	4.00×10^{-3}	m	Experimental
r_i	Membrane inner radius	1.00×10^{-4}	m	Experimental
r_o	Membrane outer radius	1.40×10^{-4}	m	Experimental
L_i	Inlet capillary length	1.10	m	Experimental
L_o	Oulet capillary length	1.10	m	Experimental
Q	Perfusate volumetric flowrate, in vitro	1.33×10^{-11}	m^3/s	Experimental
t_s	LC sampling time	45	s	Experimental
t_i	Characteristic time of the concentration profile	-24	s	Calculated
σ_{tot}	Hydrodynamic dispersion standard deviation	12.8	s	Calculated[97]
C_{in}	Perfusate analyte concentration	1.50×10^{-7}	M	Experimental
$C_{ECS\infty}$	Solute concentration "ECS" (cuvette)	0	M	Experimental
D	Analyte diffusion coefficient in free solution	6.0×10^{-10}	m^2/s	Literature[184]
λ	"ECS" (cuvette) tortuosity	1	-	Experimental
ϕ	"ECS" (cuvette) porosity	1	-	Experimental
k	Solute uptake rate constant, first order	5×10^{3}	s^{-1}	Nominal value
E_{ws}	well-stirred extraction fraction, in vitro, 37°C	0.510	-	Experimental
D_m	Solute diffusion coefficient in membrane	1.366×10^{-10}	m^2/s	Experimental

Table 4.4-2. Nomenclature.

Symbol	Unit	Name	Instrument System
C	M	Concentration	*non-specific*
D	m^2/s	Diffusion coefficient	*non-specific*
λ	*unitless*	Tortuosity	*non-specific*
ϕ	*unitless*	Porosity	*non-specific*
t_s	s	Sampling time	Chromatography
σ_{tot}	s	Hydrodynamic dispersion standard deviation	Prone and capillary tubing
t_i	s	Characteristic time of the concentration profile	Microdialysis
Q	m^3/s	Volumetric flowrate	Microdialysis
r	m	Radius of probe membrane	Microdialysis
L	m	Membrane length	Microdialysis
S	m^2	Membrane surface area	Microdialysis
k	s^{-1}	Uptake rate constant	External medium
u	*unitless*	Dummy integration variable	Mathematical variables
E_d	*unitless*	Extraction fraction	
P	m/s	1-D diffusive permeability	
R	s/m^3	1-D mass transport resistance	
Subscript	Notation		
in	Probe inlet		
out	Probe outlet		
i	Membrane inner radius		
o	Membrane outer radius		
inj	LC injector		
det	LC detector		
∞	Far away		
m	Membrane		
Hat	Notation		
^	Overall		

4.4.1 Mathematical Model

In this section we briefly outline a comprehensive theoretical description for quantitative microdialysis that accounts for the processes that contribute to an observed transient microdialysis response following a step-change in retrodialyzed concentration of a solute, e.g., dopamine, created by switching the solution being pumped through the inlet capillary to the probe. Table 4.4-2 defines parameters and super/subscripts.

4.4.1.1 Diffusive Flux and Mass Balances

In the radial dimension of a cylindrical coordinate system, the partial derivative of concentration with time can be written (Equation 4.4-1):

$$\frac{\partial C^*}{\partial t} = \frac{D}{\lambda^2 r}\frac{\partial}{\partial r}\left(r\frac{\partial C^*}{\partial r}\right) - kC^*$$

Equation 4.4-1. Diffusive mass balance, universal volume basis.

where C* is a concentration calculated in one of two ways, namely as moles in the ECS per total tissue volume, C_{tissue}, or moles in the ECS per total ECS volume, C_{ECS}. The two are related by $C_{tissue} = \phi C_{ECS}$ where ϕ is the tissue porosity. It can be demonstrated (see Supplementary Information 4.6.2.3), that as long as Equation 4.4-1 is written in a consistent volume basis, i.e. when all C^* terms are defined as either $C^* = C_{tissue}$ or $C^* = C_{ECS}$, Equation 4.4-1 is consistent with the literature[58,61,66]. Other terms are defined in Table 4.4-2. When the ECS volume basis is chosen, Equation 4.4-2 describes mass transport in the tissue. Note that no other 'corrections' to the effective diffusion coefficient, D/λ^2, or rate constant, k, are necessary.

$$\frac{\partial C_{ECS}}{\partial t} = \frac{D}{\lambda^2 r}\frac{\partial}{\partial r}\left(r\frac{\partial C_{ECS}}{\partial r}\right) - kC_{ECS}$$

Equation 4.4-2. Diffusive mass balance, ECS volume basis.

The following boundary conditions lead to a solution. The concentrations at the boundary between the membrane and the external medium are the same:

$$C_m(r = r_o, t) = C_{ECS}(r = r_o, t)$$

Equation 4.4-3. Boundary condition, membrane-ECS mass balance.

The mass flux by diffusion at the boundary between the membrane and the external medium are the same:

$$D_m \left.\frac{\partial C_m}{\partial r}\right|_{r=r_o} = \frac{\phi}{\lambda^2} D \left.\frac{\partial C_{ECS}}{\partial r}\right|_{r=r_o}$$

Equation 4.4-4. Boundary condition, membrane-ECS mass gradient balance.

where $D_m = \frac{\phi_m}{\lambda_m^2} D$ and D is the diffusion coefficient of the solute in aqueous solution and D_m, is the "effective" diffusion coefficient of the solute in the membrane. The diffusion coefficients in the tissue and membrane are handled differently because this reflects the most well-established experimental results for dopamine. That is, we have not found values for ϕ_m or λ^2_m in the membrane materials used in the literature. However, the concentration in the membrane, C_m, is defined analogously to C_{ECS}. At $t = 0$, the concentration outside the probe is uniform, a step concentration change of the analyte occurs at the probe lumen:

$$C_{ECS}(r, 0) = C_{ECS\infty}$$

Equation 4.4-5. Boundary condition, initial concentration.

The model assumes a constant concentration far from the probe:

$$C_{ECS}(r \to \infty, t) = C_{ECS\infty}$$

Equation 4.4-6. Boundary condition, distant concentration.

4.4.1.2 Permeability Solutions

Chen (2002a, b) and Bungay (2011) described a solution in one radial dimension which we have adopted here. There is no analytical solution for cylindrical models that include the axial dimension. However, for the typical microdialysis probe's radius (100-140 nm), probe length (2-4 mm) and uptake rate constants (10^{-3} to 10^{3} s^{-1}), the axial mass transport contribution is negligible (less than 5% contribution) at the time regime relevant to fast microdialysis (less than 600 s)[61]. Thus, the transient component of the response in one radial dimension can be used to obtain accurate mass transport information given the constraints above. The overall permeability is calculated from individual lumen, membrane, and external medium permeabilities. The permeability of the lumen of the microdialysis probe is assumed (with justification)[55,58,59,61,185] to be so high that it does not contribute to the overall permeability. The transient membrane permeability reaches steady state almost instantaneously[61] (Supplementary Information Figure 4.6-2), thus the membrane permeability, Equation 4.4-7, is assumed to be in steady state.

$$P_{m,t\to\infty} = \frac{D_m}{r_o \ln\left(\frac{r_o}{r_i}\right)}$$

Equation 4.4-7. Analytical solution for $P_{m,t}$.

D_m is defined above and r_o and r_i are outer and inner membrane radii, respectively. The external medium permeability is shown as Equation 4.4-8 (Bungay 2011 Eq. 20, derived from Chen 2002b Eq. 7. The derivation is shown in Supplementary Information 4.6.2.1 and 4.6.2.2. Terms are defined in Table 4.4-2).

$$P_{ECS}(t)=\frac{\phi D}{r_o\lambda^2}\left(\frac{r_o\sqrt{\frac{k\lambda^2}{D}}\cdot K_1\left(r_o\sqrt{\frac{k\lambda^2}{D}}\right)}{K_0\left(r_o\sqrt{\frac{k\lambda^2}{D}}\right)}+\frac{4}{\pi^2}\int_0^\infty\frac{\exp\left(-\left(u^2+\left(r_o\sqrt{\frac{k\lambda^2}{D}}\right)^2\right)\cdot\frac{Dt}{\lambda^2 r_o^2}\right)}{\left(u^2+\left(r_o\sqrt{\frac{k\lambda^2}{D}}\right)^2\right)\left(J_0^2(u)+Y_0^2(u)\right)}udu\right)$$

Equation 4.4-8. Analytical solution for $P_{ECS}(t)$.

In Equation 4.4-8, J_n Y_n and K_n are, respectively, Bessel functions of the first kind, the second kind, and a modified Bessel function of the second kind of order n. Overall permeability is then calculated from membrane and external medium permeabilities[61] as shown in Equation 4.4-9.

$$\frac{1}{P(t)}=\frac{1}{P_{ECS}(t)}+\frac{1}{P_{m,t\to\infty}}$$

Equation 4.4-9. Overall permeability from individual component.

4.4.1.3 Transient Extraction Fraction

Extraction fraction is calculated from overall permeability[61]:

$$E_d(t)=1-\exp\left(-\frac{S_o\bar{P}(t)}{Q}\right)$$

Equation 4.4-10. Transient extraction fraction from permeability

where S_o is the membrane's outer surface area through which diffusion occurs and Q is the microdialysate volumetric flow rate. The transient solute concentration measured at the microdialysis probe outlet $C_{out}(t)$ resulting from a retrodialyzed step concentration change in C_{in} is[61]:

$$C_{out}(t)=C_{in}-E_d(t)\cdot\left(C_{in}-C_{ECS\infty}\right)$$

Equation 4.4-11. Solute concentration at probe outlet.

Note that the extraction fraction is time dependent.

This is $C_{out}(t)$ the solute concentration at the probe outlet as typically described in the literature. However, in a practical experiment, the probe inlet and outlet are connected to inlet and outlet capillaries, which in turn are connected to perfusate pump and sample collector, respectively. The sample is then analyzed by a detector. The experimentally observable is always the concentration of the solute at the detector $C_{det}(t)$. The following subsections describe the analytical instrument's contribution to the measured $C_{det}(t)$.

4.4.1.4 Hydrodynamic Dispersion

A zone of solute in laminar flow passing through each of the capillaries and the microdialysis probe itself is broadened by hydrodynamic dispersion. The shape of a concentration profile leaving the exit of a capillary, $C_{cap\ out}(t)$, is the convolution of the solute concentration profile at the entry into the capillary, $C_{cap\ in}(t)$, with a Gaussian function whose variance is dictated by dispersion in the flow system[176,186] as shown in Equation 4.4-12:

$$C_{cap\ out}(t) = C_{cap\ in}(t) \otimes \left(\frac{1}{\sigma_{cap}\sqrt{2\pi}} \exp\left(-\frac{(t - t_i)^2}{2\sigma_{cap}^{\ 2}} \right) \right)$$

Equation 4.4-12. Solute concentration at capiliary outlet.

Here, t_i is a characteristic time of the concentration profile at the outlet, the difference between this and the time at which a step-change in concentration occurs is the time required to transport the sample through the capillary. Dispersion in the capillary spreads the initial step function into an error function with a standard deviation σ_{cap}.

There is no simple theory for the probe itself. But, is important to point out that: (1) the order in which the processes altering the signal's shape occur does not matter as long as all processes are linear and (2) the variances resulting from serial, linear processes add. Thus, here we

combined the variances from hydrodynamic dispersion into one term ("total variance", σ_{tot}^2) and imagine that the input to the probe is a perfect step function in concentration. The two parameters σ_{tot} and t_i are used with Equation 4.4-12 to model dispersion of a zone of solute caused by transport through the microdialysis probe, inlet and outlet capillaries, and the analytical system. For a chromatographic system, for example, σ_{tot} includes dispersion in the sample loop, and t_i is the characteristic time at the end of the sample loop. In reality, the inlet capillary and some portion of the probe proper alter the shape of the concentration profile in the lumen of the probe. The solution affected by the brain suffers further spreading in the latter portion of the probe proper and the outlet capillary. But this difference does not affect the outcome.

4.4.1.5 Detector Response

There are two general types of detector, continuous and discrete. A continuous detector's response to a step change is often an exponential relaxation from one steady value to another, so the transfer function, $\Pi(t)$, is exponential. A discrete detector, for example using an injection loop as in a chromatographic determination of solute concentration, is characterized by a rectangular transfer function. The concentration profile of a solute at the detector is given as Equation 4.4-13 where $C_{out}(t)$ is the concentration at the outlet of the probe proper (the entrance to the outlet capillary), σ_{tot} is the standard deviation from dispersion in the inlet and outlet capillaries, the probe itself, and any fluidic connection between the outlet capillary and the detector. $C_{det}(t)$ is the concentration inferred from a detector's signal.

$$C_{\det}(t) = C_{out}(t) \otimes \left(\frac{1}{\sigma_{tot}\sqrt{2\pi}} \exp\left(-\frac{\left(t - t_i\right)^2}{\sigma_{tot}^2} \right) \right) \otimes \Pi\left(t\right)$$

Equation 4.4-13. Solute concentration at detector

If the detector has an exponential decay response with a time constant of τ then:

$$\Pi(t < 0) = 0$$
$$\Pi(t \geq 0) = \tau^{-1} e^{-t/\tau}$$

Equation 4.4-14. Exponential decay detector

If the detector is a discrete detector with a sampling period of t_s then:

$$\Pi(t < 0) = 0$$
$$\Pi(0 \leq t < t_s) = 1 / t_s$$
$$\Pi(t \geq t_s) = 0$$

Equation 4.4-15. Discrete detector

4.4.2 Reconciliation and Clarifications to Preceding Literature

4.4.2.1 The Relationships Among Preceding Theories Related to Bungay 2011[2]

The time-dependent normalized radial concentration, $U(r,t)$, (Chen (2002a) Eq. 6) is obtained by solving the partial differential equation describing mass transport in the tissue, Equation 4.4-2, using the boundary conditions Equation 4.4-3-Equation 4.4-6. The analytical solution for overall permeability $\widehat{P}(t)$ is derived from $U(r,t)$ (Supplementary Information 4.6.2.2). From this analytical solution for $\widehat{P}(t)$, Chen (2002 a, b) devised two methods to evaluate overall permeability. The *Chen analytical* method calculates the $\widehat{P}(t)$ directly from its analytic expression. The *Chen numerical* method first takes the numerical limit of $\widehat{P}(t)$ as the ECS permeability becomes infinitely large to obtain $P_m(t)$, then takes the numerical limit of $\widehat{P}(t)$ as the membrane permeability becomes infinitely large to obtain $P_{ECS}(t)$. The overall permeability is obtained from the numerical solution of Equation 4.4-9 but with a time-dependent $P_m(t)$. The *Bungay analytical* method, adapted from Chen (2002 a, b), derived an analytical solution for $P_{ECS}(t)$ and the steady-

state membrane permeability $P_{m,t\to\infty}$ from $U(r,t)$ by making the assumptions of infinitely permeable membrane and infinitely permeable ECS at steady state, respectively. Intuitively, *Chen analytical* is the appropriate method and the other two are unnecessary. However, we will show below that it is not the case. Derivations to obtain $\widehat{P}(t)$ and $P_{ECS}(t)$ can be found in Supplementary Information 4.6.2.1 and 4.6.2.2, and a step-by-step derivation summary for all three methods can be found in Supplementary Information 4.6.2.4.

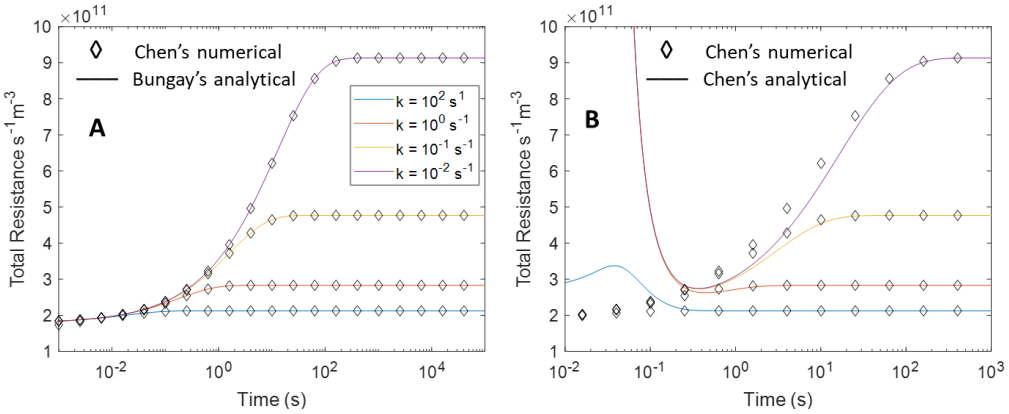

Figure 4.4-1. Comparison between (A) Chen numerical (diamond) and Bungay analytical (line) (B) Chen numerical (diamond) and Chen analytical (line).

Diffusive mass transport is calculated in term of resistance (R=1/PS_o).

4.4.2.2 Chen's Analytical and Numerical Approaches

For clarity, in this section diffusive mass transport is compared in term of resistance (R=1/PS_o) where P is a permeability and S_o is the membrane's outer surface area through which the molecular flux occurs. In their 2002 papers, Chen and colleagues postulated that *Chen analytical* and *Chen numerical* yield identical results (Supplementary Information Figure 4.6-3A, which is a reproduction of Chen 2002b Fig. 4 with our MALAB code). We found that the two approaches are reasonably comparable (relative difference less than 0.05) at long times (longer than 100 s) but do not agree at short times (shorter than 100 s, Supplementary Information Figure

4.6-3B). The former is the time regime where traditional microdialysis operates, but the latter is where transient microdialysis will operate. The disagreement between the two approaches decreases as the solute uptake rate increases (Supplementary Information Figure 4.6-3B).

While we do not expect microdialysis experiments to be possible, or practical, at the sub-second time regime, we note that computation of *Chen analytical* completely breaks down at this time regime. A closer look at the data reveals that at very short time (faster than 0.01 s), the *Chen analytical* total resistance term $R(t)$ rapidly increases (Figure 4.4-1B, dashed line), which does not accurately describe cylindrical transient diffusion at short time. In such a system, at very short time (order of milliseconds) after a concentration transient occurs, since the concentration gradient between tissue and probe lumen is at its highest, the flux of solute between tissue and probe lumen is also at its highest, thus the resistance is at its lowest. At long time, the concentration gradient relaxes, and the flux of solute reaches steady state. In other words, resistance is small at short time, and it approaches a larger, steady-state value at long time. *Chen numerical* exhibits this expected behavior (Figure 4.4-1A-B, diamond). Upon careful analysis of Chen's work, we believe that, mathematically, the *Chen analytical* was accurately derived. From our numerical investigation, however, we concluded that since the *Chen analytical* solution does not behave correctly during transient conditions (100 s or faster), it should not be used for transient analysis.

4.4.2.3 Bungay's Analytical Approach

Bungay's analytical yields almost identical results to *Chen's numerical* approach. In fact, numerical evaluation of *Bungay's analytical* $P_{ECS}(t)$ yields identical result to *Chen's numerical* $P_{ECS}(t)$, and *Bungay's analytical* $P_{m,\, t\to\infty}$ yields identical results to *Chen's numerical* $P_m(t)$ in the practical experimental time regime (10 ms or longer, Supplementary Information Figure 4.6-2). As a result, $R(t)$ from *Bungay's analytical* and *Chen's numerical* are identical in the time regime

of 10 ms or longer (Figure 4.4-1A). We have also carefully analyzed Bungay's work, and we agree with the mathematical derivation. Thus, as *Bungay's analytical* approach provides relative ease in computer code implementation and calculation speed (Supplementary Information 4.6.1.1), our method uses this approach to evaluate mass transport in transient microdialysis. *Chen's numerical* would provide identical results at times greater than milliseconds but at a steep cost of mathematical complexity and computational time (Supplementary Information 4.6.1.2, therefore we do not recommend its use.

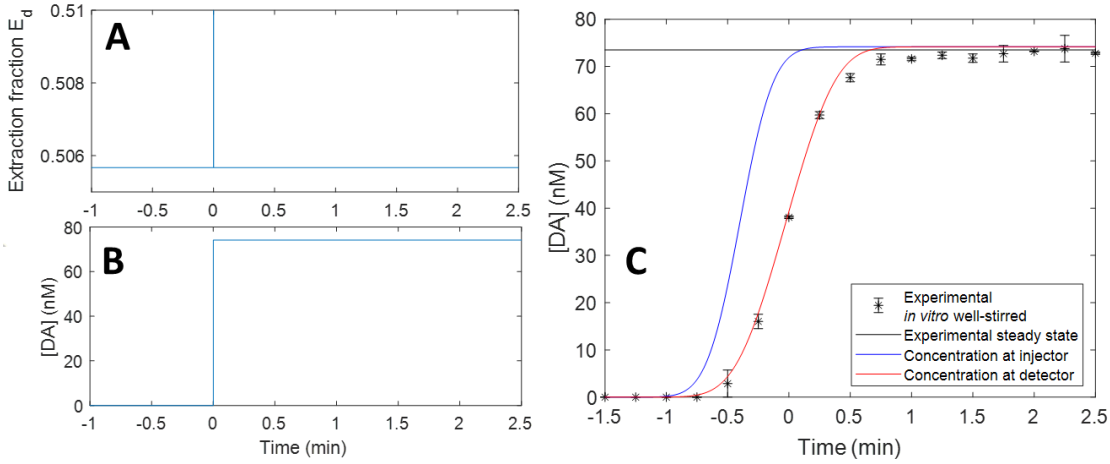

Figure 4.4-2. MATLAB Simulation of an in vitro experiment compared to experimental results.

(A) Transient extraction fraction $E_d(t)$ (B) Solute concentration at probe outlet $C_{out}(t)$ and (C) Solute concentration at injector $C_{inj}(t)$ (blue), solute concentration at detector $C_{det}(t)$ (red) and in vitro experimental (black).

4.4.3 MATLAB Simulation

To demonstrate the contribution of mass transport in the tissue and in the analytical system thereafter to time-dependent solute concentration at the probe outlet $C_{out}(t)$, injector $C_{inj}(t)$ and detector $C_{det}(t)$, and the importance of understanding these results, we simulated an *in vitro* well-stirred retrodialysis experiment. In such an experiment, the stirring creates a thin diffusion layer

having the effect of a high uptake rate, thus uptake rate constant k was chosen to be 5×10^3 s^{-1} with a tissue porosity ϕ of 1 and tortuosity λ of 1. Other simulation parameters are shown in Table 4.4-1. Characteristic time of the concentration profile t_i was calculated from experimental time when the step concentration change occurs and transport time, accounting for all transport volume in the system, namely probe inlet capillary, probe lumen, probe outlet capillary, and the LC sample loop. Hydrodynamic dispersion, particularly Taylor dispersion coefficient at our flowrate (0.6-0.8 μL/min) and capillary diameter (75 μm), was calculated from Ngo *et al.* 2017 [97], where we experimentally measured an identical probe at 0.6 μL/min flow rate. The dispersion coefficient is proportional to the square of linear velocity. From the dispersion coefficient, the dispersion standard deviation σ_{tot} was calculated for simulation.

Shown in Figure 4.4-2A, B are the simulation results in term of $E_d(t)$ (Figure 4.4-2A, resulting from evaluation of Equation 4.4-8 to Equation 4.4-10) and $C_{out}(t)$ (Figure 4.4-2B, resulting from evaluation of $E_d(t)$ and Equation 4.4-11). When the uptake rate is large, diffusive flux rapidly establishes steady state. Therefore, $E_d(t)$ displays a rapid transient near time = 0 but otherwise is constant, $C_{out}(t)$ is a near perfect step with no curvature. Shown in Figure 4.4-2C are the simulation results for $C_{inj}(t)$ (blue) from evaluation of $C_{out}(t)$ and Equation 4.4-12 and $C_{det}(t)$ (orange) from evaluation of C_{inj} and Equation 4.4-13. Measurements from an in vitro well-stirred experiment are plotted as points in Figure 4.4-2C. The *in vitro* extraction fraction was measured at 37°C with an 18 kDa MWCO membrane, using steady-state measured concentrations from six replicates of 150 nM DA step concentration retrodialysis experiments. The diffusion coefficient of dopamine in the probe membrane was determined from the experimental *in vitro* well-stirred extraction fraction using Equation 4.4-9 and Equation 4.4-10, with the assumption of fully permeable ECS ($P_{ECS} \rightarrow \infty$). There is good agreement between simulated and experimental results.

Simulated well-stirred steady-state extraction fraction is 0.506 and steady-state concentration is 74.2 nM, in comparison with experimental steady-state extraction fraction and concentration of (AVG±SEM) 0.510±0.001 and 73.4±0.2 nM, respectively. The disagreement is due to MATLAB's numerical limit in evaluating Bessel functions. Simulating with large P_{ECS} instead of large k produces steady-state extraction fraction and steady-state concentration equals to experimental results. We note that the extraction fraction was derived from eight minutes of data.

The result above demonstrates that the model can simulate an experiment and deriving quantitative results from data. But this simulation is useful for experimental design as well. Here, it demonstrates the influence of dispersion and the detector response on the transient response, and thus the importance of understanding and minimizing these influences. The difference between $C_{out}(t)$ and $C_{inj}(t)$ highlights the contribution of dispersion to the transient response. Even if the diffusive flux establishes steady state instantaneously, and if the detector is a continuous detector with perfect response time (here, represented by $C_{inj}(t)$), dispersion softens the response and limits the time resolution of the analytical system. Minimizing dispersion (e.g. using segmented flow[79]) improves the time resolution of the analytical system. In a practical microdialysis system, the detector is not perfect, and the differences between $C_{inj}(t)$ and $C_{det}(t)$ highlight the contribution of the detector to the transient response. The detector not only further softens (transform in shape) the response curve, lowering the time resolution, but also shifts the response curve in time. In principle, $C_{inj}(t)$ can be calculated from $C_{det}(t)$ using deconvolution because the detector's transfer function is known. However, this operation requires higher data density than microdialysis can realistically achieve. As shown in Figure 4.4-2C, the time shift of the curve is not straightforward. The top, middle, and bottom portion of the curve are time shifted by different amounts, for example. Thus, transport time is not obvious from a plot of the data alone. Establishing the

transport time is critically important in behavior studies[98] for example. Fortunately, the CQM curve fit[180] provides a quantitative estimate for transport time from a transient response in $C_{det}(t)$.

4.4.4 Limitations of the Method

The CQM method relies on a set of assumptions in addition to the assumptions inherent in the mass transport model we used. These assumptions are necessary to obtain an analytical solution for the mass transport model, however, they impose limitations to the method. Additionally, there are limitations inherent to the microdialysis technique and to the MATLAB software. The following section discusses these limitations.

4.4.4.1 Trauma Layer

Probe implantation creates a complex tissue environment surrounding the probe[85], including a trauma layer between healthy tissue and the probe[86]. The trauma layer leads to the extraction fraction being overestimated, thus solute ECS concentration being underestimated[55,65,88,90]. At this time, there is no experimental method using microdialysis to assess the trauma layer, and there is no analytical solution for mathematical models describing transient response that incorporates the trauma layer. Thus, the CQM model does not account for the trauma layer. However, there are active experimental efforts to reduce implantation injury and improve microdialysis measurements[86,87,92,97,122].

4.4.4.2 First-order Uptake Rate

Uptake of neurotransmitters in the extracellular space is more appropriately modeled using Michaelis-Menten kinetics[162,187,188] than a simple first-order process:

$$\frac{dC_{ECS}}{dt} = \frac{V_{\max} C_{ECS}}{K_M + C_{ECS}}$$

Equation 4.4-16. Michaelis-Menten kinetics

where V_{max} is the maximum velocity and K_M is the concentration at which the velocity is 50% of V_{max}. Michaelis-Menten kinetics can be approximated by a first order rate constant $k = V_{max}/K_M$ if K_M is much larger than C_{ECS}. For DA in the nucleus accumbens, for example, K_m was found to be about 200 nM (measured with FSCV[189]) while the basal C_{ECS} is about 10 nM (measured with No-Net-Flux microdialysis[169]) to 90 nM (measured with FSCAV[52]).

4.4.4.3 One-dimensional Radial Mass Transport

The microdialysis probe is a finite-length cylinder, thus would be more appropriately modeled with two-dimensional cylindrical mass transport. However, in typical experimental conditions, 1D and 2D calculations[61] differ by less than 5%. These typical conditions include membrane length aspect ratio at least 12 (1.7 mm length for the typical 140 nM radius), uptake rate at least 10^{-2} s^{-1} (for solute in ECS with the 140 nM radius probe), and time at most 600 s. Uptake rate is the dominant factor, with DA uptake in the nucleus accumbens (order of 10 s^{-1}) [189,190], for example, the 1D solution is accurate in all practical experimental conditions.

4.4.4.4 Numerical Precision

Due to inherent numerical precision of MATLAB in evaluating Bessel functions, the simulation program is unable to simulate uptake rate outside the range of approximately 10^{-6} to 10^{4} s^{-1} for practical experiments (D in the order of 10^{-10} m^2/s, ECS tortuosity 1-4, probe length 2-4 mm).

4.5 Conclusion

In this work, we have presented the first component of the comprehensive quantitative microdialysis technique: a mathematical model (CQM model) based on one-dimensional radial mass transport for microdialysis sampling that describes the solute concentration observed at the detector $C_{det}(t)$ as affected by the neurochemical environment outside the probe as well as the analytical system that follows the probe. The mass transport model is adapted from Chen (2002) [58,59] and Bungay (2011) [61] with appropriate corrections and clarifications to unify their analytical solutions, particularly at the minute timescale that is most relevant to Fast Microdialysis. Most notably, first-order uptake, tissue porosity, tissue tortuosity, sample transport, and detector response are all considered in this comprehensive model. This is the first mathematical model for microdialysis that illustrates an experimentally observable quantity ($C_{det}(t)$) as affected by both biological and analytical system factors. Our use of only closed-form analytic expressions that are fully consistent with preceding literature allows data analysis, simulation, and fitting methods[180] to be accessibly built upon.

4.6 Supplementary Information

4.6.1 Computer Codes

4.6.1.1 Bungay 2011 Fig. 2 Script

The script below reproduces Bungay (2011) Figure 2 exactly, using parameters and quantities defined in Bungay (2011). Notably, dimensionless ECS permeability is calculated as a function of a dimensionless clearance Θ and a dimensionless time τ.

```
%This script simulates dimensionless ECS permeability
%with parameters from Bungay 2011 10.1016/j.jpba.2011.01.005
%Fig 2 in Bungay 2011 can be reproduced using this script
%Units used in this script is S.I, conversion needed to match Bungay 2011
tic
close all
clear
warning('off','MATLAB:integral:NonFiniteValue')
%%
%Simulation parameters
Theta_array = [4 1 0.5 0.1 1e-6]; %dimensionless ECS permeability
                        %program runs extremely slow at Theta ~ 0
tau = logspace(-4,4,1e3); %dimensionless time axis
%%
P_dimensionless = zeros([length(Theta_array) length(tau)]); %preallotcate
array
for i = 1:length(Theta_array)
    Theta = Theta_array(i);
    %Define the transient part dimensionless ECS permeability
    f_int = @(u)(((4/pi^2)*u*exp(-(u^2+Theta^2)*(tau)))/...
        ((u^2+Theta^2)*((besselj(0,u))^2+(bessely(0,u))^2)));
    %Evaluate the transient part of Pext(t)
    Pext_transient = integral(f_int,0,inf,'ArrayValued',true);
    %Evaluate the steady state part Pext(t)
    Pext_ss = Theta*besselk(1,Theta)/besselk(0,Theta);
    %Evaluate dimensionless Pext(t)
    P_dimensionless(i,:) = Pext_transient+Pext_ss;
end
plot(tau,P_dimensionless)
title('Bungay 2011 Fig. 2')
legend('\Theta = 1', '\Theta = 0.5', '\Theta = 0.1', '\Theta = 10^{-6}')
xlabel('Dimensionless Time')
ylabel('Dimensionless Permeability')
```

```
set(gca, 'XScale', 'log','ylim', [0 2],'FontSize',13)
hold off
toc

plot(tau,P_dimensionless(1,:))
title('Strital DA Response to Retrodialysis')
xlabel('Dimensionless Time')
ylabel('Dimensionless Permeability')
set(gca, 'XScale', 'log','xlim', [1e-3 1],'ylim', [0 10],'FontSize',13)
      hold off
```

4.6.1.2 Chen 2002b Fig. 4 Script

```
%This script simulates membrane, external medium, and total resistance
%with parameters from Chen 2002b 10.1046/j.1471-4159.2002.00793.x
%Fig 4 in Chen 2002b can be reproduced using this script
%Units used in this script is S.I, conversion needed to match Chen 2002b
tic
close all
clear
warning('off','MATLAB:integral:NonFiniteValue')
warning('off','MATLAB:integral:MaxIntervalCountReached')
%%
%Simulation parameters
n = 1;  %1 negligible external medium resistance
        %  which, calculate membrane resistance
        %2 negligible membrane resistance
        %  which, calculate external medium resistance
        %3 calculate total resistance
%kext = [1e-3 1e-4 1e-5]; %Effective uptake rate
kext = [1e2 1e1 1e0 1e-1 1e-2 1e-3 1e-4 1e-5]; %Effective uptake rate
L = 4e-3; %m, membrane length
ro = 120e-6; %m, membrane outer radius
ri = 110e-6; %m, membrane inner radius
phi_m = 0.13; %membrane porosity
              %Chen 2002 10.1046/j.1471-4159.2002.00793.x
Dm = 1.5e-10; %Analyte diffusion coefficient in membrane, m^2/s
              %Chen 2002 10.1046/j.1471-4159.2002.00793.x
phi = 0.2; %external medium porosity
           %Chen 2002 10.1046/j.1471-4159.2002.00793.x
D = 2.2e-10; %m^2/s external medium  diffusion coefficient
lambda = 1; %external medium tortuosity
           %nominal
switch n
    case 1
        D = 1; %large external medium diffusion coefficient
        phi = 0.2; %large external medium porosity
        kext = 1e-3;
    case 2
        Dm = 1; %large membrane resistance
        phi_m = 1; %large membrane porosity
    case 3
end
```

```
De = D/lambda^2;
Dext = De*phi;
%%
%Create time axis
t = logspace(-3,5,1e4); %s, time axis
%Dependent variables calculation
So = 2*pi*ro*L; %m^2, membrane surface area
Text = ro^2/De; %s, dimensionless time scaling factor
%%
P_dimensionless = zeros([length(kext) length(t)]); %preallotcate array
for i = 1:length(kext(:))
    Theta = ro*sqrt(kext(i)/De); %dimensionless clearance
    %Compute external medium permeability Pext(t)
    %Define dimensionless components
    omega = @(u)(sqrt(u.^2+Theta^2));
    xi = @(u)(omega(u).*sqrt(De/Dm));
    nu_1 = @(u)(besselj(0,xi(u)).*bessely(0,xi(u).*ri/ro)-...
        besselj(0,xi(u).*ri/ro).*bessely(0,xi(u)));
    nu_2 = @(u)(besselj(1,xi(u)).*bessely(0,xi(u).*ri/ro)-...
        besselj(0,xi(u).*ri/ro).*bessely(1,xi(u)));
    eta_1 = @(u)((phi/phi_m).*sqrt(De/Dm).*nu_1(u).*u.*besselj(1,u)-...
        nu_2(u).*omega(u).*besselj(0,u));
    eta_2 = @(u)((phi/phi_m).*sqrt(De/Dm).*nu_1(u).*u.*bessely(1,u)-...
        nu_2(u).*omega(u).*bessely(0,u));
    %Define the transient part of Pext(t)
    f_int = @(u)((4/pi^2).*u.^2.*exp(-
omega(u).^2.*t/Text).*(eta_1(u).*bessely(1,u)-eta_2(u).*besselj(1,u))/...
        (omega(u).^2.*sqrt(De/Dm).*(eta_1(u).^2+eta_2(u).^2)));
    %Evaluate the transient part
    P_transient = integral(f_int,0,inf,'ArrayValued',true);
    %Evaluate the steady state part
    P_ss =
Theta*besselk(1,Theta)/(log(ro/ri)*(phi/phi_m)*(De/Dm)*Theta*besselk(1,Theta)
+besselk(0,Theta));
    %Evaluate dimensionless permeability
    P_dimensionless(i,:) = P_transient+P_ss;
end
%%
%Compute outputs
P = P_dimensionless*Dext/ro; %Calculate permeability P(t)
R = 1./(P*So); %Calculate resistance R(t)
plot(t,R);
if n == 1
    title('Chen 2002b Fig. 4 R_{m}(t)')
elseif n == 2
    title('Chen 2002b Fig. 4 R_{e}(t)')
    legend('k = 1\times10^{-3}','k = 1\times10^{-4}','k = 1\times10^{-
5}','Location','SouthEast')
elseif n == 3
    title('Chen 2002b Fig. 4 R(t)')
    legend('k = 1\times10^{-3}','k = 1\times10^{-4}','k = 1\times10^{-
5}','Location','SouthEast')
end
xlabel('Time (s)')
ylabel('Resistance 1/sm^(-2)')
set(gca,'xlim',[0 12000],'ylim',[0 3e12],'FontSize',13)
toc
```

4.6.1.3 Simulation Script Ngo2020_simulation.m

```
%We strongly recommend ti at time ~ 0 to reduce computational time.
%The time axis must be symmetrical for convolution to work properly
format longG
close all
clear
warning('off','MATLAB:integral:NonFiniteValue')
tic
%%
%Simulation parameters
time_resolution = 0.01; %s, higher time accuracy produces more accurate
integration
Q = 0.8; %uL/min, volumetric flow rate
Q = Q*1e-9/60; %m^3/s, volumetric flowrate
ts = 45; %s, LC sampling time
ti = -24; %s, time that step concentration arrives at injector
sigma = 12.8;%s, Taylor-Aris dispersion standard deviation
kext = 5e3; %1/s, reuptake rate
Cin = 150; %retrodialyzed concentration
Cinf = 0; %ECS concentration
D = 6.0e-10; %m^2/s, free solution diffusion coefficient
phi = 0.2; %ECS porosity
lambda = 1.6; %ECS tortuosity
Ews = 0.510; %well-stirred, 37 C extraction fraction
L = 4e-3; %m, membrane length
ro = 140e-6; %membrane outer radius, m
ri = 100e-6; %membrane outer radius, m
max_s = 5; %maximum simulation time, min
max_t = max_s*1.5*60;
t = linspace(-max_t,max_t,(2*max_t/time_resolution)+1);%s, create time axis
%Create a step function
step = zeros([1 length(t)]);
for i = 1:length(t)
    if t(i) <=0
        step(i) = 0;
    else
        step(i) = 1;
    end
end
%Dependent variables calculation
So = 2*pi*ro*L; %membrane surface area
%if Ews was measured, use the below
Pmo = -(Q/So)*log(1-Ews); %log here is ln
%if Dm was measured or looked up, use the below
%Pmo = Dm/(ro*log(ro/ri)); %m/s, this log is natural log, membrane
permeability
De = D/lambda^2; %m^2/s, membrane diffusion coefficient
Dext = De*phi;
So = 2*pi*ro*L; %m^2, membrane surface area
Text = ro^2/De; %s, dimensionless time scaling factor
Theta = ro*sqrt(kext/De); %dimensionless clearance
box_func = zeros([1 length(t)]);
for i = 1:length(t)
    if 0 <= t(i) && t(i) < ts
        box_func(i) = time_resolution/ts;
```

```
    end
end
gauss = time_resolution*(1/(sigma*sqrt(2*pi)))*exp(-(t - ti).^2/(2*sigma^2));
%normalized Gaussian
Cws = ones([1 length(t)]);
Cws = (1-Ews)*Cws.*Cin; %well-stirred concentration
Cin = Cin.*step; %create step function for Cin
s_gauss = convnfft(box_func,gauss,'same'); %conv of Gaussian and box_func
%%
%Compute external medium permeability Pext(t)
%Define the transient part of Pext(t)
f_int = @(u)(((4/pi^2)*u*exp(-(u^2+Theta^2)*(t/Text)))/...
    ((u^2+Theta^2)*((besselj(0,u))^2+(bessely(0,u))^2)));
%Evaluate the transient part of external medium permeability Pext(t)
Pext_transient = integral(f_int,0,inf,'ArrayValued',true);
%Evaluate the steady state part of external medium permeability Pext(t)
Pext_ss = Theta*besselk(1,Theta)/(besselk(0,Theta));
Pext_transient(isnan(Pext_transient)) = 0; %replace NaN with 0
Pext_transient(isinf(Pext_transient)) = 0; %replace inf with 0
%Evaluate dimensionless external medium permeability
Pext_dimensionless = Pext_transient+Pext_ss;
Pext_dimensionless(isnan(Pext_dimensionless)) = Pext_ss; %replace NaN with
P_ss
Pext_dimensionless(isinf(Pext_dimensionless)) = Pext_ss; %replace inf with
P_ss
                                                        %at t < 0, Pext =
Pext_ss
%%
%Compute concentration at probe outlet Cout(t)
Pext = Pext_dimensionless*Dext/ro; %Calculate external medium permeability
Pext(t)
P = 1./(1./Pext + 1/Pmo); %Calculate total permeability P(t)
E = 1-exp(-So*P/Q); %Calculate extraction fraction Ed
Cout = Cin-E.*(Cin-Cinf); %Calculate Cout(t)
%%
%Compute concentration arrived at injector Cinj(t)
Cinj = (1/trapz(gauss))*convnfft(Cout,gauss,'same'); %Calculate Cinj(t)
%%
%Compute concentration at detector Cdet(t)
Cdet = convnfft(Cout,s_gauss,'same');
%%
figure
hold on
yyaxis left
plot(t/60,Cout)
ylabel('[DA] (nM)')
title('Probe extraction fraction and Outlet concentration','FontSize',13)
xlabel('Time (min)')
yyaxis right
plot(t/60,E)
ylabel('Extraction fraction E_{d}')
set(gca,'xlim',[-max_s max_s],'FontSize',10)
box on
hold off
%%
figure
hold on
```

```
%title('Concentration at injector and detector','FontSize',13)
plot(t/60,Cinj,'b');
plot(t/60,Cdet,'r');
legend('Concentration at injector',...
    'Concentration at detector','Location','SouthEast','FontSize',10)
ylabel('[DA] (nM)')
xlabel('Time (min)')
set(gca,'xlim',[-max_s max_s],'FontSize',10)
box on
hold off
%%
function A = convnfft(A, B, shape, dims, options)
%   KHANH T NGO KTN@PITT.EDU
%   Adapted from:
%https://www.mathworks.com/matlabcentral/fileexchange/24504-fft-based-
convolution
%   Author: Bruno Luong <brunoluong@yahoo.com>
% Copyright (c) 2009, Bruno Luong
% All rights reserved.
%
% Redistribution and use in source and binary forms, with or without
% modification, are permitted provided that the following conditions are met:
% * Redistributions of source code must retain the above copyright notice,
this
%   list of conditions and the following disclaimer.
% * Redistributions in binary form must reproduce the above copyright notice,
%   this list of conditions and the following disclaimer in the documentation
%   and/or other materials provided with the distribution
% * Neither the name of FOGALE nanotech nor the names of its
%   contributors may be used to endorse or promote products derived from this
%   software without specific prior written permission.
% THIS SOFTWARE IS PROVIDED BY THE COPYRIGHT HOLDERS AND CONTRIBUTORS "AS IS"
% AND ANY EXPRESS OR IMPLIED WARRANTIES, INCLUDING, BUT NOT LIMITED TO, THE
% IMPLIED WARRANTIES OF MERCHANTABILITY AND FITNESS FOR A PARTICULAR PURPOSE
ARE
% DISCLAIMED. IN NO EVENT SHALL THE COPYRIGHT OWNER OR CONTRIBUTORS BE LIABLE
% FOR ANY DIRECT, INDIRECT, INCIDENTAL, SPECIAL, EXEMPLARY, OR CONSEQUENTIAL
% DAMAGES (INCLUDING, BUT NOT LIMITED TO, PROCUREMENT OF SUBSTITUTE GOODS OR
% SERVICES; LOSS OF USE, DATA, OR PROFITS; OR BUSINESS INTERRUPTION) HOWEVER
% CAUSED AND ON ANY THEORY OF LIABILITY, WHETHER IN CONTRACT, STRICT
LIABILITY,
% OR TORT (INCLUDING NEGLIGENCE OR OTHERWISE) ARISING IN ANY WAY OUT OF THE
USE
% OF THIS SOFTWARE, EVEN IF ADVISED OF THE POSSIBILITY OF SUCH DAMAGE.
if nargin<3 || isempty(shape)
    shape = 'full';
end
if nargin<5 || isempty(options)
    options = struct();
elseif ~isstruct(options) % GPU options
    options = struct('GPU', options);
end
nd = max(ndims(A),ndims(B));
% work on all dimensions by default
if nargin<4 || isempty(dims)
    dims = 1:nd;
end
```

```
dims = reshape(dims, 1, []); % row (needed for for-loop index)
% GPU enable flag
GPU = getoption(options, 'GPU', false);
% Check if Jacket is installed
GPU = GPU && ~isempty(which('ginfo'));
% IFUN function will be used later to truncate the result
% M and N are respectively the length of A and B in some dimension
switch lower(shape)
    case 'full'
        ifun = @(m,n) 1:m+n-1;
    case 'same'
        ifun = @(m,n) ceil((n-1)/2)+(1:m);
    case 'valid'
        ifun = @(m,n) n:m;
    otherwise
        error('convnfft: unknown shape %s', shape);
end
classA = class(A);
classB = class(B);
ABreal = isreal(A) && isreal(B);
% Special case, empty convolution, try to follow MATLAB CONVN convention
if any(size(A)==0) || any(size(B)==0)
    szA = zeros(1,nd); szA(1:ndims(A))=size(A);
    szB = zeros(1,nd); szB(1:ndims(B))=size(B);
    % Matlab wants these:
    szA = max(szA,1); szB = max(szB,1);
    szC = szA;
    for dim=dims
        szC(dim) = length(ifun(szA(dim),szB(dim)));
    end
    A = zeros(szC,classA); % empty -> return zeros
    return
end
power2flag = getoption(options, 'Power2Flag', true);
if power2flag
    % faster FFT if the dimension is power of 2
    lfftfun = @(l) 2^nextpow2(l);
else
    % slower, but smaller temporary arrays
    lfftfun = @(l) l;
end
if GPU % GPU/Jacket FFT
    if isa(classA,'single')
        A = gsingle(A);
    else
        A = gdouble(A);
    end
    if isa(classB,'single')
        B = gsingle(B);
    else
        B = gdouble(B);
    end
    % Do the FFT
    subs(1:ndims(A)) = {':'};
    for dim=dims
        m = size(A,dim);
        n = size(B,dim);
```

```
        % compute the FFT length
        l = lfftfun(m+n-1);
        % We need to swap dimensions because GPU FFT works along the
        % first dimension
        if dim~=1 % do the work when only required
            swap = 1:nd;
            swap([1 dim]) = swap([dim 1]);
            A = permute(A, swap);
            B = permute(B, swap);
        end
        A = fft(A,l);
        B = fft(B,l);
        subs{dim} = ifun(m,n);
    end
else % Matlab FFT
    % Do the FFT
    subs(1:ndims(A)) = {':'};
    for dim=dims
        m = size(A,dim);
        n = size(B,dim);
        % compute the FFT length
        l = lfftfun(m+n-1);
        A = fft(A,l,dim);
        B = fft(B,l,dim);
        subs{dim} = ifun(m,n);
    end
end
if GPU
    A = A.*B;
    clear B
else
    %inplace product to save 1/3 of the memory
    %inplaceprod(A,B);
    %change made by KHANH T NGO KTN6@PITT.EDU
    %for compatibility with MATLAB 2019a WINDOWS 10
    A = A.*B;
end
% Back to the non-Fourier space
if GPU % GPU/Jacket FFT
    for dim=dims(end:-1:1) % reverse loop
        A = ifft(A,[]);
        % Swap back the dimensions
        if dim~=1 % do the work when only required
            swap = 1:nd;
            swap([1 dim]) = swap([dim 1]);
            A = permute(A, swap);
        end
    end
else % Matlab IFFT
    for dim=dims
        A = ifft(A,[],dim);
    end
end
% Truncate the results
if ABreal
    % Make sure the result is real
    A = real(A(subs{:}));
```

```
else
    A = A(subs{:});
end
% GPU/Jacket
if GPU
    % Cast the type back
    if isa(class(A),'gsingle')
        A = single(A);
    else
        A = double(A);
    end
end
end % convnfft
%% Get default option
function value = getoption(options, name, defaultvalue)
% function value = getoption(options, name, defaultvalue)
    value = defaultvalue;
    fields = fieldnames(options);
    found = strcmpi(name,fields);
    if any(found)
        i = find(found,1,'first');
        if ~isempty(options.(fields{i}))
            value = options.(fields{i});
        end
    end
end
```

4.6.2 Mathematical Derivation

4.6.2.1 From Chen 2002 Eq. 7 to Bungay 2011 Eq. 20

Chen 2002: Chen, K. C.; Hoistad, M.; Kehr, J.; Fuxe, K.; Nicholson, C. *J Neurochem* **2002**, *81*, 108-121. Bungay 2011: Bungay, P. M.; Sumbria, R. K.; Bickel, U. *J Pharm Biomed Anal* **2011**, *55*, 54-63.

Note: $$P_{ECS}(t) = -\frac{D\phi}{\lambda^2 r_o}\frac{\partial}{\partial \frac{r}{r_0}} U_{ECS}\left(\frac{r}{r_o}, t\right)\Bigg|_{\frac{r}{r_o}=1}$$

$$U_{ECS}\left(\frac{r}{r_o}, \mathrm{t}\right) = \lim_{R_m \to 0} U\left(\frac{r}{r_o}, \mathrm{t}\right) = \frac{K_0\left(\frac{r_o}{\Gamma}\frac{r}{r_o}\right)}{K_0\left(\frac{r_o}{\Gamma}\right)} + \frac{2}{\pi}\int_0^\infty \frac{e^{-\left(u^2+\frac{r_o^2}{\Gamma^2}\right)\frac{D}{\lambda^2 r_o^2}t}}{u^2+\frac{r_o^2}{\Gamma^2}} \frac{J_0\left(u\frac{r}{r_o}\right)Y_0(u) - Y_0\left(u\frac{r}{r_o}\right)J_0(u)}{J_0^2(u)+Y_0^2(u)} u\,du$$

Step 1: take partial derivative with respect to $\frac{r}{r_o}$ of $U_e(t)$

$$\frac{\partial}{\partial \frac{r}{r_o}} U_{ECS}\left(\frac{r}{r_o}, \mathrm{t}\right) = \frac{\partial}{\partial \frac{r}{r_o}} \frac{K_0\left(\frac{r_o}{\Gamma}\frac{r}{r_o}\right)}{K_0\left(\frac{r_o}{\Gamma}\right)} + \frac{\partial}{\partial \frac{r}{r_o}} \frac{2}{\pi} \int_0^\infty \frac{e^{-\left(u^2+\frac{r_o^2}{\Gamma^2}\right)\frac{D}{\lambda^2 r_o^2}t}}{u^2+\frac{r_o^2}{\Gamma^2}} \frac{J_0\left(u\frac{r}{r_o}\right)Y_0(u) - Y_0\left(u\frac{r}{r_o}\right)J_0(u)}{J_0^2(u)+Y_0^2(u)} u du$$

Step 2: Using Leibniz's integral rule, move the partial derivative inside the integration. This works because the derivative is with respect to $\frac{r}{r_o}$ while the integration is with respect to u

$$\frac{\partial}{\partial \frac{r}{r_o}} U_{ECS}\left(\frac{r}{r_o}, \mathrm{t}\right) = \frac{\partial}{\partial \frac{r}{r_o}} \frac{K_0\left(\frac{r_o}{\Gamma}\frac{r}{r_o}\right)}{K_0\left(\frac{r_o}{\Gamma}\right)} + \frac{2}{\pi} \int_0^\infty \frac{\partial}{\partial \frac{r}{r_o}} \frac{e^{-\left(u^2+\frac{r_o^2}{\Gamma^2}\right)\frac{D}{\lambda^2 r_o^2}t}}{u^2+\frac{r_o^2}{\Gamma^2}} \frac{J_0\left(u\frac{r}{r_o}\right)Y_0(u) - Y_0\left(u\frac{r}{r_o}\right)J_0(u)}{J_0^2(u)+Y_0^2(u)} u du$$

Step 3: Apply the partial derivative to terms that contains the variable r

$$\frac{\partial}{\partial \frac{r}{r_o}} U_{ECS}\left(\frac{r}{r_o}, \mathrm{t}\right) = \frac{\frac{\partial}{\partial \frac{r}{r_o}} K_0\left(\frac{r_o}{\Gamma}\frac{r}{r_o}\right)}{K_0\left(\frac{r_o}{\Gamma}\right)} + \frac{2}{\pi} \int_0^\infty \frac{e^{-\left(u^2+\frac{r_o^2}{\Gamma^2}\right)\frac{D}{\lambda^2 r_o^2}t}}{u^2+\frac{r_o^2}{\Gamma^2}} \frac{\frac{\partial}{\partial \frac{r}{r_o}}\left[J_0\left(u\frac{r}{r_o}\right)Y_0(u) - Y_0\left(u\frac{r}{r_o}\right)J_0(u)\right]}{J_0^2(u)+Y_0^2(u)} u du$$

Step 4: Change of variables

$$\frac{\partial}{\partial \frac{r}{r_o}} U_{ECS}\left(\frac{r}{r_o}, \mathrm{t}\right) = \frac{\frac{\partial \frac{r_o}{\Gamma}\frac{r}{r_o}}{\partial \frac{r}{r_o}} \frac{\partial}{\partial \frac{r_o}{\Gamma}\frac{r}{r_o}} K_0\left(\frac{r_o}{\Gamma}\frac{r}{r_o}\right)}{K_0\left(\frac{r_o}{\Gamma}\right)} + \frac{2}{\pi} \int_0^\infty \frac{e^{-\left(u^2+\frac{r_o^2}{\Gamma^2}\right)\frac{D}{\lambda^2 r_o^2}t}}{u^2+\frac{r_o^2}{\Gamma^2}} \frac{\frac{\partial u\frac{r}{r_o}}{\partial \frac{r}{r_o}} \frac{\partial}{\partial u\frac{r}{r_o}}\left[J_0\left(u\frac{r}{r_o}\right)Y_0(u) - Y_0\left(u\frac{r}{r_o}\right)J_0(u)\right]}{J_0^2(u)+Y_0^2(u)} u du$$

Step 5: Apply the following relationships $d/dx\ K_0(x) = -K_1(x)$ $d/dx\ J_0(x) = -J_1(x)$ $d/dx\ Y_0(x) = -Y_1(x)$

$$\frac{\partial}{\partial \frac{r}{r_o}} U_{ECS}\left(\frac{r}{r_o}, \mathrm{t}\right) = \frac{-\frac{r_o}{\Gamma} K_1\left(\frac{r_o}{\Gamma}\frac{r}{r_o}\right)}{K_0\left(\frac{r_o}{\Gamma}\right)} + \frac{2}{\pi}\int_0^{\infty} \frac{e^{-\left(u^2+\frac{r_o^2}{\Gamma^2}\right)\frac{D}{\lambda^2 r_o^2}t}}{u^2+\frac{r_o^2}{\Gamma^2}} \frac{u\left[-J_1\left(u\frac{r}{r_o}\right)Y_0(u)+Y_1\left(u\frac{r}{r_o}\right)J_0(u)\right]}{J_0^2(u)+Y_0^2(u)} udu$$

Step 6: Evaluate the partial derivative at $\frac{r}{r_o} = 1$

$$\left.\frac{\partial}{\partial \frac{r}{r_o}} U_{ECS}\left(\frac{r}{r_o}, \mathrm{t}\right)\right|_{\frac{r}{r_o}=1} = \frac{-\frac{r_o}{\Gamma} K_1\left(\frac{r_o}{\Gamma}\right)}{K_0\left(\frac{r_o}{\Gamma}\right)} + \frac{2}{\pi}\int_0^{\infty} \frac{e^{-\left(u^2+\frac{r_o^2}{\Gamma^2}\right)\frac{D}{\lambda^2 r_o^2}t}}{u^2+\frac{r_o^2}{\Gamma^2}} \frac{u\left[-J_1(u)Y_0(u)+Y_1(u)J_0(u)\right]}{J_0^2(u)+Y_0^2(u)} udu$$

Step 7: Apply the relationship $J_1(u)Y_0(u) - Y_1(u)J_0(u) = 2/(\pi u)$

$$\left.\frac{\partial}{\partial \frac{r}{r_o}} U_{ECS}\left(\frac{r}{r_o}, \mathrm{t}\right)\right|_{\frac{r}{r_o}=1} = \frac{-\frac{r_o}{\Gamma} K_1\left(\frac{r_o}{\Gamma}\right)}{K_0\left(\frac{r_o}{\Gamma}\right)} + \frac{2}{\pi}\int_0^{\infty} \frac{e^{-\left(u^2+\frac{r_o^2}{\Gamma^2}\right)\frac{D}{\lambda^2 r_o^2}t}}{u^2+\frac{r_o^2}{\Gamma^2}} \frac{u\frac{-2}{\pi u}}{J_0^2(u)+Y_0^2(u)} udu$$

Step 8: Simplifies

$$\left.\frac{\partial}{\partial \frac{r}{r_o}} U_{ECS}\left(\frac{r}{r_o}, \mathrm{t}\right)\right|_{\frac{r}{r_o}=1} = -\frac{\frac{r_o}{\Gamma} K_1\left(\frac{r_o}{\Gamma}\right)}{K_0\left(\frac{r_o}{\Gamma}\right)} - \frac{4}{\pi^2}\int_0^{\infty} \frac{e^{-\left(u^2+\frac{r_o^2}{\Gamma^2}\right)\frac{D}{\lambda^2 r_o^2}t}}{u^2+\frac{r_o^2}{\Gamma^2}} \frac{1}{J_0^2(u)+Y_0^2(u)} udu$$

Step 9: Apply the relationship $P_{ECS}(t) = -\frac{D\phi}{\lambda^2 r_o} \frac{\partial}{\partial \frac{r}{r_0}} U_{ECS}\left(\frac{r}{r_o}, t\right)\Big|_{\frac{r}{r_o}=1}$

$$-\frac{\lambda^2 r_0 P_{ECS}(t)}{D\phi} = \frac{\frac{r_o}{\Gamma} K_1\left(\frac{r_o}{\Gamma}\right)}{K_0\left(\frac{r_o}{\Gamma}\right)} + \frac{4}{\pi^2}\int_0^{\infty} \frac{e^{-\left(u^2+\frac{r_o^2}{\Gamma^2}\right)\frac{D}{\lambda^2 r_o^2}t}}{u^2+\frac{r_o^2}{\Gamma^2}} \frac{1}{J_0^2(u)+Y_0^2(u)} udu$$

This is Eq. 20 in Bungay 2011 but with:

$$\Theta \equiv \frac{r_o}{\Gamma} \equiv r_o\sqrt{\frac{k\lambda^2}{D}} \text{ and } T_{ext} = \frac{r_o^2 K_{ext}}{D_{ext}} \text{ where } K_{ext} = \phi \text{ and } D_{ext} = \frac{D\phi}{\lambda^2}$$

4.6.2.2 From Chen 2002a Eq. 6 to Chen 2002b Eq. A6

Chen 2002a: Chen, K. C.; Hoistad, M.; Kehr, J.; Fuxe, K.; Nicholson, C. *J Neurochem* **2002**, *81*, 94-107. Chen 20002b: Chen, K. C.; Hoistad, M.; Kehr, J.; Fuxe, K.; Nicholson, C. *J Neurochem* **2002**, *81*, 108-121. Some steps are similar to the derivation above, thus they are not repeated.

Note: $\alpha^* = \phi \quad \alpha_m = \phi_m \quad D_e = D_{ECS} = \frac{D}{\lambda^2} \quad D_m = \frac{D}{\lambda_m^2}$

$$\eta_1 = \frac{\alpha^*}{\alpha_m}\sqrt{\frac{D_e}{D_m}}\nu_1 u J_1(u) - \nu_2\sqrt{u^2 + \frac{r_o^2}{\Gamma^2}}J_0(u)$$

$$\eta_2 = \frac{\alpha^*}{\alpha_m}\sqrt{\frac{D_e}{D_m}}\nu_1 u Y_1(u) - \nu_2\sqrt{u^2 + \frac{r_o^2}{\Gamma^2}}Y_0(u)$$

$$\nu_1 = J_0\left(\sqrt{\frac{u^2 + \frac{r_o^2}{\Gamma^2}}{D_m/D_e}}\right)Y_0\left(\sqrt{\frac{u^2 + \frac{r_o^2}{\Gamma^2}}{D_m/D_e}}\frac{r_i}{r_o}\right) - J_0\left(\sqrt{\frac{u^2 + \frac{r_o^2}{\Gamma^2}}{D_m/D_e}}\frac{r_i}{r_o}\right)Y_0\left(\sqrt{\frac{u^2 + \frac{r_o^2}{\Gamma^2}}{D_m/D_e}}\right)$$

$$\nu_2 = J_1\left(\sqrt{\frac{u^2 + \frac{r_o^2}{\Gamma^2}}{D_m/D_e}}\right)Y_0\left(\sqrt{\frac{u^2 + \frac{r_o^2}{\Gamma^2}}{D_m/D_e}}\frac{r_i}{r_o}\right) - J_0\left(\sqrt{\frac{u^2 + \frac{r_o^2}{\Gamma^2}}{D_m/D_e}}\frac{r_i}{r_o}\right)Y_1\left(\sqrt{\frac{u^2 + \frac{r_o^2}{\Gamma^2}}{D_m/D_e}}\right)$$

$$U\left(\frac{r}{r_o}, t\right) = \frac{K_0\left(\frac{r}{r_o}\frac{r_o}{\Gamma}\right)}{\ln\left(\frac{r_o}{r_i}\right)\frac{\phi}{\phi_m}\frac{D/\lambda^2}{D_m}\frac{r_o}{\Gamma}K_1\left(\frac{r_o}{\Gamma}\right) + K_0\left(\frac{r_o}{\Gamma}\right)} + \frac{2}{\pi}\int_0^\infty \frac{\exp\left(-\left(u^2 + \left(\frac{r_o}{\Gamma}\right)^2\right)\cdot\frac{Dt}{\lambda^2 r_o^2}\right)}{\left(u^2 + \left(\frac{r_o}{\Gamma}\right)^2\right)}\frac{\eta_1 Y_0\left(u\frac{r}{r_o}\right) - \eta_2 J_0\left(u\frac{r}{r_o}\right)}{\frac{\pi}{2}\sqrt{\frac{D/\lambda^2}{D_m}}\left(\eta_1^2 + \eta_2^2\right)}u\,du$$

Step 1: Apply Leibniz's integral rule and apply the partial derivative to terms that contains the variable *r*

$$\frac{\partial}{\partial \frac{r}{r_0}} U\left(\frac{r}{r_o}, t\right) = \frac{\frac{\partial}{\partial \frac{r}{r_0}} K_0\left(\frac{r}{r_o}\frac{r_o}{\Gamma}\right)}{\ln\left(\frac{r_o}{r_i}\right)\frac{\phi}{\phi_m}\frac{D/\lambda^2}{D_m}\frac{r_o}{\Gamma}K_1\left(\frac{r_o}{\Gamma}\right) + K_0\left(\frac{r_o}{\Gamma}\right)} + \frac{2}{\pi}\int_0^\infty \frac{\exp\left(-\left(u^2 + \left(\frac{r_o}{\Gamma}\right)^2\right)\cdot\frac{Dt}{\lambda^2 r_o^2}\right)}{\left(u^2 + \left(\frac{r_o}{\Gamma}\right)^2\right)} \frac{\frac{\partial}{\partial \frac{r}{r_0}}\left[\eta_1 Y_0\left(u\frac{r}{r_o}\right) - \eta_2 J_0\left(u\frac{r}{r_o}\right)\right]}{\frac{\pi}{2}\sqrt{\frac{D/\lambda^2}{D_m}\left(\eta_1^2 + \eta_2^2\right)}} u du$$

Step 2: Change derivative variable appropriately and apply the following relationships $d/dx\ K_0(x) = -K_1(x)$ $d/dx\ J_0(x) = -J_1(x)$ $d/dx\ Y_0(x) = -Y_1(x)$

$$\frac{\partial}{\partial \frac{r}{r_0}} U\left(\frac{r}{r_o}, t\right) = \frac{-\frac{r_o}{\Gamma} K_1\left(\frac{r}{r_o}\frac{r_o}{\Gamma}\right)}{\ln\left(\frac{r_o}{r_i}\right)\frac{\phi}{\phi_m}\frac{D/\lambda^2}{D_m}\frac{r_o}{\Gamma}K_1\left(\frac{r_o}{\Gamma}\right) + K_0\left(\frac{r_o}{\Gamma}\right)} + \frac{2}{\pi}\int_0^\infty \frac{\exp\left(-\left(u^2 + \left(\frac{r_o}{\Gamma}\right)^2\right)\cdot\frac{Dt}{\lambda^2 r_o^2}\right)}{\left(u^2 + \left(\frac{r_o}{\Gamma}\right)^2\right)} \frac{\left[-\eta_1 u Y_1\left(u\frac{r}{r_o}\right) + \eta_2 u J_1\left(u\frac{r}{r_o}\right)\right]}{\frac{\pi}{2}\sqrt{\frac{D/\lambda^2}{D_m}\left(\eta_1^2 + \eta_2^2\right)}} u du$$

Step 3: Evaluate the partial derivative at $\frac{r}{r_o} = 1$ then simplifies

$$\left.\frac{\partial}{\partial \frac{r}{r_0}} U\left(\frac{r}{r_o}, t\right)\right|_{\frac{r}{r_0}=1} = -\frac{\frac{r_o}{\Gamma} K_1\left(\frac{r_o}{\Gamma}\right)}{\ln\left(\frac{r_o}{r_i}\right)\frac{\phi}{\phi_m}\frac{D/\lambda^2}{D_m}\frac{r_o}{\Gamma}K_1\left(\frac{r_o}{\Gamma}\right) + K_0\left(\frac{r_o}{\Gamma}\right)} - \frac{2}{\pi}\int_0^\infty \frac{\exp\left(-\left(u^2 + \left(\frac{r_o}{\Gamma}\right)^2\right)\cdot\frac{Dt}{\lambda^2 r_o^2}\right)}{\left(u^2 + \left(\frac{r_o}{\Gamma}\right)^2\right)} \frac{\left[\eta_1 Y_1(u) - \eta_2 J_1(u)\right]}{\frac{\pi}{2}\sqrt{\frac{D/\lambda^2}{D_m}\left(\eta_1^2 + \eta_2^2\right)}} u^2 du$$

4.6.2.3 Equivalency of Volume Bases

Mass balance can be described in either ECS volume basis or tissue volume basis

$$\frac{\partial C_{ECS}}{\partial t} = \frac{D_{ECS}}{r}\frac{\partial}{\partial r}\left[r\frac{\partial C_{ECS}}{\partial r}\right] - kC_{ECS}$$

$$\frac{\phi \partial C_{ECS}}{\partial t} = \frac{\phi D_{ECS}}{r}\frac{\partial}{\partial r}\left[r\frac{\partial C_{ECS}}{\partial r}\right] - \phi kC_{ECS}$$

$$\frac{\partial C_{tissue}}{\partial t} = \frac{D_{tissue}}{\phi r}\frac{\partial}{\partial r}\left[r\frac{\partial C_{tissue}}{\partial r}\right] - kC_{tisue}$$

Starting from the same ECS volume basis, one can derive Nicholson 2001, Chen 2002 and Bungay 2011's expressions. Nicholson 2001: Nicholson, C. *Rep. Prog. Phys.* **2001**, *64*, 815-884. Chen 2002: Chen, K. C.; Hoistad, M.; Kehr, J.; Fuxe, K.; Nicholson, C. *J Neurochem* **2002**, *81*, 94-107 and Chen, K. C.; Hoistad, M.; Kehr, J.; Fuxe, K.; Nicholson, C. *J Neurochem* **2002**, *81*,

108-121. Bungay 2011: Bungay, P. M.; Sumbria, R. K.; Bickel, U. *J Pharm Biomed Anal* **2011**, *55*, 54-63.

Derivation to Nicholson (2001):

$$\frac{\partial C_{ECS}}{\partial t} = \frac{D_{ECS}}{r}\frac{\partial}{\partial r}\left[r\frac{\partial C_{ECS}}{\partial r}\right] - kC_{ECS}$$

All variables are defined in the same manner, the equation can simply be rewritten:

$$\frac{\partial C}{\partial t} = D^{*}\nabla^{2}C - k'C$$

Derivation to Chen (2002):

$$\frac{\partial C_{ECS}}{\partial t} = \frac{D_{ECS}}{r}\frac{\partial}{\partial r}\left[r\frac{\partial C_{ECS}}{\partial r}\right] - kC_{ECS}$$

$$\frac{\phi\partial C_{ECS}}{\partial t} = \frac{\phi D_{ECS}}{r}\frac{\partial}{\partial r}\left[r\frac{\partial C_{ECS}}{\partial r}\right] - \phi kC_{ECS}$$

$$\frac{\partial \phi C_{ECS}}{\partial t} = \frac{D_{ECS}}{r}\frac{\partial}{\partial r}\left[r\frac{\partial \phi C_{ECS}}{\partial r}\right] - k\phi C_{ECS}$$

$$\frac{\partial C_{tissue}}{\partial t} = \frac{D_{ECS}}{r}\frac{\partial}{\partial r}\left[r\frac{\partial \phi C_{tissue}}{\partial r}\right] - kC_{tissue}$$

$$\frac{\partial C_{e}}{\partial t} = \frac{D_{e}}{r}\frac{\partial}{\partial r}\left[r\frac{\partial \phi C_{e}}{\partial r}\right] - \kappa C_{e}$$

Derivation to Bungay (2011):

$$\frac{\partial C_{ECS}}{\partial t} = \frac{D_{ECS}}{r}\frac{\partial}{\partial r}\left[r\frac{\partial C_{ECS}}{\partial r}\right] - kC_{ECS}$$

$$\frac{\phi\partial C_{ECS}}{\partial t} = \frac{\phi D_{ECS}}{r}\frac{\partial}{\partial r}\left[r\frac{\partial C_{ECS}}{\partial r}\right] - \phi kC_{ECS}$$

$$\frac{\phi\partial C_{ECS}}{\partial t} = \frac{D_{tissue}}{r}\frac{\partial}{\partial r}\left[r\frac{\partial C_{ECS}}{\partial r}\right] - \phi kC_{ECS}$$

$$\frac{K_{ext}\partial c_e}{\partial t} = \frac{D_{ext}}{r}\frac{\partial}{\partial r}\left[r\frac{\partial c_e}{\partial r}\right] - k_{ext}C_e$$

4.6.2.4 Equivalency of Permeability Methods

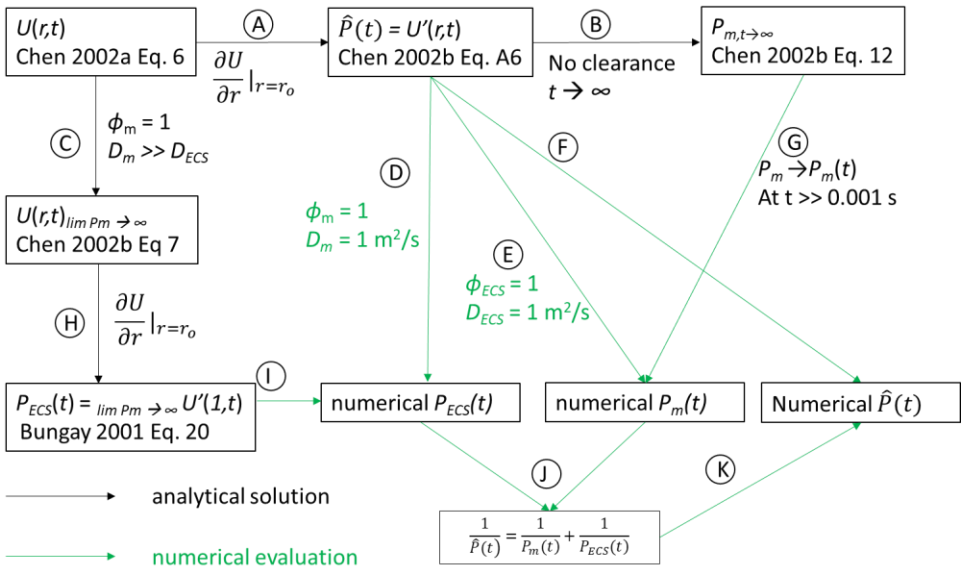

Figure 4.6-1. Relationship between methods to evaluate overall permeability.

(A) The partial derivative with respective to membrane radius, evaluated at the outer radius, of U(r,t) is the solution for the time-dependent overall permeability $P(t)$.

(B) From $U'(r,t)$, at large time t, the integral term drops out, and the time-dependent permeability expressions become steady-state permeability expressions:

$$\left(\frac{\partial U}{\partial \frac{r}{r_o}}\right)_{\frac{r}{r_o}=1,t\to\infty} = \frac{r_o\sqrt{\frac{k\lambda^2}{D}}K_1\left(r_o\sqrt{\frac{k\lambda^2}{D}}\right)}{\ln\left(\frac{r_o}{r_i}\right)\frac{\phi}{\phi_m}\frac{D/\lambda^2}{D_m}r_o\sqrt{\frac{k\lambda^2}{D}}K_1\left(r_o\sqrt{\frac{k\lambda^2}{D}}\right)+K_0\left(r_o\sqrt{\frac{k\lambda^2}{D}}\right)}$$

The membrane steady-state permeability is obtained by dropping clearance-related terms[58,59]:

$$P_{m,t\to\infty} = \frac{\phi_m D_m}{r_o \ln\left(\frac{r_o}{r_i}\right)}$$

(C) Assuming a fully permeable membrane ($\phi_m \to 1$, and $D_m >> D_{ECS}$), $U(r,t)$ simplifies to the time-dependent normalized radial concentration distribution function in the ECS:

$$\lim_{R_m\to\infty} U\left(\frac{r}{r_o}, \mathrm{t}\right) = \frac{K_0\left(\frac{r_o}{\Gamma}\frac{r}{r_o}\right)}{K_0\left(\frac{r_o}{\Gamma}\right)} + \frac{2}{\pi}\int_0^\infty \frac{e^{-\left(u^2+\frac{r_o^2}{\Gamma^2}\right)\frac{D_e}{r_o^2}t}}{u^2+\frac{r_o^2}{\Gamma^2}} \frac{J_0\left(u\frac{r}{r_o}\right)Y_0(u) - Y_0\left(u\frac{r}{r_o}\right)J_0(u)}{J_0^2(u)+Y_0^2(u)} u\,du$$

(D) $\hat{P}(t)$ is numerically evaluated with a fully permeable membrane assumption (ϕ_m = 1, and D_m = 1 m^2/s) to obtain $P_{ECS}(t)$.

(E) $\hat{P}(t)$ is numerically evaluated with a fully permeable ECS assumption (ϕ_{ECS} = 1, and D_{ECS} = 1 m^2/s) to obtain $P_m(t)$.

(F) $\hat{P}(t)$ is numerically evaluated to obtain overall permeability.

(G) At t >> 0.001 s, $P_{m,\,t\to\infty}$ approximates $P_m(t)$.

(H) The partial derivative with respective to membrane radius, evaluated at the outer radius is the solution for $P_{ECS}(t)$.

(I) $P_{ECS}(t)$ is numerically evaluated.

4.6.3 Additional Figures

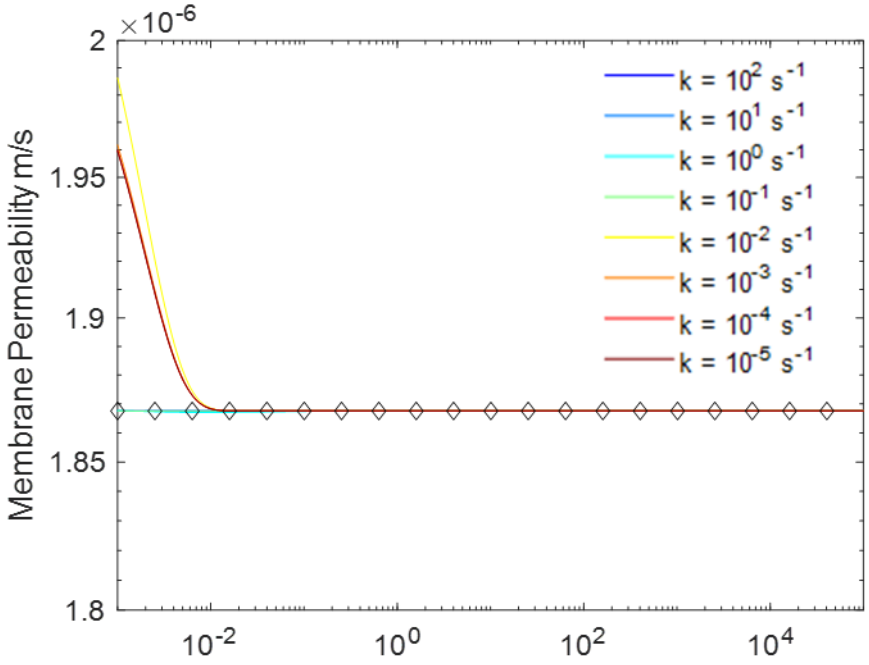

Figure 4.6-2. Membrane permeability as a function of time across a range of uptake rate constant with conditions similar to Chen (2002).

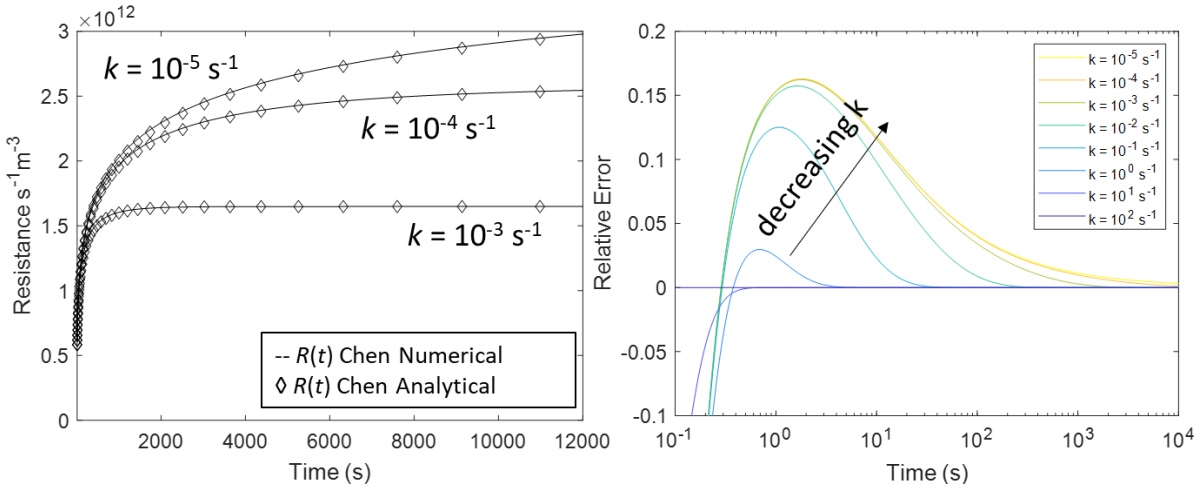

Figure 4.6-3. Comparison between Chen's analytical (diamond) and numerical (dashed line) method at long time (left) and short time (right).

5.0 Comprehensive Quantitative Microdialysis: Experimental Method and Data Fitting

5.1 Chapter Summary

The term “quantitative microdialysis” has been used to describe experimental protocols and associated assumptions that provide an estimate of the extracellular concentration of an endogenous neuroactive species like dopamine (DA) in a brain region. Most prominently, the no net flux method uses step-changes in concentration of the sought-for species in the microdialysis inlet and steady-state measurements of the concentrations in the microdialysis outlet. Here, we describe the use of measurements made during the transition of the concentration in the microdialysis outlet from initial to final steady state concentrations to infer information including the concentration of DA far from the microdialysis probe, $C_{ECS\infty}$. This procedure, comprehensive quantitative microdialysis (CQM), includes a set of assumptions, a mathematical model, an experimental method, and a curve fit method that can be used to determine physiological parameters that affect a transient response. The model based on earlier work by Bungay et al. is in the previous chapter. To improve time resolution and thus the quality of the resulting parameters derived from the curve fit, the experiment uses time-interleaved sampling. The curve fit uses an adaptive simplex optimization to adjust fitting parameters to find a minimum residual sum of squared differences between experiment and the model. Measuring transient responses to retrodialysis of 50, 100, and 150 nM DA using 45 s Fast Microdialysis in the rat nucleus accumbens, the CQM curve fit for each of three transients yielded $C_{ECS\infty}$ and extraction fraction comparable to a standard no-net-flux measurement, and an uptake rate constant comparable to literature values. With 15 s measurements, tissue porosity could also be determined. CQM

dramatically reduced the experimental time while obtaining more biologically relevant information compared to traditional quantitative microdialysis.

5.2 Introduction

Microdialysis[30,192] is not only the most widely used method for brain sampling[9,12,31,32,193], but the number of new applications and studies for it has steadily risen[35,45,194]. It provides a sample for determination of the concentrations of target analytes in the dialysate. It is a robust technique that can be used in both anesthetized and awake animals of sizes ranging from small rodents[195,196] to primates[197], including human[198,199]. In recent years, breakthroughs in brain microdialysis techniques have improved probe response time[200,201], sampling in injured tissue[86,122], the time resolution of online analysis[74,76-78], and other aspect of the technique[45]. This has proved to be immensely useful despite the difficulties inherent in inferring concentration of the analytes in the brain from measured concentrations in dialysate[103]. So called "quantitative microdialysis techniques"[54] can provide estimates of concentrations of substances in the brain with the assumption that the microdialysis recovery and extraction fractions are the same[55,90]. However, these techniques require a significant experimental time which in part is due to the low time resolution of typical microdialysis measurements[46,47] and the fact that the analyses are based on steady-state measurements.

Recent improvements in microdialysis sampling and detection speed has allowed for determination of neurotransmitters and metabolites at the time resolution of 1-3 minutes[47,72,76-78,152,175] with online analysis , and at the time resolution of 2 seconds[80,81] with offline analysis. At these data acquisition rates, transient responses to chemical[97] and behavioral[98] stimulations have

been observed and analyzed, providing a brief glimpse into what could be achieved with faster time resolution and better theoretical and data analysis tools. Research into microdialysis theory, on the other hand, has entered a period of inactivity with the most recent mass transport model[61] developed by Bungay *et at.* in 2011. This model was based on Bungay's previous work[60,84] as well as on analytical solutions obtained by Chen *et at.*[58,59]. It provided an analytical solution for mass transport in the cylindrical coordinate system that incorporates solute uptake and diffusion in the extracellular space (ECS). However, there are discrepancies[202] between Chen's and Bungay's mathematical descriptions (which are based on the same underlying differential equation for mass transport) which were clarified in the previous chapter.

Building from Bungay's work and previous literature for time-dependent microdialysis[56-66,84], we have developed a technique called Comprehensive Quantitative Microdialysis (CQM) that can be used to obtain quantitative estimates related to diffusion of solutes and solute reuptake in the extracellular space by analysis of a transient response in solute concentration experimentally measured at the detector following a step change in the solute concentration at the probe inlet. Note that the overall system time response includes physiological parameters as well as experimental parameters. Thus, to deduce the physiological parameters, the method must adequately account for the experimental parameters. The technique has three components: mathematical model and associated assumptions, experimental method, and a curve-fitting method. In the previous chapter, I described the mathematical model and associated assumptions, and demonstrated it with a simulation tool and *in vitro* experiments. Here, I describe the *in vivo* experiment and the curve-fitting method.

The fitting algorithm is based on Nelder-Mead Simplex Optimization[203,204] (NMS), a commonly used numerical method for finding a minimum of an objective function (in this case,

the residual sum of square differences between experiment and the model, "RSS") in a multidimensional space (in this case, the fitting parameters). The general principle of our NMS variant is similar to the Stochastic Nelder-Mead Simplex proposed by Chang (2012)[205], where global and local random searches are added to NMS to enhance the probability of the fit to find global minimum. We named our NMS variant "Adaptive Random Sampling Simplex" (ARS) for its main feature of performing random new searches around the current minimum, adaptively using said minimum as input for the search.

Using the comprehensive quantitative microdialysis mathematical model previously described[202], the curve fit method was able to determine microdialysis transport time, probe dispersion, tissue morphology and solute uptake in the extracellular space. We demonstrated this approach with two examples. In one, we used the curve fit to determine transport time, dispersion, and solute concentration and uptake rate in the rat nucleus accumbens from transient response to retrodialysis of DA. Quantitative estimates of solute concentration and uptake rate were compared with a no-net-flux experiment. In the second example, we designed the experimental method to improve the effective time resolution of Fast Microdialysis from 60 s to 15 s by utilizing time-interleaved sampling[182], measuring the response to identical step-changes in retrodialyzed concentrations of DA once every 60 s four times with each of the four offset by 15s. The CQM curve fit was then used to determined tissue porosity and the four physiological and system parameters above from the transient response.

5.3 Methods

5.3.1 Materials

Chemicals, analytical-grade, to make artificial cerebrospinal fluid (aCSF: 142 mM NaCl, 1.2 mM $CaCl_2$, 2.7 mM KCl, 1.0 mM $MgCl_2$, and 2.0 mM NaH_2PO_4, pH 7.4) and liquid chromatography mobile phase (sodium acetate, sodium octyl sulfonate, EDTA, acetonitrile, and acetic acid) were acquired from either Fisher Scientific (Fair Lawn, NJ) or Sigma (St. Louis, MO). Retrodialysis solution contains dopamine, aCSF and 50 μM of L-ascorbic acid to prevent oxidation of dopamine[67]. Dopamine hydrochloride and L-ascorbic acid, analytical-grade or better, were purchased from Sigma (St. Louis, MO).

5.3.2 Microdialysis Probe

Concentric probes (280 μm diameter, 4 mm length membrane) were constructed from hollow fiber membranes (13 kDa MWCO, Spectra/Por RC, Spectrum Laboratories Inc., Rancho Dominguez, CA). The probe inlet and outlet were fused silica capillaries (75 μM I.D., 150 μM O.D., 110 cm long, Polymicro Technologies, Phoenix, AZ). The inlet capillary was connected to a gastight syringe (1 mL, Hamilton 81320, Hamilton Company, Reno, NV). Perfusate flow (0.60 μL/min for 60 s sampling or 0.80 μL/min for 45 s sampling) was driven by a microliter syringe pump (PHD 4400, Harvard Apparatus, Holliston, MA). The outlet capillary of the probe was connected to the inlet port of the LC injector. A 100-psi backpressure regulator and a bubble-induced dampener[181] was added to the syringe for the time-interleaved experiment to improve flow accuracy and thus the quality for DA determination and of the curve fit.

5.3.3 Microdialysis Probe Implantation Procedure

All procedures involving animals were approved by the Institutional Animal Care and Use of Committee of the University of Pittsburgh. Male Sprague-Dawley rats (250-350 g, Hilltop, Scottsdale, PA) were anesthetized with isoflurane (5% volume for induction, 2.5% volume for maintenance, Henry Schein Animal Health, Elizabethtown, PA) then wrapped in a heating blanket (37°C) and placed in a stereotaxic frame. Using flat skull coordinates, probes were lowered slowly (5 μm/sec) using a micropositioner (Model 2660, David Kopf Instruments, Tujunga, CA) into the nucleus accumbens (1.6 mm anterior, 1.4 mm lateral from bregma, and 8.0 mm below dura). Probes were secured with bone screws and acrylic cement, and the incision was closed with sutures. Anesthesia was removed and rats were placed in a BASi Raturn chamber (West Lafayette, IN) for housing with free access to food and water. Rats were allowed a recovery period of 24 hrs priors to any dopamine measurements.

5.3.4 Online Microdialysis-LC-EC

The microdialysis/liquid chromatography system was similar that used in our previous work[97,98]. The perfusate syringe was refilled every 24 hr, at least three hours prior to any dopamine measurement. For online experiments, the outlet capillary of the probe was connected to the LC injection valve (8-port nanobore, electrically actuated, C72NX-4678D, Valco Instruments, Houston, TX) so that the dialysate is loaded into one of two fused-silica sample loops (600 nL, 75 μm I.D., 360 μm O.D, Polymicro Technologies, Phoenix, AZ). While one sample loop is being loaded from the probe, dialysate from the other loop is injected into the LC column for separation.

Capillary columns (7.5 cm long, 150 μm ID, Polymicro Technologies, Phoenix, AZ) were packed with 1.7 μm BEH C18 reversed-phase particles (Waters, Milford, MA) at a minimum pressure of 1400 bar. Mobile phase was delivered at a flow rate of 8.5 μL/min. (LC-30AD, maximum pressure of 1300 bar, Shimadzu, Columbia, MD). The column was heated to 47.5°C with a thermostatted heater. The mobile phase (100 mM sodium acetate, 1.75 mM SOS, 0.150 mM EDTA, 3.0 % v/v acetonitrile, and 2.0 % v/v acetic acid) was filtered and degassed with three passes of vacuum filtration using a 0.22 μm nylon filter (Osminics, Minnetonka, MN).

5.3.5 Amperometric Detection

Dopamine was detected at 400 mV (vs Ag/AgCl 3 M NaCl) using a BASi radial-style flowcell, 3 mm glassy carbon electrode with a 25 μm thick gasket and BASi Epsilon potentiostat (West Lafayette, IN). Dopamine peaks were integrated using MATLAB, then peak areas were compared against pre- and post-run calibration curves to determine dopamine concentration. The detector sensitivity was 0.106 ± 0.002 nA·s/nM with a limit of quantitation[98,202] of 1.0 nM.

5.4 Results and Discussion

5.4.1 Adaptive Random Sampling Simplex Fitting

All the processes that contribute to the shape of the resulting transient are included in the model[202]. Thus, our objective was to fit the model[202] to raw experimental results (nM DA vs. time) from a step-change in concentration of DA in the microdialysis system. The processes/parameters

in the model aside from physiological parameters are the transport time from the beginning of the probe inlet to the end of injector loop, hydrodynamic dispersion in the microdialysis system, and averaging of the concentration over time due to the discrete nature of the LC analysis method (See Supplementary Information 5.6.1.1). The non-linear fitting algorithm, written in MATLAB (complete, annotated computer code is shown in Supplementary Information 5.6.2.1), fits the model to experimental data by adjusting parameters of the model to minimize residual sum of squared differences (RSS) between data and the model. The model contains the following parameters: characteristic time t_i (characteristic time of the concentration profile at the end of injector loop, the difference between this and the time at which a step-change in concentration occurs in the microdialysis probe is the time required to transport the sample through the probe, inlet and outlet capillaries and injector loop), hydrodynamic dispersion standard deviation σ, ECS concentration $C_{ECS\infty}$, uptake rate constant k, ECS porosity ϕ, and ECS tortuosity λ. We will refer to the curve fit of the four parameters t_i, σ, $C_{ECS\infty}$, and k to experimental data as a "four-dimensional ARS", or 4DARS. The five-dimensional 5DARS method additionally includes the parameter ϕ, and the six-dimensional 6DARS method additionally includes the parameter λ. When discussing the Nelder-Mead algorithm we will use analogous abbreviations: 4DNMS, 5DNMS and 6DNMS.

The ARS fitting algorithm is based in part on Nelder-Mead Simplex Optimization[203,204,206]. In mathematics, a simplex is a generalization of a group of $n + 1$ points in an n-dimensional space. These points form a "surface" in the space where they reside and each n-dimensional point may be considered a "vertex". In curve fitting applications, a simplex optimization that fits for n parameters uses calculations based on the $n + 1$ vertices. The simplex optimization calculates values of an "objective function" at each vertex to find the minimum (or maximum) value of the objective function. Typically, the objective function is the RSS and the algorithm seeks to

minimize it. NMS, noted for its simplicity in implementation and its speed, often provides a significant reduction (or improvement in a maximization problem) in the objective function with a relatively small number of function evaluations. However, NMS has a strong tendency to converge to a local minimum. Due to the presence of noises in practical experimental data, local minima exist which hinder the algorithm's ability to find best-fit parameters. This a problem well-documented[59,189,207] with many proposed solutions[208-211]. The ARS algorithm, described below, was devised to improve the simplex optimization's likelihood to find the global minimum. It is an improvement over NMS based on the Stochastic Nelder-Mead Simplex[205], that increased the likelihood of finding best fit parameters.

5.4.1.1 Minimum-Searching Algorithm

An initialization protocol was created to generate favorable staring conditions. In the initialization protocol, the user must give a set of fitting parameters to use as a start point for the process. Another start point is created by obtaining estimation for $C_{ECS\infty}$ from a linear regression of the steady-state concentrations to Bungay's steady state microdialysis model[84], for t_i and σ from a curve fit to Taylor-Aris dispersion[77,97], and for k ϕ and λ from user's input. The best of these starting points is augmented with small number of points (e.g. 6 for 5DARS) in the local space and a very large number of points (e.g. 32,000) over the entire parameter space. The $n + 1$ points with the lowest RSS are taken as the initial simplex.

In the ARS process, in every iteration, the probability of the current simplex being in a local minimum is inferred through the relative standard deviation (RSD) of the objective function's values at the $n + 1$ vertices of the simplex. The lower the RSD is, the higher the probability that the simplex is in a global minimum. Then, a random search is performed to find a better minimum. The scope of this random search is a function of the RSD (see Supplementary Information 5.6.2.3).

The ARS procedure is “adaptive” as it continually uses new information (RSD of RSS of the current simplex) as input for its next action. Complete, annotated computer code is shown in Supplementary Information 5.6.2.1, the minimum-searching algorithm is outlined in Supplementary Information 5.6.2.2, and ARS formulation is explained in Supplementary Information 5.6.2.3.

5.4.1.2 Second Fitting Pass with Curvature Weight

To further enhance sensitivity for k and ϕ, the two most biologically relevant fitting parameters, a two-pass fitting strategy was developed from 5DARS, which is aptly named 5DARS2P (complete, annotated computer code is shown in Supplementary Information 5.6.2.1). In 5DARS2P, the minimum found from a normal 5DARS algorithm is kept as starting point for the second pass. The second pass relies on the same fitting algorithm as the first past, however, only experimental data around the transient portion of the measurements are used for RSS calculation. The transient portion is defined as -4σ to $+6\sigma$ (acquired from first fitting pass) from the midpoint defined as the DA concentration that is midway between the lowest and highest concentrations. The transient portion is not symmetrical because the uptake rate only affects the curvature after midpoint and not before.

5.4.1.3 Sensitivity of the Curve Fit

The curve fit optimizes a large number of parameters (4-6) to a single response, thus careful consideration of the effect of correlated parameters is needed. It is important to determine that the transient response curve has a selective and sensitive response to each of the curve fit parameters. Simulating a transient microdialysis response to a retrodialysis of 150 nM DA solution, using probe parameters from Ngo 2020a at the volumetric flowrate of 0.600 μL/min, and t_i = -60 s, σ =

30 s, $C_{ECS\infty}$ = 10 nM, k = 0.2 s^{-1}, $\phi = 0.2$, and λ = 1.6, we investigated changes in the transient response curve from to changes in each of those parameters across a reasonable experimental range (t_i = -100 to 100 s, σ = 0 to 100 s, $C_{ECS\infty}$ = 0 to 100 nM, k = 10^{-4} to 10^3 s^{-1}, $\phi = 0.01$ to 1, and λ = 1 to 3). Figure 5.4-1 shows the curve's responses to t_i, σ, $C_{ECS\infty}$, and k. The curve's horizontal displacement is governed by t_i (Figure 5.4-1A), its horizontal spread is governed by σ (Figure 5.4-1B), its vertical displacement is governed by $C_{ECS\infty}$ (Figure 5.4-1C), and its vertical spread by k (Figure 5.4-1D). While the curve's responses to t_i, σ, and $C_{ECS\infty}$ are approximately linear, the curve's response to k is roughly linear to log k. We concluded that the curve fit is sensitive to t_i, σ, $C_{ECS\infty}$, and k and that correlation among the parameters is low. As described below, 4DARS fitting of these parameters to simulated noisy data produces consistent and accurate results with narrow confidence intervals (C.I.) (Figure 5.4-4A).

The curve's response to ϕ and λ (Supplementary Information Figure 5.6-2) is similar to that of k thus these three fitting parameters are correlated. However, while they are correlated, useful information about k, ϕ, and λ, thus useful biological information, can be obtained from the curve fit. Shown in Figure 5.4-2 is the RSS surface of an *in vivo* experimental data set, obtained by varying two (k and ϕ, Figure 5.4-2A) or three (k, ϕ and λ, Figure 5.4-2B) parameters across the same range as above, while keeping the others constant. The RSS response to k and ϕ (Figure 5.4-2A) has a very narrow and well-defined "valley" that contain RSS optima, which is centered around $k \approx 0.18$ and $\phi \approx 0.20$. A robust fitting of both k and ϕ to experimental or simulated data (5DARS or 5DARS), produces accurate quantitative estimates with a small confidence interval (Table 5.4-1). An uptake rate constant and tissue porosity estimation with 10-20% RSD is on par with contemporary measurements using established methods[167,212].

The RSS response to k, ϕ and λ (Figure 5.4-2B) is a 3D sheet with a noisy RSS surface, however, it still has a well-defined segment that contain RSS optima, which is centered around $k \approx 0.2$, $\phi \approx 0.2$ and $\lambda = 1.6$. While the RSS surface is still relatively sensitive to k and ϕ, the RSS surface is not sensitive to λ, resulting a large confidence interval when 6DARS is attempted. Fortunately, it has been demonstrated by many research groups, using different techniques, that tortuosity for a certain species, measured for a certain brain region, with respective to a certain molecule is consistent[165,167,184,213-216]. Therefore, while it is possible to estimate ECS tortuosity λ using transient microdialysis, we do not recommend it if such a measurement already exists in the literature.

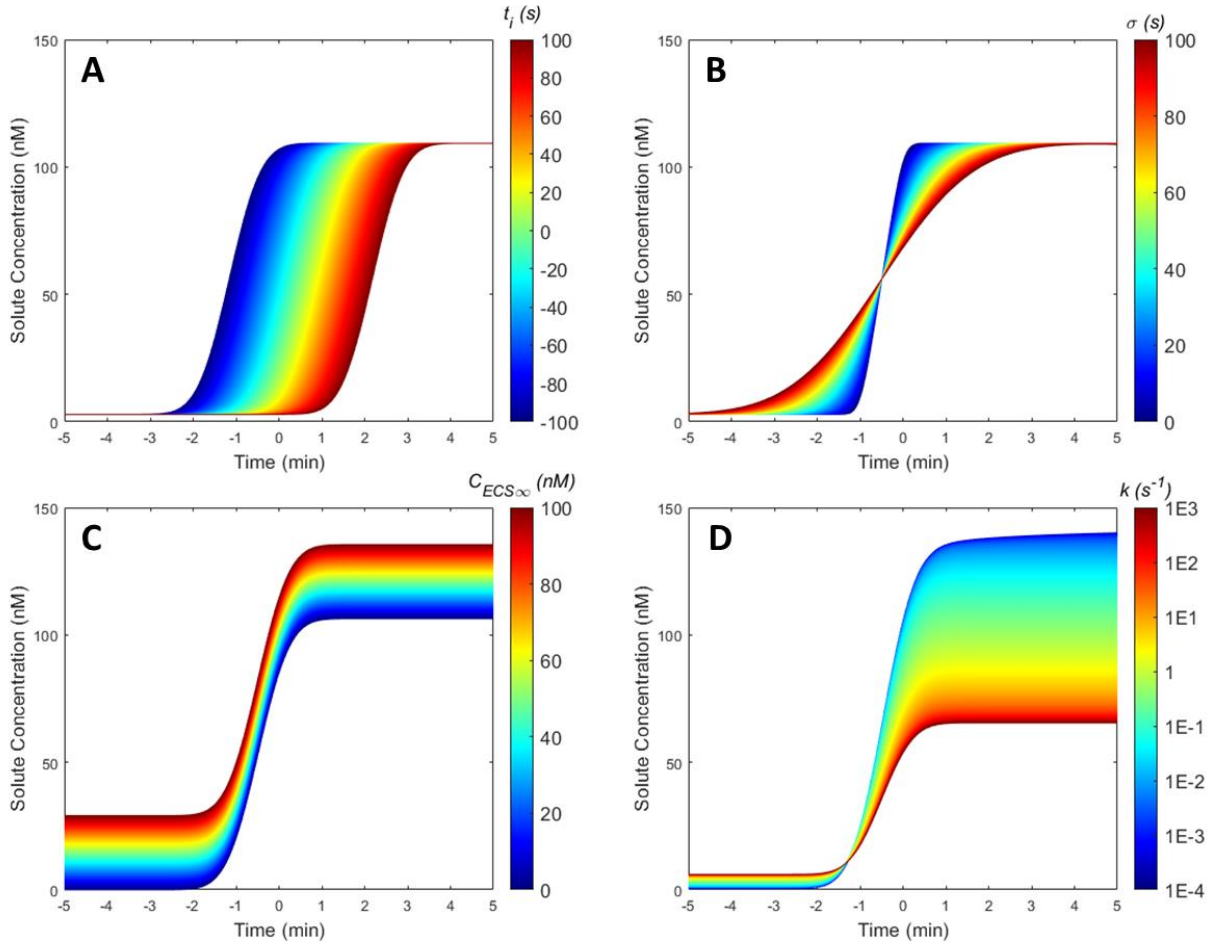

Figure 5.4-1. Simulated microdialysis transient response to a 150 nM DA retrodialysis. Shown are the responses when each of the four parameter (A) t_i (B) σ (C) $C_{ECS\infty}$ and (D) k is varied while the others stay constant. A 60 s LC sampling time was simulated, using a theoretical 1 s time-interleaved time resolution.

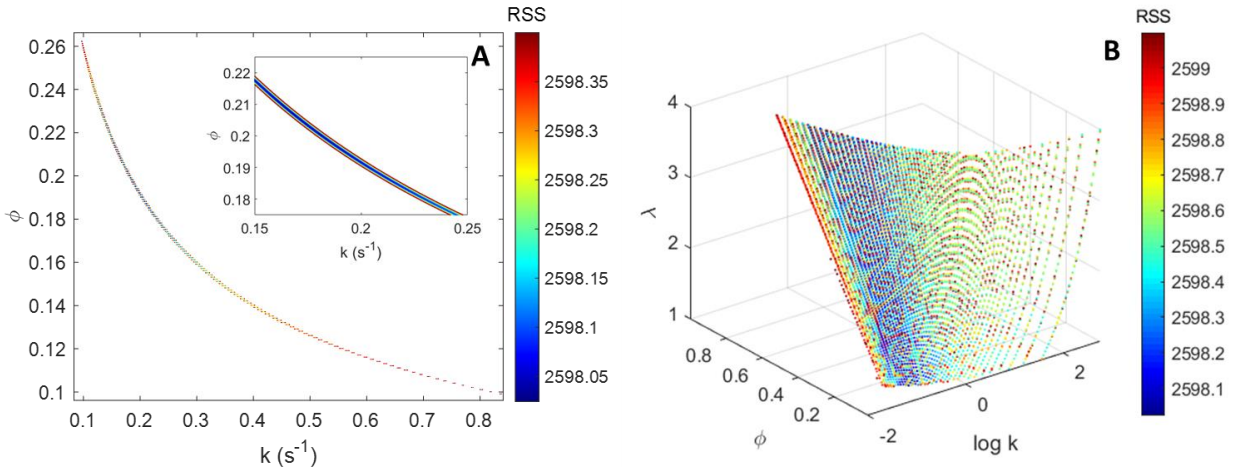

Figure 5.4-2. Residual Sum of Square Surfaces (RSS), calculating by varying the two (A) two, inset: RSS centered about minimum, or three (B) correlated parameters to in vivo experimental data.

The global minimum (blue) consists of a small, defined region with a narrow range of *k* and ϕ centered at $k \approx 0.18$ s^{-1} and $\phi \approx 0.20$, and a larger range of λ centered at $\lambda \approx 1.6$. The white space regions consist of RSS above the maximum plotted.

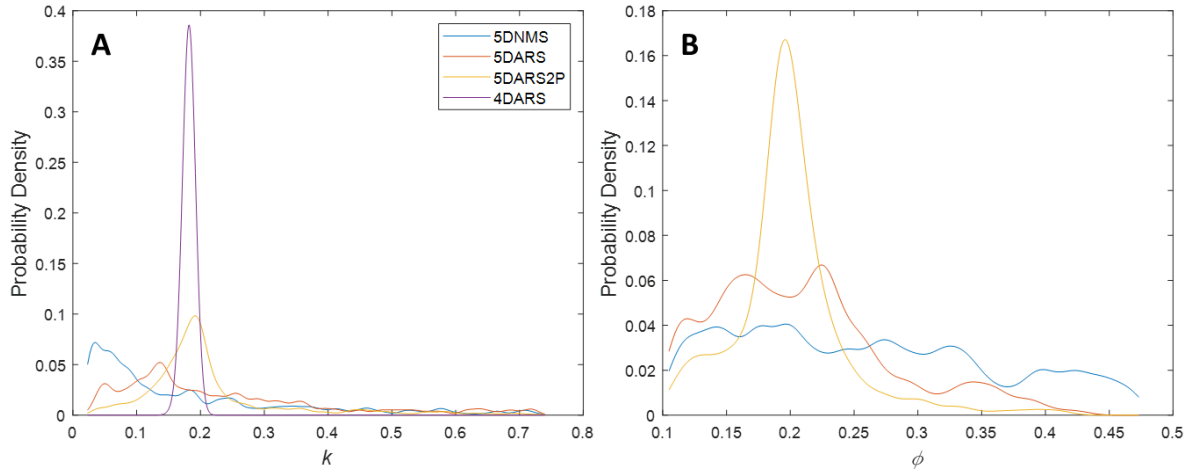

Figure 5.4-3. Comparison between distribution of *k* (A) and ϕ (B) from 1000 repeats of 5DNMS (blue), 5DARS (red), 5DARS2P (orange) and 4DARS (purple).

The probability density curve is calculated using Kernel Density Estimator with a bandwidth of 0.01 (s^{-1} for *k*, unitless for ϕ). Out of 1000 repeats, the 5DNMS, 5DARS, 5DARS2P, 4DARS methods find the best fit parameters 61.6%, 45.8%, 80.9% and 100% of the time, respectively.

5.4.1.4 Confidence Interval

The ARS fitting method is non-deterministic. Repeating the same fit to the same set of data multiple times using completely identical conditions (i.e. running an identical MATLAB script repeatedly) does not yield identical results. The NMS fitting method is deterministic; however, it is chaotic. Repeating the same fit to the same set of data using identical conditions yields identical results, however, if the starting conditions are changed then the results change in an unpredictable (but repeatable) manner. As demonstrated above, however, the global optimum is in a valley that is well defined (Figure 5.4-2). For a robust fit, even if the fit is non-deterministic, results from repeated fitting should be representative of the optimum on average. Figure 5.4-3 shows the distribution of k and ϕ from 1000 repeats of 5DNMS (blue), 5DARS (red), 5DARS2P (orange) and 4DARS (purple) to a set of *in vivo* experimental data. Distribution of the other fitting parameters is shown in Supplementary Information Figure 5.6-3. The probability density distribution curve is calculated using an alternative method to a histogram, the Kernel Density Estimator[217], to obtain a smooth and continuous probability density distribution, using a bandwidth of 0.01 (s^{-1} for k, unitless for ϕ). Out of 1000 repeats, the 5DNMS converged (successfully found best-fit parameters) 65.2% of the time, while 5DARS converged 45.8% of the time, 5DARS2P converged 80.9% of the time, and 4DARS always converged. In term of distribution quality, the curve fit improves in the order 5DNMS, 5DARS, 5DARS2P, and 4DARS. Particularly for the distribution of k and ϕ as shown in Figure 5.4-3, the two methods 5DNMS and 5DARS produce a broad distribution, while 5DARS2P and 4DARS (fixed ϕ) yield narrow distributions with a bell curve resembling a Gaussian distribution. Therefore, 5DARS2P and 4DARS are the best curve fit methods for 5D and 4D fits, respectively. The 5DNMS and 5DARS methods should not be used because of their poorly distributed fitting parameters. 5DARS2P

results in the range k of 0.02 to 0.75 (s^{-1}) and ϕ of 0.11 to 0.48 (unitless), while 4DARS gives a narrow range of k of 0.015 to 0.22 (s^{-1}) with a fixed ϕ value of 0.20 (unitless). The 4DARS produces a very sharp and narrow distribution for k, while the 5DARS2P produces a broader distribution peak for both k and ϕ. This is because the transient response curve is sensitive to k when ϕ is fixed, and k and ϕ are correlated, as discussed in the previous section. Both methods produce good parameter distribution for t_i, σ, and $C_{ECS\infty}$ (Figure 5.6-3). Repeating the fit 1000 times therefore provides a population of each fitted parameter representative of the global minima, from which a confidence interval can be calculated.

As shown in Figure 5.4-3 and Supplementary Information Figure 5.6-3, the probability density distribution curves of the fitted parameters resemble Gaussian distribution. The width of this distribution of 1000 repeats (or any large number of repeats) can be used to estimate the error of the curve fit[218,219]. Here, we use the 95% confidence intervals (95% C.I.) of the fitted parameter from the repeats to estimate the 95% C.I. of the curve fit from the repeats. We compared this estimation with the commonly used bootstrap confidence interval[220-222] (Supplementary Information 5.6.1.2 to 5.6.1.4). We found that both methods produce statistically identical 95% C.I. (F-test) for all five fitted parameters on all four curve fit methods (Table 5.6-1).

5.4.1.5 Fit Robustness

We simulated 16 data sets to test the robustness of the four fitting methods against changes in uptake rate constant, microdialysis time resolution, noise in the data, and membrane molecular weight cutoff (MWCO). The testing data are simulated with either a low ($k = 10^{-2}$ s^{-1}) or high (k = 10 s^{-1}) uptake rate constant, low (15 s) or high (1 s) sampling frequency (time-interleaved[182,202] from 60 s and 4 s microdialysis sampling interval, respectively), low (normally distributed, relative RSD = 1%) or high (normally distributed, relative RSD = 10%) noise in dialysate DA , and low

(13 kDA) or high (18 kDA) MWCO. The condition in uptake rate constant approximates the range for DA in rat nucleus accumbens that we and others[102,189] measured. The two MWCO chosen are often used in microdialysis experiments, higher MWCO results in better solute recovery[223] (higher extraction fraction for the same solute but at the same time more solutes). The sampling frequencies are based on work presented here and in the literature[80,81], and noise represents a wide range of uncertainties for such an experiment. The curve fits were repeated 100 times. Shown in Figure 5.4-4A is a comparison of relative errors in the fitting parameter k for the two selected curve fit methods (4DARS and 5DARS2P). Figure 5.4-4B has relative error in the fitting parameter ϕ from 5DARS (ϕ is fixed for 4DARS). Results for the three fitting parameters t_i, σ, and $C_{ECS\infty}$ are shown in Figure 5.6-4.

Across all simulated conditions, there is no qualitative advantage between 5DARS2P and 4DARS with respect to fitting of t_i, σ, and $C_{ECS\infty}$ (Figure 5.6-4). For fitting of k, 4DARS is the clear best method for k (relative error less than 36% for all data sets, 95% C.I. smaller than 6% for all data set) because ϕ, which is correlated with k, is not included in the fit. Fitting results for t_i, σ, and $C_{ECS\infty}$ are usually consistent and accurate (typically less than ±5% error) and have narrow confidence intervals (typically smaller than ±1%). Fitting results for k and ϕ are less accurate when fitting conditions are not favorable (e.g. high uptake rate of 10 s^{-1} or noise with relative standard deviation of 10%), typically underestimating k by 50-60% (with one edge case, set 10 is overestimated 3.5 times the actual value), and overestimate ϕ by 40-50%. As shown in Supplementary Information Figure 5.6-5 and Figure 5.6-6, even with a very high uptake rate constant k of 10^3 s^{-1}, k can be estimated with less than 70% relative error, and ϕ can be estimated with less than 90% relative error. When k is overestimated, ϕ is underestimated, and vice versa. At ideal conditions (low uptake rate and low noise, e.g. sets 9 and 11), all four curve fit methods

produce accurate and precise results. There are edge cases (e.g. set 10), where *k* estimation from 5DARS is inaccurate. We have not been able to identify the source of inaccuracy.

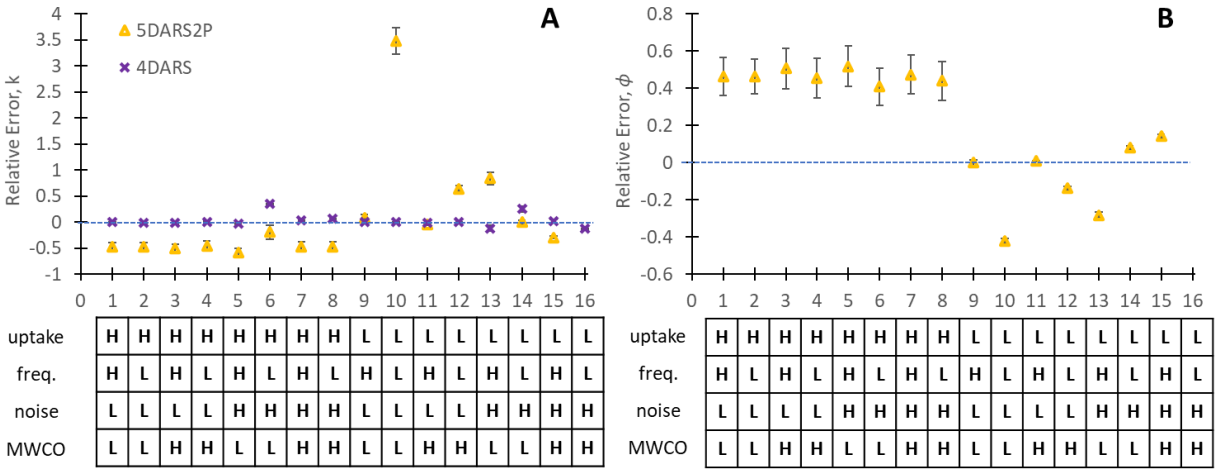

Figure 5.4-4. Comparison between relative error of (A) k and (B) ϕ from 100 repeats of 5DARS2P (orange) and 4DARS (purple, fixed $\phi = 0.2$) to 16 simulated data sets.

The tables denote experimental conditions tested: Uptake rate constant *k* (s^{-1}) Low = 10^{-2} High = 1; Microdialysis sampling frequency (s) Low = 15; High = 1; Noise σ (Normally distributed) Low = 1%; High = 10%; MWCO (kDa) Low = 13; High = 18. 5DARS2P produces no successful fit for set 16.

5.4.2 Curve Fit of In Vivo Experimental Results

5.4.2.1 Comparison between Quantitative Transient Microdialysis and No Net Flux

We used 4DARS fitting of the CQM model[202] to obtain quantitative estimates of t_i, σ, $C_{ECS\infty}$, and *k* from transient responses measured experimentally, *in vivo* online, on an awake and freely moving animal using 45 s microdialysis determinations of dopamine in rat nucleus accumbens. Tissue porosity ϕ (0.2) and tortuosity λ (1.6) were fixed, using literature values[61] for the same animal and brain region. These results are compared to quantitative estimates from the

no net flux method, which primarily estimates steady-state extraction fraction E_d, $C_{ECS\infty}$ [12] and is seldomly used to estimate k [185]. From the CQM model[202], steady state extraction fractions $E_{d,t\to\infty}$ can be estimated by calculating the time-dependent extraction fraction at large time:

$$E_d(t) = 1 - \exp\left(-\frac{S_o P(\mathrm{t})}{Q}\right)$$

Equation 5.4-1. Time-dependent extraction fraction $E_d(t)$

where Q (m^3/s) is the flow rate of the dialysate, S_o (m^2) is the outer surface area of the membrane, and $P(\mathrm{t})$ (m/s) is the time-dependent overall permeability defined in the CQM model[202]. These quantities ($E_d(t)$ and $P(\mathrm{t})$) are intermediate steps in the CQM model in predicting $C_{det}(t)$ from known and fitted parameters.

The transient responses were induced by 30-min long retrodialysis of 50, 100, or 150 nM DA. The entire response curve was used for data fitting, which also includes approximately 30-min of basal measurement before DA retrodialysis. To improve MATLAB convolution calculation speed, the time axis of each response was offset so that the midpoint as defined above is near zero. The results were then compared with the traditional quantitative technique, no net flux[54,183], in which linear regression is performed on 45 min of basal data before the first transient and the steady-state values from each transient response. Identifying the steady state is non-trivial, as Taylor-Aris dispersion and solute uptake in the brain broadens the curve, and the *in vivo* measurements are inherently noisy. The steady state of a transient response was approximated to begin when the transient responses reached 95% of the average of the 30 highest measured concentrations. Notably, there is a periodic oscillation in DA concentration at this steady state. The periods of this fluctuation are different between the three retrodialysis runs. Additionally, this fluctuation is not present in *in vitro* calibration nor in *in vivo* measurements in this or our prior

work[97,98]. There is also no literature precedent of Fast Microdialysis measurement of steady-state retrodialyzed responses. We hypothesize that this oscillation could have a biological origin[69] that we have been not able to identify.

Shown in Figure 5.4-5A is the No-Net-Flux linear regression from basal concentrations (n = 55) and retrodialysis of (nM DA) 50 (n = 38), 100 (n = 36), and 150 nM (n = 32), where the slope of the regression is the extraction fraction E_d (0.245 ± 0.007), and the X-intercept of the regression is the quantitative estimate for $C_{ECS\infty}$ (17±3 nM). This experiment was performed in 3 hours using 45 s microdialysis. For a traditional 10-min microdialysis experiment, a full day of experimental work per extraction fraction determination is common[102,185]. In contrast, each of the hour-long transients at 45 s time resolution can be used for 4DARS fitting of the CQM model to the data. Each transient fitting gives t_i, σ, $C_{ECS\infty}$, and k, as well as $E_{d,t\to\infty}$. Values of $C_{ECS\infty}$ obtained from the curve fits are 18.48±0.03, 15.8±0.3, 14.26±0.08 nM for the 50, 100, and 150 nM retrodialysis, respectively. They, as well as $C_{ECS\infty}$ averaged from all three fits (AVG±SEM) (16.2±1.2 nM), are statistically identical (t-test) to ones obtained from the No-Net-Flux regression (17±3 nM). The extraction fractions, E_d, determined from the three transients were 0.227±0.004, 0.256±0.005, 0.256±0.005 for 50, 100, and 150 nM retrodialysis, respectively, 0.246±0.01 averaged from all three). These are comparable with the No-Net-Flux regression (0.245 ± 0.007). Finally, the uptake rate constant k (0.52±0.00, 1.15±0.00 and 1.15±0.00 s^{-1} for 50, 100, and 150 nM retrodialysis, respectively, 0.94±0.21 averaged from all three) is comparable with previous measurements (1.9-2.9 s^{-1}) made in the same brain region (nucleus accumbens) of rat using microdialysis[185], but at a significant experimental time cost (2 days per k determination). The analytical instrument parameters t_i and σ cannot be obtained from a No-Net-Flux experiment and are not traditionally determined in a microdialysis experiment. However, they are of immense

usefulness to behavior studies. The value of t_i can be used to relate changes in the measured DA concentration to specific behavior recorded as a video[98]. The value of σ dictates the response time of a probe and the time resolution of the method. It is important to note that microdialysis in operant chambers is carried out with a swivel in the microdialysis flow stream. This is inimical to time resolution. We earlier reported on a rotating operant chamber which allows for video observation of behavior and fast microdialysis[98]. In short, quantitative analysis using CQM provides more information than the traditional quantitative technique, but at a fraction of the experimental time cost.

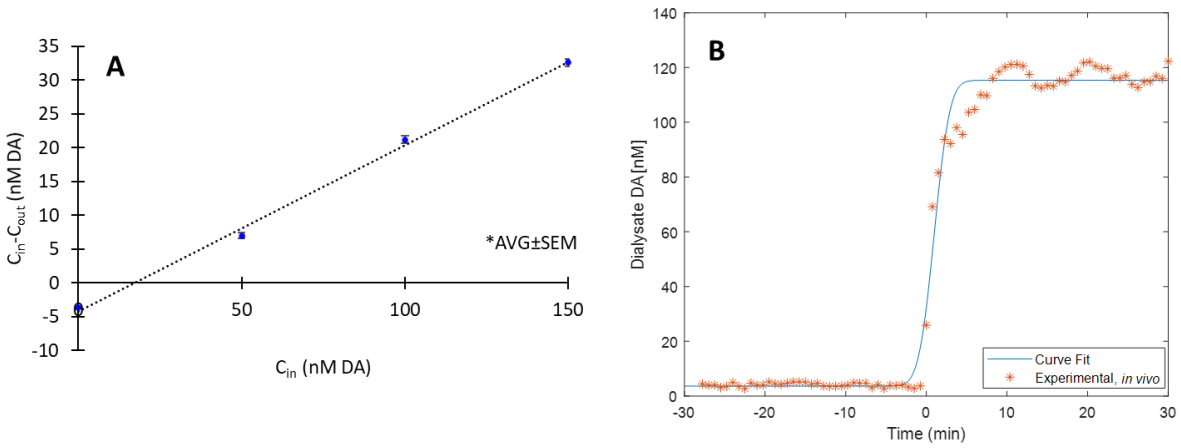

Figure 5.4-5. Comparison between two quantitative microdialysis techniques: (A) no net flux linear regression from basal concentrations (n = 55) and 50 (n = 38), 100 (n = 36), and 150 nM (n = 32) 30-min retrodialysis of DA, line of best fit (black) is generated from slope and intercept from the regression; and (B) 4DARS curve fit of 150 nM 30-min retrodialysis of DA, Blue: curve fit prediction, Orange: experimental measurements.

5.4.2.2 *In Vivo* Quantitative Transient Microdialysis at 15 S Effective Time Resolution

We obtained quantitative estimates of t_i, σ, $C_{ECS\infty}$, k and ϕ using 5DARS fitting of the CQM model to transient responses measured experimentally, *in vivo* online, on an awake and freely moving animal using microdialysis at 15 s effective resolution. Tissue tortuosity λ (1.6) was fixed,

using a literature value[61]. Additionally, the tissue porosity ϕ (0.2) was fixed for a 4DARS fitting. Eight transient responses to 5-min retrodialysis of 150 nM DA were measured using 60 s microdialysis in conjunction with time interleaved sampling (Supplementary Information 5.6.1.1) to determine duplicate responses with 15 s time resolution. As previously done, the time axis of the combined response was offset so that the middle C_{det} data point of the response near zero. Shown in Figure 5.4-6 is a comparison between the predicted curve calculated with 5DARS and the *in vivo* experimental data.

The fitted parameters from both the 4DARS and 5DARS2P curve fits are shown in Table 5.6-1. The curve fits estimated comparable even if statistically different mean (t-test) and 95% C.I. (F-test) for the fitting parameters t_i, σ, $C_{ECS\infty}$ and k. We noted that both $C_{ECS\infty}$ and k measured on this single animal were lower than results typically measured by our own method and published results, but they are in the same order of magnitude. These results are not out of the ordinary, as CECS∞ and k estimates in the literature have differed by one (k)[102,189] to two ($C_{ECS\infty}$)[49,52,90] orders of magnitudes. Lastly, tissue porosity ϕ determined by the curve fit (0.20±0.03) is comparable to literature[166,184,224]. All of these parameters had very narrow 95% C.I. (±1% or less for t_i, σ, $C_{ECS\infty}$ and k; ±15% for ϕ) because the fits were repeated 1000 times and therefore the uncertainty of the mean is small. These initial results in this work showed that transient microdialysis analyzed with CQM can greatly expand the quantitative capability of microdialysis techniques toward measurement regimes (e.g. tissue morphology) that are previously not accessible while significantly reduces experimental time cost at the same time.

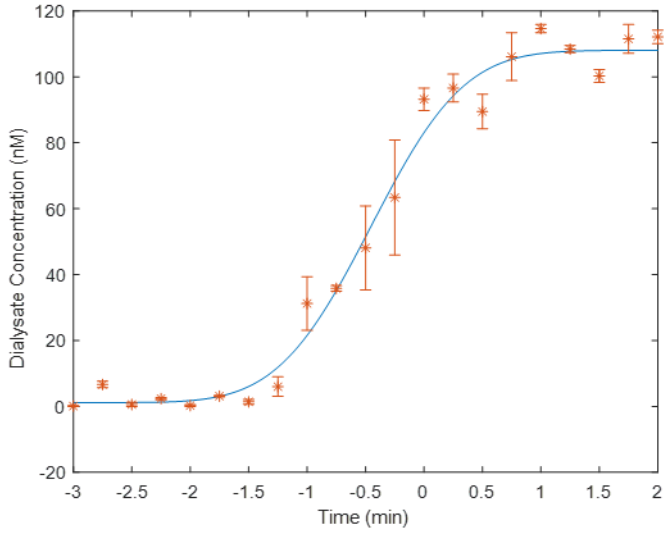

Figure 5.4-6. 5DARS curve fit of transient response to retrodialysis of 150 nM DA at 15 s effective time resolution.

Orange: in vivo experimental, Blue: curve fit.

Table 5.4-1. Comparison between 4DARS and 5DARS curve fits (1000 repeats) of in vivo experimental data at 15 s effective time resolution.

	4DARS	5DARS2P
Transport time t_i (s)	-57.93±0.01	-57.95±0.01
Dispersion standard deviations (s)	32.97±0.01	32.97±0.00
Tissue concentration $C_{ECS\infty}$ (nM)	3.95±0.04	3.92±0.01
Uptake rate constant, k (s^{-1})	0.18±0.00	0.19±0.00
Tissue porosity ϕ	0.2 (fixed)	0.20±0.03

5.4.3 Limitations of the Method

The CQM model relies on a set of assumptions and thus poses limitations that we discussed in the accompanying paper[202] and summarized here. The trauma layer is not considered thus extraction fraction is overestimated and solute concentration in the ECS is underestimated because extraction fraction and relative recovery are assumed to be equal. First-order uptake rate constant is assumed instead of Michaelis-Menten kinetics, thus is only valid for solute with high K_m -

compared to solute concentration. The model assumed one-dimensional radial mass transport and as a result, calculations are inaccurate[202] for short probe (1.7 mm or less), and for species with very low uptake rate (10^{-2} s or less) at long time (600 s or more). Lastly, MATLAB numerical precision limits the range of uptake rate calculation to 10^{-6} to 10^{4} s^{-1} for typical rates of diffusion (order of 10^{-10} m^2/s). In this work, the CQM experiment and curve fit methods made additional assumptions and therefore have additional limitations that we must recognize.

5.4.3.1 Method Validation

The present work was performed on a limited number of animals (n = 2), measuring a single neurotransmitter (DA), in a brain region specially chosen to be favorable to first-order uptake rate constant assumption (rat nucleus accumbens). Further experimental work, including validation of quantitative estimates by a separate technique (i.e. sensor), is needed to validate our findings. However, we note that these findings are consistent with existing literature; and the nature of this work focuses on developing and demonstrating the technical feasibility of a comprehensive mathematical, experimental and data analysis framework, rather than answering a biological question.

5.4.3.2 Parameter Correlation

We inferred from simulations that the curve fit is sensitive to t_i, σ, $C_{ECS\infty}$ and k, and k is correlated to ϕ and λ. We inferred from curve fits of synthesized data over a range of experimental conditions that the curve fit is robust. However, these are qualitative assessments and the curve fit can benefit from a quantitative analysis of parameter orthogonality, correlation, and insensitivity[225-227].

5.4.3.3 Time-Interleaved Sampling

We used a time-interleaving process to increase the time resolution of our transient response measurement. The success of this process depends on numerous (eight) transient responses from a retrodialysis of a neuroactive solute (dopamine) on an animal being identical. While we successfully reconstructed a single transient and elucidated useful biological information, the assumption may not always hold. Microdialysis measurements in the seconds timescale[80] is feasible and will significantly improve transient response measurements.

5.4.3.4 Parameter Space of the Curve Fit

Even though the curve fit is robust and can determine k and ϕ with respectable accuracy and precision with k as high as 10^3 s^{-1} as discussed and shown in Supplementary Information Figure 5.6-5 and Figure 5.6-6, the same figures also show that even with a "perfect" theoretical probe (1 s dispersion standard deviation) and detector (0.1 s response time) with no noise, our method cannot determine with complete accuracy k and ϕ simultaneously when k is higher than 1 s^{-1}.

5.5 Conclusion

In this work, we have presented the last two out of the three components of Comprehensive Quantitative Microdialysis (CQM): (1) a mathematical model and associate assumptions to describe the transient response of the solute measured at detector as affected by phycological and analytical system factors, (2) an experimental method to determine a transient response in solute concentration at the detector resulting from a step change in solute concentration at the probe inlet at an effective time resolution of 15 s, online, *in vivo*, on an awake and freely moving animal; and

(3) a simplex optimization method for curve fitting a model to the transient response to determine biological (tissue porosity, solute ECS concentration and uptake rate) and instrument (transport time, dispersion) factors that affect the transient response. At the time resolution of 45 s, CQM can determine transport time, dispersion, solute concentration, uptake rate, and extraction fraction from a single transient response. Extraction fraction can also be calculated. At the time resolution of 15 s, CQM can additionally determine tissue porosity. The solute ECS concentration and calculated extraction fraction from the curve fit are comparable to results from a No-Net-Flux experiment performed at the same time on the same rat. The measured uptake rate constant is comparable to literature values measured with microdialysis in the same brain region. Transient response fitting with CQM not only provides more information than traditional, steady-state microdialysis, but in addition the experimental time is also significantly reduced. These results represent a step forward for the microdialysis technique as a whole. This present work also shows a much-needed improvement in microdialysis time resolution of dopamine, which is an on-going goal in our laboratory and many others[74,80,81,174,200,228,229].

5.6 Supplementary Information

5.6.1 Methods

5.6.1.1 The Influence of Time Interleaved Sampling and Loop Averaging

Time interleaved sampling is a technique used in signal processing[182], where multiple analog-to-digital converters are used in parallel to digitize signal from a single continuous analog source at the same data acquisition rate but the timing of each converter is offset from the others

by a fraction of the time corresponding to the data acquisition rate, thus increasing the time resolution. Time interleaved sampling microdialysis is an analogous technique that uses a single detector is to measure *N* repeats of the transient response. The repeats assumed to be identical. Olson and Justice (1993) [168] showed that hour-long transient repeats made across multiple rats on multiple days are repeatable and can be used create a single response.

It is important to account for the fact that the LC injector loop provides an average concentration for the volume captured by the loop when contemplating time interleaved sampling. Figure 5.6-1 shows a graphical representation of time interleaved sampling microdialysis where the effective time resolution is tripled for a chromatographic detector. For a chromatographic detector, the concentration determined for a sampling interval is the average of the concentrations sampled in the loop (Figure 5.6-1, top). As demonstrated, even though the time interleaved sampling process increased the effective time resolution and the discrete measurements now better represent the curvature of the transient response, the response measured by a discrete detector is different than that measured by a continuous detector. This is because the concentration gradient in a loop is averaged to a single data point. The smaller the sampling loop (thus, the sampling time), the closer to the continuous measurement the discreet measurement is.

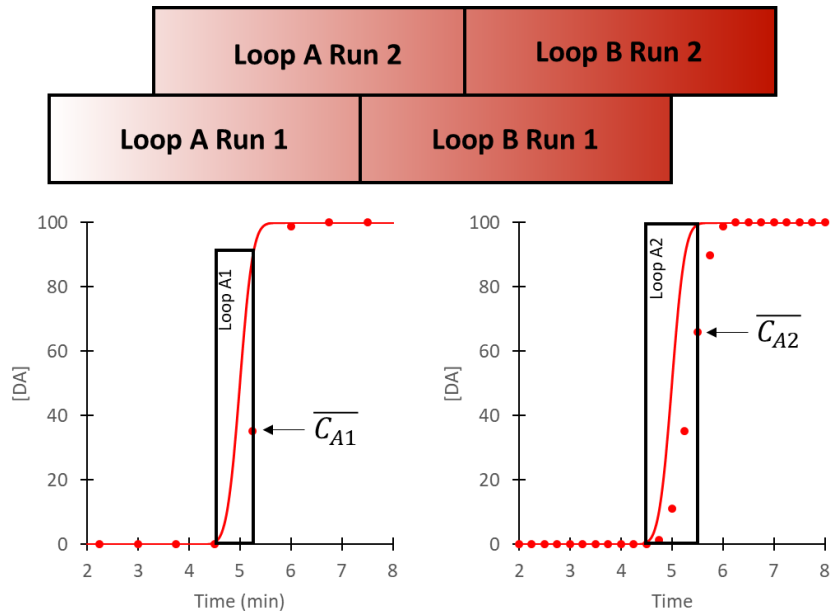

Figure 5.6-1. A graphical illustration of time interleaved sampling microdialysis which a chromatographic detector where the effective time resolution was tripled from 45 s (bottom, left) to 15 s (bottom, right). The boxes on top represent the continuous concentration gradient in the sampling loops. The solid line represents a transient response measured by a continuous detector, and the dots by a chromatographic detector. The average concentration measured from a loop is assigned to the experimental time at the injection time (end of loop).

5.6.1.2 Bootstrap Confidence Interval

The bootstrap approach[220,222,230] can be used to estimate the uncertainty of the fitted parameters. We present this uncertainty as the 95% confidence interval (95% C.I) of the fitted parameters. To *sample* a distribution of a fitting parameter, the fitting routine is repeated *N* times to acquire *N samples* of the fitting parameter. The fitting routine uses completely identical conditions, however because it is non-deterministic, each repeat produces a different result for each fitting parameter. The *N samples* are *resampled with replacement M* times. The bootstrap principle postulates that the distribution of the *M resamples* approximates the distribution of the *N samples*, and for a chosen statistic (e.g. mean), the statistic computed from *M resamples*

approximates statistic computed from *N samples*. While repeating the fitting algorithm to obtain a large number of *N* for a well-sampled distribution is hard, resampling to create a well-sampled distribution is trivial, and *M* can be many times larger than *N*. The procedure is then repeated for the remaining fitting parameters. In practice, the fitting routine is repeated 100 to 1000 times for obtain fitted parameter samples, then the results are resampled 10,000 times for bootstrap confidence interval.

5.6.1.3 Empirical Bootstrap

For each parameter, the error δ between a sampled mean $\bar{x}$ and true mean μ is:

$$\delta = \bar{x} - \mu$$

Equation 5.6-1. Error of the sampled mean

and the error δ^* between the sampled mean $\bar{x}$ and a resampled mean $\overline{x^*}$ is:

$$\delta^* = \overline{x^*} - \bar{x}$$

Equation 5.6-2. Error of the resampled mean

The bootstrap principle offers that the distribution of δ^* approximates the distribution of δ. Since the resample count *M* is a very large number, the distribution of δ^* can be found by numerical ranking, then the 95% C.I. of $\overline{x^*}$ is $\left[\overline{x^*} - \delta^*_{0.025}, \overline{x^*} - \delta^*_{0.975}\right]$, which approximates the 95% C.I. of $\bar{x}$:

$$\left[\overline{x^*} - \delta^*_{0.025}, \overline{x^*} - \delta^*_{0.975}\right] \approx \left[\bar{x} - \delta_{0.025}, \bar{x} - \delta_{0.975}\right]$$

Equation 5.6-3. Empirical 95% C.I.

5.6.1.4 Studentized Bootstrap

The symmetric *t-statistic is* calculated for each resample:

$$T^* = \frac{\sqrt{n}\left|\bar{X}^* - \bar{X}\right|}{\sigma^*}$$

Equation 5.6-4. Bootstrapped symmetric t-statistic

Where T^* is the bootstrapped t-statistic of a resample, $\bar{X}^*$ is the mean of the resample, $\bar{X}$ is the mean of the sample, σ^* is the standard deviation of the resample, and *n* is the size of the resample and of the sample. The *1-*α confidence interval for true mean μ is $\left(\bar{X} \pm T^*_{(c)}\frac{\sigma}{\sqrt{n}}\right)$. Where σ is the standard deviation of the sample, $T^*_{(c)}$ 1-α quantile of the distribution of T^*, which approximates the 1-α quantile of the distribution of *T*.

5.6.2 Computer Codes

5.6.2.1 Ngo2020_ARS2P Curve Fit

```
tic
close all
clear
format shortG
warning('off','MATLAB:integral:NonFiniteValue')
load('invivo_6D_data'); %load data
                        %x contains time in min
                        %y contains nM [DA]
%System parameters
time_resolution = 1; %s, simulation time resolution
Q = 0.6; %uL/min, volumetric flow rate
Q = Q*1e-9/60; %m^3/s, volumetric flowrate
ts = 60; %s, LC sampling time
Cin = 150; %retrodialyzed concentration
D = 6.0e-10; %m^2/s free solution diffusion coefficient
lambda = 1.6; %ECS tortuosity
Dm = 1.2734e-10; %m^2/s, membrane diffusion coefficient
phi_m = 1; %nominal membrane porosity
L = 4e-3; %m, membrane length
ro = 140e-6; %m, membrane outer radius
ri = 100e-6; %m, membrane inner radius
```

```
%Fitting parameters
start_ti = -60; %s, starting value for ti, offset raw data to as close to 0
as possible
start_sigma = 30; %s, starting value for Taylor Aris sigma
start_kext = 0.2; %1/s, starting value for reuptake rate constant
start_Cinf = 5; %nM Da, starting value for Cinf
start_phi = 0.2; %starting value for phi
no_sample = 1000; %number of fittings, to calculate fitting statistic
                %must be greater than or equal to 20 for bootstrap confident
interval
bound_ti = 200*[-1 1]; %bounds for ti
bound_sigma = 200*[1e-6 1]; %bounds for Taylor Aris sigma
bound_kext = [1e-4 5e3]; %bounds for uptake rate constant
bound_Cinf = [0 25]; %bounds for Cinf
bound_phi = [0.1 0.5]; %bounds for phi
termination_condition = 1e-8; %test criterium, std/avg last n tests, where n
is number of fit variables
second_termination_condition = 1e-6; %test criterium, std/avg last n tests,
where n is number of fit variables
max_iter = 5000; %maximum number of iterations
ARS_autostart = 0; %# of run before starting ARS
alpha = 2; %ARS variable for size, cap no_extend to alpha*200
beta = 0.2; %ARS variable for extent, must be < 1, cap size_extend to
beta*parameter value
RSS_threshold = 0.05; %threshold from global minimum to count as a result,
relative
weight_type = 1; %1. full data weight 2. curvature-centric
%Dependent variables calculation
start_point = [start_ti start_sigma start_kext start_Cinf start_phi]; %create
array of starting points
lower_bounds = [bound_ti(1) bound_sigma(1) bound_kext(1) bound_Cinf(1)
bound_phi(1)];
upper_bounds = [bound_ti(2) bound_sigma(2) bound_kext(2) bound_Cinf(2)
bound_phi(2)];
start_kext_log = log10(start_kext);
bound_kext_log = log10(bound_kext);
start_point_log = [start_ti start_sigma start_kext_log start_Cinf start_phi];
lower_bounds_log = [bound_ti(1) bound_sigma(1) bound_kext_log(1)
bound_Cinf(1) bound_phi(1)];
upper_bounds_log = [bound_ti(2) bound_sigma(2) bound_kext_log(2)
bound_Cinf(2) bound_phi(2)];
no_var = length(lower_bounds); %number of fitting variables
no_global_random = 2^15; % number of global random starting points
%!!!The time axis must be symmetrical for convolution to work properly
%!!!The time axis must be centered at zero, otherwise code runs very slow
max_t = 1.5*60*max([abs(min(x)) max(x)]); %maximum boundary to time axis,
extended by 1.5
                                                %longer than time x to
accomodate calculations
max_t = round(max_t); %prevent a bug where t is not a whole number
t = linspace(-max_t,max_t,(2*max_t/time_resolution)+1); %time vector
%Create a step function
step = zeros([1,length(t)]); %preallotcate step function
for i = 1:length(t)
    if t(i) <=0
        step(i) = 0; %step is 0 at t <=0
    else
```

```
        step(i) = 1;%step is 1 at t > 0
    end
end
So = 2*pi*ro*L; %m^2, membrane surface area
Pmo = phi_m*Dm/(ro*log(ro/ri)); %m/s, membrane permeability, this log is
natural log
Cin = Cin.*step; %create step function for Cin
%Package the system parameters for local functions
system_par.t = t;
system_par.ts = ts;
system_par.Q = Q;
system_par.D = D;
system_par.lambda = lambda;
system_par.ro = ro;
system_par.So = So;
system_par.Pmo = Pmo;
system_par.Cin = Cin;
system_par.time_resolution = time_resolution;
system_par.x = x;
system_par.y = y;
%%
%Estimate starting value for ti, sigma and Cinf
%Calculate average and standard deviation of the mean of y
avgy = zeros([length(y(:,1)),1]);
semy = zeros([length(y(:,1)),1]);
for i = 1:length(y(:,1))
    if length(y(1,:)) > 1
        avgy(i) = mean(y(i,:));
        semy(i) = std(y(i,:))/sqrt(length(y(i,:)));
    else
        avgy(i) = mean(y(i));
        semy(i) = 0;
    end
end
%Approximate point of 50% rise
midy = 0.5*(max(avgy)-min(avgy));
%Bottom-50% weight array
weight_TA = zeros([length(y(:,1)),1]);
for i = 1:length(avgy)
    if avgy(i) < midy
        weight_TA(i) = 1;
        mid_index = i;
    end
end
%Approximate basal concentration
for i = 1:floor(length(avgy)/2)
    if avgy(mid_index - i) > 0.10*(max(avgy)-min(avgy))
        pct_10_index = mid_index - i;
    else
        pct_10_index = mid_index - i;
        break
    end
end
basaly = mean(avgy(1:pct_10_index ));
%Approximate plateau concentration
for i = 1:floor(length(avgy)/2)
    if avgy(mid_index + i) < 0.90*(max(avgy)-min(avgy))
```

```
        pct_90_index = mid_index + i;
    else
        pct_90_index = mid_index + i;
        break
    end
end
plateauy = mean(avgy(pct_90_index:length(avgy)));
%Estimate Ed and Cinf
p = polyfit([0;max(Cin)],[min(Cin)-basaly;max(Cin)-plateauy],1);
Cinf_NNF = -p(2)/p(1);
start_point(4) = Cinf_NNF;
%Reformart xs, ys and weights to one column
y_temp = zeros([length(x)*length(y(1,:)),1]);
x_temp = zeros([length(x)*length(y(1,:)),1]);
weighty_temp = zeros([length(x)*length(y(1,:)),1]);
for i = 1:length(x)
    for j = 1:length(y(1,:))
        y_temp(i+(j-1)*length(x)) = y(i,j);
        x_temp(i+(j-1)*length(x)) = x(i,1);
        weighty_temp(i+(j-1)*length(x)) = weight_TA(i,1);
    end
end
y_col = y_temp;
x_col = x_temp;
weighty_col = weighty_temp;
%Fitting for ti and sigma
syms y_fit x_fit a d ti s int_ta; %define symbolic variables
ts_TA = ts/60; %sampling interval, min
y_fit = d+(a/2)*(1+erf((x_fit-ti/60)/(sqrt(2)*(s/60)))); %Taylor-Aris
function
int_ta = (int(y_fit,x_fit-ts_TA,x_fit))/ts_TA; %integrated T-A
int_ta = char(int_ta); %convert sym to char vector
%curve fitting core
fo = fitoptions('Method','NonlinearLeastSquares',... %fit options
        'DiffMinChange', 1e-15,... % Minimum change in coefficients for
finite difference gradients
        'MaxIter', 1e6,... % Maximum number of iterations allowed for fit
        'MaxFunEvals', 1e6, ....%Maximum number of evaluations of model
allowed
        'TolFun', 1e-15,... %Termination tolerance on model value
        'TolX', 1e-15,... %Termination tolerance on coefficient values
        'Lower',[-inf,bound_ti(1),bound_sigma(1),-inf],...
        'Upper',[inf,bound_ti(2),bound_sigma(2),inf],...
        'StartPoint',[max(avgy) start_point(1) start_point(2) min(avgy)]);
ft = fittype(int_ta,'coefficients',{'a','ti','s','d'},...
    'independent',{'x_fit'},'dependent',{'y_fit'},'options',fo);  %execute
fit
[f,~,~] = fit(x_col,y_col,ft,'Weight',weighty_col); %extract fit data
fit_coeff = coeffvalues(f).'; %extract fit coeff
fit_confint = confint(f).'; %extract 95% confident interval
ti_TA_fit = fit_coeff(2); %second
sigma_TA_fit = fit_coeff(3); %second
start_point(1) = ti_TA_fit; %set new start point
start_point(2) = sigma_TA_fit; %set new start point
%Calculate curvature-centric weight
if weight_type == 1
    weight_curve = ones([length(y(:,1)),1]);
```

```
elseif weight_type == 2
    weight_curve = zeros([length(y(:,1)),1]);
    lower_4_sigma = ti_TA_fit - 4*sigma_TA_fit;
    upper_6_sigma = ti_TA_fit + 6*sigma_TA_fit;
    for i = 1:length(x)
        if x(i)*60 >= lower_4_sigma
            lower_4_sigma_index = i;
            break
        end
    end
    for i = 1:length(x)
        if x(i)*60 >= upper_6_sigma
            upper_6_sigma_index = i;
            break
        end
    end
    for i = 1:length(x)
        if lower_4_sigma_index  <= i && i <= upper_6_sigma_index
            weight_curve(i) = 1;
        end
    end
end
%%
%%
%Main loop
fit_result = zeros([no_sample,no_var+2]); %preallocate fit result array
test_matrix = zeros([no_sample,3]); %preallocate test result array
parfor k = 1:no_sample %cycle through each fitting
    warning('off','MATLAB:integral:NonFiniteValue')
    BPe = zeros([1,no_var]); %Preallocate array
    BPr = zeros([1,no_var]); %same as above ^
    BPcr = zeros([1,no_var]) ;%same as above ^
    BPcw = zeros([1,no_var]); %same as above ^
    %Call variables for parfor loop optimization
    lower_bounds_log; upper_bounds_log; lower_bounds; upper_bounds;
start_point_log;
    w = ones([1,length(x)]); %create weight array, unity
    %Simplex 1: Calculated Start Points
    RS1 = start_point;
    [~, ~, ~, ~, ~, ~, RS1(no_var+1)] = fNgo2019_RSS(RS1(1),RS1(2),RS1(3),...
                            RS1(4),RS1(5),w,system_par);
    %Simplex 2: Ramdon Start Points
    %Generate global random start points in log k
    RP = zeros([no_global_random,no_var]);
    SP = zeros([no_global_random,no_var+1]);
    for i = 1:no_global_random
        for j = 1:no_var
            RP(i,j) = lower_bounds_log(j)+rand*(upper_bounds_log(j)-
lower_bounds_log(j));
        end
    end
    %Return to linear scale
    RP(:,3) = 10.^RP(:,3);
    for i = 1:no_global_random
        warning('off','MATLAB:integral:NonFiniteValue')
        RP; %call vars to reduce parfor overhead
        [~, ~, ~, ~, ~, ~, RSS] = fNgo2019_RSS(RP(i,1),RP(i,2),RP(i,3),...
```

```
                                    RP(i,4),RP(i,5),w,system_par);
        SP(i,:) = [RP(i,1) RP(i,2) RP(i,3) RP(i,4) RP(i,5) RSS];
    end
    %Set random points where RSS couldn't be computed to high RSS
    for i = 1:no_global_random
        if SP(i,no_var+1) == 0
            SP(i,no_var+1) = 9e5;
        end
    end
    %Sort random points, select best random points, with lowest RSS
    SP = sortrows(SP,no_var+1);
    RS2 = SP(1,:);
    %Compare Simplex 1 and Simplex 2
    if RS1(no_var+1) < RS2(no_var+1)
        RS = RS1;
    else
        RS = RS2;
    end
    %Generate Starting Simplex
    BP = zeros([no_var+1,no_var+1]);
    for i = 1:no_var+1
        for j = 1:no_var
            BP(i,j) = RS(j)*(0.95 +0.1*rand);
        end
        [~, ~, ~, ~, ~, ~, BP(i,no_var+1)] =
fNgo2019_RSS(BP(i,1),BP(i,2),BP(i,3),...
                                    BP(i,4),BP(i,5),w,system_par);
    end
    test = 1; %initial convergent creteria
    run = 0; %initial interation count
    no_extend = 0; %initial Adaptive Random Sampling count
    disp(['Running fit for Fitting Sample ' num2str(k)])
    %First pass

%~~~~~~~~~~~~~~~~~~~~~~~~~~~~~~~~~~~~~~~~~~~~~~~~~~~~~~~~~~~~~~~~~~~~~~~~~~~~~~~
~~~~~
    %Simplex loop
    while test > termination_condition %checking convergent creterium
    run = run+1; %run count
    %Set points where RSS couldn't be computed to high RSS
    for i = 1:length(BP(:,1))
        if BP(i,no_var+1) == 0
            BP(i,no_var+1) = 9e5;
        end
    end
    %sort points
    BP = sortrows(BP,no_var+1);
    %Remove worst points, leave (no of dimension+1) for Simplex
    BP = BP(1:no_var+1,:);
    remainder = rem(run,100);
    %Generate Simplex optimization points
    %Calculate coordinates of extended_reflect point
    for i = 1:no_var
        BPe(i) = 3*mean(BP(1:no_var,i))-2*BP(no_var+1,i);
        if BPe(i) < lower_bounds(i) %check out of bound
            BPe(i) = lower_bounds(i) + abs(BPe(i)-lower_bounds(i));
        end
```

```
        if BPe(i) > upper_bounds(i) %check out of bound
            BPe(i) = upper_bounds(i) - abs(BPe(i)-upper_bounds(i));
        end
    end
    %Calculate coordiates of reflect point
    for i = 1:no_var
        BPr(i) = 2*mean(BP(1:no_var,i))-1*BP(no_var+1,i);
        if BPr(i) < lower_bounds(i) %check out of bound
            BPr(i) = lower_bounds(i)+ abs(BPr(i)-lower_bounds(i));
        end
        if BPr(i) > upper_bounds(i) %check out of bound
            BPr(i) = upper_bounds(i) - abs(BPr(i)-upper_bounds(i));
        end
    end
    %Calculate coordiates of contracted_reflect point
    for i = 1:no_var
        BPcr(i) = 1.5*mean(BP(1:no_var,i))-0.5*BP(no_var+1,i);
        if BPcr(i) < lower_bounds(i) %check out of bound
            BPcr(i) = lower_bounds(i) + abs(BPcr(i)-lower_bounds(i));
        end
        if BPcr(i) > upper_bounds(i) %check out of bound
            BPcr(i) = upper_bounds(i) - abs(BPcr(i)-upper_bounds(i));
        end
    end
    %Calculate coordiates of contracted_worst point
    for i = 1:no_var
        BPcw(i) = .5*mean(BP(1:no_var,i))+0.5*BP(no_var+1,i);
        if BPcw(i) < lower_bounds(i) %check out of bound
            BPcw(i) = lower_bounds(i) + abs(BPcw(i)-lower_bounds(i));
        end
        if BPcw(i) > upper_bounds(i) %check out of bound
            BPcw(i) = upper_bounds(i) - abs(BPcw(i)-upper_bounds(i));
        end
    end
    %Evaluate optimization points, then select new point based on evaluation
    [~, ~, ~, ~, ~, ~, BPe(no_var+1)] = fNgo2019_RSS(BPe(1),BPe(2),BPe(3),...
                                        BPe(4),BPe(5),w,system_par);
    [~, ~, ~, ~, ~, ~, BPr(no_var+1)] = fNgo2019_RSS(BPr(1),BPr(2),BPr(3),...
                                        BPr(4),BPr(5),w,system_par);
    if  BPe(no_var+1) < BP(1,no_var+1) && BPr(no_var+1) < BP(1,no_var+1)
        NP = BPe;
    elseif  BPr(no_var+1) <= BP(floor((no_var+1)/2),no_var+1)
        NP = BPr;
    elseif  BPr(no_var+1) <= BP(no_var,no_var+1) %compare new RRS to RSS of
worst point
        NP = BPcr;
    else
        NP = BPcw;
    end
    [~, ~, ~, ~, ~, ~, NP(no_var+1)] =
fNgo2019_RSS(NP(1),NP(2),NP(3),NP(4),...
                                       NP(5),w,system_par);
    if  run > ARS_autostart
        %KTN's Adaptive Random Sampling
        %Calculate a set of random points based on new point and weighted
randomization
        %no_extend increases with run and with decreasing simplex group size
```

```
        no_extend =
round(alpha*(log10(test)*(100/log10(termination_condition)) +
100*run/max_iter));
        %size_extend increases with number of no_extend
        size_extend = beta*no_extend/(alpha*200);
        NP_extend = zeros([no_extend,no_var+1]); %preallocate array
        NP_extend_temp = zeros([no_extend,no_var+1]); %preallocate array
        for i = 1:no_extend
            for j = 1:no_var
                NP_extend(i,j) = NP(j)*(1-size_extend+2*size_extend*rand);
                if NP_extend(i,j) < lower_bounds(j) %check out of bound
                    NP_extend(i,j) = lower_bounds(j) + abs(NP_extend(i,j)-
lower_bounds(j));
                elseif NP_extend(i,j) > upper_bounds(j) %check out of bound
                    NP_extend(i,j) = upper_bounds(j) - abs(NP_extend(i,j)-
upper_bounds(j));
                end
            end
        end
        for i = 1:no_extend
            warning('off','MATLAB:integral:NonFiniteValue')
            NP_extend;
            [~, ~, ~, ~, ~, ~, RSS] = ...
                fNgo2019_RSS(NP_extend(i,1),NP_extend(i,2),NP_extend(i,3),...
                NP_extend(i,4),NP_extend(i,5),w,system_par);
            NP_extend_temp(i,:) = [NP_extend(i,1) NP_extend(i,2)
NP_extend(i,3),...
                NP_extend(i,4) NP_extend(i,5) RSS]
        end
        NP_extend = NP_extend_temp;
        %Generate global random extend points in log k
        RP = zeros([no_extend,no_var]);
        for i = 1:no_extend
            for j = 1:no_var
                if i < no_var+2
                    RP(i,j) = start_point_log(j)*(0.999+0.002*rand);
                else
                RP(i,j) = lower_bounds_log(j)+rand*(upper_bounds_log(j)-
lower_bounds_log(j));
                end
            end
        end
        %Return to linear scale
        RP(:,3) = 10.^RP(:,3);
        %Evaluate RSS of random points
        SP = zeros([no_extend,no_var+1]);
        for i = 1:no_extend
            warning('off','MATLAB:integral:NonFiniteValue')
            RP; %call var to reduce parfor overhead
            [~, ~, ~, ~, ~, ~, RSS] =
fNgo2019_RSS(RP(i,1),RP(i,2),RP(i,3),...
                                    RP(i,4),RP(i,5),w,system_par);
            SP(i,:) = [RP(i,1) RP(i,2) RP(i,3) RP(i,4) RP(i,5) RSS];
        end
        NP_extend_full = [NP_extend;SP];
        BP = [BP(1:no_var,:);NP;NP_extend_full]; %add new point(s) to Simplex
    else
```

```
        BP = [BP(1:no_var,:);NP]; %add new point(s) to Simplex
    end
    %calculate test condition without new random points
    if run < max_iter
        test = std(BP(1:no_var,no_var+1))/mean(BP(1:no_var,no_var+1));
        test_matrix(k,:) = [k,run,test]; %store #run and convergence test
    else
        test = 0;
    end
    %replace worse point with new point, append random new points to best
points array
    end %end current Simplex loop
    ti_simplex = BP(1,1);
    sigma_simplex = BP(1,2);
    Cinf_simplex = BP(1,4);
    %Generate Starting Simplex
    BP = zeros([no_var+1,no_var+1]);
    for i = 1:no_var+1
        BP(i,1) = ti_simplex; BP(i,2) = sigma_simplex; BP(i,4) =
Cinf_simplex;
        BP(i,3) = RS(3)*(0.95 +0.1*rand); BP(i,5) = RS(5)*(0.95 +0.1*rand);
        [~, ~, ~, ~, ~, ~, BP(i,no_var+1)] =
fNgo2019_RSS(ti_simplex,sigma_simplex,BP(i,3),...

Cinf_simplex,BP(i,5),weight_curve,system_par);
    end
    %End first pass

%~~~~~~~~~~~~~~~~~~~~~~~~~~~~~~~~~~~~~~~~~~~~~~~~~~~~~~~~~~~~~~~~~~~~~~~~~~~~
~~~~~
    %Second pass
    test = 1;
    run = 0;
    while test > second_termination_condition %checking convergent criterium
    run = run+1; %run count
    %Set points where RSS couldn't be computed to high RSS
    for i = 1:length(BP(:,1))
        if BP(i,no_var+1) == 0
            BP(i,no_var+1) = 9e5;
        end
    end
    %sort points
    BP = sortrows(BP,no_var+1);
    %Remove worst points, leave (no of dimension+1) for Simplex
    BP = BP(1:no_var+1,:);
    %Generate Simplex optimization points
    %Calculate coordinates of extended_reflect point
    for i = 1:no_var
        BPe(i) = 3*mean(BP(1:2,i))-2*BP(3,i);
        if BPe(i) < lower_bounds(i) %check out of bound
            BPe(i) = lower_bounds(i) + abs(BPe(i)-lower_bounds(i));
        end
        if BPe(i) > upper_bounds(i) %check out of bound
            BPe(i) = upper_bounds(i) - abs(BPe(i)-upper_bounds(i));
        end
    end
    %Calculate coordiates of reflect point
```

```
    for i = 1:no_var
        BPr(i) = 2*mean(BP(1:2,i))-1*BP(3,i);
        if BPr(i) < lower_bounds(i) %check out of bound
            BPr(i) = lower_bounds(i)+ abs(BPr(i)-lower_bounds(i));
        end
        if BPr(i) > upper_bounds(i) %check out of bound
            BPr(i) = upper_bounds(i) - abs(BPr(i)-upper_bounds(i));
        end
    end
    %Calculate coordiates of contracted_reflect point
    for i = 1:no_var
        BPcr(i) = 1.5*mean(BP(1:3,i))-0.5*BP(3,i);
        if BPcr(i) < lower_bounds(i) %check out of bound
            BPcr(i) = lower_bounds(i) + abs(BPcr(i)-lower_bounds(i));
        end
        if BPcr(i) > upper_bounds(i) %check out of bound
            BPcr(i) = upper_bounds(i) - abs(BPcr(i)-upper_bounds(i));
        end
    end
    %Calculate coordiates of contracted_worst point
    for i = 1:no_var
        BPcw(i) = .5*mean(BP(2,i))+0.5*BP(3,i);
        if BPcw(i) < lower_bounds(i) %check out of bound
            BPcw(i) = lower_bounds(i) + abs(BPcw(i)-lower_bounds(i));
        end
        if BPcw(i) > upper_bounds(i) %check out of bound
            BPcw(i) = upper_bounds(i) - abs(BPcw(i)-upper_bounds(i));
        end
    end
    %Evaluate optimization points, then select new point based on evaluation
    [~, ~, ~, ~, ~, ~, BPe(no_var+1)] = fNgo2019_RSS(BPe(1),BPe(2),BPe(3),...

BPe(4),BPe(5),weight_curve,system_par);
    [~, ~, ~, ~, ~, ~, BPr(no_var+1)] = fNgo2019_RSS(BPr(1),BPr(2),BPr(3),...

BPr(4),BPr(5),weight_curve,system_par);
    if  BPe(no_var+1) <= BP(1,no_var+1) && BPr(no_var+1) <= BP(1,no_var+1)
        NP = BPe;
    elseif  BPr(no_var+1) <= BP(1,no_var+1)
        NP = BPr;
    elseif  BPr(no_var+1) <= BP(2,no_var+1)
        NP = BPcr;
    else
        NP = BPcw;
    end
    [~, ~, ~, ~, ~, ~, NP(no_var+1)] =
fNgo2019_RSS(NP(1),NP(2),NP(3),NP(4),...
                                        NP(5),weight_curve,system_par);
    if  run > ARS_autostart
        %KTN's Adaptive Random Sampling
        %Calculate a set of random points based on new point and weighted
randomization
        %no_extend increases with run and with decreasing simplex group size
        no_extend =
round(alpha*(log10(test)*(100/log10(termination_condition)) +
100*run/max_iter));
        %size_extend increases with number of no_extend
```

```
        size_extend = beta*no_extend/(alpha*200);
        NP_extend = zeros([no_extend,no_var+1]); %preallocate array
        NP_extend_temp = zeros([no_extend,no_var+1]); %preallocate array
        for i = 1:no_extend
            for j = 1:no_var
                NP_extend(i,j) = NP(j)*(1-size_extend+2*size_extend*rand);
                if NP_extend(i,j) < lower_bounds(j) %check out of bound
                    NP_extend(i,j) = lower_bounds(j) + abs(NP_extend(i,j)-
lower_bounds(j));
                elseif NP_extend(i,j) > upper_bounds(j) %check out of bound
                    NP_extend(i,j) = upper_bounds(j) - abs(NP_extend(i,j)-
upper_bounds(j));
                end
            end
        end
        for i = 1:no_extend
            warning('off','MATLAB:integral:NonFiniteValue')
            NP_extend;
            [~, ~, ~, ~, ~, ~, RSS] = ...
                fNgo2019_RSS(ti_simplex,sigma_simplex,NP_extend(i,3),...
                Cinf_simplex,NP_extend(i,5),weight_curve,system_par);
            NP_extend_temp(i,:) = [ti_simplex sigma_simplex
NP_extend(i,3),...
                Cinf_simplex NP_extend(i,5) RSS]
        end
        NP_extend = NP_extend_temp;
        %Generate global random extend points in log k
        RP = zeros([no_extend,no_var]);
        for i = 1:no_extend
            for j = 1:no_var
                if i < no_var+2
                    RP(i,j) = start_point_log(j)*(0.999+0.002*rand);
                else
                RP(i,j) = lower_bounds_log(j)+rand*(upper_bounds_log(j)-
lower_bounds_log(j));
                end
            end
        end
        %Return to linear scale
        RP(:,3) = 10.^RP(:,3);
        %Evaluate RSS of random points
        SP = zeros([no_extend,no_var+1]);
        for i = 1:no_extend
            warning('off','MATLAB:integral:NonFiniteValue')
            RP; %call var to reduce parfor overhead
            [~, ~, ~, ~, ~, ~, RSS] =
fNgo2019_RSS(ti_simplex,sigma_simplex,RP(i,3),...

Cinf_simplex,RP(i,5),weight_curve,system_par);
            SP(i,:) = [ti_simplex sigma_simplex RP(i,3) Cinf_simplex  RP(i,5)
RSS];
        end
        NP_extend_full = [NP_extend;SP];
        BP = [BP(1:no_var,:);NP;NP_extend_full]; %add new point(s) to Simplex
    else
        BP = [BP(1:no_var,:);NP]; %add new point(s) to Simplex
    end
```

```
    %calculate test condition without new random points
    if run < max_iter
        test = std(BP(1:no_var,no_var+1))/mean(BP(1:no_var,no_var+1));
        test_matrix(k,:) = [k,run,test]; %store #run and convergence test
    else
        test = 0;
    end
    end
    %End Second pass

%~~~~~~~~~~~~~~~~~~~~~~~~~~~~~~~~~~~~~~~~~~~~~~~~~~~~~~~~~~~~~~~~~~~~~~~~~~~~~~~~
~~~~~
    [~, ~, E, ~, ~, ~, ~] = fNgo2019_RSS(BP(1,1),BP(1,2),BP(1,3),BP(1,4),...
                                         BP(1,5),weight_curve,system_par);
    E_ss = E(length(t));
    disp_point = BP(1,:);
    disp_point(no_var+2) = E_ss;
    fit_result(k,:) = disp_point; %store best point
    disp(['Fit for Fitting Sample ' num2str(k) ' finished. The parameters
are'])
    disp(disp_point)
end %end fitting
%%
%Sort fit result, remove fit that did not converge
fit_result(:,3) = log10(fit_result(:,3));
unsorted_fit_result = fit_result; %store a copy of fit_result
unsorted_test_matrix = test_matrix; %store a copy of test_matrix
minRSS = min(fit_result(:,no_var+1)); %calculate lowest RSS
threshold = minRSS*(1+RSS_threshold); %calculate rejection threshold
no_conv = no_sample; %number of convergent accepted
for i = 1:no_sample
    for j = 1:no_var
        if fit_result(i,j) >= (1-RSS_threshold)*upper_bounds_log(j)...
                || fit_result(i,j) <= (1+RSS_threshold)*lower_bounds_log(j)
            fit_result(i,no_var+1) = 9e5;
        end
    end
end
[fit_result,I_RSSsort] = sortrows(fit_result,no_var+1);
for i = 1:no_sample
    test_matrix(i,:) = unsorted_test_matrix(I_RSSsort(i),:);
end
for i = 1:no_sample
    if fit_result(i,no_var+1) > threshold
        no_conv = no_conv - 1;
    end
end
sorted_fit_result = zeros([no_conv,no_var+2]);
sorted_test_matrix = zeros([no_conv,3]);
for i = 1:no_conv
    sorted_fit_result(i,:) = fit_result(i,:);
    sorted_test_matrix(i,:) = test_matrix(i,:);
end
%Bootstrap confident interval
no_resample = 10000;
drs = zeros(no_resample, length(sorted_fit_result(1,:))); %preallocate delta
resample matrix
```

```
student_t = zeros(no_resample, length(sorted_fit_result(1,:)));
rs = zeros(length(sorted_fit_result(:,1))); %preallocate resample matrix
for i = 1:length(sorted_fit_result(1,:)) %cycle through each parameter
    for j = 1:no_resample %cycle through each resampling interation
        for k = 1:length(sorted_fit_result(:,1)) %calculate a single resample
            index = ceil(rand*length(sorted_fit_result(:,1))); %get random
index
            rs(j,k) = sorted_fit_result(index,i); %get random sample
        end
        student_t(j,i) =
sqrt(length(sorted_fit_result(:,1)))*abs(mean(rs(j,:)) -...
            mean(sorted_fit_result(:,i)))/std(rs(j,:));
        drs(j,i) = abs(mean(rs(j,:)) - mean(sorted_fit_result(:,i)));
    end
end
%Sort delta resample for all parameters
for i = 1:length(sorted_fit_result(1,:))
    student_t(:,i) = sort(student_t(:,i),'ascend');
    drs(:,i) = sort(drs(:,i),'ascend');
end
mean_par = zeros([length(sorted_fit_result(1,:)),1]);
CI_t = zeros([length(sorted_fit_result(1,:)),1]);
CI_d = zeros([length(sorted_fit_result(1,:)),1]);
CI_n = zeros([length(sorted_fit_result(1,:)),1]);
for i = 1:length(sorted_fit_result(1,:))
    mean_par(i) = mean(sorted_fit_result(:,i)); %calculate parameter means
    %calculate 95% confident interval bounds, two tail symmetrical
    CI_t(i) =
student_t(round(0.95*no_resample),i)*std(sorted_fit_result(:,i));
    CI_d(i) =
drs(round(0.95*no_resample),i)*sqrt(length(sorted_fit_result(:,1)));
    CI_n(i) =
tinv(0.975,length(sorted_fit_result(:,i)))*std(sorted_fit_result(:,i),'omitna
n');
end
result_matrix_t = [mean_par,CI_t];
result_matrix_d = [mean_par,CI_d];
result_matrix_n = [mean_par,CI_n];
fit_result = unsorted_fit_result; %restore fit_result
test_matrix = unsorted_test_matrix; %restore test_matrix
result_matrix = result_matrix_t;
%%
%%
disp('Result saved, fitting parameters and 95% CI are')
disp(result_matrix)
disp('Done. Fitting took')
toc
%%
%RSS function is defined separately from the Cdet version for compatibility
%with legacy code
function [Pext, P, E, Cout, Cdet, Csample, RSS] =
fNgo2019_RSS(ti,sigma,kext,Cinf,phi,w,system_par)
%System variables transfer
t = system_par.t; ts = system_par.ts; Q = system_par.Q; D = system_par.D;
lambda = system_par.lambda;
ro = system_par.ro; So = system_par.So; Pmo = system_par.Pmo; Cin =
system_par.Cin;
```

```
time_resolution = system_par.time_resolution; x = system_par.x; y =
system_par.y;
%Dependent variables calculation
De = D/lambda^2;
Dext = De*phi;
box_func = zeros([1 length(t)]);
for i = 1:length(t)
    if 0 <= t(i) && t(i) < ts
        box_func(i) = time_resolution/ts;
    end
end
gauss = time_resolution*(1/(sigma*sqrt(2*pi)))*exp(-(t - ti).^2/(2*sigma^2));
s_gauss = convnfft(box_func,gauss,'same'); %Sternberg Gaussian
Theta = ro*sqrt(kext/De); %dimentionless clearance
Text = ro^2/De; %s, dimentionless time scaling factor
%Define the transient part of Pext(t)
%!!! WARNING this evaluation requires symmetricat t array!!!!
%!!! assymetrical t array will slow down evaluation significantly!!!
f_int = @(u)(((4/pi^2)*u*exp(-(u^2+Theta^2)*(t/Text)))/...
    ((u^2+Theta^2)*((besselj(0,u))^2+(bessely(0,u))^2)));
%Evaluate the transient part of external medium permeability Pext(t)
Pext_transient = integral(f_int,0,inf,'ArrayValued',true);
%Evaluate the steady state part of external medium permeability Pext(t)
Pext_ss = Theta*besselk(1,Theta)/(besselk(0,Theta));
Pext_transient(isnan(Pext_transient)) = 0; %replace NaN with 0
Pext_transient(isinf(Pext_transient)) = 0; %replace inf with 0
%Evaluate dimensionless external medium permeability
Pext_dimensionless = Pext_transient+Pext_ss; %at t < 0, Pext = Pext_ss
Pext_dimensionless(isnan(Pext_dimensionless)) = Pext_ss; %replace NaN with
P_ss
Pext_dimensionless(isinf(Pext_dimensionless)) = Pext_ss; %replace inf with
P_ss
Pext = Pext_dimensionless*Dext/ro; %Calculate P1D(t)
P = 1./(1./Pext + 1/Pmo); %Calculate P(t)
E = 1-exp(-So*P/Q); %Calculate E(t)
Cout = Cin-E.*(Cin-Cinf); %Calculate Cout(t) at outlet of dialysis probe
Cdet = convnfft(Cout,s_gauss,'same'); %Compute concentration at detector
Cdet(t)
%Compute an array of time index where CSample will be sampled from Cdet
t_index = zeros([1,length(x)]);
index_offset = 1+abs(min(t)-60*min(x))/time_resolution;
t_index(1) = index_offset;
for i = 2:length(x)
    t_index(i) = round(t_index(i-1)+(x(i)-x(i-1))*60/time_resolution);
end
%Calculate Cdet at each sampling time
Csample = zeros([1,length(x)]);
for i=1:length(x)
    Csample(i) = Cdet(t_index(i));
end
%Calculate RSS
RSS = 0;
for i = 1:length(x)
    for j = 1:length(y(1,:))
        RSS = RSS+w(i)*(Csample(i) - y(i,j))^2;
    end
end
```

```
end
function A = convnfft(A, B, shape, dims, options)
%   KHANH T NGO KTN@PITT.EDU
%   Adapted from:
%https://www.mathworks.com/matlabcentral/fileexchange/24504-fft-based-
convolution
%   Author: Bruno Luong <brunoluong@yahoo.com>
% Copyright (c) 2009, Bruno Luong
% All rights reserved.
%
% Redistribution and use in source and binary forms, with or without
% modification, are permitted provided that the following conditions are met:
% * Redistributions of source code must retain the above copyright notice,
this
%   list of conditions and the following disclaimer.
% * Redistributions in binary form must reproduce the above copyright notice,
%   this list of conditions and the following disclaimer in the documentation
%   and/or other materials provided with the distribution
% * Neither the name of FOGALE nanotech nor the names of its
%   contributors may be used to endorse or promote products derived from this
%   software without specific prior written permission.
% THIS SOFTWARE IS PROVIDED BY THE COPYRIGHT HOLDERS AND CONTRIBUTORS "AS IS"
% AND ANY EXPRESS OR IMPLIED WARRANTIES, INCLUDING, BUT NOT LIMITED TO, THE
% IMPLIED WARRANTIES OF MERCHANTABILITY AND FITNESS FOR A PARTICULAR PURPOSE
ARE
% DISCLAIMED. IN NO EVENT SHALL THE COPYRIGHT OWNER OR CONTRIBUTORS BE LIABLE
% FOR ANY DIRECT, INDIRECT, INCIDENTAL, SPECIAL, EXEMPLARY, OR CONSEQUENTIAL
% DAMAGES (INCLUDING, BUT NOT LIMITED TO, PROCUREMENT OF SUBSTITUTE GOODS OR
% SERVICES; LOSS OF USE, DATA, OR PROFITS; OR BUSINESS INTERRUPTION) HOWEVER
% CAUSED AND ON ANY THEORY OF LIABILITY, WHETHER IN CONTRACT, STRICT
LIABILITY,
% OR TORT (INCLUDING NEGLIGENCE OR OTHERWISE) ARISING IN ANY WAY OUT OF THE
USE
% OF THIS SOFTWARE, EVEN IF ADVISED OF THE POSSIBILITY OF SUCH DAMAGE.
if nargin<3 || isempty(shape)
    shape = 'full';
end
if nargin<5 || isempty(options)
    options = struct();
elseif ~isstruct(options) % GPU options
    options = struct('GPU', options);
end
nd = max(ndims(A),ndims(B));
% work on all dimensions by default
if nargin<4 || isempty(dims)
    dims = 1:nd;
end
dims = reshape(dims, 1, []); % row (needed for for-loop index)
% GPU enable flag
GPU = getoption(options, 'GPU', false);
% Check if Jacket is installed
GPU = GPU && ~isempty(which('ginfo'));
% IFUN function will be used later to truncate the result
% M and N are respectively the length of A and B in some dimension
switch lower(shape)
    case 'full'
        ifun = @(m,n) 1:m+n-1;
```

```
    case 'same'
        ifun = @(m,n) ceil((n-1)/2)+(1:m);
    case 'valid'
        ifun = @(m,n) n:m;
    otherwise
        error('convnfft: unknown shape %s', shape);
end
classA = class(A);
classB = class(B);
ABreal = isreal(A) && isreal(B);
% Special case, empty convolution, try to follow MATLAB CONVN convention
if any(size(A)==0) || any(size(B)==0)
    szA = zeros(1,nd); szA(1:ndims(A))=size(A);
    szB = zeros(1,nd); szB(1:ndims(B))=size(B);
    % Matlab wants these:
    szA = max(szA,1); szB = max(szB,1);
    szC = szA;
    for dim=dims
        szC(dim) = length(ifun(szA(dim),szB(dim)));
    end
    A = zeros(szC,classA); % empty -> return zeros
    return
end
power2flag = getoption(options, 'Power2Flag', true);
if power2flag
    % faster FFT if the dimension is power of 2
    lfftfun = @(l) 2^nextpow2(l);
else
    % slower, but smaller temporary arrays
    lfftfun = @(l) l;
end
if GPU % GPU/Jacket FFT
    if isa(classA,'single')
        A = gsingle(A);
    else
        A = gdouble(A);
    end
    if isa(classB,'single')
        B = gsingle(B);
    else
        B = gdouble(B);
    end
    % Do the FFT
    subs(1:ndims(A)) = {':'};
    for dim=dims
        m = size(A,dim);
        n = size(B,dim);
        % compute the FFT length
        l = lfftfun(m+n-1);
        % We need to swap dimensions because GPU FFT works along the
        % first dimension
        if dim~=1 % do the work when only required
            swap = 1:nd;
            swap([1 dim]) = swap([dim 1]);
            A = permute(A, swap);
            B = permute(B, swap);
        end
```

```
        A = fft(A,l);
        B = fft(B,l);
        subs{dim} = ifun(m,n);
    end
else % Matlab FFT
    % Do the FFT
    subs(1:ndims(A)) = {':'};
    for dim=dims
        m = size(A,dim);
        n = size(B,dim);
        % compute the FFT length
        l = lfftfun(m+n-1);
        A = fft(A,l,dim);
        B = fft(B,l,dim);
        subs{dim} = ifun(m,n);
    end
end
if GPU
    A = A.*B;
    clear B
else
    % inplace product to save 1/3 of the memory
    %inplaceprod(A,B);
    %change made by KHANH T NGO KTN6@PITT.EDU
    %for compatibility with MATLAB 2019a WINDOWS 10
    A = A.*B;
end
% Back to the non-Fourier space
if GPU % GPU/Jacket FFT
    for dim=dims(end:-1:1) % reverse loop
        A = ifft(A,[]);
        % Swap back the dimensions
        if dim~=1 % do the work when only required
            swap = 1:nd;
            swap([1 dim]) = swap([dim 1]);
            A = permute(A, swap);
        end
    end
else % Matlab IFFT
    for dim=dims
        A = ifft(A,[],dim);
    end
end
% Truncate the results
if ABreal
    % Make sure the result is real
    A = real(A(subs{:}));
else
    A = A(subs{:});
end
% GPU/Jacket
if GPU
    % Cast the type back
    if isa(class(A),'gsingle')
        A = single(A);
    else
        A = double(A);
```

```
    end
end
end % convnfft
%% Get default option
function value = getoption(options, name, defaultvalue)
% function value = getoption(options, name, defaultvalue)
    value = defaultvalue;
    fields = fieldnames(options);
    found = strcmpi(name,fields);
    if any(found)
        i = find(found,1,'first');
        if ~isempty(options.(fields{i}))
            value = options.(fields{i});
        end
    end
end
```

5.6.2.2 Minimum-Searching Algorithm

Our minimum-searching algorithm proceeds as follows, where n is the number of fitting parameters, and a point is a set of coordinates consisting of fitting parameters, and a simplex is a set of n+1 points:

Step 1. Initialization:

- Choose a starting point.
    - A guess is given (user input).
    - A routine performs a linear regression and a logistic regression to guess t_i, σ and $C_{ECS\infty}$. The remaining parameters are copied from the above.
    - RSS of the two above are evaluated and compared.
    - The point with lower RSS is chosen to be start point.
- Generate a simplex around the starting point (range is ±0.5% about each coordinate).
- Generate a large number (e.g. 2^15) of random points over the entire parameter space.
- Evaluate RSS of the two sets above.
- Keep n+1 points with lowest RSS (“the current simplex”).

Step 2. Simplex loop

- NMS algorithm[203,204] using the current simplex to calculate direction toward local minimum.
- Adaptive Random Sampling (ARS, described below).
- Concatenate ARS result and NMS result.
- Check termination condition.

The simplex loop terminates when the spread of the current simplex's RSS is very small (i.e. relative standard deviation of the simplex's n+1 RSS is less than e.g. 10^{-8}) or when a large number of iterations is reached (e.g. 5000). Fits that are terminated at the latter conditions are rejected and their results are discarded.

Step 3. Termination

- Keep one point with the lowest RSS.

5.6.2.3 Adaptive Random Sampling

The ARS step generates random points local to the simplex, as well as in the global space. The number of ARS random point m is calculated using the following formula, where α is an adjustable parameter:

$$m = \alpha \times \left(100 \times \frac{\log(A)}{\log(B)} + 100 \times \frac{C}{D} \right)$$

Equation 5.6-5. Number of ARS random point

Where A is the current convergence criteria (defined as RSD of the simplex's RSS), B is the termination convergence criteria, C is the current iteration count, and D is the termination iteration count.

The random points have a spread of p around the NMS result. The spread p is calculated using the following formula, where β is an adjustable parameter:

$$p = \beta \times \frac{m}{200 \times \alpha}$$

Equation 5.6-6. ARS random point spread

The number of ARS random points and the spread of those points is determined by the spread of the simplex and the extend of the run. The smaller the spread of the simplex, indicating that a local optimum is near, the more ARS random points are generated to find a better minimum. The longer the loop has been run, the more ARS random points are generated to find a minimum. The spread of the ARS random points is scaled to the number of ARS random points. The more random points there are, the more they spread out to find a better minimum.

5.6.3 Additional Figures

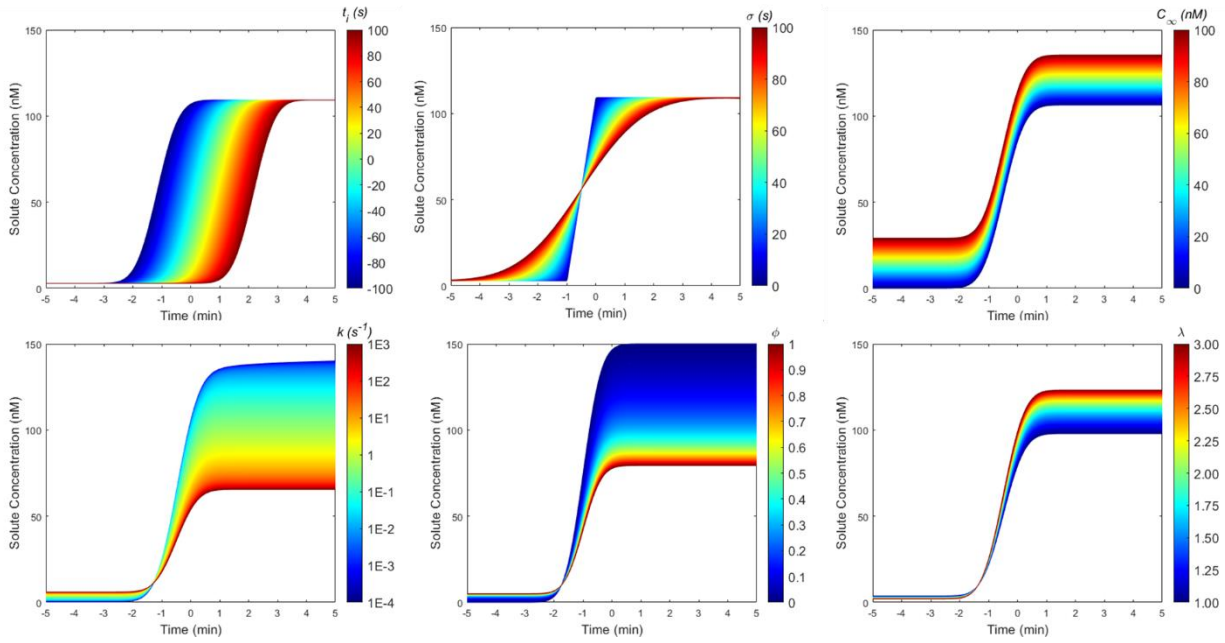

Figure 5.6-2. Simulated microdialysis transient response to a 150 nM retrodialysis.

Shown are the responses when each of the six parameters t_i, σ, $C_{ECS\infty}$, k, ϕ and λ is varied while the others stay constant. The original curve is simulated with: t_i = -60 (s), σ = 30 (s), $C_{ECS\infty}$ = 10 nM, k = 0.2 s^{-1}, ϕ = 0.2, λ = 1.6.

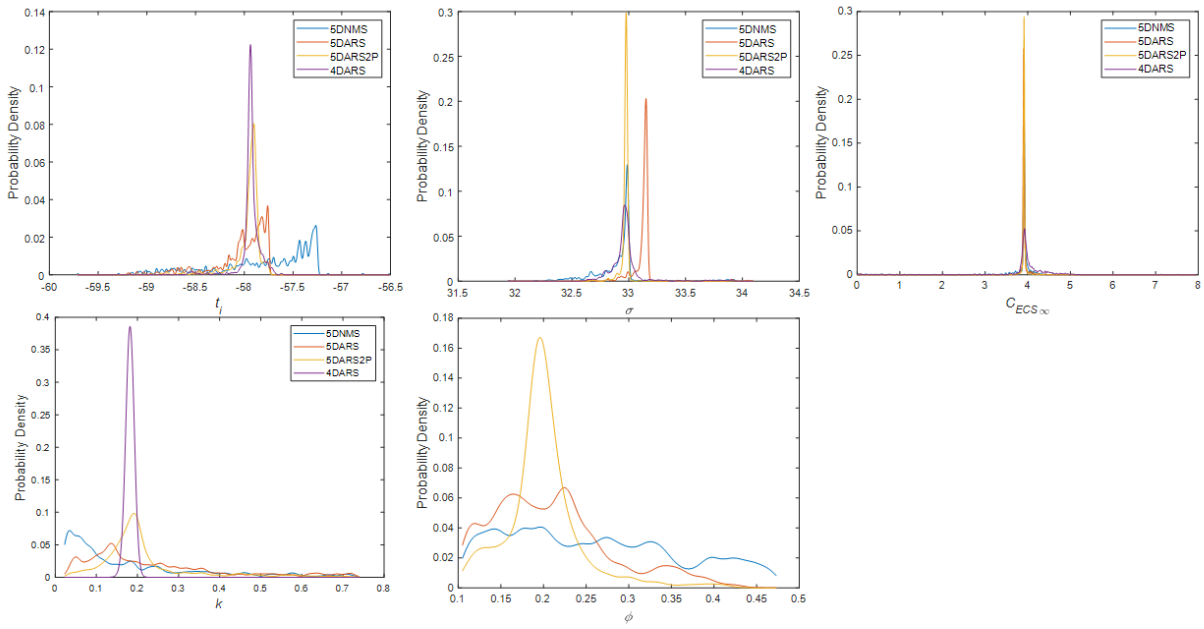

Figure 5.6-3. Comparison between distribution of t_i, σ, $C_{ECS\infty}$, k, and ϕ from 1000 repeats of 5DNMS (blue), 5DARS (red), 5DARS2P (orange) and 4DARS (purple) to in vivo experimental data.

The probability density curve is calculated using Kernel Density Estimator with a bandwidth of 0.01.

Coverage rates are 61.6%, 45.8%, 80.9% and 100%, respectively.

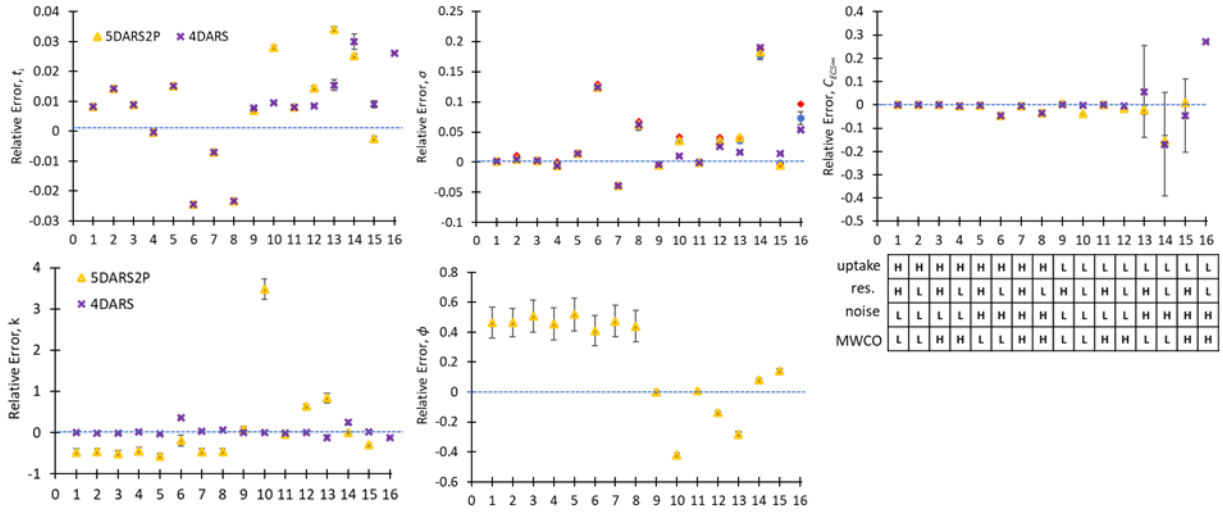

Figure 5.6-4. Comparison between relative error in t_i, σ, $C_{ECS\infty}$, k, and ϕ from 100 repeats of 5DARS2P (orange) and 4DARS (purple) to 16 simulated data sets.

Simulation parameter: Uptake rate constant k (s^{-1}) Low = 10^{-2}; High = 1; Microdialysis time resolution (s) Low = 15; High = 1; Normally Distributed Noise (σ) Low = 1%; High = 10%; Probe MWCO (kDA) Low = 13; High = 18. 5DARS2P produces no successful fit for set 16.

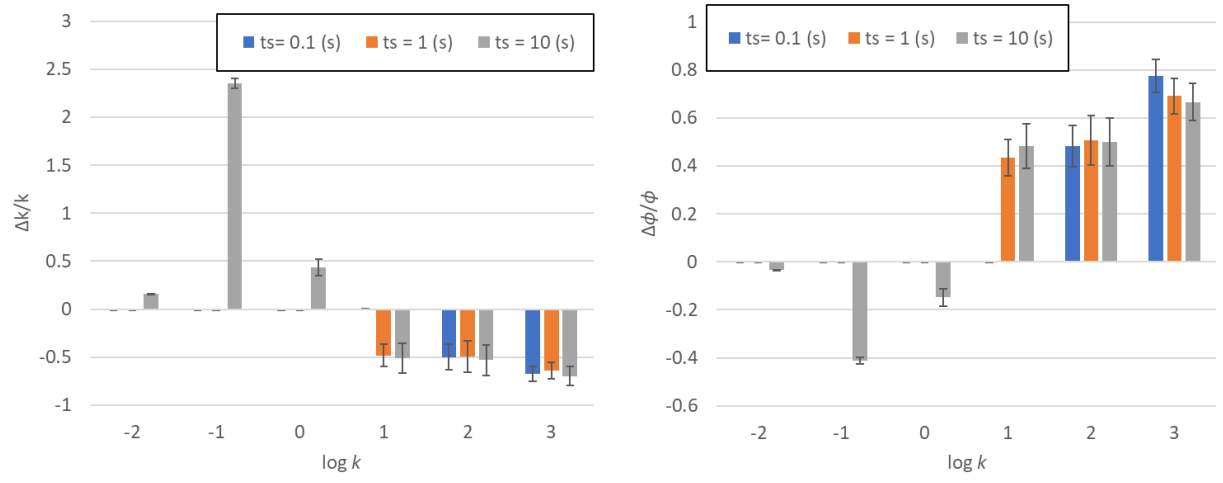

Figure 5.6-5. Comparison between error in k and relative error in ϕ from 100 repeats of 5DARS2P to 18 simulated data sets with varied chromatographic sampling time (t_s) and no noise, perfect probe dispersion (σ = 0.1 s or 1 s, $\sigma \leq t_s$).

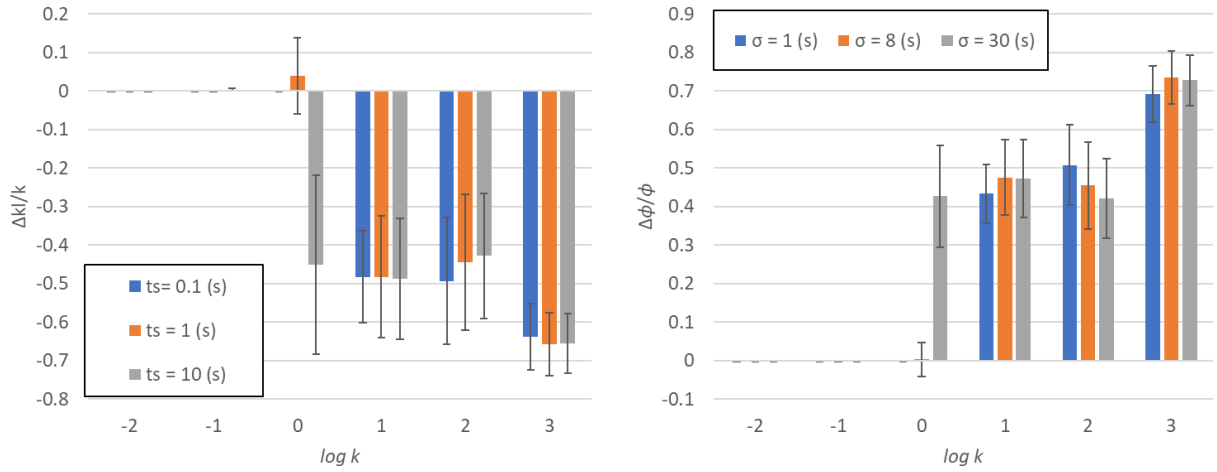

Figure 5.6-6. Comparison between error in *k* and relative error in ϕ from 100 repeats of 5DARS2P to 18 simulated data sets with varied probe dispersion (σ) and no noise, perfect chromatographic sampling time (t_s = 1 s).

Table 5.6-1. Comparison between mean and 95% C.I. of t_i, σ, $C_{ECS\infty}$, *k*, and ϕ from 1000 repeats of 5DNMS, 5DARS, 5DARS2P and 4DARS to in vivo experimental data.

Mean and 95% C.I. were calculated using both a normal distribution assumption and bootstrap-t.

	4DARS				5DNMS			
	norm. distr.		bootstrap		norm. distr.		bootstrap	
	mean	95% C.I.	mean	95% C.I.	mean	95% C.I.	mean	95% C.I.
t_i	-57.9342	0.006623	-57.9342	0.006665	-57.7936	0.040642	-58.2724	0.03823
σ	32.96693	0.009483	32.96693	0.009613	32.90799	0.017089	32.90749	0.016863
k	0.181656	0.000208	0.181656	0.000211	0.118359	0.008897	0.11831	0.008237
$C_{ECS\infty}$	3.945633	0.036622	3.945633	0.036538	3.81466	0.053159	3.828314	0.054846
ϕ					0.258807	0.008036	0.256958	0.007422
	5DARS				5DARS2P			
	norm. distr.		bootstrap		norm. distr.		bootstrap	
	mean	95% C.I.	mean	95% C.I.	mean	95% C.I.	mean	95% C.I.
t_i	-58.0282	0.026272	-57.9546	0.009933	-57.9546	0.009981	-57.4625	0.012624
σ	33.13182	0.010678	32.9696	0.003392	32.9696	0.003396	32.96966	0.003159
k	0.183122	0.012442	0.19139	0.006516	0.19139	0.006505	0.191832	0.007514
$C_{ECS\infty}$	3.865465	0.036877	3.915635	0.009792	3.915635	0.010187	3.92209	0.004577
ϕ	0.208689	0.006381	0.199428	0.003136	0.199428	0.003102	0.200296	0.003652

6.0 Conclusions

The work in this dissertation improved many experimental and theoretical aspects of Fast Microdialysis to establish new applications that answer biologically relevant questions, many of which are infeasible with steady-state microdialysis. The experimental improvements comprehensively entail the entire microdialysis analytical system. They include better perfusate delivery to generate concentration changes for retrodialysis experiments without interrupting flow, rotating operant chamber to perform behavioral studies without degrading Fast Microdialysis time resolution, chromatographic optimization to enable hours to days long experiment, and a sampling technique to increase effective time resolution, to name a few. The theoretical improvements created a mathematical framework to describe effects of experimental conditions to experimentally observable quantities and applied advance data analysis techniques to elucidate biological and system information from experimental measurements.

In the investigation of DEX treatment to traumatic penetration injury caused by probe implantation, Fast Microdialysis allowed for an unprecedented number of basal DA measurements in the striatum (approx. 2500 in 22 rats). Linear regression showed that DEX treatment potentiates (by 64%) and changes the distribution (from normal to log normal) of basal DA measurements. Most significantly, with the one-minute time resolution provided by Fast Microdialysis, retrodialysis of 100 mM K^+ was found to evoke rapid, large, oscillations in DA concentration adjacent to the probe site. Simultaneous local field potential and DA measurements validated that these oscillations were spreading depolarization events, a common pathological response to traumatic brain injury. Principle component analysis showed that the evoked response correlated to both the DEX treatment and number of recovery days. This work thus conclusively established

that tissue adjacent to probe site is capable of pathological response, and therefore is viable and has functional dopamine terminals.

The rotating operant chamber was created to conduct behavioral study with Fast Microdialysis. With the rotating operant chamber, operant behavior components and their associated controllers, power delivery, data acquisition and wireless data transmitter all rotate with a raturn so that the rat can move freely during the experiment, eliminating the need for liquid swivel which degrades time resolution. Using the rotating operant chamber, rats were trained and performed learned tasks, while DA concentrations were determined with Fast Microdialysis. Rats were also video-recorded for behavior analysis. An animal's untrained locomotive behaviors (e.g. grooming, limb movement) were found to correlate with large DA releases while the animal's trained feeding behavior correlated with smaller but rapidly oscillating DA releases. This correlation of oscillations and behavior has not been observed by other means, demonstrating the unique capabilities of Fast Microdialysis.

Comprehensive Quantitative Microdialysis (CQM) was created both as a new quantitative microdialysis technique that enables determination of solute concentration in the ECS; and a new theoretical and experimental framework that allows for determination of biological and systemic factors that influences the solute concentration observed at the detector, including sample transport time, hydrodynamic dispersion, uptake rate constant, and tissue porosity. We created a simulation tool and curve fit tool in MATLAB for these purposes. Analysis of transient responses on an awake rat using CQM found striatal tissue porosity, and striatal DA uptake rate constant comparable with established literature values. Extraction fraction and DA ECS concentration found were comparable to measurements made with traditional steady-state method (No-Net-Flux). The analysis also determined with high precision the time delay between a DA concentration change

at the probe (e.g. behavior-related DA release) and measurements at the detector. It is remarkable that all of this information can be obtained from transient responses on an awake rat using microdialysis in under an hour of experimental time. Exploration of curve fit to simulated data showed that CQM is robust to drastic changes in experimental conditions, including high noise and high uptake rate constant.

7.0 Future Work

From the work shown in this dissertation, particularly quantitative analysis of transient response using the Comprehensive Quantitative Microdialysis technique[180,202], it is apparent that there is still a pressing need for a higher time resolution, in the order of 15 s or less, for Fast Microdialysis. This will eliminate the need for time-interleaved sampling to measure transient responses, therefore improves the quality of the measurements obtained and reduces experiment time. It will also bring Fast Microdialysis to parity with Fast Scan Controlled Absorption Voltammetry[49,51] or PEDOT/functionalized carbon nanotube-coated carbon fiber microelectrodes with square wave voltammetry[52] in term of time resolution for basal level measurements of low concentration (nM) neurotransmitters. We have preliminary theoretical and experimental work making significant progress toward higher time resolution for Fast Microdialysis of Dopamine (see below).

7.1 Sub-minute Fast Microdialysis Determination of Dopamine with Online Dilution and Low Flow Microdialysis

The limit to our Fast Microdialysis DA determination is the poor peak shape and low number of theoretical plates for DA. The separation was optimized for continuous 60 s *in vivo* online separation for up to 96 hours. Chromatographically, the separation conditions are also near optimal. Well-established theories[231,232] predict a reduced plate height *h* of about 6. However, experimental *in vivo* separation of DA only achieves *h* of about 22 (Figure 7.1-1). Exploring

separation conditions, we found that the separation is better in aqueous (D.I. water) than in saline (aCSF or dialysate) conditions (Figure 7.1-2). The same conclusion holds true across different mobile phases that we tested (Figure 7.1-3).

We hypothesized that the high ionic strength of the biological saline solutions hinders ion-pairing, which is the retention mechanism of DA in our ion-pairing reversed-phase HPLC. Based on this hypothesis, we tested a number of solutions:

- Adding ion-pairing agent during injections. Theoretically, this should aid ion-paring during the injection, without significantly increase the retention time. We found that this improved the peak shape, but it causes DA to split to two peaks.
- Adding chelating agent during injections. Theoretically, we could chelate ions (e.g. Mg^{2+} and Ca^{2+}) thus reduce their impact to the separation. However, as the separation is at low pH, chelating agents are ineffective. Theoretical calculation and experiments showed that added EDTA during injection did not improve the separation.
- Working electrode surface modification. PEDOT-based coatings has been shown to improve selectivity to Dopamine[52,233,234]. By increasing DA selectivity, the separation could have fewer interferences from other biological solutes, thus providing an opportunity for better chromatographic separation. We found that the surface modification does not appreciably improve our chromatograms.
- Reducing the ionic strength of the injected solution. We tested this by diluting the saline DA standards with DI water prior to injection, and by making saline standards with lower salt concentrations. This solution proved to be effective, and peak width was reduced (i.e. better separation) as the ionic strength of the DA standard decreased (Figure 7.1-4).

Dilution of samples is typically not desirable, as it reduces the concentration of solutes in the sample, thus worsen limit of quantitation. The limit of quantitation of our Fast Microdialysis method is not significantly higher than the lowest concentration of Dopamine that we have measured in dialysate[97,98], thus a higher limit of quantitation is not acceptable. However, for a microdialysis experiment, dilution can be combined with lowering the flow rate of the dialysate. The concentration of the solute on in the dialysate is dependent to the flow rate, the lower the flow rate, the higher concentration of the solute recovered[12,60,84,235] (Figure 7.1-5). This increased recovery at lower flow rate compensates for the decreases in solute concentration as the sample is diluted. The dilution can be done online, prior to injection using a zero dead volume mixer[236,237].

Theoretical calculations and *in vitro* experiment shows that when dialysate flow rate is reduced and the dialysate is diluted with D.I. water prior to injection (total flowrate and injection volume are constant, and are identical to typical Fast Microdialysis) the peak width of the separation decreases (better separation) while peak height increases at the same time (Figure 7.1-6). Leveraging this improvement in DA separation, we have obtained preliminary results showing improved *in vivo* separation (Figure 7.1-7) and feasibility of 30 s online *in vivo* DA determination using online dilution of low flow microdialysis (Figure 7.1-8).

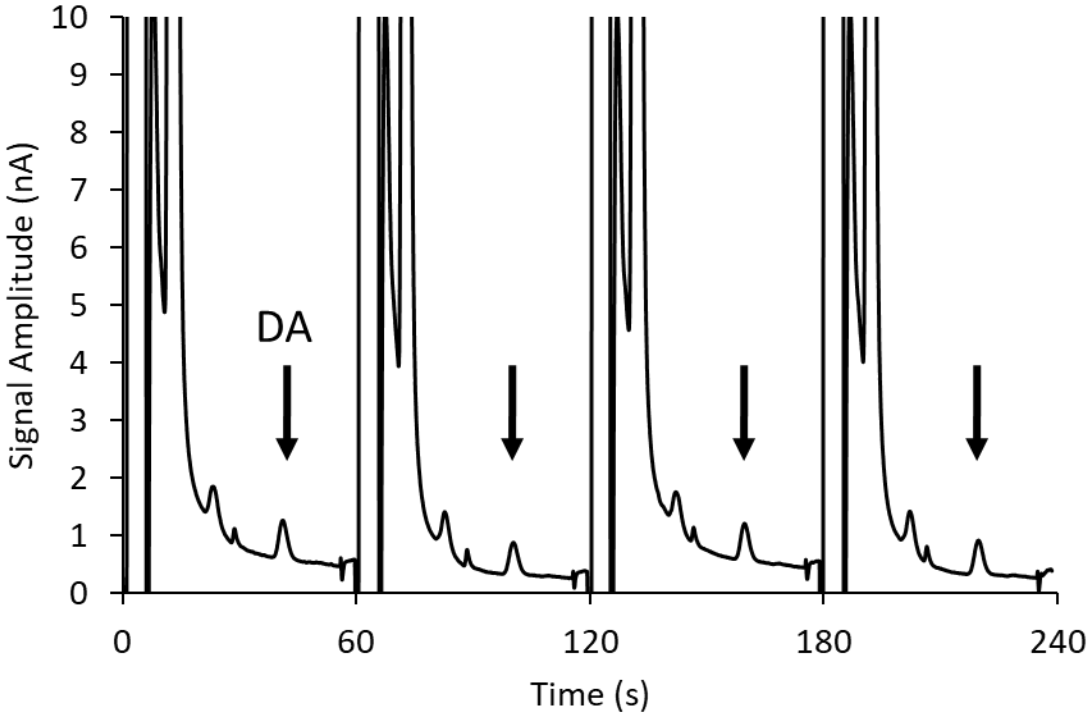

Figure 7.1-1. Typical Dopamine Separation with Fast Microdialysis. Shown are four continuous 60 s chromatograms.

The DA peak is indicated with an arrow. Column: 60 mm × 0.15 mm I.D, 1.7 µm BEH C18, 32.5°C. Mobile phase: 9 µL/min 100 mM NaOAc, 1.75 mM SOS, 0.15 mM EDTA, 3% v/v ACN, 2% v/v HOAc, pH 4.5. Detector: 400 mV vs Ag/AgCl (3M NaCl).

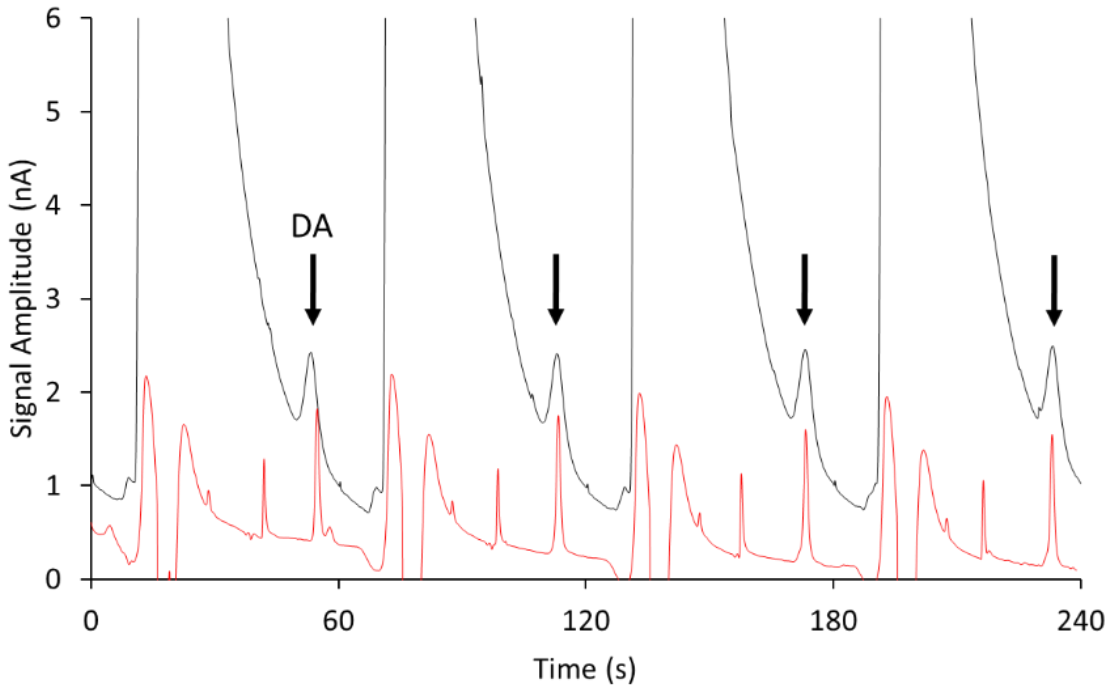

Figure 7.1-2. Comparison between separation of Dopamine in aqueous (red) and in saline (black) conditions. Shown are four continuous 60 s chromatograms. The DA peak is indicated with an arrow. . Column: 90 mm × 0.15 mm I.D, 1.7 µm BEH C18, 75°C. Mobile phase: 8 µL/min 100 mM NaOAc, 1.75 mM SOS, 0.15 mM EDTA, 3% v/v ACN, 2% v/v HOAc, pH 4.5. Detector: 400 mV vs Ag/AgCl (3M NaCl).

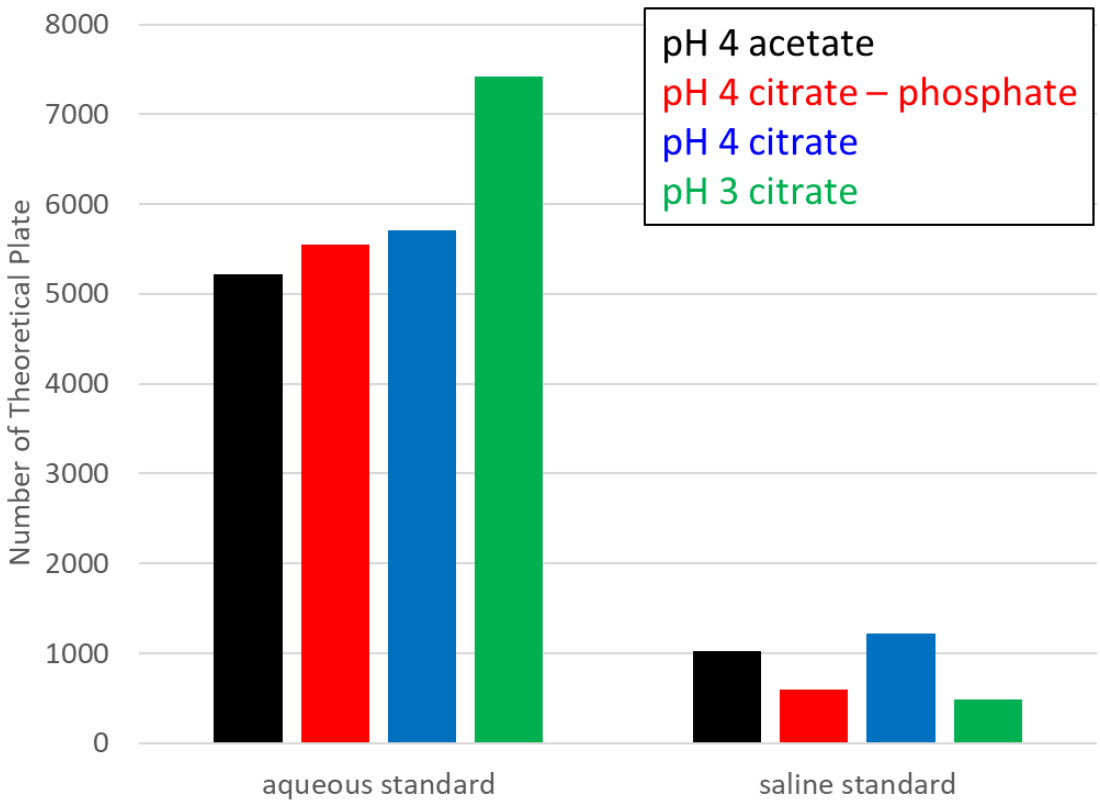

Figure 7.1-3. Comparison between separation of Dopamine in aqueous and in saline (black) conditions across different mobile phases.

Shown are number of theoretical plate for the same column and flowrate of separations in pH 4 acetate (black), pH 4 citrate-phosphate (red), pH 4 citrate (blue) and pH 3 citrate (green).

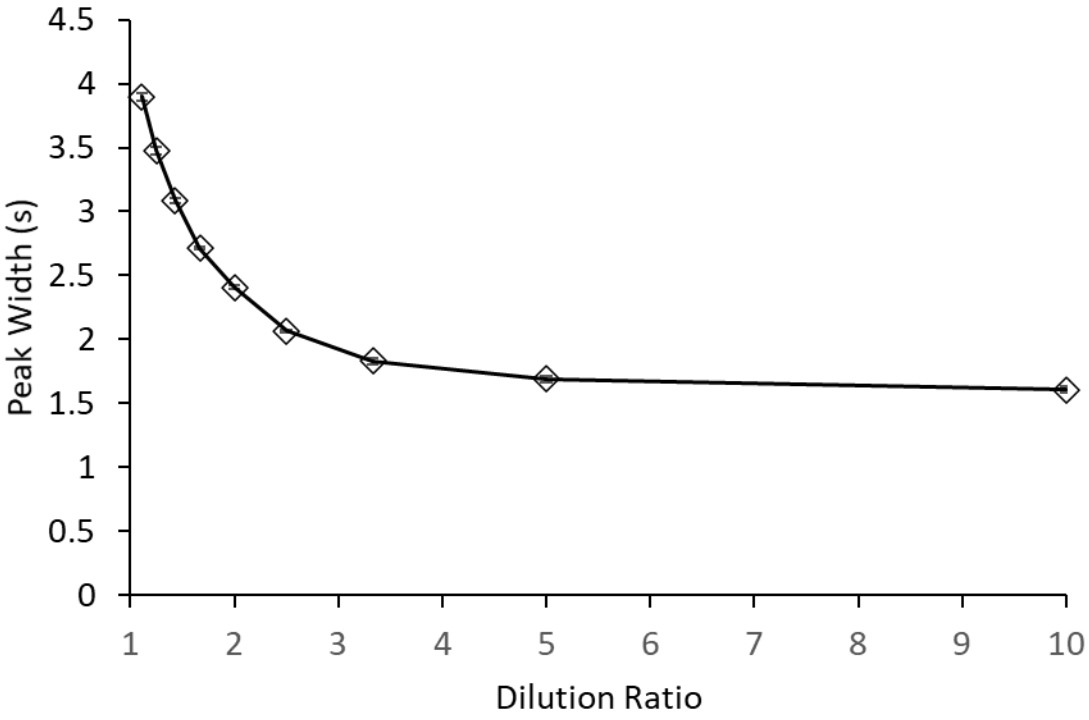

Figure 7.1-4. The effect of reducing the ionic strength of the solution to separation of DA. The ionic strength is reduced by dilution. Dilution ratio is the ratio of final volume to starting volume. Separation quality is measured in peak width.

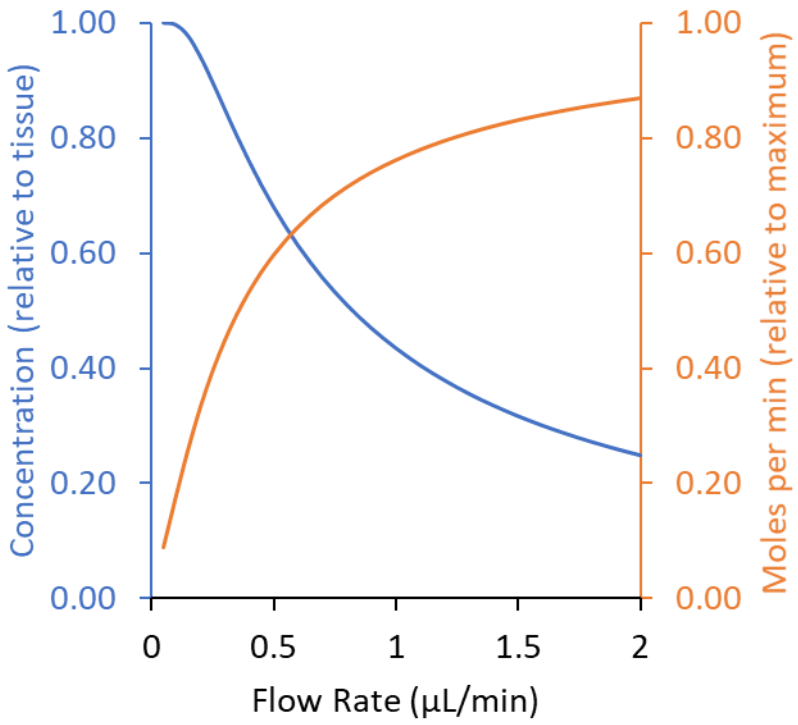

Figure 7.1-5. Relationship between dialysate flow rate and recovery in term of concentration (blue) and moles per min (orange).

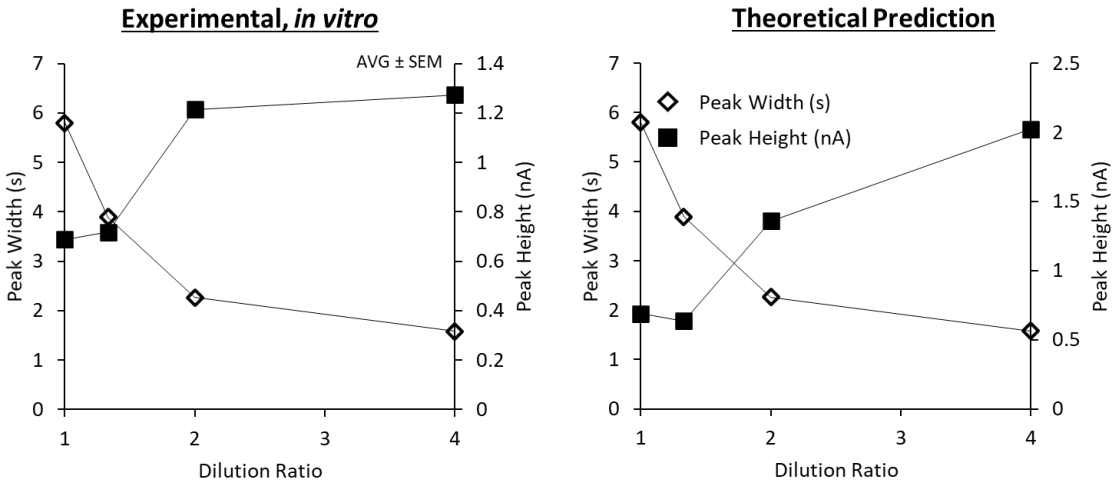

Figure 7.1-6. Comparison between in vitro experiment (left) and theoretical prediction (right) of low flow microdialysis with online dilution.

Peak width (open diamond) and peak height (solid squares) are shown.

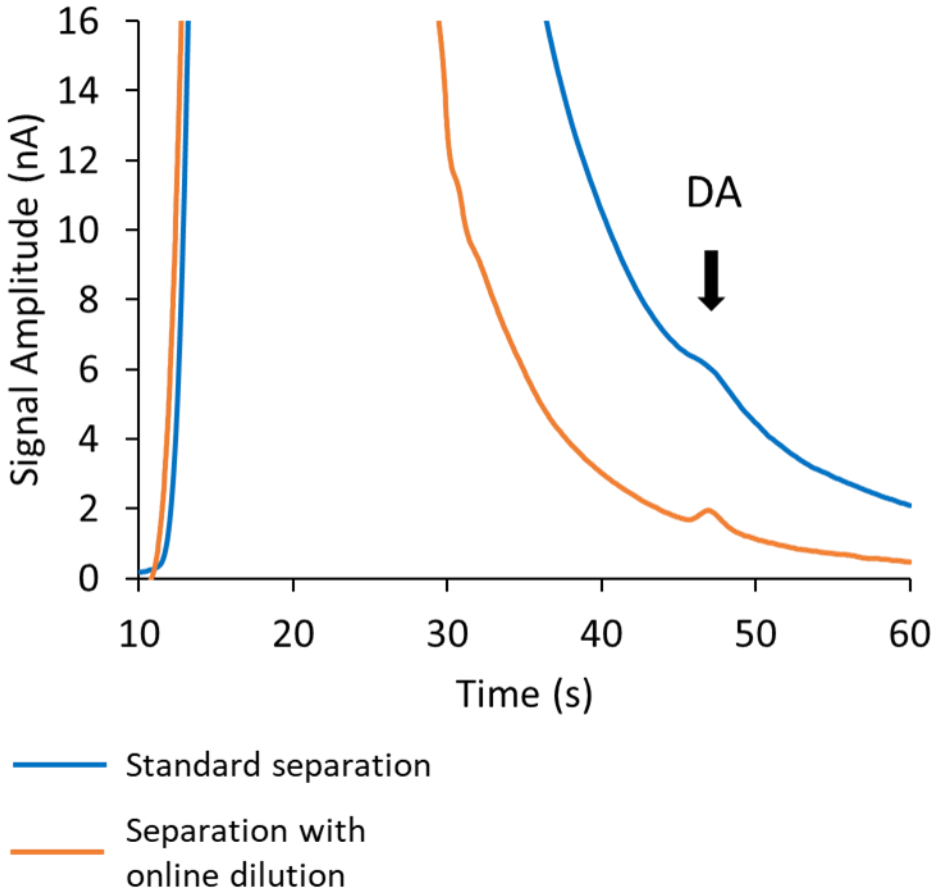

Figure 7.1-7. Comparison between typical Fast Microdialysis separation (blue) and separation using online dilution of low flow microdialysis (orange) of DA.

The DA peak is marked with an arrow. The standard separation injected 15 fmol of DA at 10.4±0.5 nM, resulting a peak width (FWHM) of 3.92±0.08 s and height of 0.54±0.01 nM, giving a plate count of 800. The diluted separation injected 5 fmol of DA at 18.90±0.00 nM, resulting a peak width (FWHM) of 1.73±0.02 s and height of 0.45±0.00 nM, giving a plate count of 4300.

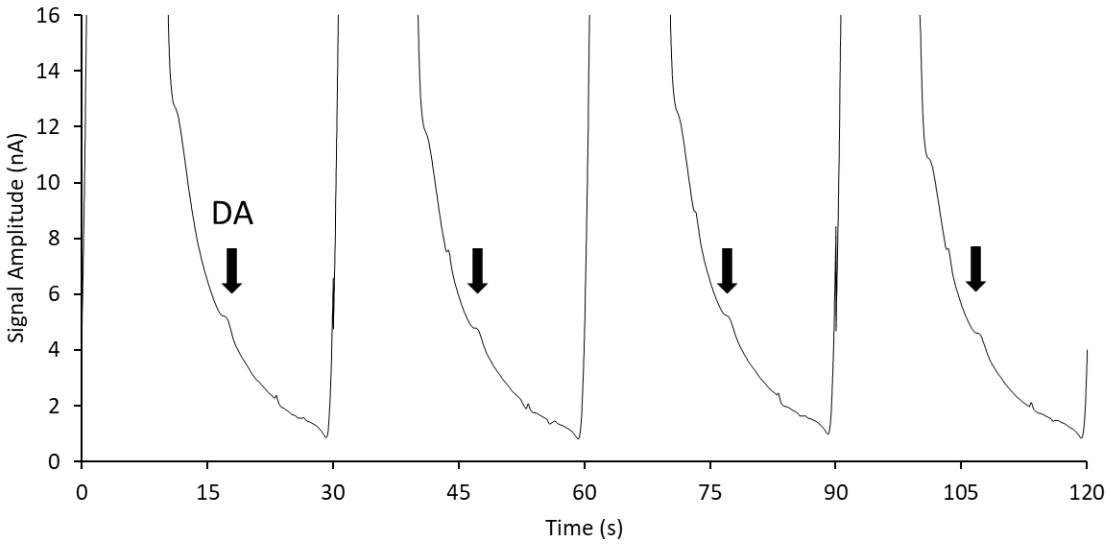

Figure 7.1-8. Online in vivo determination of DA at 30 s time resolution using Fast Microdialysis with online dilution and low flow microdialysis.

The DA peak is marked with an arrow.

References

(1) Riedel, G.; Platt, B.; Micheau, J. *Behav Brain Res* **2003**, *140*, 1-47.

(2) McEntee, W. J.; Crook, T. H. *Psychopharmacology (Berl)* **1993**, *111*, 391-401.

(3) Davis, K. L.; Kahn, R. S.; Ko, G.; Davidson, M. *Am J Psychiatry* **1991**, *148*, 1474-1486.

(4) Bradford, H. F. *Prog Neurobiol* **1995**, *47*, 477-511.

(5) Olney, J. W.; Farber, N. B. *Arch Gen Psychiatry* **1995**, *52*, 998-1007.

(6) Scatton, B.; Javoy-Agid, F.; Rouquier, L.; Dubois, B.; Agid, Y. *Brain Research* **1983**, *275*, 321-328.

(7) Brown, R. E.; Stevens, D. R.; Haas, H. L. *Prog Neurobiol* **2001**, *63*, 637-672.

(8) Qiu, Y.; Peng, Y.; Wang, J. *Adv Neuroimmunol* **1996**, *6*, 223-231.

(9) Michael, A. C.; Borland, L. M. *Electrochemical methods for neuroscience*; CRC Press/Taylor & Francis: Boca Raton, 2007, p 512 p., 518 p. of plates.

(10) Sharp, F. R.; Bernaudin, M. *Nat Rev Neurosci* **2004**, *5*, 437-448.

(11) Rupert, A. E.; Ou, Y.; Sandberg, M.; Weber, S. G. *ACS Chem Neurosci* **2013**, *4*, 838-848.

(12) Chefer, V. I.; Thompson, A. C.; Zapata, A.; Shippenberg, T. S. *Curr Protoc Neurosci* **2009**, *Chapter 7*, Unit7 1.

(13) Kegeles, L. *Neuropsychopharmacology* **1997**, *17*, 293-307.

(14) D. Badgaiyan, R. *Current Medical Imaging Reviews* **2011**, *7*, 98-103.

(15) Ungerstedt, U. *J Intern Med* **1991**, *230*, 365-373.

(16) Hammarlund-Udenaes, M. *AAPS J* **2017**, *19*, 1294-1303.

(17) Koepp, M. J.; Gunn, R. N.; Lawrence, A. D.; Cunningham, V. J.; Dagher, A.; Jones, T.; Brooks, D. J.; Bench, C. J.; Grasby, P. M. *Nature* **1998**, *393*, 266-268.

(18) Giuffrida, A.; Parsons, L. H.; Kerr, T. M.; Rodriguez de Fonseca, F.; Navarro, M.; Piomelli, D. *Nat Neurosci* **1999**, *2*, 358-363.

(19) Nicola, S. M.; Surmeier, J.; Malenka, R. C. *Annu Rev Neurosci* **2000**, *23*, 185-215.

(20) Surmeier, D. J.; Ding, J.; Day, M.; Wang, Z.; Shen, W. *Trends Neurosci* **2007**, *30*, 228-235.

(21) Rice, M. E.; Cragg, S. J. *Nat Neurosci* **2004**, *7*, 583-584.

(22) Gerfen, C. R.; Surmeier, D. J. *Annu Rev Neurosci* **2011**, *34*, 441-466.

(23) Ungerstedt, U. *Acta Physiol Scand Suppl* **1971**, *367*, 69-93.

(24) Shen, W.; Flajolet, M.; Greengard, P.; Surmeier, D. J. *Science* **2008**, *321*, 848-851.

(25) Meyer-Lindenberg, A.; Miletich, R. S.; Kohn, P. D.; Esposito, G.; Carson, R. E.; Quarantelli, M.; Weinberger, D. R.; Berman, K. F. *Nat Neurosci* **2002**, *5*, 267-271.

(26) Bernheimer, H.; Birkmayer, W.; Hornykiewicz, O.; Jellinger, K.; Seitelberger, F. *J Neurol Sci* **1973**, *20*, 415-455.

(27) Deutch, A. Y.; Cameron, D. S. *Neuroscience* **1992**, *46*, 49-56.

(28) Woodruff, G. N.; McCarthy, P. S.; Walker, R. J. *Brain Res* **1976**, *115*, 233-242.

(29) Salminen, O.; Murphy, K. L.; McIntosh, J. M.; Drago, J.; Marks, M. J.; Collins, A. C.; Grady, S. R. *Mol. Pharmacol.* **2004**, *65*, 1526-1535.

(30) Tossman, U.; Ungerstedt, U. *Neurosci Lett Suppl* **1981**, *7*, S479.

(31) Benveniste, H. *J Neurochem* **1989**, *52*, 1667-1679.

(32) Benveniste, H.; Huttemeier, P. C. *Prog Neurobiol* **1990**, *35*, 195-215.

(33) Davies, M. I. *Analytica Chimica Acta* **1999**, *379*, 227-249.

(34) Lunte, C. E.; Scott, D. O.; Kissinger, P. T. *Analytical Chemistry* **2008**, *63*, 773A-780A.

(35) Nandi, P.; Lunte, S. M. *Anal Chim Acta* **2009**, *651*, 1-14.

(36) Pettit, H. O.; Justice, J. B. *Pharmacology Biochemistry and Behavior* **1989**, *34*, 899-904.

(37) Flentge, F.; Venema, K.; Koch, T.; Korf, J. *Anal. Biochem.* **1992**, *204*, 305-310.

(38) Tsai, T. H. *J Chromatogr B Analyt Technol Biomed Life Sci* **2003**, *797*, 161-173.

(39) Hogan, B. L.; Lunte, S. M.; Stobaugh, J. F.; Lunte, C. E. *Anal Chem* **1994**, *66*, 596-602.

(40) Bowser, M. T.; Kennedy, R. T. *Electrophoresis* **2001**, *22*, 3668-3676.

(41) Parrot, S.; Bert, L.; Mouly-Badina, L.; Sauvinet, V.; Colussi-Mas, J.; Lambas-Senas, L.; Robert, F.; Bouilloux, J. P.; Suaud-Chagny, M. F.; Denoroy, L.; Renaud, B. *Cell Mol Neurobiol* **2003**, *23*, 793-804.

(42) Mecker, L. C.; Martin, R. S. *Anal Chem* **2008**, *80*, 9257-9264.

(43) Emmett, M. R.; Andrén, P. E.; Caprioli, R. M. *Journal of Neuroscience Methods* **1995**, *62*, 141-147.

(44) Liu, C.; Wu, Q.; Harms, A. C.; Smith, R. D. *Anal Chem* **1996**, *68*, 3295-3299.

(45) Kennedy, R. T. *Curr. Opin. Chem. Biol.* **2013**, *17*, 860-867.

(46) Watson, C. J.; Venton, B. J.; Kennedy, R. T. *Anal Chem* **2006**, *78*, 1391-1399.

(47) Yang, H.; Sampson, M. M.; Senturk, D.; Andrews, A. M. *ACS Chem Neurosci* **2015**, *6*, 1487-1501.

(48) Robinson, D. L.; Venton, B. J.; Heien, M. L.; Wightman, R. M. *Clin Chem* **2003**, *49*, 1763-1773.

(49) Atcherley, C. W.; Laude, N. D.; Parent, K. L.; Heien, M. L. *Langmuir* **2013**, *29*, 14885-14892.

(50) Atcherley, C. W.; Wood, K. M.; Parent, K. L.; Hashemi, P.; Heien, M. L. *Chem Commun (Camb)* **2015**, *51*, 2235-2238.

(51) Abdalla, A.; Atcherley, C. W.; Pathirathna, P.; Samaranayake, S.; Qiang, B.; Pena, E.; Morgan, S. L.; Heien, M. L.; Hashemi, P. *Anal Chem* **2017**, *89*, 9703-9711.

(52) Taylor, I. M.; Patel, N. A.; Freedman, N. C.; Castagnola, E.; Cui, X. T. *Anal Chem* **2019**, *91*, 12917-12927.

(53) Johnson, J. A.; Rodeberg, N. T.; Wightman, R. M. *Anal Chem* **2018**, *90*, 7181-7189.

(54) Menacherry, S.; Hubert, W.; Justice, J. B., Jr. *Anal Chem* **1992**, *64*, 577-583.

(55) Bungay, P. M.; Morrison, P. F.; Dedrick, R. L.; Chefer, V. I.; Zapata, A. In *Handbook of Microdialysis - Methods, Applications and Perspectives*, 2006, pp 131-167.

(56) Jacobson, I.; Sandberg, M.; Hamberger, A. *J Neurosci Methods* **1985**, *15*, 263-268.

(57) Amberg, G.; Lindefors, N. *J Pharmacol Methods* **1989**, *22*, 157-183.

(58) Chen, K. C.; Hoistad, M.; Kehr, J.; Fuxe, K.; Nicholson, C. *J Neurochem* **2002**, *81*, 108-121.

(59) Chen, K. C.; Hoistad, M.; Kehr, J.; Fuxe, K.; Nicholson, C. *J Neurochem* **2002**, *81*, 94-107.

(60) Morrison, P. F.; Bungay, P. M.; Hsiao, J. K.; Mefford, I. N.; Dykstra, K. H.; Dedrick, R. L. In *Microdialysis in the Neurosciences*, 1991, pp 47-80.

(61) Bungay, P. M.; Sumbria, R. K.; Bickel, U. *J Pharm Biomed Anal* **2011**, *55*, 54-63.

(62) Peters, J. L.; Michael, A. C. *J Neurochem* **1998**, *70*, 594-603.

(63) Yang, H.; Peters, J. L.; Allen, C.; Chern, S. S.; Coalson, R. D.; Michael, A. C. *Anal Chem* **2000**, *72*, 2042-2049.

(64) Tong, S.; Yuan, F. *J Pharm Biomed Anal* **2002**, *28*, 269-278.

(65) Bungay, P. M.; Newton-Vinson, P.; Isele, W.; Garris, P. A.; Justice, J. B. *J Neurochem* **2003**, *86*, 932-946.

(66) Nicholson, C. *Rep. Prog. Phys.* **2001**, *64*, 815-884.

(67) Wages, S. A.; Church, W. H.; Justice, J. B., Jr. *Anal Chem* **1986**, *58*, 1649-1656.

(68) Church, W. H.; Justice, J. B., Jr. *Anal Chem* **1987**, *59*, 712-716.

(69) Newton, A. P.; Justice, J. B., Jr. *Anal Chem* **1994**, *66*, 1468-1472.

(70) Justice, J. B.; Paige Newton, A.; Smith, A. D. *Journal of the Chinese Chemical Society* **1994**, *41*, 287-292.

(71) Wise, R. A.; Newton, P.; Leeb, K.; Burnette, B.; Pocock, D.; Justice, J. B., Jr. *Psychopharmacology (Berl)* **1995**, *120*, 10-20.

(72) Yang, H.; Thompson, A. B.; McIntosh, B. J.; Altieri, S. C.; Andrews, A. M. *ACS Chem Neurosci* **2013**, *4*, 790-798.

(73) Hocht, C.; Opezzo, J. A.; Taira, C. A. *J. Pharmacol. Toxicol. Methods* **2007**, *55*, 3-15.

(74) Liu, Y.; Zhang, J.; Xu, X.; Zhao, M. K.; Andrews, A. M.; Weber, S. G. *Anal Chem* **2010**, *82*, 9611-9616.

(75) Jung, M. C.; Shi, G.; Borland, L.; Michael, A. C.; Weber, S. G. *Anal Chem* **2006**, *78*, 1755-1760.

(76) Zhang, J.; Liu, Y.; Jaquins-Gerstl, A.; Shu, Z.; Michael, A. C.; Weber, S. G. *J Chromatogr A* **2012**, *1251*, 54-62.

(77) Zhang, J.; Jaquins-Gerstl, A.; Nesbitt, K. M.; Rutan, S. C.; Michael, A. C.; Weber, S. G. *Anal Chem* **2013**, *85*, 9889-9897.

(78) Gu, H.; Varner, E. L.; Groskreutz, S. R.; Michael, A. C.; Weber, S. G. *Anal Chem* **2015**, *87*, 6088-6094.

(79) Wang, M.; Roman, G. T.; Perry, M. L.; Kennedy, R. T. *Anal Chem* **2009**, *81*, 9072-9078.

(80) Wang, M.; Slaney, T.; Mabrouk, O.; Kennedy, R. T. *J Neurosci Methods* **2010**, *190*, 39-48.

(81) Wang, M.; Hershey, N. D.; Mabrouk, O. S.; Kennedy, R. T. *Anal Bioanal Chem* **2011**, *400*, 2013-2023.

(82) Yang, H.; Peters, J. L.; Michael, A. C. *J Neurochem* **1998**, *71*, 684-692.

(83) Stenken, J. A.; Holunga, D. M.; Decker, S. A.; Sun, L. *Anal. Biochem.* **2001**, *290*, 314-323.

(84) Bungay, P. M.; Morrison, P. F.; Dedrick, R. L. *Life Sci* **1990**, *46*, 105-119.

(85) Peters, J. L.; Miner, L. H.; Michael, A. C.; Sesack, S. R. *J Neurosci Methods* **2004**, *137*, 9-23.

(86) Jaquins-Gerstl, A.; Shu, Z.; Zhang, J.; Liu, Y.; Weber, S. G.; Michael, A. C. *Anal Chem* **2011**, *83*, 7662-7667.

(87) Nesbitt, K. M.; Jaquins-Gerstl, A.; Skoda, E. M.; Wipf, P.; Michael, A. C. *Anal Chem* **2013**, *85*, 8173-8179.

(88) Chen, K. C. *J Theor Biol* **2006**, *238*, 863-881.

(89) Norton, L. W.; Yuan, F.; Reichert, W. M. *Anal Chem* **2007**, *79*, 445-452.

(90) Borland, L. M.; Shi, G.; Yang, H.; Michael, A. C. *J Neurosci Methods* **2005**, *146*, 149-158.

(91) Michael, A. C.; Borland, L. M.; Mitala, J. J., Jr.; Willoughby, B. M.; Motzko, C. M. *J Neurochem* **2005**, *94*, 1202-1211.

(92) Nesbitt, K. M.; Varner, E. L.; Jaquins-Gerstl, A.; Michael, A. C. *ACS Chem Neurosci* **2015**, *6*, 163-173.

(93) Jaquins-Gerstl, A.; Michael, A. C. *Analyst* **2015**, *140*, 3696-3708.

(94) Parsons, L. H.; Justice, J. B., Jr. *J Neurochem* **1992**, *58*, 212-218.

(95) Gale, J. T.; Shields, D. C.; Ishizawa, Y.; Eskandar, E. N. *Front Behav Neurosci* **2014**, *8*, 114.

(96) Daubechies, I. *IEEE Transactions on Information Theory* **1990**, *36*, 961-1005.

(97) Ngo, K. T.; Varner, E. L.; Michael, A. C.; Weber, S. G. *ACS Chem Neurosci* **2017**, *8*, 329-338.

(98) Degreef, B.; Ngo, K. T.; Jaquins-Gerstl, A.; Weber, S. G. *J Neurosci Methods* **2019**, *326*, 108387.

(99) Wallgren, F.; Amberg, G.; Hickner, R. C.; Ekelund, U.; Jorfeldt, L.; Henriksson, J. *J Appl Physiol (1985)* **1995**, *79*, 648-659.

(100) Tuma, R.; Thomas, G. J., Jr. *Biophys. J.* **1996**, *71*, 3454-3466.

(101) Stenken, J. A.; Lunte, C. E.; Southard, M. Z.; Stahle, L. *J. Pharm. Sci.* **1997**, *86*, 958-966.

(102) Tang, A.; Bungay, P. M.; Gonzales, R. A. *J Neurosci Meth* **2003**, *126*, 1-11.

(103) Justice, J. B., Jr. *J Neurosci Methods* **1993**, *48*, 263-276.

(104) Chefer, V. I.; Thompson, A. C.; Zapata, A.; Shippenberg, T. S. **2009**.

(105) Tossman, U.; Wieloch, T.; Ungerstedt, U. *Neurosci Lett* **1985**, *62*, 231-235.

(106) Kehr, J. *J Chromatogr B Biomed Sci Appl* **1998**, *708*, 27-38.

(107) Richter, D. W.; Schmidt-Garcon, P.; Pierrefiche, O.; Bischoff, A. M.; Lalley, P. M. *J Physiol* **1999**, *514 (Pt 2)*, 567-578.

(108) Saigusa, T.; Fusa, K.; Okutsu, H.; Koshikawa, N. *J Oral Sci* **2001**, *43*, 129-134.

(109) Church, W. H.; Justice, J. B., Jr. *Adv Chromatogr* **1989**, *28*, 165-194.

(110) Tellez, S.; Forges, N.; Roussin, A.; Hernandez, L. *J Chromatogr B Biomed Sci Appl* **1992**, *581*, 257-266.

(111) Saylor, R. A.; Lunte, S. M. *J Chromatogr A* **2015**, *1382*, 48-64.

(112) Yoshitake, T.; Kehr, J.; Todoroki, K.; Nohta, H.; Yamaguchi, M. *Biomed Chromatogr* **2006**, *20*, 267-281.

(113) Yoshitake, T.; Fujino, K.; Kehr, J.; Ishida, J.; Nohta, H.; Yamaguchi, M. *Anal Biochem* **2003**, *312*, 125-133.

(114) Hows, M. E.; Lacroix, L.; Heidbreder, C.; Organ, A. J.; Shah, A. J. *J Neurosci Methods* **2004**, *138*, 123-132.

(115) Shackman, H. M.; Shou, M.; Cellar, N. A.; Watson, C. J.; Kennedy, R. T. *J Neurosci Methods* **2007**, *159*, 86-92.

(116) Butcher, S. P.; Fairbrother, I. S.; Kelly, J. S.; Arbuthnott, G. W. *J Neurochem* **1988**, *50*, 346-355.

(117) Donzanti, B. A.; Yamamoto, B. K. *Life Sci* **1988**, *43*, 913-922.

(118) Reinhoud, N. J.; Brouwer, H. J.; van Heerwaarden, L. M.; Korte-Bouws, G. A. *ACS Chem Neurosci* **2013**, *4*, 888-894.

(119) Perry, M.; Li, Q.; Kennedy, R. T. *Anal Chim Acta* **2009**, *653*, 1-22.

(120) Westerink, B. H. C.; Hofsteede, R. M.; Tuntler, J.; Vries, J. B. *J Neurochem* **1989**, *52*, 722-729.

(121) Nesbitt, K. M.; Varner, E. L.; Jaquins-Gerstl, A.; Michael, A. C. *ACS Chemical Neuroscience* **2015**, *6*, 163-173.

(122) Varner, E. L.; Jaquins-Gerstl, A.; Michael, A. C. *ACS Chem Neurosci* **2016**, *7*, 728-736.

(123) Ripley, T. L.; Jaworski, J.; Randall, P. K.; Gonzales, R. A. *J Neurosci Methods* **1997**, *78*, 7-14.

(124) Tang, A.; Bungay, P. M.; Gonzales, R. A. *J Neurosci Methods* **2003**, *126*, 1-11.

(125) Kametani, H.; Iijima, S.; Spangler, E. L.; Ingram, D. K.; Joseph, J. A. *Neurobiol Aging* **1995**, *16*, 639-646.

(126) Oyamada, T.; Hayashi, T.; Kagaya, A.; Yokota, N.; Yamawaki, S. *Neurochem Int* **1998**, *32*, 171-176.

(127) Kihara, T.; Ikeda, M.; Miyazaki, H.; Matsushita, A. *J Neurochem* **1993**, *61*, 1859-1864.

(128) Cosford, R. J.; Parsons, L. H.; Justice, J. B., Jr. *Neurosci Lett* **1994**, *178*, 175-178.

(129) Dreier, J. P. *Nat Med* **2011**, *17*, 439-447.

(130) Lauritzen, M.; Dreier, J. P.; Fabricius, M.; Hartings, J. A.; Graf, R.; Strong, A. J. *J Cereb Blood Flow Metab* **2011**, *31*, 17-35.

(131) Pusic, K. M.; Pusic, A. D.; Kemme, J.; Kraig, R. P. *Glia* **2014**, *62*, 1176-1194.

(132) Szalay, G.; Martinecz, B.; Lenart, N.; Kornyei, Z.; Orsolits, B.; Judak, L.; Csaszar, E.; Fekete, R.; West, B. L.; Katona, G.; Rozsa, B.; Denes, A. *Nat Commun* **2016**, *7*, 11499.

(133) Levi, G.; Raiteri, M. *Trends Neurosci* **1993**, *16*, 415-419.

(134) Hurd, Y. L.; Ungerstedt, U. *Life Sci* **1989**, *45*, 283-293.

(135) Hauber, W.; Fuchs, H. *Behav Brain Res* **2000**, *111*, 39-44.

(136) Chen, K. C. *J. Neurochem.* **2005**, *92*, 46-58.

(137) Peters, J. L.; Michael, A. C. *J. Neurochem.* **1998**, *70*, 594-603.

(138) Yang, H.; Peters, J. L.; Allen, C.; Chern, S.-S.; Coalson, R. D.; Michael, A. C. *Anal. Chem.* **2000**, *72*, 2042-2049.

(139) Sykova, E.; Nicholson, C. *Physiol. Rev.* **2008**, *88*, 1277-1340.

(140) Brimblecombe, K. R.; Cragg, S. J. *ACS Chemical Neuroscience* **2016**.

(141) Hoebel, B. G.; Hernandez, L.; Schwartz, D. H.; Mark, G. P.; Hunter, G. A. *Ann N Y Acad Sci* **1989**, *575*, 171-191; discussion 192-173.

(142) Minami, A.; Meguro, Y.; Ishibashi, S.; Ishii, A.; Shiratori, M.; Sai, S.; Horii, Y.; Shimizu, H.; Fukumoto, H.; Shimba, S.; Taguchi, R.; Takahashi, T.; Otsubo, T.; Ikeda, K.; Suzuki, T. *J Biol Chem* **2017**, *292*, 5645-5654.

(143) Kawano, T.; Oshibuchi, H.; Kawano, M.; Muraoka, H.; Tsutsumi, T.; Yamada, M.; Ishigooka, J.; Nishimura, K.; Inada, K. *Eur J Pharmacol* **2018**, *833*, 247-254.

(144) Muraoka, H.; Oshibuchi, H.; Kawano, M.; Kawano, T.; Tsutsumi, T.; Yamada, M.; Ishigooka, J.; Nishimura, K.; Inada, K. *Eur J Pharmacol* **2018**, *834*, 1-9.

(145) Papouin, T.; Dunphy, J. M.; Tolman, M.; Dineley, K. T.; Haydon, P. G. *Neuron* **2017**, *94*, 840-854 e847.

(146) Bassareo, V.; Cucca, F.; Frau, R.; Di Chiara, G. *Front Behav Neurosci* **2017**, *11*, 71.

(147) Doherty, J. M.; Schier, C. J.; Vena, A. A.; Dilly, G. A.; Gonzales, R. A. *Alcohol Clin Exp Res* **2016**, *40*, 1662-1670.

(148) D'Cunha, T. M.; Daoud, E.; Rizzo, D.; Bishop, A. B.; Russo, M.; Mourra, G.; Hamel, L.; Sedki, F.; Shalev, U. *Neuropsychopharmacology* **2017**, *42*, 1136-1145.

(149) Rogers, M. L.; Brennan, P. A.; Leong, C. L.; Gowers, S. A.; Aldridge, T.; Mellor, T. K.; Boutelle, M. G. *Anal Bioanal Chem* **2013**, *405*, 3881-3888.

(150) Ciriacks, C. M.; Bowser, M. T. *Anal Chem* **2004**, *76*, 6582-6587.

(151) Klinker, C. C.; Bowser, M. T. *Anal Chem* **2007**, *79*, 8747-8754.

(152) Harstad, R. K.; Bowser, M. T. *Anal Chem* **2016**, *88*, 8115-8122.

(153) Rossell, S.; Gonzalez, L.; Hernandez, L. *Journal of Chromatography B* **2003**, *784*, 385-393.

(154) Ngernsutivorakul, T.; Steyer, D. J.; Valenta, A. C.; Kennedy, R. T. *Anal Chem* **2018**, *90*, 10943-10950.

(155) Bungay, P. M.; Dedrick, R. L.; Fox, E.; Balis, F. M. *Pharmaceutical Research* **2001**, *18*, 361-366.

(156) Gowers, S. A. N.; Hamaoui, K.; Cunnea, P.; Anastasova, S.; Curto, V. F.; Vadgama, P.; Yang, G. Z.; Papalois, V.; Drakakis, E. M.; Fotopoulou, C.; Weber, S. G.; Boutelle, M. G. *The Analyst* **2018**, *143*, 715-724.

(157) Degreef, B.; Ngo, K. T.; Jaquins-Gerstl, A.; Weber, S. G., 2019.

(158) Degreef, B.; Ngo, K. T.; Jaquins-Gerstl, A.; Weber, S. G., 2019.

(159) Oppenheim, A. V.; Schafer, R. W.; Buck, J. R. *Discrete-time signal processing*, 2nd ed.; Prentice Hall: Upper Saddle River, N.J., 1999, p xxvi, 870 p.

(160) Nuttall, A. *IEEE Transactions on Acoustics, Speech, and Signal Processing* **1981**, *29*, 84-91.

(161) Priestley, M. B. *Journal of Time Series Analysis* **1996**, *17*, 85-103.

(162) Hendley, E. D. In *Handbook of Neurochemistry*, Lajtha, A., Ed.; Springer US: Boston, MA, 1984, pp 411-429.

(163) Grace, A. A. *Neuroscience* **1991**, *41*, 1-24.

(164) Grace, A. A. *Addiction* **2000**, *95 Suppl 2*, S119-128.

(165) Nicholson, C.; Phillips, J. M. *J Physiol* **1981**, *321*, 225-257.

(166) Nicholson, C.; Rice, M. E. **1988**, *9*, 247-362.

(167) Sykova, E.; Nicholson, C. *Physiol Rev* **2008**, *88*, 1277-1340.

(168) Olson, R. J.; Justice, J. B., Jr. *Anal Chem* **1993**, *65*, 1017-1022.

(169) Yim, H. J.; Gonzales, R. A. *Alcohol* **2000**, *22*, 107-115.

(170) Hoistad, M.; Chen, K. C.; Nicholson, C.; Fuxe, K.; Kehr, J. *J Neurochem* **2002**, *81*, 80-93.

(171) Yang, H.; Thompson, A. B.; McIntosh, B. J.; Altieri, S. C.; Andrews, A. M. *ACS Chemical Neuroscience* **2013**, *4*, 790-798.

(172) Rogers, M. L.; Feuerstein, D.; Leong, C. L.; Takagaki, M.; Niu, X.; Graf, R.; Boutelle, M. G. *ACS Chemical Neuroscience* **2013**, *4*, 799-807.

(173) Zhang, J.; Ngo, K. T.; Groskreutz, S. R.; Weber, S. G. In *Compendium of In Vivo Monitoring in Real-Time Molecular Neuroscience*, 2017, pp 141-170.

(174) Ouimet, C. M.; D'Amico, C. I.; Kennedy, R. T. *Anal Bioanal Chem* **2019**, *411*, 6155-6163.

(175) Hogerton, A. L.; Bowser, M. T. *Anal Chem* **2013**, *85*, 9070-9077.

(176) Probstein, R. F. *Physicochemical hydrodynamics : an introduction*, 2nd ed.; John Wiley & Sons: New York, 1994, p xv, 400 p.

(177) Beisler, A. T.; Schaefer, K. E.; Weber, S. G. *J Chromatogr A* **2003**, *986*, 247-251.

(178) Stenken, J. A.; Church, M. K.; Gill, C. A.; Clough, G. F. *AAPS J* **2010**, *12*, 73-78.

(179) Mou, X.; Lennartz, M. R.; Loegering, D. J.; Stenken, J. A. *J Diabetes Sci Technol* **2011**, *5*, 619-631.

(180) Ngo, K. T.; Weber, S. G. *Anal Chem* **2020**, *Submitted for Publication*.

(181) Lee, J.; Rahman, F.; Laoui, T.; Karnik, R. *Phys Rev E Stat Nonlin Soft Matter Phys* **2012**, *86*, 026301.

(182) Black, W. C.; Hodges, D. A. *IEEE Journal of Solid-State Circuits* **1980**, *15*, 1022-1029.

(183) Lonnroth, P.; Jansson, P. A.; Smith, U. *Am J Physiol* **1987**, *253*, E228-231.

(184) Rice, M. E.; Gerhardt, G. A.; Hierl, P. M.; Nagy, G.; Adams, R. N. *Neuroscience* **1985**, *15*, 891-902.

(185) Chefer, V. I.; Zapata, A.; Shippenberg, T. S.; Bungay, P. M. *J Neurosci Methods* **2006**, *155*, 187-193.

(186) Sternberg, J. C. In *Adv. Chromatogr.*, Giddings, J.; Keller, R. A., Eds.; Marcel Dekker: New York, NY, USA, 1966, pp 205-270.

(187) Iversen, L. L. *Br J Pharmacol* **1971**, *41*, 571-591.

(188) Michaelis, L.; Menten, M. L.; Johnson, K. A.; Goody, R. S. *Biochemistry* **2011**, *50*, 8264-8269.

(189) Wu, Q.; Reith, M. E.; Wightman, R. M.; Kawagoe, K. T.; Garris, P. A. *J Neurosci Methods* **2001**, *112*, 119-133.

(190) Tang, A.; George, M. A.; Randall, J. A.; Gonzales, R. A. *Alcohol Clin Exp Res* **2003**, *27*, 1083-1089.

(191) Brady, S. T.; Siegel, G. J.; Albers, R. W.; Price, D. L.; Benjamins, J. *Basic neurochemistry : principles of molecular, cellular, and medical neurobiology*, 8th ed.; Elsevier/Academic Press: Amsterdam ; Boston, 2012, p xxiv, 1096 p.

(192) Hernandez, L.; Stanley, B. G.; Hoebel, B. G. *Life Sci* **1986**, *39*, 2629-2637.

(193) Shippenberg, T. S.; Thompson, A. C. *Curr Protoc Neurosci* **2001**, *Chapter 7*, Unit7 1.

(194) McLawhorn, M.; James, M. L. In *Neuromonitoring Techniques*, 2018, pp 235-247.

(195) Boschi, G.; Launay, N.; Rips, R.; Scherrmann, J. M. *J. Pharmacol. Toxicol. Methods* **1995**, *33*, 29-33.

(196) Zapata, A.; Chefer, V. I.; Shippenberg, T. S. *Curr Protoc Neurosci* **2009**, *Chapter 7*, Unit7 2.

(197) Kolachana, B. S.; Saunders, R. C.; Weinberger, D. R. *J Neurosci Methods* **1994**, *55*, 1-6.

(198) Hutchinson, P. J.; O'Connell, M. T.; Al-Rawi, P. G.; Maskell, L. B.; Kett-White, R.; Gupta, A. K.; Richards, H. K.; Hutchinson, D. B.; Kirkpatrick, P. J.; Pickard, J. D. *J Neurosurg* **2000**, *93*, 37-43.

(199) Brunner, M.; Derendorf, H. *TrAC Trends in Analytical Chemistry* **2006**, *25*, 674-680.

(200) Lee, W. H.; Slaney, T. R.; Hower, R. W.; Kennedy, R. T. *Anal Chem* **2013**, *85*, 3828-3831.

(201) Lee, W. H.; Ngernsutivorakul, T.; Mabrouk, O. S.; Wong, J. M.; Dugan, C. E.; Pappas, S. S.; Yoon, H. J.; Kennedy, R. T. *Anal Chem* **2016**, *88*, 1230-1237.

(202) Ngo, K. T.; Weber, S. G. *Anal Chem* **2020**, *Submitted for Publication*.

(203) Nelder, J. A.; Mead, R. *The Computer Journal* **1965**, *7*, 308-313.

(204) Shavers, C. L.; Parsons, M. L.; Deming, S. N. *J. Chem. Educ.* **1979**, *56*.

(205) Chang, K.-H. *European Journal of Operational Research* **2012**, *220*, 684-694.

(206) Nelder, J. A. *Biometrics* **1961**, *17*.

(207) Walters, S. H.; Taylor, I. M.; Shu, Z.; Michael, A. C. *ACS Chem Neurosci* **2014**, *5*, 776-783.

(208) Barton, R. R.; Ivey, J. S. In *1991 Winter Simulation Conference Proceedings.*, 1991, pp 945-953.

(209) Bűrmen, Á.; Puhan, J.; Tuma, T. *Computational Optimization and Applications* **2006**, *34*, 359-375.

(210) Kucukdeniz, T.; Esnaf, S. *Journal of Enterprise Information Management* **2018**, *31*, 908-924.

(211) Li, Z.; Zhan, Y. In *2014 4th IEEE International Conference on Information Science and Technology*, 2014, pp 821-824.

(212) Yorgason, J. T.; Calipari, E. S.; Ferris, M. J.; Karkhanis, A. N.; Fordahl, S. C.; Weiner, J. L.; Jones, S. R. *Neuropharmacology* **2016**, *101*, 471-479.

(213) Garrouch, A. A.; Ali, L.; Qasem, F. *Industrial & Engineering Chemistry Research* **2001**, *40*, 4363-4369.

(214) Hrabetova, S.; Nicholson, C. *Neurochem Int* **2004**, *45*, 467-477.

(215) Rusakov, D. A.; Kullmann, D. M. *Proc Natl Acad Sci U S A* **1998**, *95*, 8975-8980.

(216) Saripall, K. P.; Serne, R. J.; Meyer, P. D.; McGrail, B. P. *Ground Water* **2002**, *40*, 346-352.

(217) Rudemo, M. *Scandinavian Journal of Statistics* **1982**, *9*, 65-78.

(218) Duller, G. A. T., 2007.

(219) Berger, G. W. *Anc. TL* **2010**, *28*, 55-66.

(220) Efron, B. *Journal of the American Statistical Association* **1987**, *82*, 171-185.

(221) Léger, C.; Romano, J. P. *Annals of the Institute of Statistical Mathematics* **1990**, *42*, 709-735.

(222) Efron, B.; Tibshirani, R. *An introduction to the bootstrap*; Chapman & Hall: New York, 1993, p xvi, 436 p.

(223) Torto, N. *Chromatographia* **2009**, *70*, 1305-1309.

(224) Rice, M. E.; Nicholson, C. In *Voltammetric Methods in Brain Systems*, 1995, pp 27-80.

(225) Godambe, V. P. *Biometrika* **1991**, *78*, 143-151.

(226) Johnson, M. L. In *Numerical Computer Methods, Part C*, 2000, pp 424-446.

(227) Jorgensen, B.; Knudsen, S. J. *Scandinavian Journal of Statistics* **2004**, *31*, 93-114.

(228) Singh, Y. S.; Sawarynski, L. E.; Dabiri, P. D.; Choi, W. R.; Andrews, A. M. *Anal Chem* **2011**, *83*, 6658-6666.

(229) Song, P.; Mabrouk, O. S.; Hershey, N. D.; Kennedy, R. T. *Anal Chem* **2012**, *84*, 412-419.

(230) DiCiccio, T. J.; Efron, B.; Hall, P.; Martin, M. A.; Canty, A. J.; Davison, A. C.; Hinkley, D. V.; Gleser, L. J.; Lee, S. M. S.; Young, G. A.; DiCiccio, T. J.; Efron, B. *Statistical Science* **1996**, *11*, 189-228.

(231) Carr, P. W.; Wang, X.; Stoll, D. R. *Anal Chem* **2009**, *81*, 5342-5353.

(232) Groskreutz, S. R.; Weber, S. G. *Anal Chem* **2016**, *88*, 11742-11749.

(233) Samba, R.; Schuhmann, W.; Sebastian, E.; Matychin, I.; Lydia, K.; Stelzle, M. In *Miniaturized Systems for Chemistry and Life Sciences*: Freiburg, Germany, 2013, pp 886-888.

(234) Vreeland, R. F.; Atcherley, C. W.; Russell, W. S.; Xie, J. Y.; Lu, D.; Laude, N. D.; Porreca, F.; Heien, M. L. *Anal Chem* **2015**, *87*, 2600-2607.

(235) Levich, V. G. *Physicochemical hydrodynamics*; Prentice-Hall: Englewood Cliffs, N.J., 1962, p 700 p.

(236) Jung, M. C.; Weber, S. G. *Anal Chem* **2005**, *77*, 974-982.

(237) Jung, M. C.; Munro, N.; Shi, G.; Michael, A. C.; Weber, S. G. *Anal Chem* **2006**, *78*, 1761-1768.